Quantum Chaos in Cold Atoms and Spin Waves

The Double Kicked Rotor

A Novel Classical and Quantum Mechanical Chaotic System

Mischa Stocklin

University College London, September 2007

ProQuest LLC
789 East Eisenhower Parkway
P.O. Box 1346
Ann Arbor, MI 48106-1346

I would like to thank my supervisor Prof. Tania Monteiro for her guidance and support throughout my time as a research student, which has been indispensable to the completion of the present work. I also thank Prof. Sougato Bose, Dr. Charles Creffield and Dr. Phil Jones for collaborations, helpful explanations and providing some of the figures in this thesis.

Furthermore I am very grateful to my fellow Ph.D. students, past and present, Matt Isherwood, Gwangok Hur, Malika Goonasekera and Tom Boness, for very helpful discussions concerning my work.

I also thank Tom Boness and Nicholas Powell for proof reading the thesis and making useful comments.

My thanks are also extended to my friends and co-workers at University College London and elsewhere, especially members of the TAMPA group, who have helped along in a number of ways. Finally special thanks go to my mother in Switzerland for her support and encouragement.

The Kicked Rotor is a well studied example of a classical Hamiltonian chaotic system, where the momentum of a particle is altered periodically in time through a series of external impulses or kicks, forming a sinusoidal potential. In the chaotic regime this results in a diffusion mechanism, where the average energy of an ensemble of particles grows linearly in time, including certain corrections to the diffusion rate, arising from correlations between kicks at different times. This system has a quantum analogue, the Quantum Kicked Rotor, which exhibits the phenomenon of dynamical localization (DL), a quantum destructive interference effect, where the average energy increase is halted after a given time, and an asymptotic exponential momentum distribution is obtained. Experiments have been performed using ultracold atoms and standing waves of laser light. This thesis investigates the newly discovered Double Kicked Rotor, where pairs of closely spaced kicks are applied to particles. This results in momentum space being divided into a number of cells in which fast energy absorption occurs, whereas at the cell boundaries, termed momentum trapping regions, particles absorb almost no energy. It is shown that the effect is almost entirely independent of the time interval between the kick pairs. It is further shown that the diffusion mechanism is due to a strong momentum dependence of the kick correlations. Novel global long-range correlations in time are found to control the system behaviour significantly - a very unusual situation for a chaotic system. The Quantum Double Kicked Rotor is also investigated, both in the context of laser pulses applied to cold atoms and magnetic fields applied to Heisenberg spin chains. Trapping in momentum and position space occurs respectively, and DL results in an asymptotic imprint of the asymmetries in momentum or spin distributions. The classical diffusion calculations are used to explain the experimental results. Novel scaling properties are also discussed.

Contents

Chapter 1

Introduction: Classical and Quantum Chaos

A brief introduction to classical and quantum chaos theories is given here, in particular concerning phenomena relevant to the investigations presented in this thesis. The need for a theory of quantum chaos arises from the correspondence principle requiring a quantum counterpart to classical chaotic motion. Although some characteristics of classical chaos, such as exponential separation of trajectories and extreme sensitivity to initial conditions, are absent in the quantum case, signatures of chaotic motion have nevertheless been observed in quantum mechanics. Erratic behaviour of quantum observables can be obtained in quantum systems whose classical analogues display chaos, as well as sensitivity to changes in the system dynamics. Certain clear correspondences between classical and quantum systems exist. Some of the complexity in classically chaotic motion is however lost in quantum mechanics, since quasiperiodic evolution of average values of variables occurs, instead of exponential amplification of tiny changes. The behaviour of energy level spacings in quantum systems is also discussed, depending on if the corresponding classical systems display regular or chaotic motion. In the last section an overview of the material presented in the later chapters of the thesis is given, including some background to the motivation for the study of the novel double kicked rotor system, which forms the main focus of this thesis.

Chaos theory is essentially the study of certain nonlinear dynamical systems, which may, under specific conditions, display complex dynamics that are extremely sensitive to initial conditions and system parameters. The resulting behaviour of chaotic systems appears random and unpredictable, despite being fundamentally deterministic. This is in contrast to simpler dynamics of systems where future behaviour may be predicted at least approximately.

The first discovery of chaotic motion may arguably have been by Jacques Hadamard in 1898, relating to the study of free particles gliding without friction on a surface of constant negative curvature, Hadamard's billiards. All trajectories of particles were found to be unstable, in the sense that they diverge exponentially from one another. The other early observation of chaos was made by Henri Poincaré in the early 1900s when studying the famous three-body problem of determining the motion in time of three particles, in this case astronomical objects, obeying Newton's laws of motion and gravitational attraction. He found that there can be orbits which are nonperiodic, but neither increase forever in radius nor approach a fixed point. His work laid many of the foundations of deterministic chaos theory. Later studies were carried out by Birkhoff (three-body problem), Kolmogorov (turbulence and astronomical problems), Cartwright and Littlewood (radio engineering) and Smale (mathematical studies of dynamical systems).

Another important milestone was reached by Edward Lorenz in 1961. The advent of computers had greatly aided research in the area of chaos theory, since repeated iterations of mathematical formulae are impractical to do by hand. While running a weather simulation on a basic computer, Lorenz noticed that the results changed completely if the initial data was even slightly altered. Since then computing power has increased continuously, and many more investigations into chaotic motion have been carried out, although ultimately of course the complexity of chaotic systems is too great for any computer to generally predict the motion in detail.

Chaos appears in almost all branches of science and even everyday life. Motion of astronomical objects, molecular vibrations, fluid dynamics, electrical circuits and lasers all display chaotic behaviour under certain conditions, as well as many mechanical and magneto-mechanical devices. The latter include for example a variety of magnetic and multi-segmented pendulums, which are often used to illuminate properties of chaos theory. Other areas in which chaos appears are weather and climate studies, as well as models of population growth in ecology. Examples such as the famous butterfly effect,

relating to a chaotic system's extreme sensitivity to initial conditions, have become well known, and have sparked much general interest in chaos theory outside of the scientific community as well. Indeed many people are fascinated by the intriguing complexity of chaotic systems, even if there are a number of common misconceptions.

Before turning to the study of particular chaotic systems, the kicked and novel double kicked rotors, which forms the main body of this thesis, short introductions to the dynamical theories of both classical and quantum chaos are given below. Since detailed accounts of these could easily become very lengthy and much literature exists on these topics [1], only a few of the most important key features are presented, in particular where relevant to the study of the systems in later chapters.

1.1 Classical Chaos

Broadly speaking there are two limiting cases of motion in classical dynamical systems. One is the regular, integrable motion of such systems as harmonic oscillators and simple pendulums. The motion is governed by a set of differential equations showing the evolution of the variables of the system in time. A completely integrable system possesses a full set of N integrals of motion for N degrees of freedom, and therefore a full set of action-angle coordinates defining invariant tori. Many systems can at least be approximated by an integrable mathematical model, and thus a prediction of the future state of a system becomes possible. The simplest cases are of course periodic systems. Complete integrability is however an untypical property of real systems, since it is destroyed by an arbitrarily weak perturbation.

The other type of motion is the irregular, nonintegrable one, which has been termed chaotic. Here the motion is seemingly random and unpredictable, due to its inherent complexity and sensitivity to system parameters. The mathematical behaviour includes nonlinearities. Chaotic motion arises in many systems, as mentioned above, including ones as simple as an externally driven pendulum. Indeed the kicked rotor models presented in this thesis, and the mathematical formulation that is the Standard Map, are examples of simple systems displaying chaos. Iterative equations of motion can be written down for chaotic systems to show the evolution of a given particle from one time step to the next, but the general time evolution of the particle's trajectory cannot be expressed analytically in such a way as to predict an arbitrary future state of the system. However, in systems comprising a large number of particles, all displaying chaotic

motion, statistical averages may be taken and certain predictions of the time evolution of the ensemble are possible. This is the case for example in studies of diffusion mechanisms, which will play a significant role in the kicked rotor models.

Despite the inability to predict the behaviour of classical chaotic systems, they do of course still follow the same deterministic motion equations as regular systems. Hence the difficulty lies merely in the complex nature of the system dynamics. Specifically there is an extreme sensitivity to both the initial starting conditions that a system is prepared or found in, and any subsequent changes to the parameters or dynamics. Even tiny changes may result in completely different behaviour; indeed a system may display regular or chaotic motion depending on the conditions. It would thus seem that theoretically one could predict the motion of a chaotic system, given enough computing power to calculate all possible starting conditions and system parameters. However in practice, not only could the calculation require an infinite computing time for a continuous spectrum of motion, but it will be seen below that not even a full knowledge of the previous behaviour of a chaotic system is sufficient to make a long term prediction of the subsequent behaviour.

If one looks at a bundle of trajectories in a chaotic system, all starting at nearby points, it is found that the distance between any two trajectories increases exponentially with time, defining an exponential local instability of motion. For regular systems the distance between two trajectories may increase as a power of time but never exponentially. The growth rate of the trajectory separation is measured by the maximal Lyapunov exponent, which thus characterises how stable the motion is. Two trajectories with an initial separation $|\delta_0|$ at time $t = 0$ will evolve to a later separation:

$$|\delta_t| \approx e^{\Lambda t}|\delta_0| \tag{1.1}$$

where Λ is the maximal Lyapunov exponent, hence defined as:

$$\Lambda = \lim_{|t|\to\infty} \frac{1}{t} \ln \frac{|\delta_t|}{|\delta_0|} \tag{1.2}$$

There can actually be several Lyapunov exponents for different orientations of the initial separation vector, corresponding to the number of dimensions of phase space. The largest one is the maximal Lyapunov exponent and determines the predictability of the system; for exponential separation $\Lambda > 0$. Of course neither power law or exponential separation continues indefinitely. Either the separation is halted by the system dimensions or recurrences of trajectories to their initial starting point occur. According to

the Poincaré theorem these recurrences occur infinitely many times for both regular and chaotic motion, but while the time for a recurrence in the former case is bounded from above, arbitrarily large recurrence times are possible in the latter.

The exponential instability of the chaotic motion results in the inability to predict the evolution of a trajectory. From the Alekseev-Brudno theorem [2] the information $I(t)$ associated with a segment of a trajectory of length t is asymptotically:

$$\lim_{|t|\to\infty} \frac{I(t)}{|t|} = \sum \Lambda_+ \tag{1.3}$$

where $\sum \Lambda_+$ is the sum of all positive Lyapunov exponents. This result shows that to predict a segment of a chaotic trajectory, one needs additional information proportional to the length of this segment, but independent of the full previous length of the trajectory. This means that a prediction of the evolution of a trajectory is not possible from the observation of the previous motion, even for an infinite time. If on the other hand there is only a power law behaviour of the separation of trajectories, the required information is inversely proportional to the previous length of the trajectory, and a prediction becomes asymptotically possible. Note that for short enough time intervals one can of course predict the behaviour of a chaotic trajectory, however this is not sufficient to make a general prediction of the motion of the system.

Exponential instabilities of chaotic trajectories also imply necessarily a continuous spectrum of the motion and hence a continuous phase space. In a discrete spectrum the instability is at most linear in time [3], but for chaotic motion the behaviour is nonlinear. The requirement of a continuous spectrum will be seen to be a difficulty when defining the phenomenon of quantum chaos in the next section.

Furthermore, the existence of exponential instability and continuous spectra imply a rapid decay of correlations between different parts of a trajectory in time. Although the memory of the initial state of the system is retained in the fine spatial oscillations of the distribution function representing the final continuum of trajectories, the latter is too complicated to examine on a detailed scale. Instead the statistics of the ensemble are studied. The main focus of this thesis is a new chaotic system, the double kicked rotor, which displays longer lived correlations and hence a more detailed memory than previously studied systems. This will be seen to affect the diffusion properties of the ensemble in a significant way.

It is of course possible for systems to display both regular and chaotic motion, depending on the initial conditions and system parameters. KAM-integrable systems (named

after Kolmogorov, Arnol'd and Moser) are formed through a weak perturbation of a completely integrable system. At first the motion is still integrable for most initial conditions, but as the perturbation increases there is a gradual increase to chaotic behaviour for more and more conditions. The kicked rotor model presented in this thesis, described mathematically by the Standard Map, is one of the leading examples of a KAM system. An effective way of examining the possible behaviour of trajectories, depending on the initial conditions, is to plot successive iterations of the values of the system variables in phase space, thereby building up a Poincaré surface of section (SOS). This shows the evolution of trajectories in phase space, depending on the values of the variables at a given time. Fig.1.1 (taken from Chapter 2, Fig.2.1) shows a series of SOS for the kicked rotor with different values of the perturbing parameter. For small values of the latter

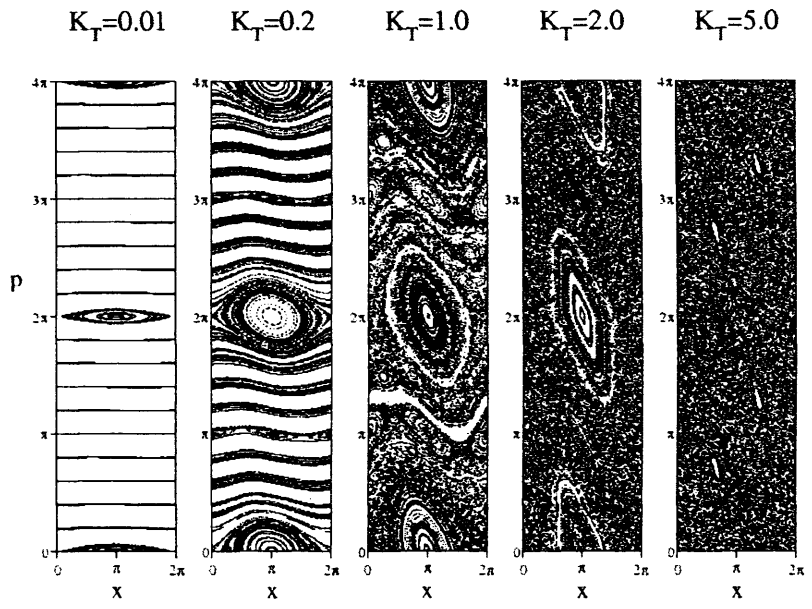

Figure 1.1: Poincaré surface of sections for the kicked rotor with different values of the perturbing parameter K_T. Position and momentum are shown in modulo 2π. At low K_T trajectories are predominantly regular, but as the perturbation increases phase space becomes increasingly chaotic, until for $K_T \gtrsim 5$ chaotic motion is observed for nearly all starting conditions. Taken from Chapter 2, Fig.2.1.

almost all trajectories are regular, but as the parameter is increased phase space becomes mixed, with certain starting conditions leading to regular periodic orbits and others to chaotic motion. For large values of the perturbation all trajectories eventually become

chaotic and no regular orbits remain in phase space. It is interesting to note that while the transition from a completely integrable system to a KAM system happens for an arbitrarily weak perturbation, the resulting chaotic motion is very robust to external interferences.

In contrast to KAM behaviour there are also systems where the transition from integrable to chaotic motion caused by a perturbation is very rapid. The novel random-pair-kicked rotor presented in Chapters 5 and 7 is an example of a non-KAM system, where periodic trajectories in phase space are almost instantly destroyed for a sufficient value of the perturbing parameter.

1.2 Quantum Chaos

Quantum mechanics is the probabilistic theory describing the microscopic world, with systems being in superpositions of several states at once. The correspondence principle states that quantum theory should tend towards its classical counterpart in the classical limit of $\hbar \to 0$ or high excitations leading to the energy continuum. For regular motion such a correspondence between the two theories has been found in many cases. The same principle should apply to classically chaotic motion as spatial scales are reduced, hence the need for a theory of quantum chaos. Indeed one may define quantum chaos as the study of quantum systems whose classical counterparts exhibit chaotic behaviour. This is not a completely satisfactory definition, but is conceptually easy and does indicate the strong quantum-classical correspondence seen in some systems, including the double kicked rotor in this thesis.

However, the characteristic features of classical chaos theory do not all simply carry over into the quantum world. The obvious problem in quantum theory is the loss of the notion of a particle trajectory in the classical sense. The Heisenberg Uncertainty Principle essentially defines a quantum phase space cell of minimum finite size $\Delta x \Delta p \gtrsim \hbar$. The phase space variables cannot be resolved further within this cell, hence there cannot be an extreme sensitivity to initial conditions in quantum chaos. Formally the unitarity of quantum dynamics ensures that the overlap of two wavefunctions remains independent of time, $|\langle\phi(t)|\psi(t)\rangle|^2 = |\langle\phi(0)|\psi(0)\rangle|^2$, provided the time dependence of $\phi(t)$ and $\psi(t)$ is generated by the same Hamiltonian. Furthermore it was shown in the previous section that both a continuous spectrum of motion (and hence energy) and a continuous phase space are required for dynamical chaos, whereas in quantum

theory these are both discrete. The lack of well defined trajectories, and hence lack of exponential separation thereof, of course also results in the Lyapunov exponent having no clear meaning in quantum chaos. It is found that even for expectation values of observables, exponential separation does not occur (instead quasiperiodicity is observed, as will be mentioned below).

Despite these inherent problems, quantum signatures of chaos have been found, although the definition of chaos itself becomes somewhat tricky. While sensitivity to initial data cannot occur, sensitivity to small changes in the dynamics of a system is possible in the quantum world. It has been found that the time dependent overlap of two wavefunctions, derived from the same initial state but evolving slightly differently due to a tiny change in one control parameter between the two cases (relative difference of 10^{-4}), can behave in dramatically different ways, depending on if the states are started with conditions corresponding to classically regular or chaotic motion [4]. In the former case the overlap remains near unity at all times, with oscillations occurring which can be a signature of the classical periodic motion. In the latter case however the overlap decreases exponentially and fluctuates erratically around a much lower value than unity.

Differences in behaviour of quantum observables have also been seen for cases of corresponding classical regular or chaotic motion. As mentioned above, exponential separation does not occur for expectation values; instead recurrences to the initial state in a quasiperiodic manner are seen, with the typical recurrence time inversely proportional to the typical energy level spacing, and of course tending towards infinity in the classical limit. If the quantum state variables correspond to classically regular motion the recurrences are nearly periodic, while for the case of classically chaotic motion they occur as an erratic sequence. Quasiperiodicity is shown for the case of the quantum kicked rotor in Fig.1.2 (taken from Chapter 3, Fig.3.5), where random fluctuations about the mean saturation energy occur.

Both of the above effects are striking examples of quantum-classical correspondences. Although there are no particle trajectories in quantum theory, one may of course construct Gaussian wavepackets of given minimum width, which can be evolved in a quantum phase space, similar to the case of classical ensembles of deterministic particles described by statistical averages. The classical and quantum phase spaces may then be compared directly and quantum states placed in classically integrable or chaotic regions. Obviously the behaviour of an ensemble of particles is not as simple as for a single-particle

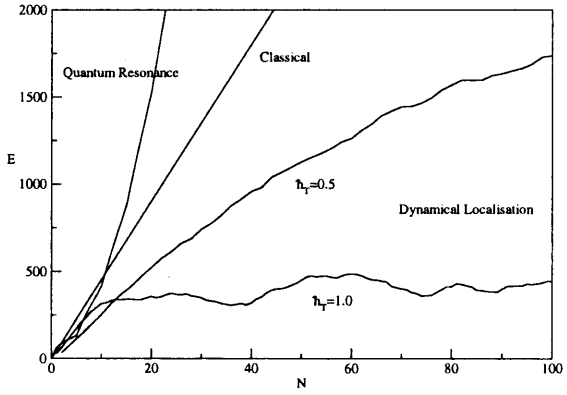

Figure 1.2: Three cases of energy diffusion in time (measured by the number of kicks N) for the kicked rotor. The straight line shows the classical linear diffusion rate denoting chaos. The lower curves show the saturation of energy in the quantum kicked rotor and in the case of $\hbar_T = 1$ the subsequent quasiperiodicity. The top curve shows the case of a quantum resonance, where the energy growth is quadratic. Taken from Chapter 3, Fig.3.5.

trajectory, since the former can be split into different parts if placed in a mixed phase space area containing both periodic orbits and chaotic surfaces. Furthermore a quantum wavepacket can also display reflection or quantum interference, as well as tunnelling, e.g. out of an area filled with classical periodic orbits into the surrounding chaotic regions. Thus the propagation of a Gaussian wavepacket is not entirely straightforward, and the analogy to phase space evolution of classical trajectories is obviously not perfect. Yet the correspondence is useful since for example quantum scarring can be observed, where the probability of finding a quantum state is enhanced along a stable trajectory in the classical phase space.

The existence of quasiperiodicity in quantum chaos, as opposed to the exponential separation of trajectories in the classical case, has an interesting effect on predictions of the time evolution of systems. As was mentioned in the previous section, predictions of the future behaviour of a classically chaotic system are not possible on any significant time scales, since small changes amplify exponentially in time. For a quantum chaotic system this is however not the case. The finite size of a wavepacket removes the instabilities of the motion due to small changes in phase space variables, and the state recurrences make a prediction of the future behaviour of mean values of the observables much easier. An illustration of this is given in Fig.1.3 (taken from Chapter 3, Fig.3.6), where both the mean classical and quantum energies of the kicked rotor are shown again. The former increases quasilinearly in a diffusive manner while the evolution of the latter

shows quasiperiodicity. Furthermore, if the direction of time is reversed in numerical simulations, the quantum mean retraces its history fairly accurately back to the initial value (zero in this case), while the classical mean soon reverts to further diffusive growth and does not return to its initial state. Although somewhat counterintuitive, since quantum theory is usually associated with notions of indeterminacy due to its probabilistic nature, quantum predictions for chaotic systems outdo their classical counterparts.

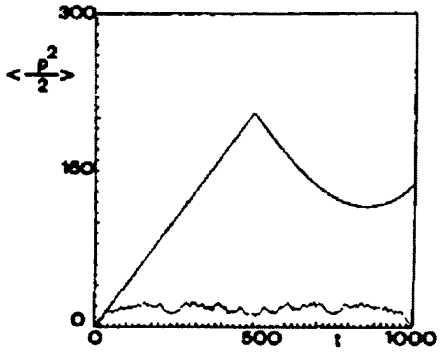

Figure 1.3: Classical (solid curve) and quantum (dotted curve) mean energy evolution in the kicked rotor. At $t = 500$ the direction of time is reversed. Up to this point the evolution of both curves is as in Fig.1.2, with linear classical growth and quasiperiodicity in the quantum case. After time reversal the quantum mean accurately retraces its history to end at its initial value, while the classical energy evolution eventually reverts back to diffusive growth. This shows it is easier to predict evolution of observables in quantum chaos than in its classical counterpart, due to the absence of extreme sensitivity to changes in conditions in the quantum case. Taken from Chapter 3, Fig.3.6.

From the above discussions on signatures of chaos in quantum systems and comparisons with classical systems, it becomes clear that while some correspondences exist, other characteristics of classical chaos are completely absent in the quantum case or present only in a modified form. This has led to the idea of a quantum suppression of classical chaos, at least with respect to certain phenomena. Indeed some of the complexity involved with classical chaos is no longer present in analogous quantum systems. The evolution of the wavefunction itself follows the linear Schrödinger equation, as opposed to the nonlinear equations governing classical chaos. However, in addition to this coherent deterministic evolution, there is also the probabilistic collapse of the wavefunction when an actual measurement of the system takes place. The coherent pure superposition state is converted into an incoherent mixture of probabilistic individual states. No proper

dynamical theory exists to describe this collapse, and an interesting idea put forward by several authors [5, 6], is that the inherent randomness of the measurement process is a manifestation of dynamical chaos. The measuring device itself can be viewed as a chaotic system, since a microscopic intervention when applying it to the quantum system causes a macroscopic effect in the device. Usually the loss of coherence of the pure state is ascribed to the effect of external noise or coupling to the environment. This could be interpreted as the result of interaction with the chaotic measuring device.

A way to get round the apparent lack of classical chaos in quantum systems due to the discrete spectrum, is the concept of finite-time dynamical chaos, restricted to certain timescales only, during which the quantum behaviour is comparable to that of the classically chaotic system. Casati and Chirikov [5] identified the relaxation and random timescales, both related to the time at which the quantum system starts behaving differently from its classical counterpart. It will be seen in Chapter 3 that the evolution of the quantum kicked rotor follows the classical model for a short time, during which diffusion of energy is observed. This was shown above in Figs.1.2 and 1.3 for early times, and is also shown in experimental results in Fig.3.2 in Chapter 3. During this short time the quantum system displays the same complexity in terms of chaotic behaviour as the classical one. After the quantum break time however, intimately connected with the relaxation time, the mean energy of the quantum kicked rotor fluctuates around a saturation value, while that of the classical kicked rotor keeps increasing. It will be seen that this is due to the quantum mechanical process of dynamical localisation, which can be considered to be different to the quantum pseudo-chaos existing before the break time. More details are given in Chapter 3.

The random timescale on the other hand is connected to the length of time for which a quantum wavepacket can be considered to be narrow enough in phase space to approximately follow a bundle of classical trajectories. The minimum size of the wavepacket is obviously restricted by the finite quantum phase space cell, but as shown previously, the quantum evolution can be compared to the evolution of classical trajectories in phase space. Up to the point at which the wavepacket spreads out too much and the minimum uncertainty state is lost, the behaviour can be as random as for classical chaos; in particular, the packet spreads exponentially at a classical rate.

1.3 Energy Level Spacings

A final example of different behaviour of quantum systems, depending on whether the classical analogues are integrable or chaotic, is that of energy level spacings and hence spectral statistics. The varying statistics can be seen as further signatures of chaos in quantum systems. For a system that would classically be integrable there is a clustering of energy levels with crossings possible between these [7]. The levels behave in an uncorrelated way and the distribution of nearest neighbour spacings (NNS) is exponential:

$$P(s) = e^{-s} \tag{1.4}$$

where $s_i = E_{i+1} - E_i$ is the energy difference between two consecutive levels, and hence $P(s)$ is the probability distribution of finding a neighbouring energy level between s and $s + ds$. This distribution shows Poisson statistics as for random independent processes. The probability of levels being clustered together closely is very high.

For systems that would classically be chaotic however, level repulsion is observed [8], where crossings are strongly suppressed and the separation between energy levels may be significantly larger than for the Poisson distribution in Eq.1.4. The levels now behave in a correlated way. The NNS distributions in general behave as $P(s) \sim s^{\beta}$ with $\beta = 1, 2, 4$, corresponding to three classes of level repulsion depending on time reversal and geometric symmetries of the system. Linear level repulsion ($\beta = 1$) is found in systems which are invariant under time reversal and display sufficiently high geometric invariances as well. Quadratic level repulsion ($\beta = 2$) occurs in systems without time reversal symmetry and finally the quartic case ($\beta = 4$) occurs in systems which are invariant under time reversal but have no geometric symmetries.

The three classes of level repulsion correspond closely to the three classes of Gaussian ensembles of random Hermitian matrices found in random matrix theory (RMT) [9], namely the Gaussian Orthogonal Ensemble (GOE) for the linear case of $\beta = 1$, the Gaussian Unitary Ensemble (GUE) for the quadratic case of $\beta = 2$, and the Gaussian Symplectic Ensemble (GSE) for the quartic case of $\beta = 4$. The exact forms of the NNS spacings for the three RMT cases are:

$$\begin{aligned} P(s) &= \frac{\pi}{2} s e^{-\frac{\pi s^2}{4}} \quad (GOE) \\ P(s) &= \frac{32}{\pi^2} s^2 e^{-\frac{4s^2}{\pi}} \quad (GUE) \\ P(s) &= \frac{2^{18}}{3^6 \pi^3} s^4 e^{-\frac{64 s^2}{9\pi}} \quad (GSE) \end{aligned} \tag{1.5}$$

The four different types of NNS for energy levels, including the Poisson distribution for integrable systems, are shown in Fig.1.4. While the highest probability for the Poisson distribution occurs at $s \to 0$, in the case of level repulsion for the classically chaotic systems, the highest probability is near $s \simeq 1$ and level clustering tends not to occur.

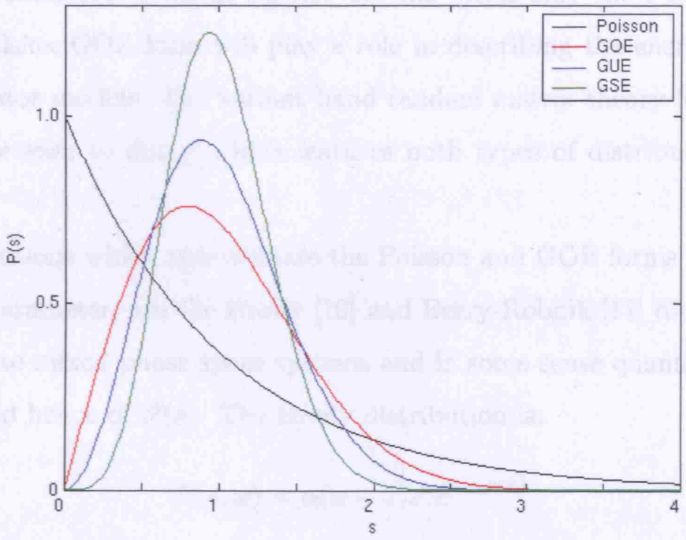

Figure 1.4: Different cases of probability distributions of nearest neighbour spacings for energy levels of quantum systems, depending on the chaoticity of classical analogues and system symmetries. The energy difference between neighbouring levels is denoted by s. The black curve shows the Poisson distribution (Eq.1.4) for classically regular motion, which features level crossings and clustering, with a high probability of $s \to 0$. The other curves show the distributions obtained from random matrix theory for classically chaotic motion. These correspond to GOE, GUE and GSE distributions and linear, quadratic and quartic level repulsion respectively, as shown. Formulae are given in Eq.1.5.

From the symmetries of the Hamiltonian, random matrix theory describes certain average properties of a quantum system, including in particular quantum spectral fluctuations. The three matrix ensembles in RMT correspond to the three known groups of canonical transformations (orthogonal, unitary and symplectic), and members of the ensembles serve as models for Hamiltonians, with matrix elements drawn randomly from statistical distributions. The spectral fluctuations are then represented by suitable ensemble averages. From RMT, with the assumption that in an expansion of an eigenfunction of the Hamiltonian $\phi = \sum_j^N a_j u_j$, with u_j as a basis, all probabilities are on average equal, $\langle |a_j|^2 \rangle = 1/N$, with N the size of the matrix, the distribution of NNS is

then given approximately by the Wigner-Dyson law:

$$P(s) \simeq As^{\beta}e^{-Bs^2} \tag{1.6}$$

Setting the repulsion parameter β as 1,2 or 4 and determining A and B from normalisation, one recovers the forms in Eq.1.5. In this thesis only the Poisson distribution and linear repulsion GOE form will play a role in describing the energy level spacings of the kicked rotor models. The variant band random matrix theory for band diagonal matrices will be seen to apply, which features both types of distributions in different limits.

Two distributions which approximate the Poisson and GOE forms in the limits of a characteristic parameter, are the Brody [10] and Berry-Robnik [11] distributions. Both can be applied to mixed phase space systems and in some sense quantify the chaoticity of this space and hence of $P(s)$. The Brody distribution is:

$$P(s,\omega) = \alpha(\omega+1)s^{\omega}e^{-\alpha s^{\omega+1}} \tag{1.7}$$

with $\alpha = (\Gamma[(\omega+2)/(\omega+1)])^{\omega+1}$ and ω the Brody parameter measuring the strength of the repulsion between levels. The $\omega = 0$ limit corresponds to the Poisson distribution, while the $\omega = 1$ limit tends to the linear repulsion GOE form, although it has been shown [12] that in the latter limit the values obtained are not accurate for large spacings $s \gg 1$.

The Berry-Robnik distribution is:

$$P(s,\rho) = \rho^2 e^{\rho s}\,\mathrm{erfc}(\frac{\sqrt{\pi}}{2}\rho s) + (2\rho\bar{\rho} + \frac{\pi}{2}\bar{\rho}^3 s)e^{-\rho s - \frac{\pi}{4}\bar{\rho}^2 s^2} \tag{1.8}$$

where $\bar{\rho} \equiv 1-\rho$ and $\mathrm{erfc}(x) = (2/\sqrt{\pi})\int_x^{\infty}\exp(-t^2)dt$ is the complement of the error function. The parameter ρ indicates the fraction of phase space which is chaotic, hence $\rho = 0$ corresponds to the Poisson distribution and $\rho = 1$ to the GOE limit. More formally ρ in fact is the mean level density in the chaotic regions of phase space.

It should be noted here that further intermediate statistics and level distributions exist, particularly for the additional effect of localisation on the level spacings. Some statistics show an intermediate form termed semi-Poissonian which will be shown in Chapter 7. It will be seen that the quantum double kicked rotor investigated in this thesis shows intermediate level spacing distributions.

A final note here is on the number variance of the energy spectrum [13], which is

calculated as:

$$\Sigma_2(l) = \langle (n - \langle n \rangle)^2 \rangle \tag{1.9}$$

where n is the number of levels contained in an energy interval of length l. The number variance depends on all correlation functions between the energy levels and is valid in the large l limit. For uncorrelated integrable systems showing Poissonian behaviour the variance is $\Sigma_2(l) = l$. In contrast, for GOE behaviour with level repulsion the variance is $\Sigma_2(l) \simeq \ln(l)$. For the intermediate statistics of the quantum double kicked rotor a different near linear form of the number variance is found.

1.4 The Kicked and Double Kicked Rotors: Overview of Thesis

A textbook example of a classical KAM system capable of displaying chaotic motion is the kicked rotor, where particles are periodically kicked by a series of external impulses, represented by δ-functions in time. Position and momentum evolution of the particles follow the Standard Map (Eq.2.1). As the kick strength K is increased, the system displays a gradual transition from predominantly regular to chaotic motion, as described earlier for a generic KAM system and shown in Fig.1.1. In the chaotic regime the momentum variable follows a random walk to lowest order, and thus the energy of an ensemble of particles grows diffusively at a linear rate, as expected for chaos. This was shown in Figs.1.2 and 1.3. Chapter 2 will introduce the classical kicked rotor in detail, including the derivation of corrections to the basic diffusion rate obtained from the random walk. These originate from short-ranged correlations between impulses a few time steps apart. Special cases of resonances, where energy growth is quadratic instead of linear, will also be briefly mentioned (again shown in Fig.1.2).

Chapter 3 will extend the kicked rotor model into the quantum regime by expressing the Standard Map in terms of quantum mechanical evolution operators. Due to the time periodicity these are Floquet operators with corresponding periodic eigenstates and quasienergies. The quantum kicked rotor displays the same diffusive behaviour as in the classical case for a short time, but after a characteristic timescale dynamical localisation occurs, where the mean energy saturates. The momentum distribution becomes localised over a restricted set of momenta. This well-studied effect, also shown in Figs.1.2 and 1.3, is essentially caused by quantum destructive interference and will be shown to

be analogous to Anderson localisation of electronic wavefunctions in disordered metal lattices. Previous experimental realisations of the quantum kicked rotor, using cold atoms pulsed by standing waves of laser light, are presented showing the localisation effects. Quantum resonances are also discussed near the end of the chapter.

This thesis focuses on a newly discovered system: the double kicked rotor, where particles are kicked by pairs of impulses closely spaced in time. Although essentially just a mathematical extension of the kicked rotor, this system displays surprisingly different diffusive behaviour. Temporal asymmetries had been added to the kicked rotor system in previous studies, where kicking periods were slightly altered. Including also spatial asymmetries, this led to certain types of ratchet mechanisms, where particles travelling in one direction diffuse differently from those travelling in the opposite direction. This was seen to be due to correlations between kicks becoming dependent on the initial momentum of particles. In experiments with cold atoms, quantum currents were observed in the fully chaotic regime, consistent with the ratchet effect. Chapter 4 briefly introduces these Hamiltonian ratchet systems, including the basic perturbed-period kicked rotor, with slight asymmetries in the kicking periods.

The motivation for the double kicked rotor originally stemmed from the ratchet systems described above. During the experimental studies of adding asymmetries to the kicked rotor, it was decided to take this to its limit and create a periodic sequence of short and long time intervals. This effectively results in pairs of impulses in time. The experimental results for energy absorption of the cold atoms from the laser light, as a function of initial momentum of the atoms, are shown in Fig.1.5 (taken from Chapter 7, Fig.7.3), for various values of the short time interval ϵ between kicks in a pair, in comparison to approximate numerical calculations. A dependence of the energy absorption on the initial momentum was expected, as this is also the case for lesser asymmetries in the ratchet systems. The exact form of the energy variation, particularly for higher values of ϵ, is however rather different, with narrow regions of low absorption observed. While the roughly cosinusoidal curve in (a) was similar to diffusion in the ratchet systems, the curves in (b) and (c) could not be explained. This prompted a detailed study of the diffusive behaviour in the double kicked rotor, in particular of kick correlations leading to corrections of the momentum dependent diffusion rate.

It was found that the existence of the short timescale ϵ results in higher order correlations becoming important, which in turn influence the diffusion in the fully chaotic

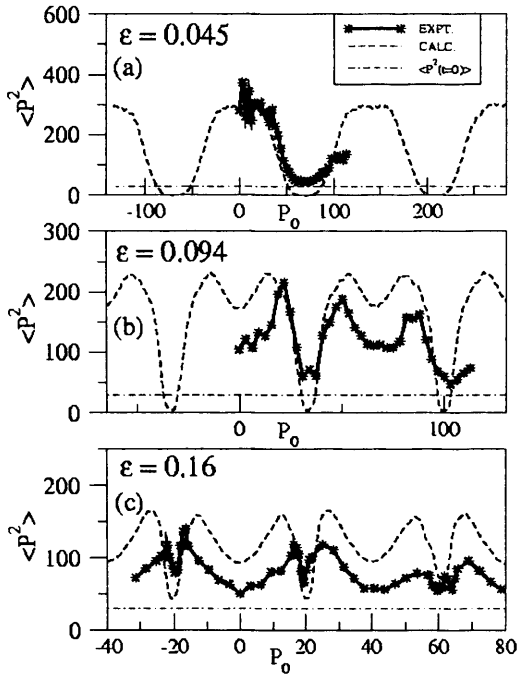

Figure 1.5: Experimental results for the quantum double kicked rotor (solid lines), in comparison with numerical calculations (dashed lines). Energy absorption of an ensemble of cold caesium atoms, pulsed by standing waves of laser light, is shown for varying values of the short time interval ϵ between kicks in a pair. Other parameters are $K = 3.3$ and $\hbar = 1$. Measurements are taken after the quantum break time when the energies have saturated and momentum diffusion has been terminated. For lower ϵ a cosinusoidal variation of energy absorption with initial momentum of the atoms is observed. At certain momenta, corresponding to trapping regions, atoms absorb almost no energy. As ϵ increases, narrow dips in absorption are seen at such momenta. The overall shape of the curve changes as well. Taken from Chapter 7, Fig.7.3.

regime of the double kicked rotor significantly. Areas of fast and slow diffusion of particles alternate in momentum space, thereby giving the latter a cellular structure. Within individual cells, particles diffuse in a similar way as in the chaotic kicked rotor, essentially displaying a random walk, but at certain momenta defining the cell boundaries, diffusion slows down to almost zero. These boundaries have been termed momentum trapping regions and correspond to the dips in energy absorption seen in Fig.1.5. Although the trapping effect is only transient for individual particles, areas of slow diffusion persist asymptotically. The cellular form of phase space is furthermore found to exist for a wide parameter range in the chaotic regime. Chapter 5 will introduce the phenomenology of the classical double kicked rotor, including system equations and a detailed analysis of trapping regions. For certain values of the long time interval τ between pairs of kicks,

fractal structures, namely cantori, are discovered inside the trapping regions. These cantori were at first believed to be fully responsible for the slow diffusion of particles. Further studies however showed importantly that in the limit of large τ, where the system displays non-KAM behaviour, all fractal structures are destroyed, whilst the momentum trapping effect persists. This limit corresponds to randomising the position variable and hence has been termed the random-pair-kicked rotor. It will be shown that the trapping mechanism is very insensitive to the value of τ. The existence of the characteristic diffusive behaviour of the double kicked rotor, independent of any regular structures in phase space, is atypical of previously studied examples of systems displaying chaotic motion.

Chapter 6 presents the detailed mathematical analysis of the diffusion corrections in the double kicked rotor, leading to the trapping mechanism. The approach is the same as in Chapter 2 for the kicked rotor, in that correlations between kicks at different time steps are studied. However, a large number of previously (justifiably) neglected higher order terms are found to contribute in the double kicked case. The interesting property of these is that they combine to form entire families of long-ranged correlations in time, which decay very slowly with temporal separation of kicks. As was mentioned earlier, one of the trademarks of classical chaos are short lived correlations. In contrast, the double kicked rotor seems to be the first system displaying some kind of long term memory, due to a complex correlation behaviour. The derivation of the main types of correlations are shown in detail in Chapter 6, with exact forms of various terms given in the appendix. Further diffusion corrections, originating from correlations independent of initial momentum, are also investigated, which significantly lower the overall asymptotic diffusion rate of particles through momentum space, in comparison to the kicked rotor, even in regimes where the trapping mechanism is absent. A summary of the diffusive behaviour of the classical double kicked rotor is given at the end of the chapter.

Chapter 7 investigates the quantum double kicked rotor, which is seen to display the same trapping mechanism as in the classical case. Clear quantum-classical correspondences are observed, both in numerical simulations and the aforementioned cold atom experiment. Both the energy variation (as shown in Fig.1.5) and momentum distributions obtained from the experiment, as well as the Floquet states of the system and the form of the matrix representation of the evolution operator, all indicate a cellular structure of momentum space. Dynamical localisation is affected significantly by the trapping regions, giving quantum probability distributions a characteristic staircase

structure (denoting the cellular momentum space). Quantum transport through trapping regions is investigated for different localisation regimes. The experimental results can be explained fully by localisation arresting the diffusive behaviour in various regimes dominated by different kick correlation terms. Furthermore, unusual fractional scaling of localisation lengths with $\hbar$ is found for the quantum double kicked rotor, as well as intermediate energy level spacing distributions. Both are attributed to the existence of trapping regions. Similar scaling properties are found for regular structures in the kicked rotor, but since the trapping effect in the double kicked case can exist independently of fractal structures, it is shown that the scaling of various parameters is more likely to be of pure quantum origin. This is a new situation since fractional scaling is generally due to mixed phase space dynamics.

A different theoretical realisation of both the kicked and double kicked rotors in the quantum case is presented in Chapter 8. An analogy to the rotor models exists in magnetically pulsed Heisenberg spin chains, with spin excitations travelling along the chains. Position and momentum variables are mapped inversely, so diffusion of excitation occurs in the space of spin sites. In the presence of a static external magnetic field a coherent spin excitation can be transmitted almost perfectly along the chain. This corresponds to the resonant quantum kicked rotor. The analogy to the general non-resonant case is completed by adding a periodically pulsed external magnetic field. A single spin flip somewhere along the chain then spreads into a distribution of spin excitations, which eventually localises over a range of spin sites. Other resonant cases, where excitations can travel rapidly along the chain, are also observed numerically.

The double kicked rotor is implemented in the spin chain case by alternating the strength of the pulsed magnetic field, upon which trapping of spin excitations along short segments of the chain can occur. Clear correspondences between the spin chain systems and the theoretical kicked and double kicked rotor models are seen. Although not yet experimentally realised, this particular implementation may be promising for future investigations and applications in the area of quantum state transfer and quantum information. Potential uses of the characteristic diffusion mechanism of the double kicked rotor, in either one of the two given representations, as well as ideas for further studies, are given after the concluding summary to the thesis in Chapter 9.

Chapter 2

The Standard Map and Classical Kicked Rotor

In this chapter a common example of a mathematical system displaying classical Hamiltonian chaos will be introduced, the Standard Map, and the associated physical interpretation as the δ-kicked rotor. This system is the starting point of the present work in this thesis, concerning the novel double kicked rotor, presented in Chapter 5. Particles with given positions and momenta are periodically kicked by a series of external impulses, represented by a sinusoidal potential. As the kick strength is increased, a transition to chaotic motion occurs. The momentum evolution of a Gaussian ensemble of particles is then found to display a random walk, as expected for a diffusion mechanism. The energy of the ensemble correspondingly increases in time at a linear rate, for most starting conditions and system parameters. Correlations between external impulses a few time steps apart will be calculated and result in corrections to the basic diffusion rate. Cases of resonance with quadratic energy growth are given at the end of the chapter.

2.1 The Standard Map as a KAM system

The Standard Map (SM), first obtained by Casati, Chirikov *et al* in 1979 [14], is one of the most widely used examples of classical Hamiltonian chaos. In a one-dimensional version a particle's momentum p_N is increased by a series of impulses in a random manner, while its position x_N changes according to the momentum obtained after each impulse:

$$p_{N+1} = p_N + K \sin x_N; \qquad x_{N+1} = x_N + p_{N+1}T \tag{2.1}$$

Here K is the impulse strength and T is the period of free evolution in between impulses. For dimensional consistency it is assumed that $K = K\delta t$ and $T = T/m$, where the time interval δt, over which the impulse K acts, and the mass of the particle m, are both set to unity without loss of generality. Given its apparent simplicity, the fact that a dynamical system described by the SM can display fully chaotic motion, is at first surprising, but it underlines that governing equations of motion for chaos do not necessarily need to be particularly complicated. It should however be noted that the SM cannot be solved analytically and must be iterated through successive time steps to gain information about the system. Note also that the system described by the SM is completely noise and dissipation free.

Although the SM is a generic system applicable to many practical situations (a further reason for its popularity), the most common physical interpretation is as the 'kicked particle' or 'kicked rotor'. The former refers to the 1D model above, where a particle is 'kicked' periodically by a series of impulses $K \sin x_N$ and motion in x is unbounded. The effective potential during an impulse is sinusoidal and takes the form:

$$V(x,t) = -K \cos x \sum_N \delta(t - NT) \tag{2.2}$$

By integrating over Hamilton's equations of motion with this potential, one recovers Eq.2.1. The name 'kicked rotor' is related to a similar interpretation as a rotating bar or particle executing circular motion with angular momentum L_N and turning through an angle θ_N, in which case $p \rightarrow L$ and $x \rightarrow \theta$ in Eq.2.1. Sometimes the system is referred to as the 'δ-kicked' particle or rotor (δ-KP or δ-KR), with reference to the instantaneous kicks, graphically approaching δ-functions in the impulse strength at times NT.

Formally the Hamiltonian for the kicked rotor is:

$$H(L,\theta,t) = \frac{L^2}{2I} + K \cos\theta \sum_N \delta(t - NT) \tag{2.3}$$

with angular momentum L, moment of inertia I (which is set to unity) and kick amplitude K. Hamilton's equations of motion are then given by:

$$\dot{L} = -\frac{\partial H(L,\theta,t)}{\partial \theta} = K \sin\theta \sum_N \delta(t - NT)$$
$$\dot{\theta} = \frac{\partial H(L,\theta,t)}{\partial L} = L \tag{2.4}$$

where $\dot{a}$ denotes the time derivative of variable a. By integrating the first equation over the short time period during which a kick occurs (and the angular momentum changes), and the second equation over the free evolution period in between kicks, Eq.2.1 is essentially obtained again:

$$L_{N+1} - L_N = \int_t^{t+\delta t} K \sin\theta \sum_N \delta(t - NT)dt = K \sin\theta$$
$$\theta_{N+1} - \theta_N = \int_t^{t+T} L dt = LT \tag{2.5}$$

where again δt is set to unity. The kicked rotor can either be considered for unbounded motion in momentum space (an infinite cylinder) or for bounded motion (a finite torus) with periodic boundary conditions on the angular momentum, $L + 2\pi n/T = L$, with n as an integer.

By performing successive iterations of the SM for different starting conditions of x and p, a Poincaré surface of section (SOS) can be produced, showing the possible trajectories of the system in phase space. It is seen that the SM describes a KAM system (as introduced in Chapter 1), where the gradual transition from integrable to chaotic dynamics depends only on the single stochasticity parameter $K_T = KT$. This becomes obvious by writing out the equation for the position x in Eq.2.1 as:

$$x_{N+1} = x_N + p_{N+1}T = x_N + p_N T + KT \sin x_N \tag{2.6}$$

The Standard Map can hence also be rewritten as:

$$p^T_{N+1} = p^T_N + K_T \sin x_N; \qquad x_{N+1} = x_N + p^T_{N+1} \tag{2.7}$$

where $p^T = pT$. In much of the theoretical work on the kicked rotor, the period is in fact set to unity, $T = 1$, resulting in $p^T = p$ and $K_T = K$.

Fig.2.1 shows a series of SOS for increasing values of K_T. Both position and momentum are plotted in modulus 2π, so the aforementioned torus representation is chosen. At $K_T = 0$ the system is fully integrable and phase space consists solely of a set of flat

tori at given momenta. As K_T is increased slightly, these are deformed into KAM tori, but still run across the entirety of position space as solid curves. Elliptical curves or islands also appear, corresponding to periodic trajectories. In both cases the motion is still integrable and particles starting on any such closed curve will remain on it for all subsequent times. For starting conditions in between the invariant tori however, the motion is chaotic. Such areas of phase space are characterised by a complete lack of regular structures, and as K_T is increased further, these areas increase in size, as shown in Fig.2.1.

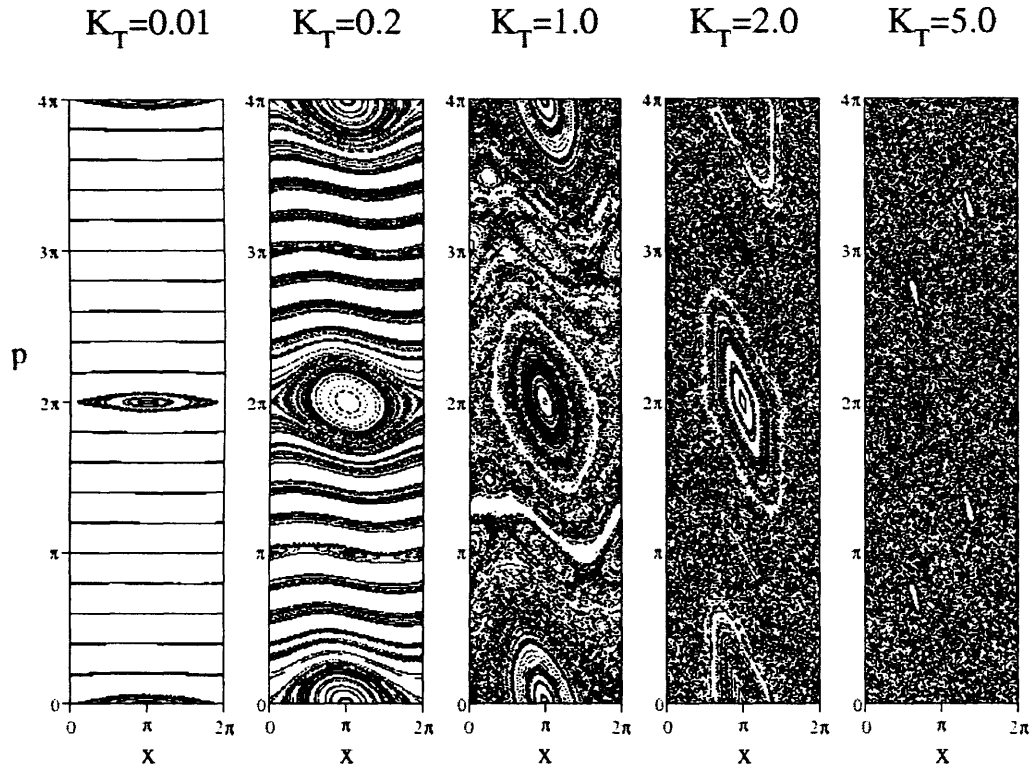

Figure 2.1: Surface of Sections for different values of the control parameter K_T, showing trajectories given by the Standard Map. Position and momentum are shown in modulus 2π. At low K_T trajectories are predominantly regular with tori and islands dominating phase space. At $K \simeq 1$ the last invariant torus breaks and diffusion in momentum becomes unbounded. Chaotic trajectories start dominating phase space and at $K \gtrsim 5$ global chaos exists for nearly all starting conditions.

For $K_T < 1$ the motion is always bounded, both for regular and chaotic trajectories, since the latter are restricted to small areas of the mixed phase space. With increasing

K_T however, the KAM tori start to break up and disappear, leaving behind broken remnants called cantori. The last invariant tori are found to break at $K_{crit} \approx 0.97$; the corresponding phase space picture is shown in Fig.2.1. These tori correspond to momenta $p \simeq 2\pi R \pm 2\pi n$ or $p \simeq 2\pi(1-R) \pm 2\pi n$, where $R = (\sqrt{5}-1)/2$ is the golden mean. Thus these tori lie either side of a comparatively narrow region around $p = \pm(2n+1)\pi$ and can be considered as the most robust structures in phase space hindering the momentum increase of particles. This phenomenon will be compared to the case of the double kicked rotor in Chapter 5, where particle movement through momentum space can be hindered by similar structures.

For $K_T \gtrsim 1$ the particle motion is unbounded in momentum space, in the sense that, given appropriate starting conditions in the chaotic parts, a particle's momentum can take on any value. All phase space points other than remaining islands are connected by chaotic components. As K_T is increased even further, these islands also start disappearing, and for $K_T \gtrsim 5$ phase space is said to be globally chaotic: almost all starting conditions will result in chaotic motion, and particles will, given enough time, explore the entirety of phase space (exceptions are mentioned at the end of the chapter). For large enough K_T, random numbers are generated for the momentum and position changes, explaining the chaotic motion. For $K_T \gg 1$, the system is exponentially unstable with a Lyapunov exponent per step of $\Lambda \approx \ln(KT/2)$.

2.2 Energy Diffusion in the Kicked Rotor

In the chaotic regime of the δ-KR for high K_T, to a first approximation the phase randomisation of the sine term in the SM (Eq.2.1) after each iteration, causes a random walk in the momentum of a given trajectory. This is termed uncorrelated momentum diffusion, where one assumes no correlations between kicks at different times. Since for $K_T \gtrsim 1$ there are no more KAM tori, the momentum, and hence energy, of a particle can increase diffusively without limit (other than dictated by the system dimensions). Rather than study individual particle trajectories however, one can instead look at an ensemble of particles such as a classical Gaussian wavepacket, described by statistical averages of position and momentum. Such a distribution will remain Gaussian in time upon evolution governed by the SM, but its width will increase gradually according to the momentum diffusion taking place. The average energy of the ensemble will grow diffusively in time with a quasi-linear diffusion rate, as obtained from a Fokker-Planck

description of particle motion for a random walk, $\langle E \rangle = D_0 N$, where D_0 is the uncorrelated lowest-order diffusion rate and N the kick number. Here, unscaled momenta $E = p^2/2$ are used and time is counted in numbers of kicks $t = N$. It is found that the diffusion rate depends solely on K:

$$D_0 = \frac{K^2}{4} \tag{2.8}$$

This can be seen from considering the average energy of an ensemble of particles after the Nth kick:

$$\begin{aligned} \langle E_{N+1} \rangle &= \frac{\langle p_{N+1}^2 \rangle}{2} = \frac{1}{2}\langle (p_N + K \sin x_N)^2 \rangle \\ &= \langle E_N \rangle + K\langle p_N \sin x_N \rangle + \frac{K^2}{2}\langle \sin^2 x_N \rangle \end{aligned} \tag{2.9}$$

If one assumes that both x_N and p_N are uncorrelated from one time step to the next with zero average, then $\langle p_N \sin x_N \rangle = 0$ and $\langle \sin^2 x_N \rangle = 1/2$, and hence:

$$\langle E_{N+1} \rangle = \langle E_N \rangle + \frac{K^2}{4} \tag{2.10}$$

which, remembering that $t = N$, corresponds to Eq.2.8. Note that for $\langle p^2 \rangle$, a quantity that will be used extensively throughout the remainder of this thesis, the diffusion rate is of course $K^2/2$. It should further be noted that for scaled momenta $p_T = pT$ as in Eq.2.7, the rate is then found to depend on the actual control parameter $K \rightarrow K_T$.

2.3 Kick Correlations and Corrections to the Diffusion Rate

Upon closer inspection of the kicked rotor system, it turns out that the δ-kicks, and hence the momentum evolution at different times are in fact not entirely uncorrelated, and there are a number of significant correction terms to the quasi-linear energy diffusion rate given above. These terms were first obtained by Rechester and White in 1980 [15], by using a probabilistic version of a Vlasov equation, a continuity equation of phase space flow. Since correction terms to the diffusion rate play a key role for the novel double-δ-kicked system in Chapter 5, the method of obtaining such terms for the SM will be shown here in detail. A slightly modified approach from that given in [15] is used, where the term representing external stochasticity or noise is absent. In [15] this was included to account for non-diffusive trajectories in stable islands contained in mixed phase spaces and in fact made a negligible contribution to the diffusion rate. Given that the focus of this thesis is on the globally chaotic regimes of δ-kicked systems ($K_T \gtrsim 5$),

where no major islands remain, such a term is not needed in what follows. It should be noted however that the calculation for the diffusion rate by this method is thus mainly valid for predominantly chaotic phase spaces, and as more regular structures appear at lower K_T, the approach begins to fail (this is obvious since diffusive regions of phase space decrease in size as islands and KAM tori appear).

From the unscaled SM (Eq.2.1) it can be seen that the momentum of a given trajectory evolves by a sequence of impulses $K \sin x_i$, such that:

$$p_N = p_0 + K \sin x_0 + K \sin x_1 + \ldots + K \sin x_{N-1} = p_0 + S_{N-1} \tag{2.11}$$

where $S_l = \sum_{j=0}^{l} K \sin x_j$ and p_0 is the initial momentum of the particle. The positions of a trajectory evolve correspondingly as:

$$x_N = x_{N-1} + p_0 T + S_{N-1} T \tag{2.12}$$

If one now considers an ensemble of particles with an initial probability distribution in position and momentum $G_0(x_0, p_0, t = 0)$, then at a later time (measured in number of kicks $t = N$) the distribution will be given by:

$$\begin{aligned} G(x_t, p_t, t) = \sum_{n_t=-\infty}^{+\infty} \cdots \sum_{n_1=-\infty}^{+\infty} \int_{-\infty}^{+\infty} dp_0 \int_0^{2\pi} dx_{t-1} \cdots \int_0^{2\pi} dx_0 G_0 \delta(p_t - p_0 - S_{t-1}) \\ \times \delta(x_t - x_{t-1} - p_0 T - S_{t-1} T - 2\pi n_t) \ldots \delta(x_1 - x_0 - p_0 T - S_0 T - 2\pi n_1) \end{aligned} \tag{2.13}$$

Here the sums over $n_1, \ldots, n_t$ appear because of the periodicity of phase space in $x_0, \ldots, x_t$, either for the circular motion of the kicked rotor or the 2π-periodicity of the effective potential in position space (Eq.2.2). The above equation is essentially an expression of evolving the system through a series of time steps from $t = 0$ to $t = N$, with the δ-functions giving the conditional probability densities that the system has evolved from x_i and p_i to x_{i+1} and p_{i+1} at each time step. The momentum diffusion rate D is now given by:

$$D = \lim_{t \to \infty} \frac{1}{t} \langle (p_t - p_0)^2 \rangle = \frac{1}{t} \int_0^{2\pi} dx_t \int_{-\infty}^{+\infty} dp_t G(x_t, p_t, t)(p_t - p_0)^2 \tag{2.14}$$

This is a simple statement of averaging over all possible energies of the system at time t, however it should be noted that the trivial factor $1/2$ in the energy expression has been dropped here, so the calculation is for $\langle p^2 \rangle$, as in the remainder of this thesis unless stated otherwise. Above $(p_t - p_0)^2$ represents a possible energy difference of the system

in comparison to the initial value and $G(x_t, p_t, t)$ the probability of having reached this particular difference. By integrating over all possible position and momentum (and hence energy) values and dividing by the number of time steps, one recovers the rate of diffusion. The infinite limit is taken to ensure one obtains the asymptotic diffusion rate in cases where the rate changes at earlier times.

If the initial probability distribution of particles is now taken as:

$$G_0 = \frac{1}{2\pi}\delta(p - p_0) \tag{2.15}$$

that is a uniform spatial distribution with all particles at initial non-zero momentum p_0, and using the Poisson sum formula giving the Fourier transform of a δ-spectrum:

$$\sum_n \delta(y - 2\pi n) = \frac{1}{2\pi}\sum_m e^{imy} \tag{2.16}$$

Eq.2.14 can be rewritten as:

$$D = \lim_{t\to\infty}\frac{1}{t}\sum_{m_t=-\infty}^{+\infty}\cdots\sum_{m_1=-\infty}^{+\infty}\int_0^{2\pi}\frac{dx_t}{2\pi}\cdots\int_0^{2\pi}\frac{dx_0}{2\pi}(S_{t-1})^2 \times \exp(\sum_{j=1}^{t} im_j(x_j - x_{j-1} - p_0T - S_{j-1}T)) \tag{2.17}$$

This equation represents the total diffusion rate of $\langle p^2\rangle$ including all possible corrections, and by choosing individual terms with different values for the m_j coefficients, one can evaluate individual diffusion corrections due to correlations between kicks at different times. To lowest order, the term with all m_j equal to zero results in the quasi-linear uncorrelated rate D_0 being recovered:

$$D = \lim_{t\to\infty}\frac{1}{t}\int_0^{2\pi}\frac{dx_t}{2\pi}\cdots\int_0^{2\pi}\frac{dx_0}{2\pi}K^2\sum_{j=0}^{t-1}\sin^2 x_j = \lim_{t\to\infty}\frac{1}{t}\frac{K^2}{2}t = \frac{K^2}{2} = D_0 \tag{2.18}$$

where the following standard results have been used:

$$2K^2\int_0^{2\pi}\frac{dx_i}{2\pi}\sin x_i \sin x_j = 0 \tag{2.19}$$

for all $i \neq j$, and:

$$K^2\int_0^{2\pi}\frac{dx_i}{2\pi}\sin^2 x_i = \frac{K^2}{2} \tag{2.20}$$

Since $\langle \sin x_i \sin x_j\rangle = 0$ for all $i \neq j$, correlations between kicks and hence momentum values at different times are not considered for this term.

By setting certain m_j coefficients to a non-zero value, higher order corrections to D can be obtained. These generally arise from non-zero averages $C_k \propto \langle \sin x_i \sin x_{i+k}\rangle$

denoting correlations between the momentum evolution due to kicks which are k time steps apart. For the most dominant corrections in [15], it is found that $|m_j| = 1, 2$. In these cases the integrals contain exponentials and for corrections to be non-zero all arguments of these exponentials must vanish for 2π-periodic integration. The integrals are solved in all cases using the following relation:

$$e^{\pm i\beta \sin x} = \sum_{n=-\infty}^{+\infty} J_n(\beta) e^{\pm inx} \tag{2.21}$$

where $J_n(\beta)$ are Bessel functions of the first kind of order n.

The two main corrections are a correlation between a given kick and the one occurring two time steps later, obtained from setting any $m_j = \pm 1$ and $m_{j-1} = \mp 1$, and a correlation between a given kick and the one occurring three time steps later, obtained from setting any $m_j = \pm 1$ and $m_{j-2} = \mp 1$. For the former 2-kick correlation, in the case of $m_j = 1$ and $m_{j-1} = -1$, one obtains from Eq.2.17:

$$\begin{aligned} D &= \lim_{t\to\infty} \frac{1}{t} \int_0^{2\pi} \frac{dx_t}{2\pi} \cdots \int_0^{2\pi} \frac{dx_0}{2\pi} (S_{t-1})^2 \sum_{j=2}^{t} e^{i(x_j - x_{j-1} - p_0 T - S_{j-1}T)} e^{-i(x_{j-1} - x_{j-2} - p_0 T - S_{j-2}T)} \\ &= \lim_{t\to\infty} \frac{1}{t} \int_0^{2\pi} \frac{dx_t}{2\pi} \cdots \int_0^{2\pi} \frac{dx_0}{2\pi} (\sum_{l=0}^{t-1} K \sin x_l)^2 \sum_{j=2}^{t} e^{i(x_j - 2x_{j-1} + x_{j-2} - KT \sin x_{j-1})} \end{aligned} \tag{2.22}$$

Notice the simplification of the S summations in the exponentials to a single remaining sine term. Given that $\int_0^{2\pi} \exp(\pm icx) dx = 0$ for any constant c, the only terms in $\sum_{l=0}^{t-1} (K \sin x_l)^2$ resulting in a non-zero correction are $2K^2 \sin x_j \sin x_{j-2}$, denoting the 2-kick correlation. Note that there is of course no $\sin x_t$ kick, since $p_t = p_{t-1} + K \sin x_{t-1}$, hence the $j = t$ term leads to a zero-valued correction. This is a consequence of the form of the SM map in Eq.2.1 consisting of a kick followed by a period of free evolution at each time step. If instead a time step was defined as a period of free evolution followed by a kick, there would be no $\sin x_0$ kick and the $j = 0$ term would be zero.

Using the identity in Eq.2.21 one now obtains:

$$\begin{aligned} D = \lim_{t\to\infty} \frac{1}{t} \int_0^{2\pi} \frac{dx_t}{2\pi} \cdots \int_0^{2\pi} \frac{dx_0}{2\pi} 2K^2 \sum_{j=2}^{t-1} \sin x_j \sin x_{j-2} \\ \times e^{i(x_j - 2x_{j-1} + x_{j-2})} \sum_{n=-\infty}^{+\infty} J_n(KT) e^{-inx_{j-1}} \end{aligned} \tag{2.23}$$

where $\int_0^{2\pi} dx_i/(2\pi) = 1$ of course for all variables absent from the exponential. Perform-

ing the following trivial integrations:

$$\int_0^{2\pi} \frac{dx_j}{2\pi} \sin x_j e^{ix_j} = \frac{i}{2} \tag{2.24}$$

(and equally for x_{j-2}), and:

$$\int_0^{2\pi} \frac{dx_{j-1}}{2\pi} e^{-2ix_{j-1}} \sum_{n=-\infty}^{+\infty} J_n(KT) e^{-inx_{j-1}} = J_2(KT) \tag{2.25}$$

where $n = -2$ is the only term in the Bessel summation resulting in a non-zero integral and $J_{-n} = J_n$ for even n, the diffusion correction can be written as:

$$D = -\lim_{t\to\infty} \frac{1}{t} \frac{K^2}{2} \sum_{j=2}^{t-1} J_2(KT) \tag{2.26}$$

The choice of $m_j = -1$ and $m_{j-1} = 1$ in Eq.2.17 leads to the same diffusion correction as in Eq.2.26, hence the total 2-kick correction is:

$$C_2 = -\lim_{t\to\infty} \frac{t-2}{t} K^2 J_2(KT) = -K^2 J_2(K_T) \tag{2.27}$$

This correction to the momentum diffusion rate represents the correlation between impulses $\sin x_j$ and $\sin x_{j-2}$ in the SM (Eq.2.1).

For the 3-kick correction the calculation is similar; for the case of $m_j = 1$ and $m_{j-2} = -1$ one obtains:

$$\begin{aligned} D &= \lim_{t\to\infty} \frac{1}{t} \int_0^{2\pi} \frac{dx_t}{2\pi} \cdots \int_0^{2\pi} \frac{dx_0}{2\pi} (S_{t-1})^2 \sum_{j=3}^{t} e^{i(x_j - x_{j-1} - p_0 T - S_{j-1} T)} e^{-i(x_{j-2} - x_{j-3} - p_0 T - S_{j-3} T)}) \\ &= \lim_{t\to\infty} \frac{1}{t} \int_0^{2\pi} \frac{dx_t}{2\pi} \cdots \int_0^{2\pi} \frac{dx_0}{2\pi} 2K^2 \sum_{j=3}^{t-1} \sin x_j \sin x_{j-3} e^{i(x_j - x_{j-1} - x_{j-2} + x_{j-3})} \\ &\qquad \times \sum_{m=-\infty}^{+\infty} J_m(KT) e^{-imx_{j-1}} \sum_{n=-\infty}^{+\infty} J_n(KT) e^{-inx_{j-2}} \end{aligned} \tag{2.28}$$

Using Eq.2.24 and:

$$\int_0^{2\pi} \frac{dx_{j-1}}{2\pi} e^{-ix_{j-1}} \sum_{n=-\infty}^{+\infty} J_n(KT) e^{-inx_{j-1}} = -J_1(KT) \tag{2.29}$$

where $J_{-n} = -J_n$ for odd n and equally for x_{j-2}, the correction is:

$$D = \lim_{t\to\infty} \frac{1}{t} 2K^2 \sum_{j=3}^{t-1} (\frac{i}{2})^2 (-J_1(KT))^2 = -\lim_{t\to\infty} \frac{1}{t} \frac{K^2}{2} \sum_{j=3}^{t} J_1^2(KT) \tag{2.30}$$

The case of $m_j = -1$ and $m_{j-2} = 1$ in Eq.2.17 again gives an equal contribution, hence the total 3-kick correction is:

$$C_3 = -\lim_{t\to\infty} \frac{t-3}{t} K^2 J_1^2(KT) = -K^2 J_1^2(K_T) \tag{2.31}$$

This correction represents the correlation between impulses $\sin x_j$ and $\sin x_{j-3}$ in the SM (Eq.2.1).

Further to these corrections a higher-order 3-kick correlation derived from $m_j = \pm 1$, $m_{j-1} = \mp 2$, $m_{j-2} = \pm 1$ was also obtained in [15]:

$$C_3' = K^2 J_3^2(K_T) \tag{2.32}$$

and a 4-kick correlation is cited in [16] derived from $m_j = \pm 1$, $m_{j-1} = m_{j-2} = \mp 1$, $m_{j-3} = \pm 1$:

$$C_4 = K^2 J_2^2(K_T) \tag{2.33}$$

(there is also a lower order 4-kick correlation $-K^2 J_1^2(K_T) J_0(K_T)$ of lesser importance). Both terms above are obtained from Eq.2.17 in a similar way as C_2 and C_3 shown previously. Combining all these main correlations, the corrected diffusion rate of $\langle p^2 \rangle = Dt$ in the SM can be written as:

$$D = K^2[\frac{1}{2} - J_2(K_T) - J_1^2(K_T) + J_3^2(K_T) + J_2^2(K_T)] \tag{2.34}$$

where the first term is the uncorrelated quasi-linear diffusion rate from Eq.2.18. Remember that for $\langle E \rangle = \langle p^2/2 \rangle$ the rate is of course halved. Also, for scaled momenta $p_T = pT$, one obtains $K \to K_T$ in the above equation, thus showing that there is only one control parameter in the system.

It should be noted that all these kick correlations are short range, i.e. they correlate kicks a few time steps apart only. Kicks which lie temporally far apart are almost entirely uncorrelated in the kicked rotor. The linearity of the corrections with time however means that the correlations between kicks a few time steps apart remain the same, independent of the time at which these kicks occur. In Chapter 6 it will be seen that for the newly discovered double-δ-kicked rotor there are important diffusion corrections resulting from long range, but transient kick correlations, negligible in all previously studied kicked systems including the usual δ-kicked rotor. The behaviour of those correlations will be seen to be exactly opposite to the ones presented here.

2.3 Kick Correlations and Corrections to the Diffusion Rate

Due to all diffusion corrections in the kicked rotor having a linear time dependence, the overall diffusion rate is obviously also linear in time, but, in contrast to D_0, oscillates with the kick strength K_T due to the Bessel functions. This is shown graphically in Fig.2.2 taken from [15], which displays the relationship between the ratio D/D_0 with K_T (where D is given by Eq.2.34, bar the later added 4-kick correlation C_4). The behaviour is oscillatory as expected and as K_T increases $D \to D_0$, since $J_n(K_T) \to 0$ as $K_T \to \infty$ for all n. The Bessel functions decay as $1/\sqrt{K_T}$ for large K_T and also decay with order n, which is a reason why only a few lowest order corrections contribute significantly to the diffusion rate. At values of K where the analytical diffusion rate is maximal, accelerator modes are found, which further increase the numerical rate; these will be explained at the end of the chapter.

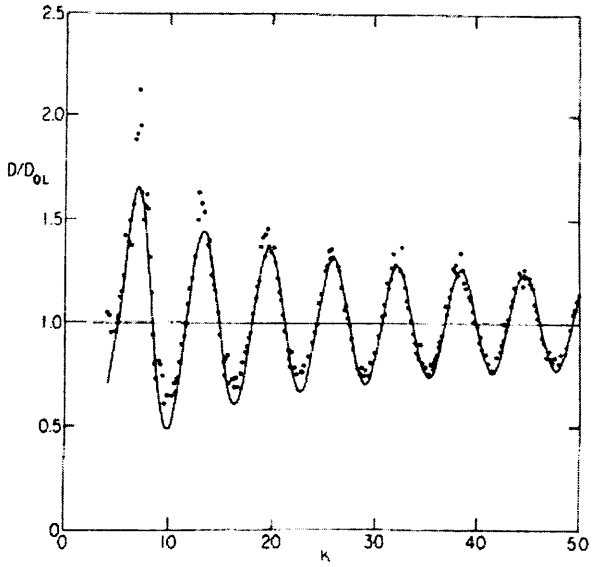

Figure 2.2: Ratio of the corrected diffusion rate in the kicked rotor D and the uncorrected quasilinear random walk $D_{ql} = D_0 = K^2/2$ as a function of the control parameter $K_T = K$ for $T = 1$. Numerical results are shown with dots, superposed with the analytical curve obtained from Eq.2.34, bar the 4-kick correlation term. Oscillations are observed depending on Bessel functions, as expected from the diffusion corrections. As $K \to \infty$ the diffusion rate $D \to D_0$. Accelerator modes are found at values of K for which the diffusion rate is a maximum, hence the numerical rate is higher still in those cases. Taken from [15].

As mentioned earlier the diffusion rates obtained from calculating kick correlations are mainly valid in the completely chaotic regime of $K_T \gtrsim 5$. As phase space becomes more regular for $K_T < 5$ the calculations start to break down, and indeed, as will be

shown later in Chapter 6, following the approach given in Eq.2.17 blindly can lead to unphysical negative diffusion rates in the mixed and near-integrable phase space regimes. Hence the curve in Fig.2.2 is only shown for $K_T \gtrsim 4$. Furthermore it should be noted that given the oscillatory behaviour, there are of course values of K_T for which $D \simeq D_0$ and the main corrections are eliminated due to zeros of the Bessel functions, particularly J_2, occurring. One important value for which this happens is in fact $K_T \simeq 5$, the point at which phase space first becomes globally chaotic and a much used value in numerical simulations and experiments involving the SM and the δ-kicked rotor. Hence it will be seen in the next chapter that $K_T \simeq 5$ is avoided if the effect of kick correlations on the diffusion rate is being investigated.

2.4 The Kick-to-kick Correlation

A question one might ask is if there is a 1-kick correlation present in the SM, which correlates subsequent kicks. Given the existence of important correlations between kicks a few time steps apart, it would naively seem obvious that a correlation between kicks that follow each other directly should contribute as well, perhaps even more than the other ones. However, it can be shown that this is not the case, since the 1-kick correlation is of a different form to those calculated above. In Eq.2.17, setting a single $m_j = 1$ gives a term involving $\sin x_j \sin x_{j-1}$:

$$D = \lim_{t\to\infty} \frac{1}{t} \int_0^{2\pi} \frac{dx_t}{2\pi} \cdots \int_0^{2\pi} \frac{dx_0}{2\pi} 2K^2 \sum_{j=1}^{t-1} \sin x_j \sin x_{j-1} \times e^{i(x_j - x_{j-1} - p_0 T - \sum_{l=0}^{j-1} KT \sin x_l)} \tag{2.35}$$

Here the situation is different than for previous correlations, since the presence of only one exponential means that there is no cancellation of any terms in the S summation, nor of the initial momentum p_0. The integral involving x_j is solved as in Eq.2.24, whilst the integral for x_{j-1} is:

$$\begin{aligned} &\int_0^{2\pi} \frac{dx_{j-1}}{2\pi} \sin x_{j-1} e^{-ix_{j-1}} \sum_{n=-\infty}^{+\infty} J_n(KT) e^{-inx_{j-1}} \\ &= \frac{1}{2i} \int_0^{2\pi} \frac{dx_{j-1}}{2\pi} (1 - e^{-2ix_{j-1}}) \sum_{n=-\infty}^{+\infty} J_n(KT) e^{-inx_{j-1}} \\ &= -\frac{i}{2}(J_0(KT) - J_2(KT)) \end{aligned} \tag{2.36}$$

This leaves integrals over variables $x_0 \dots x_{j-2}$ for which individually:

$$\int_0^{2\pi} \frac{dx_l}{2\pi} \sum_{n=-\infty}^{+\infty} J_n(KT)e^{-inx_l} = J_0(KT) \tag{2.37}$$

Hence:

$$D = \lim_{t\to\infty} \frac{1}{t}\frac{K^2}{2} \sum_{j=1}^{t-1} (J_0(KT) - J_2(KT))J_0^{j-1}(KT)e^{-ip_0T} \tag{2.38}$$

The case $m_j = -1$ gives a complex conjugate solution involving $\exp(+ip_0T)$, so upon addition of the two cases $m_j = \pm 1$ one obtains $e^{ip_0T} + e^{-ip_0T} = 2\cos p_0T$, so the 1-kick correlation is:

$$C_1 = K^2 \cos p_0^T (J_0(K_T) - J_2(K_T)) \lim_{t\to\infty} \frac{1}{t} \sum_{j=1}^{t-1} J_0^{j-1}(K_T) \tag{2.39}$$

This is a diffusion correction which is dependent on the initial momentum of the particles p_0. There are two reasons why this correlation is negligible in the SM. Firstly, given that for large K_T typically $|J_0(K_T)| < 0.5$, the Bessel product $J_0^{j-1} \to 0$ as j and hence time increases. This means the correlation decays rapidly with increasing number of kicks. Secondly, in an experimental realisation of the δ-kicked rotor (see Chapter 3) the initial momentum distribution of the particles, usually cold atoms, has a natural width of $\Delta p_0 \sim 2\pi$. Hence the 1-kick correlation above oscillates on a comparable scale to this natural width for $T = 1$ and averages to zero over the distribution in any experimental situation. Since the oscillations with initial momentum are too small in comparison to the width of an ensemble of particles, they do not cause any significant changes to the diffusion rate.

In general, all diffusion corrections dependent on the momentum of the particles can be neglected in the SM; any significant kick correlations simply alter the magnitude of the overall linear rate of energy absorption or momentum diffusion. Indeed any system with equal time intervals of order unity between impulses and no other asymmetries, displays no momentum dependent diffusion. It will be seen in Chapters 4 and 6 that in δ-kicked systems with temporal asymmetries, momentum dependent correlations can depend on quantities $p_0\epsilon$ and $K\epsilon$, with ϵ being a small positive number, and hence can become very important.

2.5 Accelerator Modes

A final note on energy growth in the kicked rotor concerns a form of anomalous diffusion, due to a classical resonance. In the globally chaotic regime small regular islands can

reappear in phase space for resonant values of $K_T \simeq 2\pi n$, where n is an integer. As can be seen by inspecting the scaled SM (Eq.2.7), it is possible for certain initial values of $x_N \simeq (2m+1)\pi/2$, with integer m, that a maximum momentum transfer K is imparted to the system at a given time step. For $K_T \simeq 2\pi n$ and $T = 1$ the same momentum transfer $\simeq 2\pi n$ occurs at every time step, since from the Map the position of a particle remains roughly constant in modulo 2π. Effectively particles can be considered to be jumping between transporting islands roughly 2π apart in momentum space. This results in a linear momentum and hence quadratic energy growth in time, as opposed to the usual linear energy diffusion from the random walk occurring in the chaotic regions of phase space. Hence this special case of energy evolution in the kicked rotor has been termed an accelerator mode.

In Fig.2.2 it can be seen that the maxima of the ratio of the diffusion coefficients D/D_0 correspond closely to $K_T \simeq 2\pi n$; in fact the average numerical diffusion rate (solid dots) is found to be higher still than the analytical curve at these values, particularly for small values of n, the strongest effect seen for $n \simeq 1$. This discrepancy is accounted for mainly by the existence of the accelerator modes. Particle trajectories can also be attracted to the vicinity of accelerator islands and spend a considerable amount of time there, before being transported to the next island. This effect, essentially equivalent to a Levy flight, is partly responsible for the maxima in the analytical curve around the exact resonant accelerator values.

Chapter 3

The Quantum Kicked Rotor

Here the quantum mechanical version of the kicked rotor is introduced. Floquet operators are used to evolve the quantum system through a succession of time steps in analogy to the classical map. Details of the first experimental realisation of the quantum kicked rotor are given. The results show the phenomenon of dynamical localisation, where only a finite number of energy levels are excited by the external impulses, and hence the rotor wavefunction is localised over a restricted set of eigenstates. The energy of an ensemble of atoms does not grow indefinitely, but saturates to a near constant value after a short time. The localisation effect is shown to be analogous to the case of Anderson localisation in solid state physics, concerning electronic wavefunctions in one-dimensional disordered lattices. Quantum resonances and other investigations related to the kicked rotor are also described.

3.1 Floquet Theory and the Quantum Evolution Operator

So far the kicked rotor has only been considered as a classical ensemble of particles kicked periodically by a sinusoidal impulse, or some analogous system that can be represented by the δ-KR. There is however also a quantum analogy to the kicked rotor [17]. By expressing the SM (Eq.2.1) in terms of quantum mechanical evolution operators, a periodically kicked quantum system can be described. The original motivation for this was of course to see if there are signatures of quantum chaos in such a system, analogous to the classical Hamiltonian chaos found in the SM. It will be seen both in this chapter and in Chapter 7 that although there are some significant differences between the classical and quantum cases of δ-kicked systems, there are also some clear quantum-classical correspondences, and that the classical diffusion calculations performed in Chapter 2 are valid for certain regimes of quantum systems.

The Hamiltonian for the quantum kicked rotor (QKR) can be written in analogy to the classical case (Eq.2.3). In this thesis the linear version for the δ-kicked particle, with variables $x \rightarrow \hat{x} = x$ and $p \rightarrow \hat{p} = -i\hbar\partial/\partial x$, will be used extensively, which is simpler to achieve in experimental realisations of the QKR. However, the position variable x is of course still considered to be 2π-periodic for the usual sinusoidal potential, and so is completely analogous to θ. The Hamiltonian in the (x, p) representation is thus:

$$\hat{H} = \frac{\hat{p}^2}{2m} + K\cos x \sum_N \delta(t - NT) \tag{3.1}$$

where the mass m will be set to unity in what follows. For the quantum evolution of the system the Hamiltonian must satisfy the time-dependent Schrödinger equation:

$$i\hbar\frac{\partial\Psi(t)}{\partial t} = \hat{H}\Psi(t) \tag{3.2}$$

with solutions:

$$\Psi(t) = \hat{U}(t, t_0)\Psi(t_0) = \hat{T}e^{-\frac{i}{\hbar}\int_{t_0}^{t}\hat{H}dt}\Psi(t_0) \tag{3.3}$$

where $\hat{U}(t, t_0)$ is a unitary time evolution operator transforming the initial state $\Psi(t_0)$ into the state at a later time $\Psi(t > t_0)$, and $\hat{T}$ is a time ordering operator ensuring that time is evolved consecutively.

As for the classical kicked rotor, each individual time step can be considered as consisting of an impulse and the free evolution preceding or following it. Since the evolution is the same for all time steps, i.e. the Hamiltonian (Eq.3.1) has a periodic

time dependence $\hat{H}(t) = \hat{H}_0 + V(t)$, where $\hat{H}_0$ is the Hamiltonian of the free evolution with no perturbation and $V(t+T) = V(t)$, the evolution operator $\hat{U}(t, t_0)$ can be split into identical operators for one time step only:

$$\Psi(t+NT) = \hat{U}(t+NT, t)\Psi(t) = [\hat{U}(t+T, t)]^N \Psi(t) \tag{3.4}$$

For periodic systems such as the QKR, this one-period evolution operator is in fact the Floquet operator, $\hat{U}(t+T, t) \equiv \hat{U}^F$, yielding a stroboscopic description of the dynamics of the system. The Floquet theorem for temporally periodic systems is analogous to the Bloch theorem in solid state physics for spatially periodic systems such as crystal lattices. In the latter type of system the wavefunction of a state for individual quasimomentum q, the Bloch state, where $-0.5 < q \leq 0.5$, can be expanded as:

$$\psi_q(x) = e^{iqx}\phi_q(x) \tag{3.5}$$

where ϕ_q is the Bloch envelope, periodic in x, which can be expanded further as a set of plane wave states of integer momentum l for each q:

$$\phi_q(x) = \sum_l A_l^q e^{ilx} \tag{3.6}$$

with coefficients A_l^q. It should be noted that the Bloch theorem of course still holds for the QKR, since the potential (Eq.2.2) is not only pulsed on regularly in time, but is also 2π-periodic in x. In the majority of this thesis quasimomenta will however not be used, unless mentioned otherwise, i.e. $q = 0$ in all cases, resulting in an integer-momentum system ($l = 0, \pm 1, \pm 2, ...$). Since the Bloch theorem essentially states that, if the total momentum state is $l + q$, evolution occurs individually for each q, this results in the quasimomentum being conserved over time in both the QKR and the quantum version of the double kicked rotor investigated in Chapter 7. Hence for most of the thesis it is sufficient to consider one fixed value of $q = 0$ only. There are however differences in behaviour when quantum resonances and statistics are studied, depending on the values of q allowed; these differences will be pointed out later.

In analogy to the Bloch theorem, the time-dependent wavefunction of a state in the Floquet theorem can be written in terms of Floquet states:

$$\psi_n(t) = e^{-i\omega_n t} u_n(t) \tag{3.7}$$

where $u_n(t) = u_n(t+T)$ is a function periodic in time. Since the Hamiltonian (Eq.3.1) is invariant under time shifts NT for a T periodic system, the wavefunction at time $t+T$

can only differ by a phase factor λ_n from that at time t, hence:

$$\hat{U}^F \psi_n(t) = \psi_n(t+T) = e^{-i\phi_n}\psi_n(t) \tag{3.8}$$

From Eq.3.7 it is clear that $\psi_n(0) = u_n(0)$ and setting $\omega_n = \phi_n/T$ one further finds that $\psi_n(T) = e^{-i\phi_n}u_n(T) = e^{-i\phi_n}\psi_n(0)$, which is consistent with Eq.3.8. This shows that the Floquet states are the eigenstates of the Floquet or one-period evolution operator $\hat{U}^F$, with eigenvalues $\lambda_n = e^{-i\phi_n}$. It is clear that this is analogous to a conservative system with energy eigenstates and eigenvalues, however here the Floquet states are not stationary with respect to time evolution but periodic. Hence one can instead introduce quasienergy levels, where the quantity $\epsilon_n = \hbar\omega_n = \hbar\phi_n/T$ is the quasienergy. Since the Floquet phase ϕ_n is only defined up to integer multiples of 2π, due to the underlying periodicity, the quasienergies are only defined up to integer multiples of $\hbar/T$.

The Floquet states and quasienergies of a periodic system can be found by diagonalising the Floquet operator $\hat{U}^F$, in analogy to the diagonalisation of a time-independent Hamiltonian to find its energy levels. The overall quantum state of the periodic system can thus be expanded in terms of the Floquet states as:

$$\Psi(t) = \sum_n c_n e^{-i\frac{\epsilon_n T}{\hbar}}\psi_n(t) \tag{3.9}$$

where c_n are time-independent expansion coefficients. In general one can then express the evolution of any quantity as a sum over the set of eigenfunctions, and the statistics of the evolution can be related to the statistics of these eigenfunctions and the corresponding eigenvalues.

The QKR can however of course also be evolved through subsequent time steps by applying the Floquet operator $\hat{U}^F$ repeatedly to the total rotor state Ψ as in Eq.3.4, and quantum observables such as momentum or energy can be calculated directly at each time step. The evolution of the QKR over one time step can be separated into:

$$\hat{U}^F = \hat{U}_{kick}\hat{U}_{free} \tag{3.10}$$

where the kick operator is obtained by integrating over the potential energy term of the Hamiltonian (Eq.3.1), for the infinitesimally small kick duration δt to give:

$$\hat{U}_{kick} = e^{-\frac{i}{\hbar}\int_t^{t+\delta t} K\cos x \sum_N \delta(t-NT)dt} = e^{-\frac{i}{\hbar}K\cos x} \tag{3.11}$$

where, as in Eq.2.5, one may set $\delta t = 1$. The free evolution operator is obtained by integrating over the kinetic energy term, which for unchanging momentum is of course

constant over the time interval T:

$$\hat{U}_{free} = e^{-\frac{i}{\hbar}\int_t^{t+T}\frac{\hat{p}^2}{2}dt} = e^{-\frac{i}{\hbar}\frac{\hat{p}^2}{2}T} \tag{3.12}$$

where, as mentioned previously, the mass m is set to unity. The total evolution operator for one time period is then:

$$\hat{U}^F = e^{-\frac{i}{\hbar}K\cos x}e^{-\frac{i\hat{p}^2T}{2\hbar}} \tag{3.13}$$

In comparison to the classical kicked rotor, the QKR depends on two control parameters, $K_T = KT$ and a scaled version of Planck's constant $\hbar_T = \hbar T$, the latter describing the effective strength of quantum fluctuations, or in some sense the degree of departure from classical behaviour. Eq.3.13 may be rescaled using these parameters in a similar way to the SM in Eq.2.7. As an aside, one can obtain the discrete-time Heisenberg equations, of the same form as the unscaled SM (Eq.2.1), by using the Heisenberg-picture evolution:

$$X_{N+1} = \hat{U}^\dagger X_N \hat{U} \tag{3.14}$$

for variable X, and the usual commutation relation between x and p.

The simplest way of evolving the system with the Floquet operator in Eq.3.13 is to expand the initial rotor state Ψ_0 as a complete set of angular momentum eigenstates:

$$\Psi_0 = \sum_l A_l^0 |l\rangle \tag{3.15}$$

where the initial amplitude coefficients are given by $A_l^0 = \langle l|\Psi_0\rangle$, and a basis of plane wave states can be used:

$$|l\rangle = \frac{1}{\sqrt{2\pi}}e^{ilx} \tag{3.16}$$

Note that these plane wave states are of course the eigenstates of the free evolution operator $\hat{U}_{free}$. To calculate A_l^0, it is useful to consider the overlap of momentum states with a Gaussian wavepacket for Ψ_0, with minimum uncertainty in both position and momentum. For a wavepacket centred on (x_0, p_0) a general form is:

$$\Psi_0 = \Psi_G(p, t=0) = \sqrt{\frac{1}{\sigma\sqrt{\pi}}}e^{-\frac{(p-p_0)^2}{2\sigma^2}}e^{-\frac{ipx_0}{\hbar}} \tag{3.17}$$

for which the usual Heisenberg uncertainty relation $\Delta x_0 \Delta p_0 = \hbar/2$ holds.

Once the initial expansion coefficients A_l^0 in Eq.3.15 have been calculated, the rotor state can then simply be evolved by propagating these probability amplitudes A of the angular momentum expansion, according to:

$$A_m^{N+1} = \sum_l U_{lm} A_l^N \tag{3.18}$$

The coefficients are evolved from one kick to the next, where U_{lm} are the matrix elements of the Floquet operator given in Eq.3.13 in the momentum basis:

$$\begin{aligned} U_{lm} &= \langle m|\hat{U}_F|l\rangle = \frac{1}{2\pi}\int_0^{2\pi} e^{-imx}\hat{U}_F e^{ilx}dx \\ &= \frac{1}{2\pi}e^{-\frac{il^2\hbar T}{2}}\int_0^{2\pi} e^{-\frac{i}{\hbar}K\cos x}e^{i(l-m)x}dx \end{aligned} \tag{3.19}$$

where the substitution $p = l\hbar$ has been made, and the angular momentum state $|l\rangle$ is of course an eigenstate of the operator $\hat{l}$. To solve the integral, a similar identity to Eq.2.21 involving the cosine is used:

$$e^{\pm i\beta\cos x} = \sum_{n=-\infty}^{+\infty} i^n J_n(\beta)e^{\pm inx} \tag{3.20}$$

for some constant β, and for the integral to be non-zero all exponentials must vanish. Thus the matrix elements for the QKR are:

$$U_{lm} = i^{l-m}e^{-\frac{il^2\hbar T}{2}}J_{l-m}(\frac{K}{\hbar}) \tag{3.21}$$

It should be noted that alternatively the kick operator can be written as $U_{kick} = e^{-\frac{i}{\hbar}K\sin x}$, which results in the absence of the factor i^{l-m} in the matrix elements. Both versions are equally valid; the unimportant phase factor makes no difference to the underlying physics. Observables for the QKR, such as the energy of the rotor state, can be evaluated as expectation values at each time step from the probability amplitudes A_l^N:

$$\langle E\rangle = \langle\Psi_N|\frac{\hat{p}^2}{2}|\Psi_N\rangle = \frac{1}{2}\sum_l l^2\hbar^2|A_l^N|^2 \tag{3.22}$$

where, as mentioned previously, in this thesis the quantity $\langle p^2\rangle$ will normally be used instead.

The rotor state Ψ_N can also be graphically represented at each time step by a Husimi distribution [18]:

$$H(x,p) = |\langle\Psi_N(p = l\hbar)|\Psi_G(x,p)\rangle|^2 \tag{3.23}$$

This is a quantum quasi-probability distribution calculating the overlap of the quantum state Ψ_N with a coherent state such as the Gaussian minimum uncertainty wavepacket Ψ_G given in Eq.3.17. By evaluating $H(x,p)$ for a set of x,p coordinates, a direct comparison can be made with the classical phase space for the kicked rotor. It will be seen throughout this thesis that structures in classical phase space (or the absence thereof) can influence quantum behaviour, and indeed Husimi distributions can show a striking correspondence to the phase space of the classical equivalent of the quantum system [19]. Gaussian quantum wavepackets can be considered to behave in a similar way in relation to phase space, as a classical Gaussian ensemble of particles.

For a large number of momentum states l,m, the evolution matrix U_{lm} could become quite large, however in practice computational resources can be saved by realising that the Bessel coupling J_{l-m} between momentum states only acts significantly over a restricted range of momentum differences $|l-m|$, since $J_n(K/\hbar) \to 0$ very rapidly for large Bessel orders $n \gtrsim K/\hbar$. This effectively gives the evolution matrix a banded structure along the diagonal, with a half-bandwidth of $b = K/\hbar$, as shown in Fig.3.1. On average the momentum change during the quantum evolution from one time step to the next is not greater than $\simeq K/\hbar$.

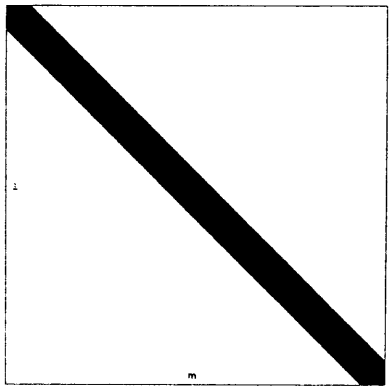

Figure 3.1: Diagonal band structure of the evolution matrix for the QKR given by Eq.3.21. The black band represents significant non-zero entries, while the remaining white area represents negligible entries $\simeq 0$.

As for the classical kicked rotor, the free evolution term in Eq.3.12 approximately randomises the quantum phase of a plane wave between successive kicks. Random matrix theory is expected to apply to the eigenvalue statistics of U_{lm}, as described in Chapter 1, and thus level repulsion is expected to occur, in this case of the linear type. Given the banded structure of the matrix, the statistics however instead correspond to the variant

band random matrix theory (BRMT) [20], which means that if the dimensionality of U_{lm} is N, the statistics are Poissonian for $N \gg b$. States separated in momentum by $\gg b$ will be largely uncorrelated, as shown by Fig.3.1. As $b \to N$, and the band structure of the matrix is effectively lost, the eigenvalue statistics then revert to the linear repulsion form of the Wigner-Dyson law [12],[21].

Again in analogy to the classical δ-KR, the QKR can either be considered for an unbounded momentum space, or with toroidal boundary conditions making the momentum periodic [20],[22]. The latter effectively truncate the potentially infinitely dimensional band diagonal matrix into a number of diagonal blocks of finite dimension. These finite sized matrices can still be diagonalised to find N eigenstates and eigenvalues of the QKR Floquet operator, although there can be inaccuracies when considering eigenstates near the edges of the blocks; these can however usually be discarded when studying the statistics of the system. The periodic boundary conditions are achieved by choosing a value of $N\hbar_T = 2M\pi$, where M is an integer noncommensurate with the matrix dimension N (for rational M/N special cases of quantum resonances are observed, described later in this chapter). It should be noted that non-zero quasimomenta are usually used for these toroidal conditions, as well as additional Bloch phases, in order to eliminate parity conservation effects, which can lead to degeneracies in the eigenvalue spectrum of U_{lm}. Some further details are given in Chapter 7, and remarks about the QKR eigenstates are given later in this chapter.

As a final comment it should be noted that the diagonalisation of the Floquet operator, to find the eigenstates and eigenvalues of the system, can be simplified since states of unequal parity do not couple to each other. The eigenstates are found to be symmetric or antisymmetric combinations of plane waves:

$$\psi_l^{\pm} = \frac{1}{\sqrt{2}}(|l\rangle \pm |-l\rangle) \tag{3.24}$$

where $|\pm l\rangle = (1/\sqrt{2\pi})\exp(\pm ilx)$ as previously (except for $l = 0$ where $\psi_0^+ = \sqrt{2}|0\rangle$). It can easily be shown that coupling occurs only with states of the same symmetry, i.e. $\langle\psi_n^{\pm}|\hat{U}^F|\psi_l^{\mp}\rangle = 0$. Expanding this and using the matrix elements in Eq.3.21:

$$\begin{aligned}
&\langle\psi_n^{\pm}|e^{-\frac{il^2\hbar T}{2}}e^{-\frac{i}{\hbar}K\cos x}|\psi_l^{\mp}\rangle = \\
&\frac{1}{2}e^{-\frac{il^2\hbar T}{2}}(\langle n|\hat{U}_{kick}|l\rangle \pm \langle -n|\hat{U}_{kick}|l\rangle \mp \langle n|\hat{U}_{kick}|-l\rangle \mp \langle -n|\hat{U}_{kick}|-l\rangle) = \\
&\frac{1}{2}e^{-\frac{il^2\hbar T}{2}}(i^{l-n}J_{l-n}(\frac{K}{\hbar}) \pm i^{l+n}J_{l+n}(\frac{K}{\hbar}) \mp i^{-l-n}J_{-l-n}(\frac{K}{\hbar}) \mp i^{n-l}J_{n-l}(\frac{K}{\hbar})) = 0
\end{aligned} \tag{3.25}$$

remembering that $i^{-\beta} = (-1)^{\beta} i^{\beta}$ and $J_{-\beta}(x) = (-1)^{\beta} J_{\beta}(x)$, and hence $i^{-\beta} J_{-\beta}(x) = i^{\beta} J_{\beta}(x)$. Similarly it can be shown that:

$$\langle \psi_n^{\pm} | e^{-\frac{i l^2 \hbar T}{2}} e^{-\frac{i}{\hbar} K \cos x} | \psi_l^{\pm} \rangle = e^{-\frac{i l^2 \hbar T}{2}} (i^{l-n} J_{l-n}(\frac{K}{\hbar}) \pm i^{l+n} J_{l+n}(\frac{K}{\hbar})) \tag{3.26}$$

3.2 Experimental Realisation of the Quantum Kicked Rotor

The QKR was first investigated in an experimental situation in 1995 by Raizen and his group at the University of Texas at Austin [23], following a suggestion by Graham et al [24]. This particular setup consisted of a cloud of ultracold sodium atoms (some later experiments used caesium or rubidium) in a periodic standing wave of near-resonant laser light, pulsed on periodically in time to approximate the series of δ-kicks. The atoms are considered as two level systems in the ground state, with the laser light (frequency ω_L) detuned from the transition frequency ω_0 between the two levels, to eliminate the excited state population. Cooling and trapping of the atoms takes place in a room temperature magneto-optic trap (MOT), creating an optical molasses. A single-mode dye laser, pumped by an argon ion laser, is used for the trapping, cooling and later detection of the atoms. After passing through an acousto-optic modulator (AOM), the beam is split into three counterpropagating pairs, aligned to overlap orthogonally in the centre of the magnetic field gradient. Temperatures in the μK regime can be achieved using Sisyphus cooling, involving pumping between sub-levels of the ground state.

The optical lattice is created by a second single-mode dye laser, the beam being retroreflected from a mirror to create a standing sinusoidal wave of laser light interacting with the trapped cloud of atoms at periodic intervals. In between the laser pulses the atoms evolve freely for $T \simeq 2\mu s$, with the pulse duration $t_p \ll T$ (not exceeding $\simeq 100ns$). However t_p is of course still finite, creating a sequence of narrow Gaussian pulses of laser power in time, rather than the theoretical δ-functions. The finite pulse width does cause some problems, insofar as resonances are created which result in diffusion in a band of momentum only. However, decreasing the pulse duration with constant area causes the width of this band to become arbitrarily large. This approximates the δ-function limit.

The Hamiltonian of the standing wave of laser light is given by:

$$H = \frac{p^2}{2M} - \frac{\hbar \Omega_{\text{eff}}}{8} \cos 2k_L x \tag{3.27}$$

where M is the atomic mass and $k_L = 2\pi/\lambda$ is the wavenumber. Furthermore, $\Omega_{\text{eff}} = \Omega^2/\delta_L$ is the effective Rabi frequency ($\Omega_{\text{eff}}/(2\pi) = 75.6$MHz in the experiment), where $\Omega/2$ is the resonant Rabi frequency proportional to the square root of the standing wave intensity. Finally $\delta_L = \omega_0 - \omega_L$ is the detuning between the laser light frequency and the transition frequency between the ground and excited states of the atoms (20MHz in the experiment). This detuning is sufficiently large for spontaneous emission events to be neglected on the timescale of the experiment. The Hamiltonian of the Gaussian pulse sequence can be written in scaled units as:

$$H' = \frac{\rho^2}{2} - K\cos\phi \sum_{n=0}^{N} e^{-\frac{(\tau-n)^2}{2\alpha^2}} \tag{3.28}$$

where $\rho = (2k_L T/M)p$, $K = \Omega_{\text{eff}}\omega_r T^2$ with $\omega_r = \hbar k_L^2/2M$ being the atomic recoil frequency, $\phi = 2k_L x$, $\tau = t/T$, T is the free evolution time in between the pulses as before, α is the pulse width ($\alpha = 0.027$ in the experiment), and $H' = (4k_L^2 T^2/M)H$. The time dependent potential can be rewritten as a discrete Fourier series (for an infinite train of pulses), leading to:

$$H' = \frac{\rho^2}{2} - \sqrt{2\pi}\alpha K \sum_{n=-\infty}^{+\infty} e^{-2\pi^2\alpha^2 n^2}\cos(\phi - 2\pi n\tau) \tag{3.29}$$

The aforementioned resonances due to the finite pulse width α are located at $\rho = 2\pi n$. In the limiting case $\alpha \to 0$ and $K \to \infty$, such that αK remains finite, all the Fourier weights are equal, and using a particular version of the Poisson sum formula, one obtains the usual kicked rotor Hamiltonian:

$$H' = \frac{\rho^2}{2} - \kappa\cos\phi \sum_{n=-\infty}^{+\infty} \delta(\tau - n) \tag{3.30}$$

with stochasticity parameter $\kappa = \sqrt{2\pi}\alpha K$. In the Texas experiment $\kappa = 11.6$, resulting in a fully chaotic phase space for the kicked rotor with no stable trajectories present. It should be noted that in these scaled units $[\phi, \rho] = i\hbar'$ and the scaled Planck constant is $\hbar' = 8\omega_r T$. Typically, $\hbar' \simeq 1$ in experimental realisations of the kicked rotor.

The detection of the momentum distribution of the atomic cloud is achieved by letting the atoms drift freely for $\simeq 2ms$ after the final pulse, and then turning on the trapping laser beams with zero magnetic field, thus forming an optical molasses which freezes the positions of the atoms. The positions are recorded on a charge-coupled device (CCD) via fluorescence imaging, and from the spatial distribution and the free drift time, the final momentum distribution of the atomic cloud can be calculated.

3.3 Dynamical Localisation

The results from the experimental realisation of the QKR are shown in Fig.3.2, as obtained in [23]. Average energy increase $\langle (p/2\hbar k_L)^2 \rangle /2$ with increasing number of pulses or kicks N is shown for the globally chaotic regime of the kicked rotor. The solid line shows the classical linear energy growth expected of a system displaying random walks in momentum diffusion, and as given by Eq.2.10 ($\langle E \rangle = DN$), with $K \rightarrow \kappa$ and allowing for the rescaled units. It should be remembered that the diffusion corrections C_k for k-kick correlations do not affect the linearity of the diffusion rate, but only alter the gradient of the solid line shown in Fig.3.2, so one would still expect a linear growth of the average energy in time.

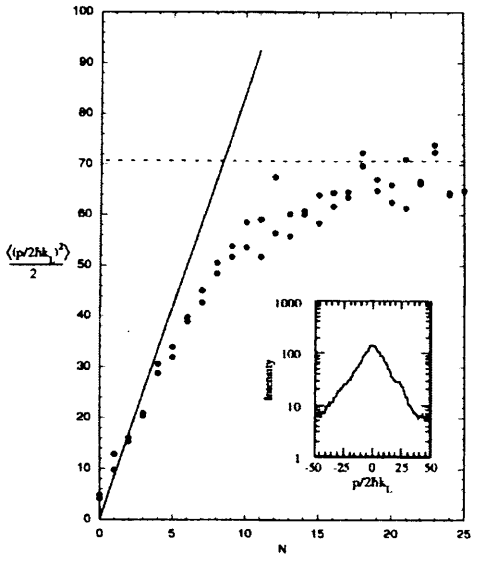

Figure 3.2: Experimental results from the first atom optics realisation of the QKR. Average energy absorption of the atomic ensemble in scaled units is shown in time (counted in number of kicks N) with dots, in comparison to the classical linear absorption rate (solid line). Parameters are $\Omega_{\text{eff}}/(2\pi) = 75.6\text{MHz}$, $T = 1.58\mu\text{s}$, $\alpha = 0.027$ and hence $\kappa = 11.6$. The quantum mean energy saturates after a few kicks, the dashed line showing the approximate saturation value. The crossing of the two lines defines roughly the quantum break time after which localisation occurs. The inset shows the momentum distribution of the atomic ensemble in scaled units and with a logarithmic intensity scale. A characteristic triangular lineshape is observed, which persists asymptotically. Taken from [23].

The solid dots show the experimental results, and it is seen that after a few kicks the energy growth begins to slow and eventually saturates to a roughly constant value. This

suppression of energy increase, first noticed by Casati et al in 1979, is due to destructive quantum interference, resulting in an excitation of only a finite number of momentum levels of the atoms, and has been termed dynamical localisation (DL) [17],[25] (of energy and correspondingly the rotor state). The atomic distribution gradually stops spreading in momentum space after a characteristic 'break time' t^*, which marks the departure from classical behaviour. Formally the break time can be defined as the crossing point of the asymptote to the quantum saturation energy with the classical linear energy growth, as shown in Fig.3.2.

The inset shows the final momentum distribution of the atomic cloud after DL has set in, on a logarithmic amplitude (intensity) scale. A typical exponential lineshape characteristic of DL is obtained following the approximation for the distribution as:

$$N(p) \sim e^{-\frac{2|p|}{L}} \tag{3.31}$$

where L is the localisation length, which can be defined as the distance in momentum space from the centre of the distribution to the point at which the probability amplitude is $1/e$ of its maximum value, or alternatively in terms of the variance $L = \sqrt{\langle p^2 \rangle - \langle p \rangle^2}$. It has been found [26] that for the QKR, $L \simeq D_0/\hbar = K^2/(4\hbar)$ and $t^* \sim L/\hbar$, thus both the localisation length and the break time depend on $\hbar$, characterising the degree of departure from classical results. It should be noted that $L \propto D_0$ is only valid in the regime $D_0 \gg 1$, i.e. $K_T \gg 2$, so in the fully chaotic regime where one expects momentum diffusion to take place. Fig.3.3 shows the progression from an originally Gaussian lineshape before activating the laser pulses, to an exponentially localised one. The break time is about 8 kicks, in agreement with the energy growth in Fig.3.2.

When one investigates the Floquet states of the QKR, it is found that DL arises from the individual localisation of each state in momentum space. Fig.3.4 shows the form of these states for $K_T = 3.4$ and $\hbar_T = 1$, with the amplitudes shown on a logarithmic scale; all are exponentially localised as expected. The behaviour is identical to the momentum distribution of the overall rotor state in Fig.3.2. All states have approximately similar localisation lengths.

Fig.3.5 shows another example of DL in the QKR system over longer times, this time for a numerical calculation from the matrix evolution given previously (the top curve shows a quantum resonance which is investigated later). Fluctuations of the quantum mean energy around the nominal saturation value are observed. This is due to the inherent quantum nature of DL, but also due to the use of discrete time steps and

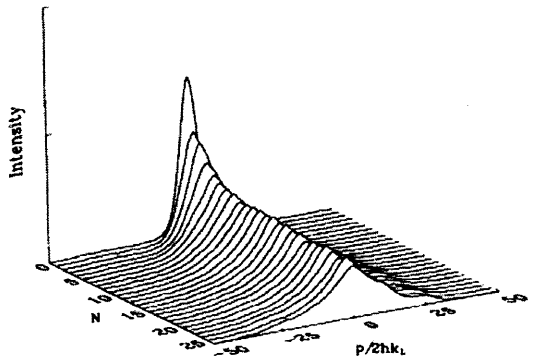

Figure 3.3: Evolution of the momentum distribution for the atomic ensemble in the cold atom QKR experiment. Scaled units are used and intensity is shown on a logarithmic scale. Parameters are the same as in Fig.3.2. The rapid change from an initially Gaussian distribution to an exponentially localised one is clearly seen. Taken from [23].

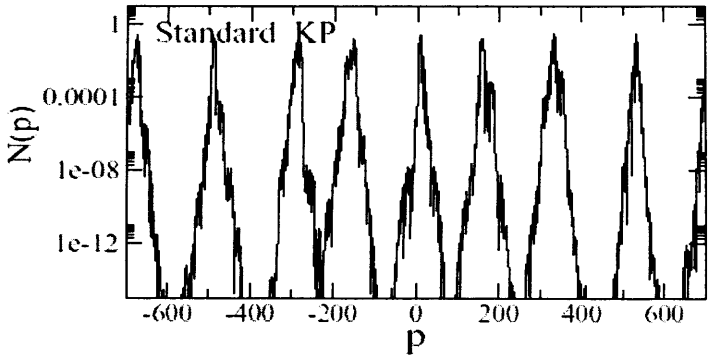

Figure 3.4: Floquet states in the QKR for $K = 3.4$ and $\hbar = 1$ ($T = 1$). States are localised almost symmetrically in all cases, as was observed for the momentum distribution of the entire QKR state in Fig.3.2. All states have roughly similar localisation lengths. Courtesy of Gwangok Hur.

other approximations made. Of course the quasiperiodicity and erratic fluctuations observed also provide us with a signature of quantum chaos, as mentioned in Chapter 1. The quasiperiodicity means that the QKR system will recur to almost the same state repeatedly, while the classical kicked rotor system grows more and more complicated in time, thus highlighting the differences between classical and quantum chaos. This also means that localisation in fact makes energy predictions easier, since in the quantum case exponential amplifications of inaccuracies, as occur in classical chaos, are not possible, as again mentioned in Chapter 1. In particular, the time evolution of the quantum

mean energy accurately retraces its history upon time reversal, while the classical mean energy quickly reverts to diffusive growth under the same conditions [28]. This is shown in Fig.3.6, taken from [29].

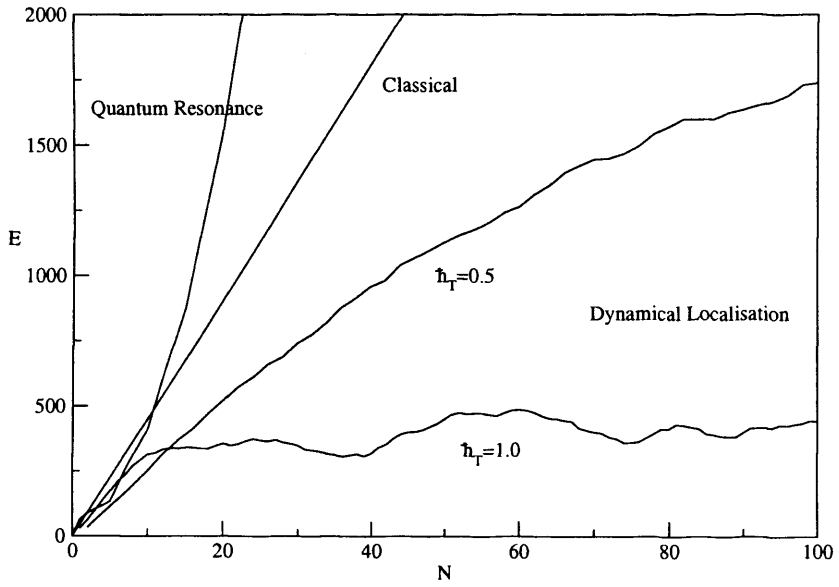

Figure 3.5: Three cases of energy diffusion in time (measured by the number of kicks N) in the kicked rotor for $K_T = 7$. The straight line shows the classical linear diffusion rate calculated from Eq.2.34. The lower curves show dynamical localisation and energy saturation after the quantum break time t^*. As $\hbar_T$ decreases, the classical limit is approached and the localisation effect becomes weaker. Fluctuations of the quantum energy around the saturation value are observed. The top curve shows the special case of a quantum resonance for the case $\hbar_T/2 = 2\pi n$, where the energy growth is quadratic (in this case $\hbar_T = 4\pi$).

It must be remembered that since DL is a wave-coherent effect, the system must preserve coherence until at least the break time for localisation to take place. Deviation from time periodicity or external perturbations may destroy DL quite rapidly and a reversal to purely diffusive behaviour is observed [30]. Small asymmetries in the time periodicity do however preserve DL, although additional features appear, as will be seen in Chapters 4 and 7. Spontaneous emission events can generally be neglected in experiments, since the break time is very short compared to the timescale for which emission or photon scattering events start affecting the coherence. Finally, given that DL is a quantum effect with no classical analogy, the localisation effect becomes weaker as $\hbar_T \rightarrow 0$ in the classical limit, as shown in Fig.3.5.

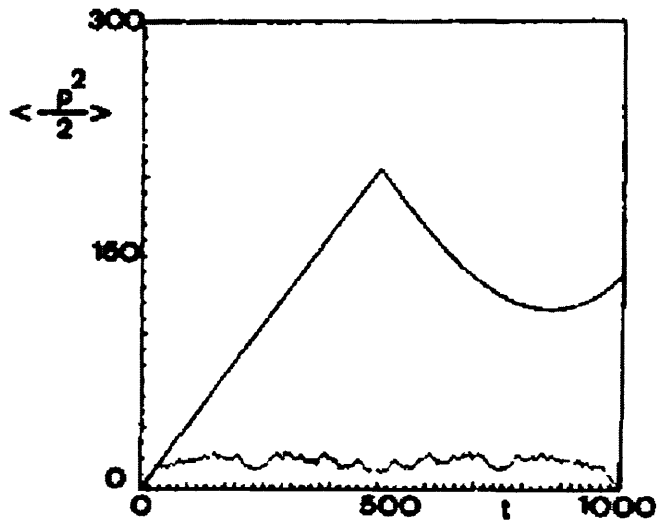

Figure 3.6: Classical (solid curve) and quantum (dotted curve) mean energy evolution in the kicked rotor. At $t = 500$ time is reversed. Up to this point the evolution is as in Fig.3.5 showing linear energy growth classically and localisation in the quantum case. After time reversal the quantum mean accurately retraces its history to end at its initial value, while the classical energy evolution eventually reverts back to diffusive growth. This shows it is easier to predict evolution of observables in quantum chaos than in its classical counterpart, due to the absence of extreme sensitivity to changes in conditions in the quantum case. Taken from [29].

3.4 Analogy to Anderson Localisation

Dynamical localisation in the kicked rotor system has been shown by Fishman et al to be analogous to Anderson localisation in solid state physics [31]. In the latter, a system of electrons and the resulting conduction in a one-dimensional disordered lattice is considered. The irregularity of the lattice provides random scattering potentials for the electrons, thus if they were behaving as classical particles one would expect them to execute random walks, as the classical particles in the kicked rotor system. It was first realized by Anderson [32] that a quantum particle instead may remain eternally in the vicinity of its initial position, thus resulting in a tight-binding model with localised electronic wavefunctions, quasiperiodic in time. This of course limits the conductance of the system. In a one dimensional model, any randomness in the lattice potential localises all electronic states, much like the quantum chaos in the QKR.

Since there are similarities between the Bloch theorem for spatial periodicity, such as in atomic lattices, and the Floquet theorem for temporal periodicity, such as in the

QKR, the kicked rotor can be mapped onto the tight-binding Anderson model. To show this one starts with the basic expansion of the Floquet states of the kicked rotor for individual quasi-energies $\epsilon_n = \hbar\omega_n$ in terms of periodic time functions u_n, as in Eq.3.7:

$$\psi_n(t) = e^{-i\omega_n t} u_n(t) \tag{3.32}$$

where $u_n(t) = u_n(t+T)$ has the same periodicity as the QKR Hamiltonian. From Eq.3.8 the action of the one-period Floquet operator $\hat{U}^F$ on the Floquet states is:

$$\hat{U}^F \psi_n(t) = e^{-i\phi_n} \psi_n(t) \tag{3.33}$$

where $\phi_n = \omega_n T$. It should be remembered that the Floquet operator for the QKR in the momentum representation is given by Eq.3.13 as:

$$\hat{U}^F = e^{-i\frac{V}{\hbar}} e^{-\frac{i\hat{l}^2\hbar T}{2}} \tag{3.34}$$

where the substitution $p = l\hbar$ has been made and the potential is given by $V = K\cos x$. Denoting u_n^- to be the state just before a δ-kick and u_n^+ the state just after the kick, one obtains for the action of the actual kick:

$$u_n^+ = e^{-i\frac{V}{\hbar}} u_n^- \tag{3.35}$$

On the other hand for the free evolution, combining Eq.3.33-Eq.3.35 one obtains:

$$u_n^- = e^{+i\frac{V}{\hbar}} u_n^+ = e^{i(\phi_n - \frac{\hat{l}^2\hbar T}{2})} u_n^+ \tag{3.36}$$

In the momentum representation u_l one of course simply has $\hat{l} \to l$. Now the state $\bar{u}$ can be defined as:

$$\bar{u} = \frac{1}{2}(u^+ + u^-) \tag{3.37}$$

Furthermore, representing the unitary kick operator in terms of a Hermitian operator W:

$$e^{-i\frac{V}{\hbar}} = \frac{1+iW}{1-iW} \tag{3.38}$$

where $W = -\tan(V/(2\hbar))$, and using Eq.3.35 the state $\bar{u}$ can now be rewritten as:

$$\bar{u} = \frac{u^+}{1+iW} = \frac{u^-}{1-iW} \tag{3.39}$$

Substituting for u_n^+ and u_n^- in Eq.3.36 in terms of $\bar{u}_n$, and projecting the states u onto the angular momentum basis $u_l = \langle l|\bar{u}_n\rangle$, one obtains an expression equivalent to a one-dimensional tight-binding Anderson model:

$$T_l u_l + \sum_{r\neq 0} W_r u_{l+r} = E u_l \tag{3.40}$$

where $E = -W_0$ and T_l is given by:

$$T_l = i\frac{1 - e^{i(\phi - \frac{l^2\hbar_T}{2})}}{1 + e^{i(\phi - \frac{l^2\hbar_T}{2})}} = \tan(\frac{\phi - \frac{l^2\hbar_T}{2}}{2}) \tag{3.41}$$

In the Anderson model Eq.3.40 describes the wavefunctions u_l on a time dependent one-dimensional spatial lattice, with l denoting the individual lattice sites, T_l representing the (random) potentials at each site and W_r being the hopping amplitudes between sites.

It should be noted that there is a subtle difference [33] between the Anderson model and the kicked rotor, in that T_l is pseudorandom in the QKR, in the sense that this quantity, depending on the quasienergies ϵ_n via ϕ, is not completely independent from one value of l to the next. However, as seen from the experimental results, localisation still occurs for a pseudorandom sequence of numbers for T_l. There is also another difference between the simplest tight-binding Anderson model and the QKR, namely that W_r in the former allows for hopping between nearest neighbour sites, however the hopping amplitudes in the latter can be shown to fall off exponentially with increasing r [33].

From the above analogy one finds that both the eigenstates of the electronic wavefunction in a disordered lattice in the Anderson problem, and those of the QKR wavefunction are localised, about a given lattice site or mean momentum respectively, with the aforementioned localisation length L. It is found in both cases that eigenstates lying close in energy (or quasienergy in the rotor) are localised at sites or momenta far apart, while eigenstates that are localised close to each other are typically separated in (quasi)energy by $\sim 1/L$ times the bandwidth in the absence of disorder [31]. From the localisation, it is also concluded that the local quasienergy spectrum of the kicked rotor is discrete, as is the case for the local density of states in the Anderson model [31].

A final comment on localisation is that it results in the absence of energy level repulsion in the QKR. Two eigenstates further apart than the localisation length L have no overlap, are hence uncorrelated and have no reason to stay apart in quasienergy. Thus, Poisson short-range level statistics applies, although there is a transition from

Poisson to Wigner (GOE) statistics as the kicking parameter K_T increases. This was already seen in relation to the banded matrix in Fig.3.1, whose bandwidth increases significantly for larger $K/\hbar$, since the Bessel functions $J_{l-m}(K/\hbar)$ decay more slowly for larger orders $l-m$ if K_T is increased, in contrast to the case of $K_T \to 0$ where $J_n \to 0$ for all $n \neq 0$.

3.5 Quantum Resonances

Localisation occurs for most parameters of the QKR, however there are exceptions for resonant values of the quantum parameter $\hbar_T$ [34]. If one looks at the free evolution operator $\hat{U}_{free}$ in the l representation:

$$\hat{U}_{free} = e^{-\frac{il^2\hbar_T}{2}} \tag{3.42}$$

it is obvious that for $\hbar_T/2 = 2\pi n$ with integer n and l^2, the matrix element of this operator is set to unity, and there is no free evolution between kicks. This in turn means there is no randomisation of the quantum phase between kicks, and the effects of the kicking accumulate over time to produce quadratic energy growth. For the above resonant condition, the potential T_l in the Anderson localisation analogy is essentially no longer random, resulting in delocalisation of rotor eigenstates. Instead this case corresponds to the free motion of a quantum particle in an exactly periodic potential [5], i.e. a Bloch state. From an experimental point of view, one can use the simple picture where the rotor has energy levels $l^2/2$, and the photon energy from the laser is considered to be $2\pi/\hbar_T$. The resonance condition is met when an integer number of photons matches the energy for a transition between the rotor energy levels.

Fig.3.5 shows the evolution of the energy in the QKR for the two cases investigated, in comparison to the classical linear diffusion. For irrational, non-resonant values of n in the above condition for $\hbar_T/2$, localisation is obtained in all cases, shown by the energy saturation in the lower curve. For quantum resonances one obtains the ballistic energy growth shown in the top curve, resulting in much faster energy absorption than in the classical linear case. The general resonant case is in fact where $n = a/b$, with both a, b integers, i.e. a rational value of 2π for the scaled Planck constant. For even multiples of π the free evolution factor is unity, for odd multiples there is a change of sign between each kick and an antiresonance is observed for integer momenta, and for other rational values intermediate behaviour is obtained. It should be noted that to

observe the full set of possible quantum resonances in the QKR, quasimomenta $-0.5 < q \leq 0.5$ need to be included in the operators, since only certain values of q allow resonant driving [35]. For the case $\hbar_T/2 = \pi(2n+1)$ described above, i.e. an odd multiple of π, at least one $q \neq 0$ is needed to observe a resonance, otherwise, for integer momenta ($q = 0$), the aforementioned antiresonance with phase flips is observed, where there is almost no energy growth (instant saturation). For a large number of quasimomenta it is also possible for the system to revert to quasilinear energy diffusion again, due to the interference between resonant driving for some q and antiresonances, localisation or buffer phases for others.

Finally, there has also been the discovery of quantum accelerator modes [35],[36], in analogy with the classical case described earlier, although for a slightly different system than the usual QKR (see the next section). For the resonant condition on the 'classical parameter' $K_T \simeq 2\pi n$, transporting islands appear in an otherwise completely chaotic phase space. Provided that a quantum state has a small enough uncertainty to parametrically 'fit' inside one of these islands, the same quadratic energy growth can be observed as in the classical case. For large uncertainty states there can be an overlap into the chaotic regions, and the resonant effect is reduced (the same applies for quantum states that cover mixed phase space areas for lower values of K_T). The condition for quantum accelerator modes to appear is roughly $\hbar < A$, where A is the fraction of phase space area covered by transporting islands. If about 10% of phase space consists of stable islands, one requires $\hbar < 1/10$. Since in many experiments $\hbar \gtrsim 1$, the effect of quantum accelerator modes is often diluted by states overlapping into the chaotic regions of phase space. For very small $\hbar$ it could of course be possible to support more than one quantum eigenstate inside an island, resulting in oscillations in the probability amplitudes for the accelerator modes.

3.6 Other investigations related to the QKR

Before moving on to introducing temporal asymmetries in the standard QKR system, it is worth briefly mentioning a few other examples of work that has been carried out in relation to the quantum kicked rotor or δ-kicked systems in general.

For mixed phase spaces there has been considerable interest in quantum chaos assisted tunnelling of states between regular islands [37]. It was found that the chaotic regions in between the islands greatly enhance the tunnelling effect, resulting in momen-

tum oscillations between the values at which islands are located. There has also been much work on quantum scars [38], where there is an enhanced probability amplitude for a quantum state along the classical periodic orbits of a mixed phase space system. Both of these examples again highlight the strong classical-quantum correspondence present in the QKR.

Other studies have included using the usual standing wave of laser light experiment in a vertical orientation [39], where a gravity term appears in the equations for atomic behaviour (in fact the system can be used to measure very exactly the gravitational acceleration). Quantum accelerator modes were observed in this particular experiment. Localisation of the wavefunction has been used for sub-Fourier resonances [40], where tiny frequency shifts between two series of kicks in a QKR system (i.e. T differs by a small amount between the two kick sequences) can be resolved due to the sensitivity of the localisation effect to these frequency shifts. For rational values of $r = T_1/T_2$, the ratio between the time periods of the two sequences, localisation is observed, with the strongest effect obviously obtained for $T_1 = T_2$. For irrational values of r, localisation is effectively destroyed and diffusive behaviour dominates.

Finally there have been investigations of the effect of decoherence in δ-kicked systems. As mentioned earlier, dynamical localisation is a wave-coherent effect, and thus decoherence destroys DL, the system again reverting to long-term quasilinear momentum diffusion instead. Non-periodic system parameters in the QKR can lead to a loss of coherence resulting in the absence of DL, however decoherence may also occur through interaction with the surrounding environment of the system. It was found in [30] that even one spontaneous emission event in about 100 kicks, caused by decreasing the detuning δ_L between the laser frequency and the transition frequency between two atomic levels in the cold atom experiment (or correspondingly any other interaction with the environment), is sufficient to destroy localisation. For one emission event every 20 kicks, the system almost completely reverts back to the quasilinear $D_0 = K^2/4$ behaviour for $\langle E \rangle$ predicted by the classical calculations. In comparison to these studies the emission rate in kicked rotor experiments (as well as the subsequent experiments including temporal asymmetries described in Chapters 4 and 7) for sufficiently large detuning δ_L can be of order one emission in about 5000 kicks. Hence this source of dissipation can generally be neglected in these experiments, since localisation occurs much earlier.

Chapter 4

The Perturbed-Period Kicked Rotor and Quantum Ratchets

Before introducing the main focus of this thesis, the newly discovered double kicked rotor, in the next chapter, a brief account of earlier kicked systems including asymmetries will be given here. This is chronologically accurate, since the motivation for the double kicked rotor came from investigating the perturbed-period kicked rotor, where small asymmetries in the timing of kick sequences lead to energy diffusion dependent on the initial momentum of particles. If spatial asymmetries are added as well, this system can display a quantum Hamiltonian ratchet effect, where particles travelling in one direction are accelerated strongly by the external impulses, while those travelling in the opposite direction pass through the system almost unperturbed. This is shown to be due to kick correlations depending on the initial momentum of particles as well.

4.1 Mathematical Formalism

Most of the features found in the kicked rotor depend on the periodicity of the system, both in space (the interaction potential) and time (kicking periods). Beyond the standard case of a periodic kicking sequence (period T), it is also possible to introduce a sequence of varying periods T_i over several kicks, without falling into the decoherence regime. Indeed such temporal asymmetries lead to interesting classical and quantum effects. This thesis will be concerned with a novel δ-kicked system, the double kicked rotor, where particles are kicked by a sequence of *pairs* of kicks, introducing anomalous diffusion different to that observed in the QKR.

Before exploring this particular system in Chapter 5, it is useful (and chronologically accurate) first to consider the original motivation for the double kicked rotor, namely the perturbed-period kicked rotor (PPKR) [27],[41] and a closely related form of quantum ratchet. The kicking periods of the standard rotor T are altered slightly by a small amount to result in a periodic kicking sequence $T_1 = T + \epsilon$, $T_2 = T - \epsilon$, where ϵ is a small number. This small period alteration is sometimes called chirping. The sequence $T_{tot} = T_1 + T_2$ results in diffusion corrections becoming dependent on the initial momentum of the particles in the system, with kick correlations including $f(K\epsilon)$ and $f(p\epsilon)$ terms. By adding a spatial asymmetry to the PPKR, such momentum-dependent diffusion rates can lead to quantum ratchet mechanisms [42].

A classical ratchet is defined as any spatially periodic device which allows motion in one direction only, thereby producing a momentum current ($\langle p_t \rangle \neq 0$ for an initial momentum distribution $\langle p_0 \rangle = 0$) without the presence of a net bias in the system, i.e. there are no unbalanced forces present. To extract useful work from a ratchet however, a system must either include some form of external force (this includes trivial cases) or be in a state away from thermal equilibrium (as illustrated by the Smoluchowski-Feynman ratchet [43]), otherwise the second law of thermodynamics would be violated. Furthermore the ratchet should display a persistent transporting momentum current in the asymptotic long time limit, to result in a finite non-zero average classical momentum, for an initial momentum distribution centred on $p_0 = 0$. Quantum ratchets are defined much in the same way, allowing for the peculiarities of quantum mechanics.

For chaotic systems, ratchets can exist in the presence of asymmetries. Most of the literature deals with dissipative or Brownian ratchets [44], such as the aforementioned Feynman ratchet. Often the ratchet effect depends on structures in mixed phase spaces,

i.e. periodic orbits. The system described here, the rocking ratchet [41],[42],[45],[46], which is the PPKR with an added linear potential alternating in direction from one time step to the next, is an example of the less frequently encountered Hamiltonian ratchet, which is noise and dissipation free. It will be seen that this ratchet operates in the fully chaotic regime, hence does not depend on phase space structures, but on the system asymmetries alone, causing momentum dependent diffusion rates. In fact the rocking ratchet was the first experimental realisation of a Hamiltonian ratchet and one of the first ratchet systems not to rely on regular phase space structures.

Prior to the rocking ratchet, there was an investigation into a different Hamiltonian ratchet [46],[47], where a double-well potential was used to replace the usual sinusoidal potential of the standard kicked rotor (Eq.2.2):

$$V(a,x,\phi) = -\cos x - a\cos(2x+\phi) \tag{4.1}$$

where the ratio between the two terms a and the relative phase between them ϕ can both be varied. This leads to a Hamiltonian:

$$H(p,x,t) = \frac{p^2}{2} - KVf(t) \tag{4.2}$$

where in comparison to Eq.2.3 for the kicked rotor, variables x, p are used and as usual the mass of the particles is set to unity. To break temporal symmetry a periodic sequence of three kicks is introduced, namely $T_1 = T+\epsilon$, $T_2 = T$ and $T_3 = T-\epsilon$, in comparison to the Standard Map where all $T_i = T$. Thus the time function in the Hamiltonian can be written as:

$$f(t) = \sum_{s=0}^{\infty}\sum_{M=1}^{n}\delta(t-(sT_{tot}+\sum_{i=1}^{M}T_i)) \tag{4.3}$$

where $n = 3$ is the number of kicks in a cycle, s is the cycle number counting the number of sequences $T_{tot} = T_1+T_2+T_3$, and the individual kick number is now $N = s+M$.

The classical map for the double well ratchet is (in unscaled variables):

$$\begin{aligned} x_{N+1} &= x_N + p_{N+1}(T+\epsilon) \\ x_{N+2} &= x_{N+1} + p_{N+2}T \\ x_{N+3} &= x_{N+2} + p_{N+3}(T-\epsilon) \end{aligned} \tag{4.4}$$

and

$$p_{N+1} = p_N + K\sin x_N + 2aK\sin x_N \tag{4.5}$$

with p_{N+2} and p_{N+3} calculated identically. It should be noted that for the double well ratchet at least a 3-kick periodic cycle is needed; a 2-kick cycle as for the rocking ratchet $T_{tot} = T_1 + T_2$ does not produce a ratchet effect here, as the two momentum dependent diffusion correction terms are equal and opposite in magnitude for a 2-kick cycle.

It is found that the quasilinear diffusion rate for $\langle E \rangle$ in the double well ratchet, taking $T = 1$, is

$$D_0 = \frac{K^2(1 + 4a^2)}{4} \tag{4.6}$$

and by using the same approach as for the classical kicked rotor, in terms of propagating probability distributions in time (Eq.2.14), correction terms can be obtained which depend on the product of the initial momentum of the particles and the small chirp parameter: $C = C(p_0\epsilon)$. It should be remembered that for the standard kicked rotor there are no momentum dependent diffusion terms, since in that case the correlations depend on the product p_0T, resulting in sinusoidal oscillations comparable to the natural width of the atom distribution in an experiment, and thus the corrections average to zero. In the ratchet however terms involve e.g. $\sin \alpha p_0 \epsilon$ (integer α), which are oscillations on a much larger scale and hence affect an atomic system (and equally a classical Gaussian distribution).

In the rocking ratchet, spatial symmetry is broken in a different way, by simply introducing a 'rocking' linear term to the potential:

$$V(x) = -(K \cos x + (-1)^N Ax) \tag{4.7}$$

where A is the amplitude of the linear term and N is the kick number. The sign of the rocking term hence alternates between time steps, as well as the kicking period. The Hamiltonian in this case can be written as:

$$H(p, x, t) = \frac{p^2}{2} - \sum_{N=0}^{\infty} V(N)\delta(t - N(T + (-1)^N \epsilon)) \tag{4.8}$$

and the classical map for the rocking ratchet is then:

$$\begin{aligned} p_{N+1} &= p_N + K \sin x_N + Ax \\ x_{N+1} &= x_N + p_{N+1}(T + \epsilon) \\ p_{N+2} &= p_{N+1} + K \sin x_{N+1} - Ax \\ x_{N+2} &= x_{N+1} + p_{N+2}(T - \epsilon) \end{aligned} \tag{4.9}$$

where the kicking cycle is $T_1 = T + \epsilon$, $T_2 = T - \epsilon$ and $A \neq \pi$ to avoid symmetries in the system. The case $A = 0$ of course corresponds to the PPKR with no spatial asymmetries. As opposed to the double well ratchet, here a 2-kick cycle is sufficient to create a momentum current, since the alternating linear term means there are no equal and opposite diffusion correction terms. As for the double well ratchet, momentum diffusion rates are found to depend on $p_0\epsilon$ in the rocking ratchet, with the quasilinear background rate being equivalent to that of the kicked rotor: $D_0 = K^2/4$.

Phase spaces for both ratchet systems are given in [46]; it is worth noting that introducing the chirping parameter ϵ destroys regular structures in phase space quicker as K_T increases, than in the case of the Standard Map. Typically global chaos prevails for $K_T \gtrsim 2 - 3$, as opposed to the SM where the transition occurs nearer $K_T \simeq 5$. Note also that the control parameter for the ratchets has the general form KT_i, so actually changes with kick number; however for small enough ϵ, one can approximate it to the same form as for the kicked rotor $K_T \simeq KT$. In the same way, the quantum parameter for these Hamiltonian ratchets can be approximated as $\hbar T$. It will be seen in Chapter 7 that for the double kicked rotor, the control parameters in fact become $K\epsilon$ and $\hbar\epsilon$.

The quantum operators and matrix elements for the two ratchets are derived in the same way as shown for the QKR. For the double well (dw) ratchet one obtains:

$$\hat{U}_{dw} = e^{-i\frac{K}{\hbar}(\cos x + a\cos(2x+\phi))} e^{-\frac{i\hat{p}^2 T_i}{2\hbar}} \tag{4.10}$$

and

$$\langle m|\hat{U}_{dw}|l\rangle = i^{m-l} e^{-\frac{i(l+q)^2\hbar T_i}{2}} \sum_s J_{m-l-2s}(\frac{K}{\hbar}) J_s(\frac{\alpha K}{\hbar}) e^{is\phi} \tag{4.11}$$

For the rocking ratchet (rr) on the other hand:

$$\hat{U}_{rr} = e^{-\frac{i}{\hbar}(K\cos x \pm Ax)} e^{-\frac{i\hat{p}^2 T_i}{2\hbar}} \tag{4.12}$$

and the matrix elements are calculated over the cycle of two kicks resulting in a momentum change $l \to m \to n$:

$$\langle n|\hat{U}_{rr}|l\rangle = i^{n-l} e^{-\frac{i(l+q)^2\hbar T_1}{2}} \sum_m e^{-\frac{i(m+q')^2\hbar T_2}{2}} J_{l-m+\mathrm{int}(q-A)}(\frac{K}{\hbar}) J_{m-n-\mathrm{int}(q-A)}(\frac{\alpha K}{\hbar}) \tag{4.13}$$

In both cases T_i are the individual kicking periods within the defined cycles, and quasi-momenta are used for the ratchets, i.e. $p = (l + q)\hbar$. For the double well ratchet

quasimomenta are conserved for each kick, hence the system can be evolved separately for each q, as is the case for the QKR. Thus, strictly speaking, quasimomenta are not necessary for the double well ratchet. For the rocking ratchet however, q is not conserved from kick to kick, but instead only over the two-kick cycle $T_{tot} = T_1 + T_2$. In Eq.4.13 the following notation is used: q is the conserved quasimomentum before the first kick in the cycle and after the second kick, q' is the quasimomentum in between the kicks in a cycle ($q' \neq q$), and $\mathrm{int}(q - A)$ is the nearest integer to $q - A$ (for mathematical details see [46]). Thus the matrix elements are written including two time steps, and individual quasimomenta are conserved over the entire cycle, for which the system can again be evolved for each q separately.

4.2 Experimental and Numerical Results

The rocking ratchet was investigated in a system of pulsed ultracold caesium atoms in an optical lattice at University College London. Most of the experimental details are similar to the case of the QKR described earlier and can be found in [42] and [48]. The atoms are again trapped and cooled in a 6-beam MOT and optical molasses. The optical lattice is formed by splitting a single laser beam using a half-wave plate and a polarising beam splitter, to create parallel linear polarisations, and then directing the two resulting beams at each other (the experimental setup is identical to that used for the double kicked rotor in Chapter 7, Fig.7.2). Scaled variables identical to those presented for the QKR in the Texas experiment were used.

In order to probe momentum dependent effects it may be desirable in some cases to start with an initial non-zero momentum distribution. This is achieved by having two beams of frequencies $f \pm \Delta f$, and therefore a controlled frequency difference $2\Delta f$ between them, resulting in an optical lattice moving with constant velocity in the laboratory frame. Atoms that are stationary in the laboratory frame then have a non-zero momentum $\rho_L = 4\pi T \Delta f$ in the rest frame of the optical potential. It should be noted that this means that the energy diffusion rates in fact depend on the initial relative momentum between the atoms and the optical lattice. To simulate the rocking linear potential, an accelerating optical lattice is then used to break the spatial symmetry. This is done by modulating the frequency of one of the laser beams in a linear manner by an amount $\pm\delta f$ in the time interval T. The gradient of the linear potential term in the rocking ratchet is then $A = 2\pi t_p \delta f$ for finite pulses of temporal width t_p.

Results were obtained for both the PPKR without the rocking term and the rocking ratchet, and in both cases momentum asymmetries were observed. Fig.4.1 shows the first moments $\langle\rho\rangle$ of the final momentum distributions after system evolution as a function of ρ_L, the initial momentum of the atoms in the lattice frame, for two values of ϵ in the PPKR ($A = 0$). Fig.4.2 shows $\langle\rho\rangle$ as a function of the potential gradient A for the rocking ratchet. The values of K used in the experiments are 3.3 and 2.6 respectively. For the SM neither value corresponds to global chaotic motion, however as mentioned earlier, the presence of the chirping parameter ϵ results in global chaos being reached at lower values of K. Note that as in the QKR experiment, time is rescaled as $\tau = t/T$; hence the evolution of the system is counted in the dimensionless number of kicks N. This effectively sets the scaled kicking period to roughly unity $T_i \simeq T = 1$ and hence $K_T \rightarrow K$ (or to be precise KN).

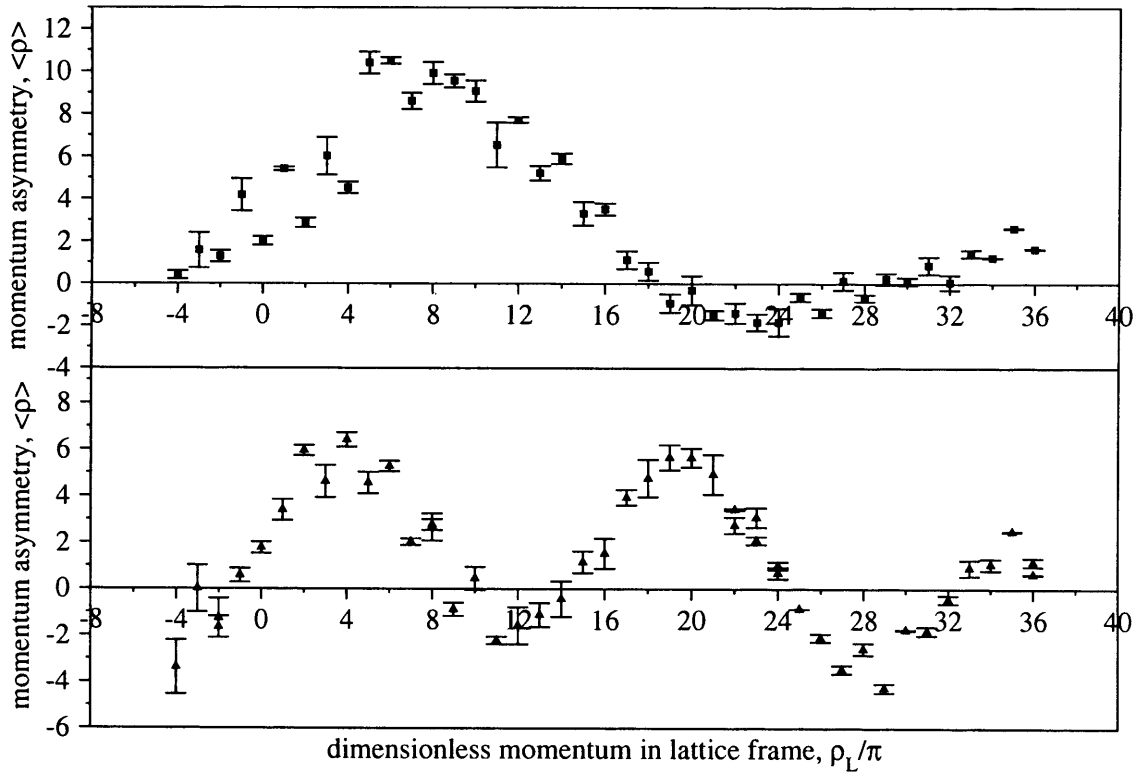

Figure 4.1: Experimental momentum currents in the PPKR after evolution of the system. The deviation $\langle\rho\rangle$ from zero current is shown vs. initial momentum of the atoms in the optical lattice frame ρ_L/π. Parameters are $K = 3.3$, $\hbar_{\text{eff}} = 1$ and $\epsilon = 1/32$ in the top panel and $\epsilon = 1/16$ in the bottom panel. Courtesy of Phil Jones.

Both for the PPKR and the rocking ratchet sinusoidal variations in the amount of momentum asymmetry are observed, with initial mean momentum of the atoms and

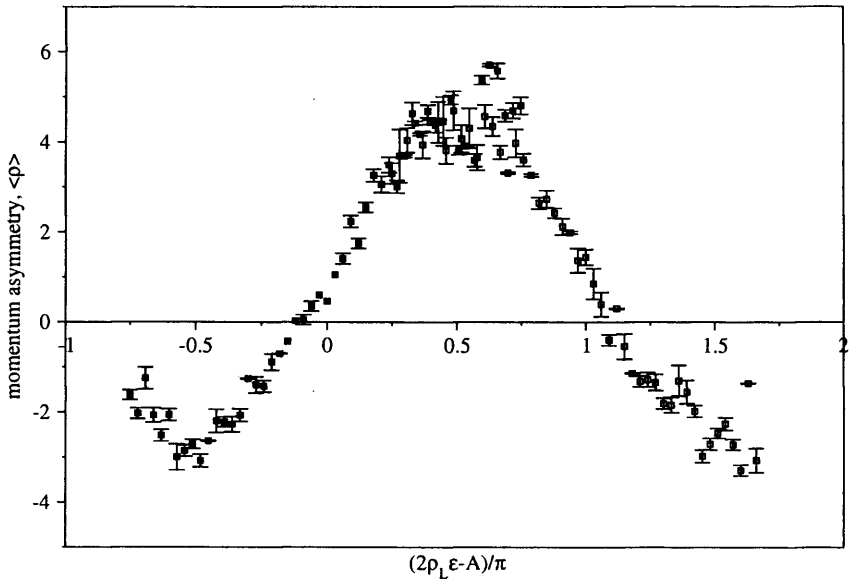

Figure 4.2: Experimental momentum current in the rocking ratchet as a function of $(2\rho_L\epsilon - A)/\pi$. The filled squares denote results for $\rho_L = 0$ and the open squares for $\rho_L = 8\pi$. Parameters for this experiment are $K = 2.6$, $\hbar_{\text{eff}} = 1$ and $\epsilon = 1/16$. The momentum asymmetry is found to oscillate with a period of 2π. Courtesy of Phil Jones.

amount of spatial asymmetry A. If the actual momentum distributions are plotted, as in Fig.4.3, again taken from [42], it can be seen that the full ratchet mechanism only appears for $A \neq 0, \pi$. All three distributions are for zero initial mean momentum and for the PPKR ($A = 0$) the distribution is almost symmetric after kicking. Whilst there can be asymmetries in the PPKR, with respect to the amount of momentum diffusion for particles with initial non-zero momentum, for $\langle p_0 \rangle = 0$, there is no ratchet effect and an equal number of particles diffuse in the positive x-direction as in the negative. The same applies for the case of $A = \pi$. For values of $A = \pm\pi/2$ however, there are large asymmetries in the final momentum distributions. Depending on the sign of A in the rocking ratchet, far more particles diffuse in the positive or negative direction than in the opposite one. This existence of an asymptotic momentum current in one direction, despite initial symmetric conditions, is the definition of a ratchet. Directional bulk transport of particles is observed, moreover in the absence of regular phase space structures, thus defining a Hamiltonian ratchet.

It can be shown that the cause of the preferred momentum diffusion in one direction is the dependence of the classical diffusion rate on the initial momentum of the particles (and on the chirp parameter ϵ), leading to a sinusoidal variation in the amount of energy

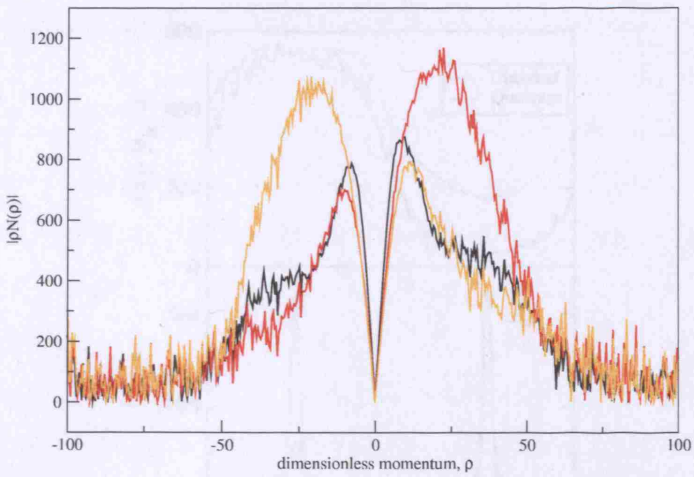

Figure 4.3: Asymmetric momentum distributions for the rocking ratchet after system evolution. The almost symmetric black curve is for the case $A = 0$ with no spatial asymmetry in the system, showing that the ratchet effect is absent in this case. The red curve for the case $A = -\pi/2$ shows a strong bias in the distribution towards positive momenta, while the orange curve for $A = +\pi/2$ shows a strong bias towards negative momenta. In both cases with spatial asymmetries the ratchet effect is obvious. Parameters are as for Fig.4.2. Courtesy of Phil Jones.

absorption. This is shown again in the top panel of Fig.4.4 (a numerical calculation taken from [46]) for unscaled momenta. It is notable that the energy absorption curve has rotational symmetry about $p_0 = 0$. In the bottom panel the evolution of two initially Gaussian wavepackets is shown, one with positive initial momentum, one with negative initial momentum. The wavepacket on the right, corresponding to a mean momentum for which energy absorption is at a minimum, experiences much less spreading than the one on the left, for which absorption is at a maximum.

The preferred movement of particles in one direction only in the rocking ratchet can be exploited to create an atom filter, according to the direction of movement. By changing the system parameters, such a filter can be tuned to a range of momenta. The simple form of the energy absorption dependence on initial momentum also makes evolution predictions easier. It can be seen in [46] that for the previously mentioned double-well ratchet, particles with different initial momenta also absorb different amounts of energy, however the dependence is more complex. In Chapters 5 and 6 it will be seen that the double kicked rotor actually provides a better momentum filter, where a narrow range of specific momenta can be selected, for which energy absorption is different than for other momenta. However, there is no ratchet effect as such in the double kicked rotor,

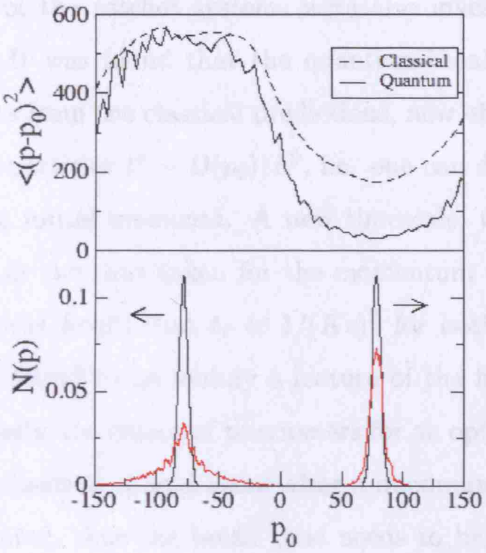

Figure 4.4: Asymmetries in the energy absorption for the rocking ratchet. Parameters are $K = 3.2$, $\hbar = 1$, $\epsilon = 0.01$ and $A = \pi/2$. The top panel shows the numerical calculation of the energy absorption vs. initial momentum p_0 both in the classical and quantum cases. A sinusoidal variation is seen as expected, with particles travelling in the positive x-direction absorbing very little energy, while those travelling in the negative x-direction absorb a large amount of energy. This is also shown by the evolution of initially Gaussian momentum distributions centred on $\pm\pi/(4\epsilon)$ in the bottom panels. The distribution centred on negative momenta is found to spread significantly, while that centred on positive momenta does not evolve much. Courtesy of Matt Isherwood.

although similarities to the rocking ratchet system are observed.

It should be noted that despite the asymmetries in the ratchet systems, localisation of the momentum distributions still takes place (showing the robustness of DL). This is important as localisation actually enhances the filtering effect, since the momentum asymmetries thus remain in the system asymptotically. In a classical system the asymmetric growth of a momentum distribution due to a ratchet effect would in fact be diluted in time as the distribution continues to spread. The expansion of a classical Gaussian wavepacket would eventually mask the ratchet effect at long times. The same would apply to a bounded quantum system if localisation was absent. Eventually a uniform distribution in momentum space would be obtained for a completely chaotic phase space; however dynamical localisation prevents this from happening. In this way DL makes the quantum ratchet, perhaps somewhat counterintuitively, asymptotically more reliable than the analogous classical system.

Some other features of the ratchet systems were also investigated, which shall be briefly mentioned here. It was found that the quantum break time t^*, at which the quantum diffusion departs from the classical predictions, now effectively depends on the initial momentum of the particles $t^* \sim D(p_0)/\hbar^2$, i.e. one can define a local break time for particles with specific initial momenta. A new timescale, the ratchet time t_r, was also introduced, defined as the time taken for the momentum current to reach 95% of its saturation value. It was found that $t_r \propto 1/(K\epsilon)^2$ for both ratchet systems. The ratchet time was further found to be mainly a feature of the finite lifetime of a 2-kick diffusion correlation. Finally, the choice of parameters for an optimal ratchet system was discussed. Obviously localisation should occur after a maximum amount of momentum asymmetry has been created, thus the break time needs to be long enough for this to occur. However, at the same time the localisation length $L \sim t^*\hbar$ must not be too large, to avoid dilution of the ratchet effect due to excessive spreading of the wavepacket. It was found that for the ideal ratchet $t^* \simeq t_r$, leading to restraints on the chirp parameter ϵ.

In [27] the localisation of the Floquet states of the rocking ratchet and PPKR was investigated. As mentioned earlier, DL arises from the underlying localisation of the individual eigenstates of the periodic Floquet operator of a system. Thus, as expected, the localisation lengths L of the Floquet states for the rocking ratchet depend sinusoidally on the mean momentum of the states, in analogy with Figs.4.2 and 4.4. This is shown in Fig.4.5, where the comparison to the QKR, where localisation lengths are independent of the atomic momenta, is also shown. Note the line of eigenstates with $L \simeq 1$ in the QKR: these are states highly localised on a series of stable islands separated by 2π, due to the momentum periodicity of the phase space in the kicked rotor.

Fig.4.6 shows the actual forms of the Floquet states for the rocking ratchet. It is found that the same asymmetries appear as for the momentum distributions shown earlier. The case of a quantum wavepacket starting at $p_0 = 0$ and moving in the positive x-direction is shown (i.e. the opposite case to Fig.4.4). Eigenstates localised near $p = 0$ are highly asymmetric compared to the QKR case, being significantly extended towards positive momenta, but localised towards negative momenta. Furthermore, eigenstates at negative momenta near the minimum of the energy absorption are much more localised than those at positive momenta. This behaviour can be compared to the Floquet states for the QKR shown in Chapter 3 in Fig.3.4, which were found to be localised roughly

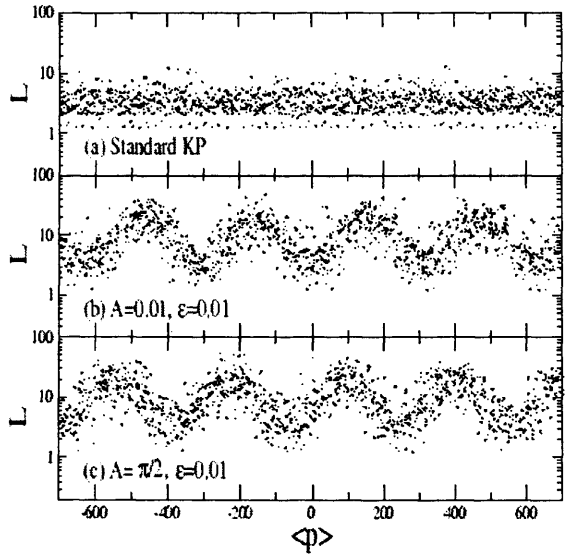

Figure 4.5: Localisation lengths L of the Floquet states vs the average momentum $\langle p \rangle$ of these states are plotted for the case of the standard QKR (a) and two cases of the rocking ratchet (b) and (c). Parameters for all three panels are $K = 3.4$ and $\hbar = 1$. In the case of the QKR a value of $A = 0.01$ was used to break spatial symmetry. For the QKR localisation lengths are independent of momentum, while for the rocking ratchet, even with only a slight spatial asymmetry present, L is seen to depend sinusoidally on $\langle p \rangle$, as suggested by Figs.4.2 and 4.4. Courtesy of Gwangok Hur.

symmetrically.

In conclusion it has been shown that by adding spatial and temporal asymmetries to the basic δ-kicked rotor, anomalous momentum and energy diffusion can be obtained, which is dependent on the initial momentum of the particles in the system. Some particles absorb more energy from the external driving than others; in particular a ratchet effect is observed, where particles travelling in a given direction are accelerated in preference to those travelling in the opposite direction. Both classical and quantum momentum currents exist, which can be enhanced, destroyed and reversed by careful experimental parameter choice, thus providing a significant amount of control over the system. The ratchet effects are due to the correlations between kicks at different times depending sinusoidally on the initial momentum of the particles, a situation absent in the δ-kicked rotor.

In the next chapter a new asymmetrical kicked system will be introduced: the double- or 2δ-kicked rotor, where evolution is by pairs of kicks. It will be seen that momentum-dependent diffusion is obtained purely through temporal asymmetry and that the ve-

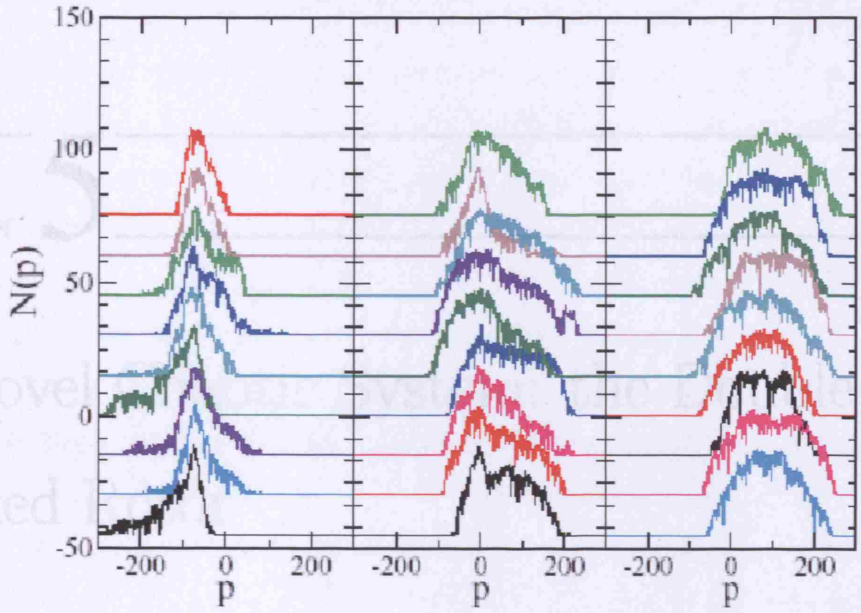

Figure 4.6: Floquet states in the rocking ratchet for the same parameters as in Fig.4.5c. The states are for a quantum wavepacket moving in the positive x-direction, hence the eigenstates at positive momenta are far less localised than those at negative momenta. Eigenstates localised near $p = 0$ are found to be extended towards positive momenta but localised towards negative momenta. The ratchet effect is obvious from the form of the Floquet states. Courtesy of Gwangok Hur.

locity selection effect is much stronger than in the rocking ratchet. New types of kick correlations, insignificant in previously studied systems, will be found to control the anomalous diffusion.

Chapter 5

A Novel Chaotic System: the Double Kicked Rotor

The starting point for the discovery of this new chaotic kicked system was the cold atom experiment presented in the introduction to this thesis. In contrast to the ratchet systems mentioned in the last chapter, a large asymmetry in the timing of the external impulses was introduced, effectively defining a sequence of kick pairs. This again resulted in energy diffusion dependent on the initial momentum of particles, however the mechanism was found to be very different from the perturbed-period kicked rotor. This led to a thorough investigation of the double kicked rotor, which includes alternating regions of fast and slow diffusion in phase space. At certain momenta particles absorb almost no energy from the external impulses, while at other momenta energy absorption is very high. The behaviour is found to stem from entire families of kick correlations depending on the initial momentum of particles, which will be analysed in the next chapter. Here the double kicked rotor is first investigated classically from the map, including an analysis of the slow diffusion areas, termed momentum trapping regions. The insensitivity of the specific diffusion mechanism to the time between kick pairs will be highlighted. The next chapter will introduce all the important kick correlations, while the quantum double kicked rotor will be investigated in Chapters 7 and 8 for two different systems.

5.1 The Double-Kick Map

The double-δ-kicked rotor (2δ-KR) is at first sight a trivial extension of the previously investigated PPKR, where a repeating cycle of 2 kicks is used with kicking periods $T_1 = \epsilon$ and $T_2 = \tau$, where $\epsilon \ll \tau$. This effectively defines a sequence of closely spaced kick pairs, as opposed to the single kicks in the δ-KR. The very short time interval between kicks in a pair is ϵ, and the much longer interval between pairs is τ. As the limiting case of the PPKR, a value of $\tau = 2T - \epsilon$ for the 2δ-KR can be chosen, where T is the usual kicking period of the δ-KR. For $\epsilon \rightarrow 0$ the δ-KR with period $2T$ is thus recovered. It will be seen below that the 2δ-KR system is in fact very insensitive to the value of the long time interval, as long as $\tau \gg \epsilon$.

Since there is no spatial asymmetry in the 2δ-KR, the kicking potential $V(x) = -K\cos x$ is as for the δ-KR in Eq.2.2, however the timing of the kicks is different, leading to a modified Hamiltonian:

$$H(p,x,t) = \frac{p^2}{2} + \sum_{N=0}^{\infty} K\cos x\delta(t - N(\frac{\tau+\epsilon}{2} + (-1)^N\frac{\tau-\epsilon}{2})) \tag{5.1}$$

and modified iterative map:

$$\begin{aligned} p_{N+1} &= p_N + K\sin x_N \\ x_{N+1} &= x_N + p_{N+1}\epsilon \\ p_{N+2} &= p_{N+1} + K\sin x_{N+1} \\ x_{N+2} &= x_{N+1} + p_{N+2}\tau \end{aligned} \tag{5.2}$$

For $N = 0$ the first free evolution from x_0 to x_1 must be for a time interval ϵ, in order to define a sequence of kick pairs in time (if the time intervals were interchanged in Eq.5.2, a single kick at the start would be followed by a series of kick pairs, thus adding an unwanted asymmetry into the system). There could of course be a period of free evolution for a time interval τ before the first kick pair; this would not change the dynamics of the subsequent system evolution.

Looking at the above map, it would seem that the double kicked rotor now depends on two control parameters in comparison to the δ-KR, namely $K\epsilon$ and $K\tau$. It will however be shown that the important momentum diffusion effects arising from the system evolution do not depend significantly on $K\tau$, provided that $\tau \gg \epsilon$ (although there is a dependence on the kick strength K, the system is very insensitive to τ in the above limit). This results in one control parameter $K_\epsilon = K\epsilon$ only. As for the Standard

Map (Eq.2.1 and Eq.2.7), the double kicked map can be rewritten in terms of rescaled momenta $p^\epsilon = p\epsilon$ to show the emergence of a single control parameter:

$$\begin{aligned} p^\epsilon_{N+1} &= p^\epsilon_N + K_\epsilon \sin x_N \\ x_{N+1} &= x_N + p^\epsilon_{N+1} \\ p^\epsilon_{N+2} &= p^\epsilon_{N+1} + K_\epsilon \sin x_{N+1} \\ x_{N+2} &= x_{N+1} + p^\epsilon_{N+2}\frac{\tau}{\epsilon} \end{aligned} \tag{5.3}$$

Since $\tau/\epsilon \gg 1$, there is a strong phase randomisation of the sine term in between kick pairs, as intuitively expected. It will be seen that for small enough ϵ, there is a strong kick-to-kick correlation within a pair. This partially explains the insensitivity of the system to τ, although one finds there are nevertheless correlations between kicks in different pairs. For most of what follows the aforementioned value of $\tau = 2T - \epsilon$ will be used, with $T = 1$, unless otherwise stated. Further investigations into the insensitivity of the system to τ will follow.

5.2 Momentum Trapping

Fig.5.2 shows a series of SOS for the 2δ-KR with increasing values of K_ϵ, in comparison to the δ-KR case (control parameter K_T) in Fig.5.1. Unscaled momenta are used in both cases for clarity, and the representation is on an infinite cylinder with periodicity only in position space (in comparison to the torus representation of the δ-KR in Fig.2.1). Important differences between the two systems are observed. Firstly, due to the introduced asymmetry, the main regular structures in the 2δ-KR system are destroyed at much smaller values of the control parameter. This effect has already been mentioned in Chapter 4 relating to the PPKR and other ratchet systems with asymmetries. Since the asymmetry is much larger here, the transition from a KAM-integrable system to complete chaos is even faster. It is found that $K_\epsilon^{crit} \simeq 0.014$; for larger values of the control parameter diffusion becomes unbounded in momentum space, and KAM tori disappear. For $K_\epsilon \gtrsim 0.075$ no large islands remain in phase space. Both transitions thus occur much faster with increasing control parameter in the double kicked rotor, than in the δ-KR, where $K_T^{crit} \simeq 0.97$, and large islands disappear for $K_T \gtrsim 5$.

The more significant difference however becomes apparent for higher values of the control parameters. For the kicked rotor in Fig.5.1 phase space is globally chaotic without any additional features for large values of K_T (neglecting accelerator modes); hence

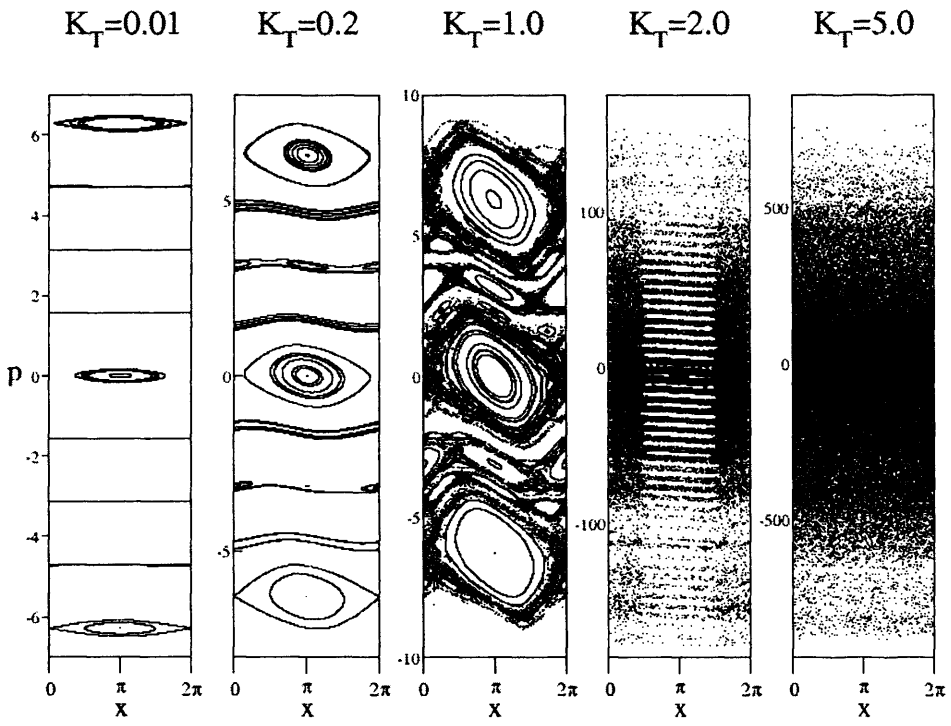

Figure 5.1: Surface of Sections for different values of the control parameter K_T in the Standard Map. Position is shown in modulo 2π and initial momentum for all particles is $p_0 \simeq 0$. Here, momentum space is not periodic, hence note the varying scales. The behaviour is as in Fig.2.1, with diffusion of particles becoming unbounded in momentum space for $K_T \gtrsim 1$ and phase space becoming globally chaotic for $K_T \gtrsim 5$. Obviously as K_T increases particles gain more energy and hence spread further in momentum space.

diffusion is simply a random walk. In the double kicked rotor however a momentum space partitioned into a number of distinct sections or cells of roughly equal width is observed for $0.1 \lesssim K_\epsilon \lesssim 2$. This is shown again in Fig.5.3 for $K_\epsilon = 0.35$. Within each section particles diffuse randomly as usual and are free to move in position space. It will be shown that diffusion rates at the centre of the sections are in fact higher than in the δ-KR. However, although particle trajectories eventually explore the entirety of phase space, at certain critical momentum values defining the boundaries between sections, diffusion of particles seems to be slowed down, hence the apparent lower density of particles at high $|p|$ at long times. Particles thus rapidly diffuse over the distance of one cell in momentum space, but diffuse very slowly across a boundary. For smaller values of $0.1 \lesssim K_\epsilon \lesssim 0.3$ it should be noted that the impulse strength may not be large

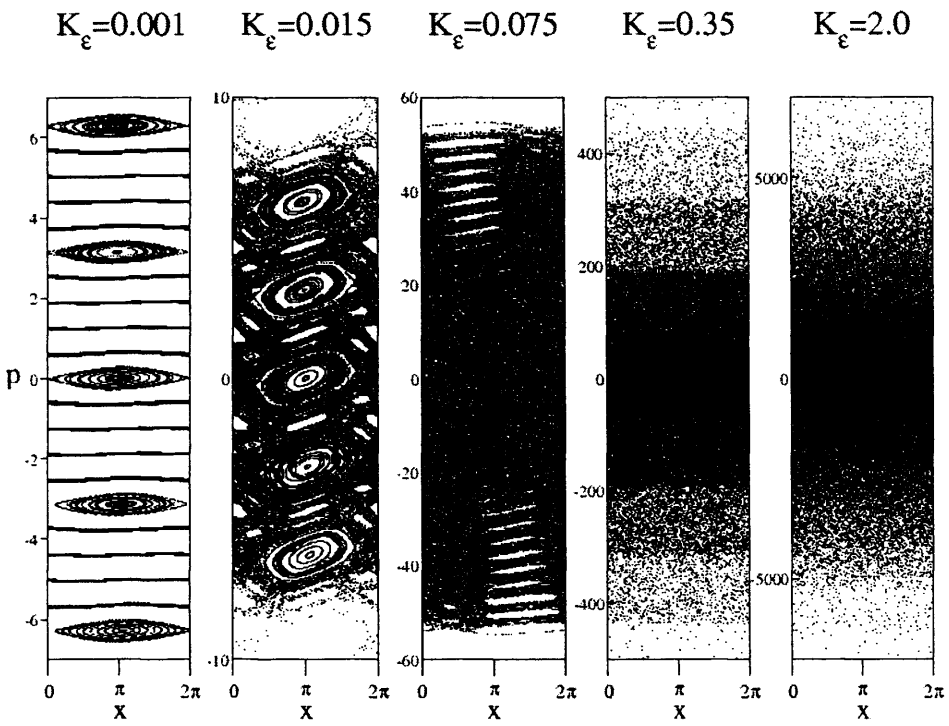

Figure 5.2: Surface of Sections for different values of the control parameter K_ϵ in the double kicked map (Eq.5.2). Here $\epsilon = 0.05$ for all panels, but K is increased from left to right. Position and momentum of trajectories are plotted after each kick pair, with position shown in modulo 2π and momentum space unbounded as in Fig.5.1. Initial momentum for all particles is $p_0 \simeq 0$. Note the different momentum scales for the panels. For $K_\epsilon \lesssim 0.015$ regular KAM tori and islands exist in phase space, and diffusion is bounded by these regular structures. As K_ϵ is increased, large regular structures disappear very quickly, and for $K_\epsilon \gtrsim 0.075$ no large islands remain. The double kicked system becomes globally chaotic at much lower values of the control parameter than in the Standard Map. After the transition to global chaos the phase space in the 2δ-KR is divided into diffusion cells in momentum space of equal width. Within these cells momentum diffusion is faster than in the Standard Map, but at cell boundaries diffusion is very slow. For $K_\epsilon \gtrsim 2$ the cellular structure of phase space disappears, and the behaviour becomes similar to that of the Standard Map.

enough for particles to diffuse much further than the first cell centred on $p = 0$, as seen in Fig.5.2. For large values of the control parameter $K_\epsilon \gtrsim 2$ on the other hand, the cellular structure of phase space vanishes, and the diffusion behaviour is similar to that found in the Standard Map. These limits will be discussed again later.

Fig.5.4 shows a typical individual trajectory of a particle in momentum space with

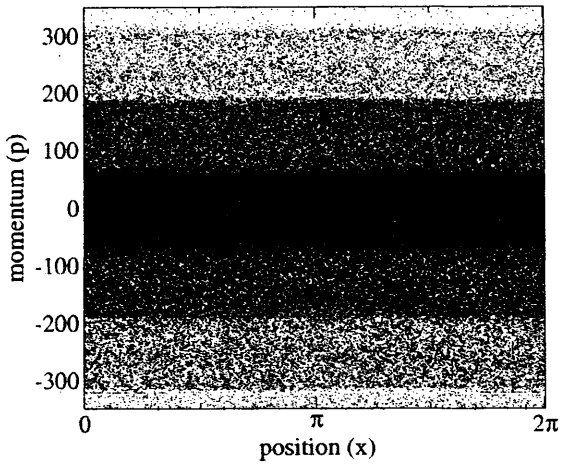

Figure 5.3: Surface of Section for the 2δ-KR for $K_\epsilon = 0.35$ as in Fig.5.2. Phase space is divided into a number of cells displaying fast diffusion of particles, while at certain momenta corresponding to the cell boundaries diffusion is very slow. Particles thus spend a significant time trapped within one cell before moving on to the next. This division of momentum space into alternating regions of fast and slow particle acceleration persists for a broad range of values of the control parameter $0.1 \lesssim K_\epsilon \lesssim 2$.

time in the double kicked rotor, compared to the δ-KR. A value of $K = 7$ is used in both cases, and for the 2δ-KR the short time interval is $\epsilon = 0.05$, resulting in the same value of $K_\epsilon = 0.35$ as in Fig.5.3 (for the δ-KR the period is $T = 1$ as before). While the trajectory for the δ-KR seems to be completely random with no discernible patterns, the cellular structure of phase space is evident for the 2δ-KR. Random diffusion local to a small area of momentum space (within a cell) is interspersed with infrequent ballistic transport to other regions (cells). Particles spend, on average, a significant amount of time trapped within one momentum cell before moving on to the next. The situation is somewhat similar to particles near accelerator islands in the δ-KR, however there are no large stable structures in the 2δ-KR phase space, and particles may execute a random walk over the entirety of one cell until being transported to the next.

Furthermore, particles starting at different initial momenta will initially diffuse at different rates, depending on their location within momentum space. This can be shown by plotting SOS at different times and for different starting momenta in phase space. Fig.5.5 shows sequences of distributions of particles in the 2δ-KR with increasing time

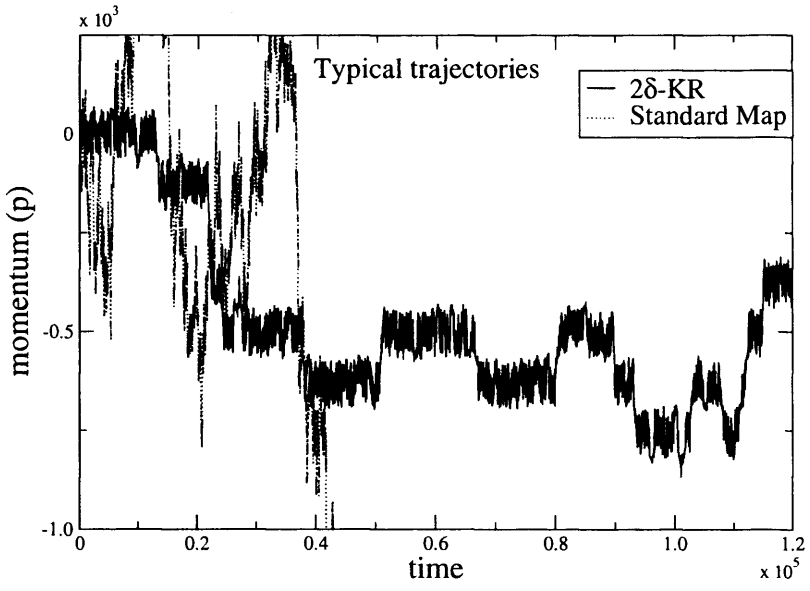

Figure 5.4: Typical trajectories of individual particles in time in the Standard Map and the 2δ-KR. Parameters are $K = 7$ and $\epsilon = 0.05$, resulting in $K_\epsilon = 0.35$, and $\tau = 1.95$. The initial momentum of both particles is $p_0 = 0$. While the SM trajectory describes a simple random walk in momentum space, the cellular structure of the latter for the double kicked rotor is evident. The particle spends a considerable amount of time trapped within one cell, before moving on to the next one. Note that in both cases particles may diffuse in either direction along the momentum axis. Courtesy of Tania Monteiro.

for $p_0 = 0$ and $p_0 = 63$ (near the first cell boundary in Fig.5.3) respectively, as well as a sequence of SOS for the δ-KR for comparison. For clarity, position space is now non-periodic and unbounded, thus showing actual cells in the complete phase space rather than in momentum space only.

The left panel (Fig.5.5a) essentially shows the movement of particles with initially zero momentum through the phase space of Fig.5.3. Particles rapidly distribute themselves uniformly in the central cell around $p = 0$, but take much longer to accelerate on to the neighbouring cells, which are then again filled uniformly in a short amount of time. It should be remembered at this point that the trapping or hindered diffusion effect is in momentum space only; particles are free to move anywhere in position space.

The middle panel (Fig.5.5b) also shows the movement of particles through the phase space of Fig.5.3, but for an initial momentum of $p_0 = 63$. Here particles start at a cell boundary where diffusion is initially very slow. After remaining at roughly the starting momentum for some time, particles then rapidly move either way to fill the two adjacent

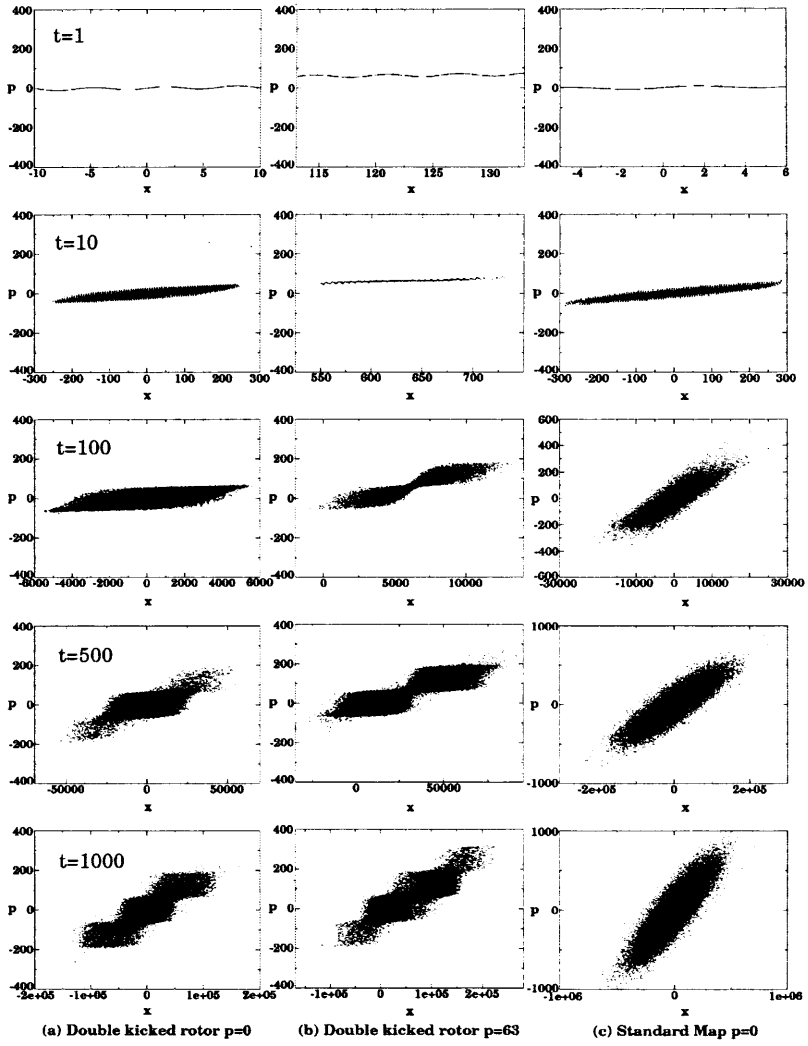

Figure 5.5: Momentum diffusion in time in the double kicked rotor (a,b) in comparison to the Standard Map (c). Parameters are $K = 7$, $\epsilon = 0.05$ and $\tau = 1.95$. Time increases from top to bottom, and both position and momentum space are unbounded, hence note the different scales. In (a) all particles start with initial momentum $p_0 = 0$ in the centre of a diffusion cell; in (b) particles start at $p_0 = 63$ near a cell boundary. In both cases particles diffuse rapidly within cells, but very slowly across boundaries. Particles starting at a boundary absorb more energy after a given time than those starting in the centre of a cell, since the former only traverse half a boundary region on average at the start of the system evolution. In (c) the SM diffusion for $K = 7$ is shown for comparison, and no cells exist. Thus overall diffusion occurs faster, and the SM ensemble gains more energy than the double kicked one, after a given amount of time.

cells. After the same amount of time, it can be seen that the ensemble of particles starting at a cell boundary in a slow diffusion area has in fact on average gained more energy than that started at the centre of a cell. The panel on the right (Fig.5.5c) shows the particle distributions in the δ-KR at the same time steps. Here diffusion occurs at the same rate throughout phase space, and a uniform distribution is observed.

The cell boundaries have been termed momentum trapping regions, due to the slow diffusion rates occurring there. It can be seen from phase space and individual particle trajectories that the trapping is only transient, in the sense that particles clearly do escape these regions after a while, and eventually diffuse over the entirety of phase space (within the actual system boundaries). However, the existence of fast and slow diffusion regions in momentum space is an asymptotic effect persisting for all times, given suitable system parameters. An imprint of this momentum-dependent diffusion remains in the cellular structure of phase space and the distributions of the particle ensembles over a long period of time (as seen in Fig.5.5). Eventually of course, actual physical system boundaries confine diffusion to a restricted area, over which a uniform distribution will be obtained at long times, however locally particles still experience varying diffusion rates (although this will then be masked when plotting SOS).

It is found that the cell boundaries are at momenta $p_N \simeq \pm(2n+1)\pi/\epsilon$ with $n = 0, 1, 2\ldots$, giving the 2δ-KR a $2\pi/\epsilon$ periodicity in p. Hence the cellular structure of phase space provides a natural choice of periodicity in momentum space for representing the 2δ-KR on a torus. Periodic boundary conditions are $p + 2\pi n/\epsilon = p$, for integer n, which is analogous to the kicked rotor case. The torus then represents one single diffusion cell in phase space. This is also the case for the quantum mechanical version of the double kicked rotor in Chapter 7.

The momentum trapping regions and resulting delayed diffusion can be explained simplistically from the unscaled double-kick map (Eq.5.2). For particles at $p_N \simeq \pm(2n+1)\pi/\epsilon$, the first kick in a pair adds an impulse $K \sin x_N$ to the momentum, as shown by the map. Substituting the previous expression for p_N into the map, one obtains for the second kick:

$$\begin{aligned} p_{N+2} &= p_{N+1} + K\sin(x_N + p_{N+1}\epsilon) = p_{N+1} + K\sin(x_N \pm (2n+1)\pi + K\epsilon\sin x_N) \\ &\simeq p_N + K\sin x_N + K\sin(x_N \pm (2n+1)\pi) = p_{N+1} - K\sin x_N = p_N \end{aligned} \tag{5.4}$$

for small K_ϵ. Since the particles have moved a distance of roughly π along the sinusoidal

potential, this means that for these trapping momenta the second kick in a pair roughly cancels the first, thus leaving the momentum unchanged. An exact kick cancellation occurs for values of $p_N = \pm(2n+1)\pi/\epsilon - K\sin x_N$, dependent on the position of the particle, where a kick is effectively deducted from the momentum just before an applied kick pair.

Conversely to this behaviour, at the centre of a diffusion cell particles have momenta $p_N \simeq \pm 2n\pi/\epsilon$, leading to $p_{N+2} \simeq p_N + 2K\sin x_N$, showing roughly maximal absorption of energy for each kick pair. Since for small ϵ the double kicked rotor essentially features two kicks for each single kick $K\sin x_N$ in the δ-KR, the above result shows that at the centre of the diffusion cells, the energy absorption is in fact roughly twice that of the δ-KR. Momentum space is thus divided into a series of resonances and antiresonances in terms of diffusion or acceleration rates, and hence energy absorption. Given the form of the applied potential to the system, the change from maximal absorption at a cell centre to the trapping region at the boundary is roughly sinusoidal. As particles approach a resonant or antiresonant region of momentum space they are accelerated or decelerated respectively. This explains the diffusive behaviour seen in Figs.5.3 and 5.5.

The trapping regions can be further investigated by plotting a magnified section of phase space local to one of the cell boundaries. This is shown in Fig.5.6 for a trapping region for $K = 4.8$ and $\epsilon = 0.02$, leading to $K_\epsilon = 0.096$. Upon magnification one discovers small regular structures within the trapping regions, absent in the remainder of phase space. These can be related to the golden ratio cantori found in the kicked rotor, which result from the destruction of the last invariant KAM tori as KT is increased. These cantori were found in Chapter 2 to lie either side of a region around $p \simeq \pm(2n+1)\pi/T$ for $T = 1$ in the δ-KR, and provide the strongest barrier to diffusion in momentum space. Correspondingly the small regular structures in the 2δ-KR lie in the vicinity of the trapping regions $p \simeq \pm(2n+1)\pi/\epsilon$. The cantori provide no permanent barrier for particles (given suitable values of K and ϵ), however acceleration of particles through these fractal regions is considerably slower than in the completely chaotic regions, as one would expect. It will however be shown later in this chapter that trapping regions can exist even in the absence of cantori, so the regular structures are not fully responsible for the slow diffusion effect, although they do of course contribute.

The fractal structures at the trapping regions can be analysed from the kick map (Eq.5.2). If one looks closely at the magnified phase space of Fig.5.6, the islands at the

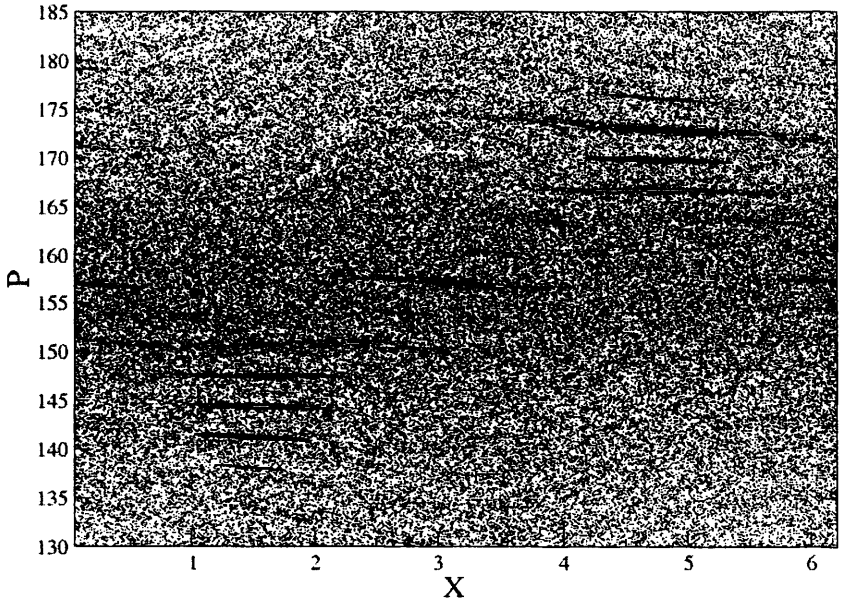

Figure 5.6: Magnified section of a trapping region for $K = 4.8$ and $\epsilon = 0.02$, leading to $K_\epsilon = 0.096$, and $\tau = 1.98$ (hence $\tau/\epsilon = 99$). Small cantori structures are found to be present within the trapping regions, located at positions $x \simeq n\pi$ near the centre and at positions $x \simeq 2n\pi + \pi/2$ and $x \simeq 2n\pi - \pi/2$ elsewhere.

exact centre are located at positions $x \simeq n\pi$, whereas in the surrounding near resonant area, they are positioned at $x \simeq 2n\pi + \pi/2$ and $x \simeq 2n\pi - \pi/2$. The islands approximately follow the curve $-K \sin x$ around $p_N \simeq \pm(2n+1)\pi/\epsilon$, along which exact trapping occurs, as shown previously. At this point it should be remembered that the main islands in the Standard Map are located at $x \simeq (2n+1)\pi$ (Fig.2.1). Since the SM is defined by kicks $K \sin x$ at regular time intervals, resulting in islands spaced at 2π intervals in position space, the islands at the centre of the double-kick trapping regions effectively correspond to a $\sin 2x$ iterative map. On the other hand, in the near resonant region the phase shift of $\pm\pi/2$ in the island positions indicates a $\cos x$ map.

These results can be shown mathematically from the double kick map. An approximate momentum value within a trapping region can be written as $p_N = p_R \pm \delta p$, where $p_R = \pm(2n+1)\pi/\epsilon$ is the (anti)resonant momentum at the centre of a trapping region, and δp represents a small deviation from this value. Substituting this expression as the momentum just before a double kick into the map, Eq.5.2, and keeping the term previ-

ously neglected for the kick cancellation, one obtains for the momentum after the kick pair:

$$\begin{aligned} p_{N+2} &= p_{N+1} + K\sin(x_N \pm (2n+1)\pi \pm \epsilon\delta p + K_\epsilon \sin x_N) \\ &= p_N + K\sin x_N + K[\sin(x_N \pm (2n+1)\pi)\cos(\pm\epsilon\delta p + K_\epsilon \sin x_N) \\ &\quad + \cos(x_N \pm (2n+1)\pi)\sin(\pm\epsilon\delta p + K_\epsilon \sin x_N)] \end{aligned} \tag{5.5}$$

Assuming small angle identities such that $\cos(f(\epsilon)) \simeq 1$ and $\sin(f(\epsilon)) \simeq f(\epsilon)$, this expression reduces to:

$$\begin{aligned} p_{N+2} &\simeq p_N - K\cos x_N(K_\epsilon \sin x_N \pm \epsilon\delta p) \\ &= p_N - \frac{K^2\epsilon}{2}\sin 2x_N \mp K_\epsilon \delta p \cos x_N \end{aligned} \tag{5.6}$$

This shows the form of the map over a kick pair at the trapping regions. At the resonant centre of the trapping region ($\delta p = 0$) the double-kick map is essentially equivalent to an effective $\sin 2x$ single-kick standard map, as mentioned previously:

$$p_{N+2} \simeq p_N - K_R \sin 2x_N \tag{5.7}$$

with $K_R = K^2\epsilon/2$. Further away from the centre where $\delta p > K/2$ (i.e. the last term in Eq.5.6 is dominant) the map is cosinusoidal, again as observed in Fig.5.6:

$$p_{N+2} \simeq p_N - K_{\delta p}\cos x_N \tag{5.8}$$

with $K_{\delta p} = K_\epsilon \delta p$. The approximate half width of the trapping regions can be estimated as $\delta p \simeq \pi/(6\epsilon)$, i.e. trapping occurs within a region about one sixth of the total cell area. For large K_ϵ the trapping regions become slightly narrower due to the requirement that $|\pm\delta p| + K\sin x \ll |\pi/\epsilon|$ (cf. Eq.5.4), however this effect is largely negligible.

Fig.5.7 shows further enlargements of the trapping region shown in Fig.5.6. The top panels show the change from a $\sin 2x$ map at the centre to a $\cos x$ map further out. The bottom panels are standard single kick maps with periodic impulses $K_R \sin 2x$ (a) and $K_{\delta p}\cos x$ (b) respectively, with the kick strengths as given above. The correspondence to the 2δ-KR trapping regions is evident. It should be noted that using the scaled map, Eq.5.3, the emergence of the single control parameter K_ϵ for the above maps is again clear, since Eq.5.6 becomes, in scaled momenta p^ϵ:

$$p^\epsilon_{N+2} \simeq p^\epsilon_N - \frac{K_\epsilon^2}{2}\sin 2x_N \mp K_\epsilon \epsilon\delta p \cos x_N \tag{5.9}$$

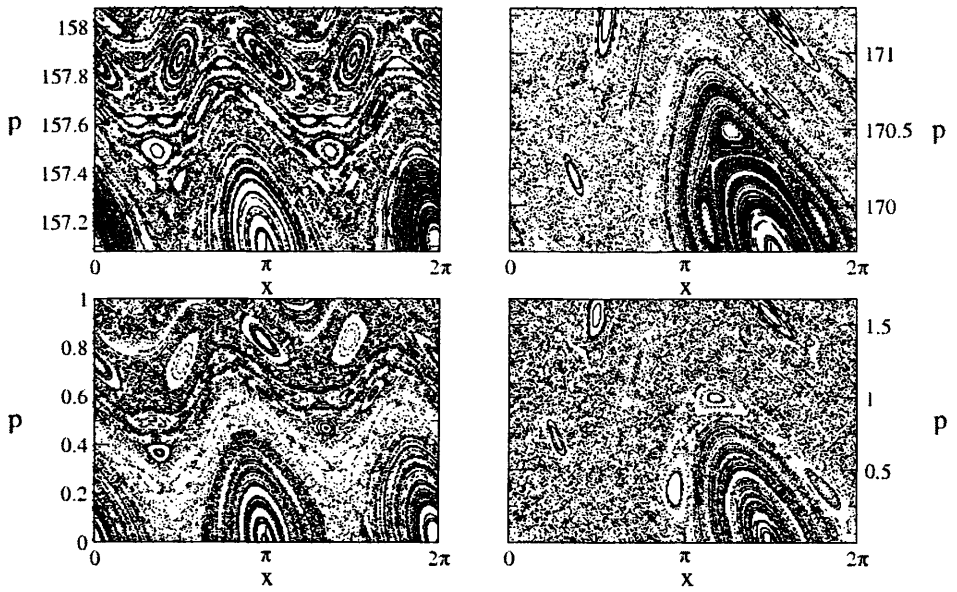

Figure 5.7: Magnified sections of the trapping region shown in Fig.5.6 for the double kicked rotor (top panels), in comparison to standard single kick maps (bottom panels). Parameters for the 2δ-KR are as for Fig.5.6, and the single kick period in the bottom panels is $T = 2$. In (a) the correspondence between the local phase space at the resonant central momentum value p_R of a trapping region, and a standard map with a kick $p_2 = p_0 - K_R \sin 2x_0$ is shown, where $K_R = K^2\epsilon/2 = 0.24$. In (b) the correspondence between the outer phase space near the resonant momentum of a trapping region, and a $\pi/2$ phase-shifted cosinusoidal standard map with a kick $p_2 = p_0 - K_{\delta p} \cos x_0$ is shown, where $K_{\delta p} = K\epsilon\delta p = 0.75$. Courtesy of Tania Monteiro.

It can also be seen from Eqs.5.2 and 5.4 that τ does not influence the trapping effect significantly, provided $\tau \gg \epsilon$, or alternatively the ratio $\tau/\epsilon \gg 1$. The approximate kick cancellations shown in Eq.5.4, and the exact cancellations at $p_N = \pm(2n+1)\pi/\epsilon - K \sin x_N$, occur at each kick pair, regardless of the long period of free evolution in between. If one assumes that $p_{N+2} \simeq p_N$ for the trapping regions and neglects terms including $K\epsilon$, then for p_{N+3} after the first kick in the next pair, the following expression

is obtained:

$$p_{N+3} = p_{N+2} + K\sin(x_{N+1} + p_{N+2}\tau) \simeq p_{N+2} + K\sin(x_N \pm (2n+1)\pi + p_N\tau)$$
$$= p_{N+2} - K\sin(x_N + p_N\tau) \tag{5.10}$$

For the momentum after the second kick in the pair:

$$p_{N+4} = p_{N+3} + K\sin(x_{N+2} + p_{N+3}\epsilon) \simeq p_{N+2} - K\sin(x_N + p_N\tau)$$
$$+K\sin(x_N + p_N\tau \pm (2n+1)2\pi) = p_{N+2} \tag{5.11}$$

This shows that the important feature of the 2δ-KR is largely independent of τ. Since diffusion is fast across the cells in Fig.5.3 for any sizeable value of τ, and the trapping regions exist independently of this parameter, the diffusion mechanism is almost solely dependent on K_ϵ. Note however that the free evolution in between kick pairs randomises the position of particles and thus leads to a dephasing of the trapping effect in time for individual particles located at the cell boundaries. Since exact trapping is restricted to a position dependent curve $p_N = \pm(2n+1)\pi/\epsilon - K\sin x_N$ in momentum space, the randomisation of x after each kick pair may move particles off this curve into an area where the kick cancellation is only approximate. This is particularly the case for large values of K and hence large amplitudes of the sine curve. Hence $p_{N+\beta} \not\simeq p_N$ for $\beta \gg N$ (but the slow diffusion regions exist asymptotically).

The control parameter K_ϵ thus controls both the width of the momentum cells (and hence the positions of the cell boundaries), and the amount of trapping of trajectories occurring at the boundaries. Equivalently K_ϵ controls the rate of diffusion of particles in momentum space. This will be seen in the next chapter to be due to kick correlations, and thus diffusion corrections, depending on this control parameter as well as the initial momenta of particles. Although for scaled momenta (Eq.5.3) K_ϵ is the only control parameter, as previously mentioned, it is found that individually ϵ mainly controls the positions and spacing of the trapping regions in phase space, while K mainly controls the strength of the trapping effect, and thus transport of particles through trapping regions.

Since trapping regions occur at $p \simeq \pm(2n+1)\pi/\epsilon$, as $\epsilon \to 0$ with fixed K the trapping regions move further apart, and eventually the momentum cells become infinitely wide, thus resulting in the δ-KR limit. Very low values of K_ϵ however also result in large regular structures reappearing in phase space and the system becoming KAM integrable, before

the kicked rotor limit is reached. Large values of ϵ for fixed K on the other hand result in continuously narrowing cells, as trapping regions move closer together, again eventually leading to the δ-KR limit as $\epsilon \to \tau$. In this limit, either large KAM structures reappear at values of $K\tau \lesssim 5$, or the fractal trapping regions are destroyed for values of $K\tau \gtrsim 5$ in the globally chaotic δ-KR limit. The structure of phase space for variation of ϵ with fixed K is shown in Fig.5.8.

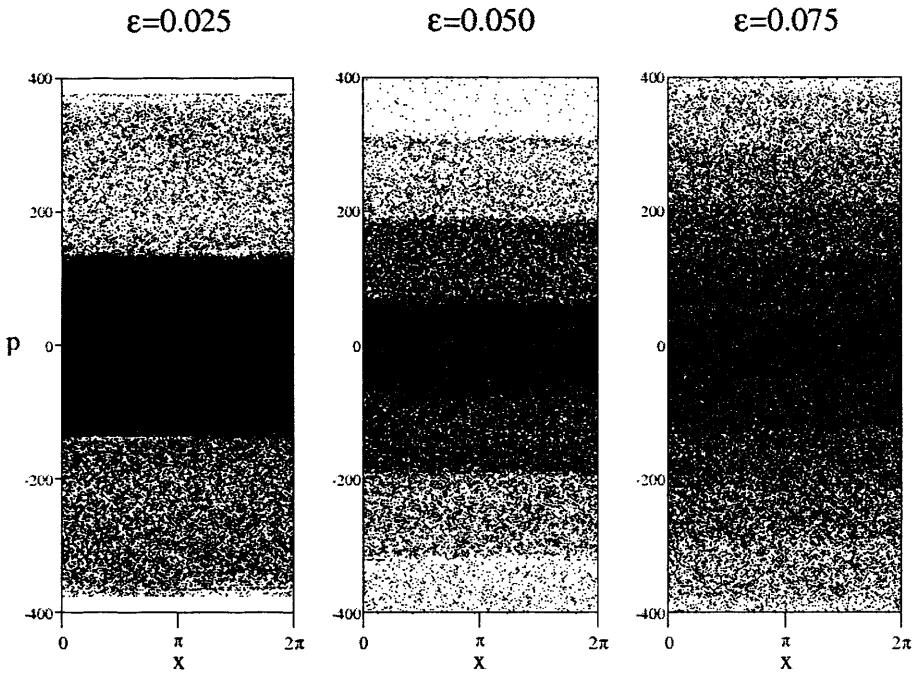

Figure 5.8: Surface of sections for varying short time interval ϵ in the double kicked rotor. Here $K = 7$ and $\tau = 1.95$ in every case, leading to values of the control parameter $K_\epsilon = 0.175, 0.350, 0.525$ from left to right. Hence all three cases are in the regime where momentum trapping occurs and a cellular phase space is seen. Increasing ϵ with fixed K results in continuously narrower cells, since the location of the trapping regions depends on ϵ. Note that the overall diffusion rate is similar for all cases.

Fig.5.2 shows variation of K for fixed $\epsilon = 0.05$. As $K \to 0$ with fixed ϵ diffusion through phase space is continuously reduced, and for very low K particles are no longer able to escape or pass through trapping regions (which effectively become KAM tori for $K_\epsilon \lesssim 0.015$). For large K with fixed ϵ, the trapping mechanism is weakened, and for $K_\epsilon \gtrsim 2$ particles gain enough momentum to pass through phase space essentially unperturbed, as in the δ-KR. For large K_ϵ the approximation made in Eq.5.4 is no longer

valid, and hence trapping regions no longer exist. Although exact kick cancellations at $p_N = \pm(2n+1)\pi/\epsilon - K\sin x_N$ are still possible, the large amplitude of this curve in momentum space results in very rapid dephasing of trapping due to randomisation of the position variable. The clearest signatures of the momentum trapping effect characteristic of the double kicked rotor are seen for $0.1 \lesssim K_\epsilon \lesssim 1$, for which in Eq.5.4 $K\epsilon\sin x_N$ is small enough to neglect in comparison to π. For $1 \lesssim K_\epsilon \lesssim 2$ the effect is still present but somewhat weaker; $K\epsilon\sin x_N$ is starting to become a sizeable term.

A further limit is reached for the case $\tau \to \epsilon$, i.e. the standard kicked rotor but with very short time intervals between subsequent kicks. In the usual δ-KR there is no momentum trapping effect, since $KT\sin x_N$ is a sizeable term in comparison to π, for values of K for which phase space is globally chaotic. Although trapping regions can exist at momenta $p_N = \pm(2n+1)\pi/T - K\sin x_N$, the amplitudes of these curves in momentum space are larger than the separation of the central trapping values ($\sin x_N = 0$), which are 2π apart. This means the regions overlap, and on average the same diffusion rate is observed for all momenta. For a series of closely spaced kicks where $T \to \epsilon$ one might assume that trapping regions should be possible, since their centres would then be $2\pi/\epsilon$ apart again. However, the temporal asymmetry present in the 2δ-KR between ϵ and τ is essential for the momentum-dependent acceleration through phase space, as it causes regular structures to be destroyed at lower values of the control parameter, as mentioned previously. Due to the perfect symmetry in a kicked rotor with closely spaced kicks, regular structures remain present for much larger values of K_ϵ than in the 2δ-KR, which would completely obscure any momentum trapping (if K is very large to obtain a chaotic phase space, the width of the trapping regions again becomes comparable to the separation of their centres). It will also be seen in the next chapter that mathematically a series of closely spaced kicks would add additional kick correlations to the system, again obscuring the trapping effect.

5.3 The Random-Pair-Kicked Rotor

A final interesting limit in the 2δ-KR is encountered for very large values of $\tau \to \infty$. This completely randomises the phase of the sine term between subsequent kick pairs in Eq.5.2. Thus one can replace the long free evolution in the map by a random change in

the particle's position on a 2π-periodic cylinder or torus:

$$\begin{aligned} p_{N+1} &= p_N + K \sin x_N \\ x_{N+1} &= x_N + p_{N+1}\epsilon \\ p_{N+2} &= p_{N+1} + K \sin x_{N+1} \\ x_{N+2} &= x_{N+1} + \zeta_{N+1} \end{aligned} \tag{5.12}$$

where ζ is a random number in the interval $[0, 2\pi]$. It is found that this system, termed the random-pair-kicked rotor (RP-KR) [50], corresponds to the non-KAM limit, where a critical transition from (near) integrable motion to complete chaos occurs for very low K_ϵ, graphically approaching a step function. This is in contrast to the gradual transition observed in Fig.5.2. It is furthermore found that the fractal remains located in the trapping regions are destroyed in this limit. Unexpectedly however, as opposed to the case of large K_ϵ, the actual momentum trapping effect persists for large but finite values of τ, since kick cancellations only depend on ϵ as shown previously. This not only demonstrates the insensitivity of the double kicked system to τ, provided $\tau \gg \epsilon$, but also to the presence of fractal cantori in phase space, provided they do not occupy a too large portion. The persistence of the anomalous diffusion in the double kicked rotor in regimes where cantori are absent, is very unusual and will be seen to result in further important effects in the quantum 2δ-KR in Chapter 7.

Given the unimportance of the value of τ for the momentum trapping, one can take the randomisation even further and choose a different $\tau \gg \epsilon$ at each time step, resulting in a double kicked system which is no longer time periodic. Despite the varying time intervals between kick pairs, the double-kick diffusion mechanism with alternating fast and slow diffusion regions still persists. Again, momentum trapping regions are free of cantori, however the trapping of trajectories occurs as for a fixed value of τ.

In summary, Fig.5.9 shows a series of SOS for the 2δ-KR for different values of the ratio τ/ϵ, with insets showing the local phase space around the momentum trapping regions. $K = 7$ and $\epsilon = 0.05$ in all cases, hence only the period of free evolution τ changes. It can be seen that for low values of $\tau \to \epsilon$, there are denser and wider regions of cantori, eventually resulting in the closely spaced kicked rotor, as mentioned previously. At $\tau \simeq \epsilon$ large regular structures appear, and any momentum trapping effects are negligible. As the ratio τ/ϵ increases, fractal cantori progressively vanish from the trapping regions. The middle panels for $\tau/\epsilon = 39$ show the same phase space as in Fig.5.3. For these values some fractal structures are still present in the trapping

regions. The subsequent panels for $\tau/\epsilon = 99$ correspond to the ratio in Fig.5.6. In that case fractal structures were clearly seen in the trapping regions (at different positions to here, since a different value of ϵ was used). Here however, the kick strength K and control parameter K_ϵ are both higher than in Fig.5.6, hence almost no cantori remain.

Since the SOS are all generated for the same number of iterations or time steps, it is seen that the cantori still have a weak effect on the overall rate of diffusion for $\tau/\epsilon < 100$. The ensemble of particles gains slightly more energy as τ increases. For $\tau/\epsilon \gtrsim 100$ however, the SOS are nearly unchanged, and fractal structures rapidly disappear. The latter are also found to be absent in the random case, which is completely equivalent to the panels on the far right.

As a preliminary note on the potential uses of the double kicked system, it is evident that the momentum trapping regions could be used to select particles according to their velocities. Potential applications will be looked at again in Chapters 7 and 8, where the quantum version of the 2δ-KR is investigated in both cold atoms and spin chains, however it should be noted here that the momentum dependence of the energy absorption in the double kicked rotor displays a clearer signature than in the PPKR and the ratchet systems presented in the previous chapter, despite the absence of spatial asymmetries. The reasonably narrow trapping regions where momentum diffusion is very slow can be used to distinguish particles at these velocities from the others in the system, which are accelerated much faster by the external impulses. The specific transport mechanism through momentum space with alternating acceleration and deceleration may also have practical applications.

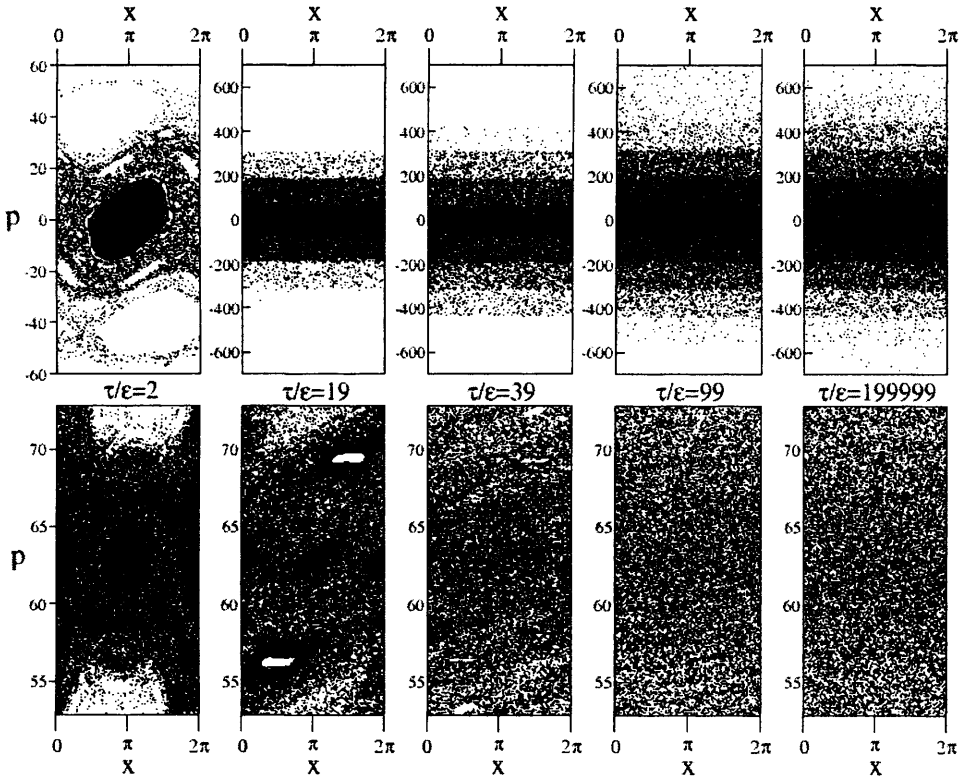

Figure 5.9: Surface of sections for varying long time interval τ in the double kicked rotor, and thus varying ratio τ/ϵ. Parameters $K = 7$ and $\epsilon = 0.05$ are fixed, leading to $K_\epsilon = 0.35$ for all panels. Top panels show the entire momentum space over which diffusion occurs. Bottom panels show the corresponding local phase space near the trapping momenta. On the far left $\tau \simeq \epsilon$, and regular structures appear throughout phase space, masking any characteristic trapping effects specific to the 2δ-KR. As τ, and hence τ/ϵ, is increased from left to right, large regular structures disappear from phase space, and the typical cellular structure is observed. In the bottom panels it is seen that the cantori present in the trapping regions for $\tau/\epsilon \lesssim 100$ also vanish as τ is increased. The trapping effect and corresponding cellular phase space however persist for all values $\tau \gg \epsilon$. For very large values of τ as in the far right panel, phase space is completely insensitive to the time interval between kick pairs. Changing τ randomly in time, resulting in a non-periodic system, does not change the SOS. Neither does a complete randomisation of the positions of particles after each kick pair. Both cases equally correspond to the far right panel.

Chapter 6

Energy Diffusion in the Double Kicked Rotor: Kick Correlations

In this chapter the mathematical details of the kick correlations found in the double kicked rotor will be given, and thus the diffusion mechanism will be further analysed. The same approach as in Chapter 2 for the Standard Map is used, but entire families of correlations are found to contribute to the energy diffusion, in contrast to the few correction terms in the Standard Map. A strong correlation between kicks in a pair exists, dependent on the initial momentum of particles, which is partially responsible for the trapping at certain momenta. Of greater interest however are sets of global long-range momentum dependent kick correlations, coupling all impulses in time, and which are of roughly equal strength regardless of temporal separation. This results in a transient long term memory in the double kicked rotor which affects the diffusive behaviour significantly, a situation highly unusual for chaotic systems. Some further correlations, independent of the initial momentum of particles, are also investigated, which act to lower the overall diffusion rate significantly in comparison to the background random walk, for nearly all system parameters. These correlations also appear in global families and affect the asymptotic diffusion rate. While momentum dependent correlations are transient, but at a given time couple all kicks roughly equally, those independent of initial momentum decay with kick separation at a given time, but exist asymptotically. A summary of the energy diffusion in the double kicked rotor is given at the end of the chapter.

6.1 The Modified Diffusion Rate

As seen in the previous chapter, the double kicked rotor exhibits a strong momentum dependence of the energy absorption of particles in the system from the external impulses. As particles pass through momentum space they are alternately accelerated and decelerated. Sections of high energy absorption are interspersed with comparatively narrow sections of very low energy absorption. The average momentum and hence energy diffusion of an ensemble of particles in the 2δ-KR can be analysed by investigating the kick correlations between impulses at different times, as for the kicked rotor in Chapter 2. It will be shown here that the diffusion mechanism in the double kicked rotor is due both to a strong momentum dependent correlation between kicks in a pair, and novel long-range kick correlations coupling all kicks in time.

If one ignores the trapping regions at first, then within the individual cells in phase space, particles obviously still execute a random walk in momentum, as for the Standard Map. Hence there is an identical uncorrelated diffusion rate D_0 in the 2δ-KR. Here however the scaling of the time variable is different; since the system so heavily depends on the temporal proximity of two kicks, time is counted in numbers of pairs of kicks, $t = N/2$ for even N (physical time is $t(\tau + \epsilon)$). This means that to be consistent with the result from the SM the average energy absorption in time is:

$$\langle E \rangle = D_0 t = \frac{K^2 N}{4} \tag{6.1}$$

Hence the uncorrelated diffusion rate is in fact $D_0 = K^2/2$, in other words half that of the SM. This however only arises due to the redefinition of the time variable and does not signify any difference in the underlying random walk behaviour. For $\langle p^2 \rangle$ the rate is now correspondingly $D_0 = K^2$. Also, for scaled momenta p^ϵ, the rate then depends on the actual control parameter $D_0 = K_\epsilon^2$. In the remainder of this chapter however, unscaled momenta will be used for clarity.

Given the cellular structure of phase space and the alternating regions of fast and slow momentum diffusion, the uncorrelated diffusion rate D_0 is however not very useful in the 2δ-KR. The corrections to the diffusion rate arising from correlations between kicks at different times have a much larger effect in this system than in the kicked rotor, in particular in terms of momentum dependence $C(p)$. These corrections will be derived in the same way as introduced in Chapter 2, although the introduction of temporal asymmetries alters the forms of the equations used slightly. In comparison to the δ-

KR two kicks are included per time step (again, $t = N/2$), denoted by (1) (the first kick in a pair) and (2) (the second kick in a pair), i.e. $t_{(2)} > t_{(1)}$. Furthermore, for the purpose of calculating kick correlations and diffusion corrections only, the order of long free evolutions (of duration τ) and kick pairs in the double kick map (Eq.5.2) is interchanged to result in:

$$\begin{aligned} x_t^{(1)} &= x_{t-1}^{(2)} + p_{t-1}^{(2)}\tau \\ p_t^{(1)} &= p_{t-1}^{(2)} + K\sin x_t^{(1)} \\ x_t^{(2)} &= x_t^{(1)} + p_t^{(1)}\epsilon \\ p_t^{(2)} &= p_t^{(1)} + K\sin x_t^{(2)} \end{aligned} \tag{6.2}$$

A period of free evolution now precedes the first kick pair, which of course, as previously mentioned, does not alter the subsequent behaviour in time. Naturally $x_0^{(2)} = x_0$ and $p_0^{(2)} = p_0$. This slight change in the system evolution is introduced to make the subsequent notation simpler.

The momentum of a given trajectory now evolves as:

$$p_t^{(2)} = p_0 + K\sin x_1^{(1)} + K\sin x_1^{(2)} + \ldots + K\sin x_t^{(1)} + K\sin x_t^{(2)} = p_0 + S_t^{(2)} \tag{6.3}$$

The form of the S summation is now:

$$\begin{aligned} S_l^{(2)} &= \sum_{j=1}^{l}\sum_{r=1}^{2} K\sin x_j^{(r)} \\ S_l^{(1)} &= K\sin x_l^{(1)} + \sum_{j=1}^{l-1}\sum_{r=1}^{2} K\sin x_j^{(r)} \end{aligned} \tag{6.4}$$

where of course for $l = 1$, the second summation is simply $S_1^{(1)} = K\sin x_1^{(1)}$. Correspondingly to above, the positions of particles evolve as:

$$\begin{aligned} x_t^{(2)} &= x_t^{(1)} + p_0\epsilon + S_t^{(1)}\epsilon \\ x_t^{(1)} &= x_{t-1}^{(2)} + p_0\tau + S_{t-1}^{(2)}\tau \end{aligned} \tag{6.5}$$

With the redefinition of time to include two kicks per time step and the changes above, the diffusion rate in the double kicked rotor can now be written:

$$\begin{aligned} D = \lim_{t\to\infty}\frac{1}{t}\sum_{m_t^{(2)}=-\infty}^{+\infty}\sum_{m_t^{(1)}=-\infty}^{+\infty}\cdots\sum_{m_1^{(2)}=-\infty}^{+\infty}\sum_{m_1^{(1)}=-\infty}^{+\infty}\int_0^{2\pi}\frac{dx_t^{(2)}}{2\pi}\int_0^{2\pi}\frac{dx_t^{(1)}}{2\pi}\cdots\int_0^{2\pi}\frac{dx_1^{(2)}}{2\pi}\int_0^{2\pi}\frac{dx_1^{(1)}}{2\pi} \\ (S_t^{(2)})^2\exp(\sum_{j=1}^{t}[im_j^{(2)}(x_j^{(2)} - x_j^{(1)} - p_0\epsilon - S_j^{(1)}\epsilon) + im_j^{(1)}(x_j^{(1)} - x_{j-1}^{(2)} - p_0\tau - S_{j-1}^{(2)}\tau)]) \end{aligned} \tag{6.6}$$

where $S_0^{(2)} \equiv 0$ for the case $j = 1$. The derivation of the above equation is exactly analogous to the case of the kicked rotor in Chapter 2. It should be noted that as for the δ-KR this equation is only valid in the predominantly chaotic regime, which for the double kicked rotor of course extends down to much lower values of the control parameter K_ϵ.

The lowest order term in Eq.6.6 is again obtained by choosing all $m_j^{(2)} = m_j^{(1)} = 0$:

$$D = \lim_{t\to\infty} \frac{1}{t} \int_0^{2\pi} \frac{dx_t^{(2)}}{2\pi} \int_0^{2\pi} \frac{dx_t^{(1)}}{2\pi} \cdots \int_0^{2\pi} \frac{dx_1^{(2)}}{2\pi} \int_0^{2\pi} \frac{dx_1^{(1)}}{2\pi} K^2 \sum_{j=1}^{t} \sum_{r=1}^{2} \sin^2 x_j^{(r)}$$
$$= \lim_{t\to\infty} \frac{1}{t} \frac{K^2}{2} 2t = K^2 \qquad (6.7)$$

which, as mentioned before, is now $D_0 = K^2$ since each time step includes two kicks. As for the δ-KR, corrections to this diffusion rate can be obtained by allowing certain m_j coefficients to take non-zero values. It will be seen that the introduction of the short time scale ϵ results in strongly momentum dependent diffusion corrections, absent in the kicked rotor. The momentum trapping effect is, unsurprisingly, partially due to a strong kick-to-kick correlation within a pair, leading to a correction dependent on $\cos p_0 \epsilon$. A quick inspection of the cellular phase space in Fig.5.3, shows that the maxima of this cosine function correspond to the centres of the cells, where fast diffusion occurs, and the minima correspond to the trapping regions at the boundaries. In the kicked rotor the 1-kick correlation was found not to contribute to the momentum diffusion, since the term depended on $\cos p_0 T$ with $T = 1$. Maxima and minima are only a distance of π apart in momentum space, resulting in oscillations on a comparable scale to the width of an initial Gaussian ensemble of particles (whether classically or quantum mechanically). Hence, in that case, the momentum dependence of the diffusion is too insignificant in comparison to the linear background diffusion shown in Chapter 2.

Following the argument above, any correction terms in Eq.6.6 depending on $\cos p_0 \tau$ result in very fast oscillations with p_0, completely negligible in comparison to the large oscillations in momentum space causing the trapping regions. For the 1-kick correlation, setting any $m_j^{(2)} = \pm 1$ results in the $\cos p_0 \epsilon$ term, while $m_j^{(1)} = \pm 1$ results in the negligible $\cos p_0 \tau$ term. Effectively one can thus set all $m_j^{(1)} = 0$ in Eq.6.6, a valid approximation for all momentum dependent corrections, provided that $\tau \gg \epsilon$. This

reduces the equation for the diffusion rate to:

$$D = \lim_{t\to\infty} \frac{1}{t} \sum_{m_t=-\infty}^{+\infty} \cdots \sum_{m_1=-\infty}^{+\infty} \int_0^{2\pi} \frac{dx_t^{(2)}}{2\pi} \int_0^{2\pi} \frac{dx_t^{(1)}}{2\pi} \cdots \int_0^{2\pi} \frac{dx_1^{(2)}}{2\pi} \int_0^{2\pi} \frac{dx_1^{(1)}}{2\pi} (S_t^{(2)})^2 \times \exp(\sum_{j=1}^{t} i m_j (x_j^{(2)} - x_j^{(1)} - p_0\epsilon - S_j^{(1)}\epsilon)) \tag{6.8}$$

where for simplicity $m_j^{(2)} \equiv m_j$ in what follows. It should be noted that linear background corrections, such as found in the kicked rotor, which do not depend on p_0, may depend on both ϵ and τ. However, since all kick correlations depend on Bessel functions whose arguments in turn depend on the time intervals between kicks, the τ dependent corrections are still less significant, as $J_n(x) \to 0$ for large x and all orders n. Oscillations of the Bessel functions decrease in amplitude as x increases, so in all cases ϵ dependent diffusion corrections are more dominant in the 2δ-KR.

Although more similar to the case of the kicked rotor, the linear corrections, independent of momentum, in the double kicked case, will be investigated later. First, the corrections dependent on p_0, responsible for the particular 2δ-KR diffusion mechanism, will be derived, including new long-range correlations between kicks that lie temporally far apart. Such long-range correlations will also be shown to exist for the linear background diffusion rate, in contrast to the kicked rotor; hence the order of the following sections.

6.2 The kick-to-kick correlation

To derive this correlation the same approach is used as in Chapter 2. A single $m_j \equiv m_j^{(2)} = 1$ in Eq.6.8 results in:

$$D = \lim_{t\to\infty} \frac{1}{t} \int_0^{2\pi} \frac{dx_t^{(2)}}{2\pi} \int_0^{2\pi} \frac{dx_t^{(1)}}{2\pi} \cdots \int_0^{2\pi} \frac{dx_1^{(2)}}{2\pi} \int_0^{2\pi} \frac{dx_1^{(1)}}{2\pi} (S_t^{(2)})^2 \times \exp(\sum_{j=1}^{t} i (x_j^{(2)} - x_j^{(1)} - p_0\epsilon - S_j^{(1)}\epsilon)) \tag{6.9}$$

Similarly to Eq.2.35 one chooses in the squared S summation the $\sin x_j^{(2)} \sin x_j^{(1)}$ term, representing the kick-to-kick correlation between kicks in a pair:

$$D = \lim_{t\to\infty} \frac{1}{t} \int_0^{2\pi} \frac{dx_t^{(2)}}{2\pi} \int_0^{2\pi} \frac{dx_t^{(1)}}{2\pi} \cdots \int_0^{2\pi} \frac{dx_1^{(2)}}{2\pi} \int_0^{2\pi} \frac{dx_1^{(1)}}{2\pi} 2K^2 \sum_{j=1}^{t} \sin x_j^{(2)} \sin x_j^{(1)}$$
$$\times \exp(i(x_j^{(2)} - x_j^{(1)} - p_0\epsilon - K\epsilon \sin x_j^{(1)} - \sum_{l=1}^{j-1} \sum_{r=1}^{2} K\epsilon \sin x_l^{(r)})) \quad (6.10)$$

As for the kicked rotor, integrals are solved using the relation given in Eq.2.21 linking the exponentials to Bessel functions:

$$e^{\pm i\beta \sin x} = \sum_{n=-\infty}^{+\infty} J_n(\beta) e^{\pm inx} \quad (6.11)$$

and for 2π-periodic integration all arguments of exponentials must vanish for terms to be non-zero.

The integral involving $x_j^{(2)}$ is solved as in Eq.2.24 and that involving $x_j^{(1)}$ as in Eq.2.36. Integrals over variables $x_1^{(r)} \ldots x_{j-1}^{(r)}$ with $r = 1, 2$ are then solved as in Eq.2.37, and finally $\int_0^{2\pi} dx_i^{(r)}/(2\pi) = 1$ of course for all $i > j$ and $r = 1, 2$. Performing all the integrations, a similar expression to Eq.2.38 is obtained:

$$D = \lim_{t\to\infty} \frac{1}{t} \frac{K^2}{2} \sum_{j=1}^{t} (J_0(K\epsilon) - J_2(K\epsilon)) J_0^{2(j-1)}(K\epsilon) e^{-ip_0\epsilon} \quad (6.12)$$

The only differences here are the new short timescale ϵ and the inclusion of two kicks per time step, resulting in $2(j-1)$ factors of $J_0(K\epsilon)$. Once again, the case $m_j = -1$ gives a complex conjugate term involving $\exp(+ip_0\epsilon)$. Adding the two terms gives the kick-to-kick correlation as:

$$C_1 t = K^2 \cos p_0\epsilon (J_0(K_\epsilon) - J_2(K_\epsilon)) \sum_{j=1}^{t} J_0^{2j-2}(K_\epsilon) \quad (6.13)$$

where $t = N/2$ with N even.

Note the dependence of the correlation on the control parameter K_ϵ and the scaled momentum p_0^ϵ. The K^2 factor is due to using unscaled momenta in Eq.6.8, otherwise this is K_ϵ^2. Note also that, as opposed to the main corrections derived in Chapter 2 for the δ-KR, due to the summation over J_0 in Eq.6.13, this correction is transient and decays to zero in time, i.e. $C_1(p_0, t \to \infty) = 0$. Hence the infinite limit in Eq.6.12 is not taken, and instead the quantity Ct is calculated, which is seen to saturate to a constant value after a certain time. Given the geometric sum in Eq.6.13:

$$\sum_{j=1}^{t} J_0^{2j-2}(K_\epsilon) = \frac{1 - J_0^{2t}(K_\epsilon)}{1 - J_0^2(K_\epsilon)} \quad (6.14)$$

and taking the infinite limit of this summation, the saturation value of the kick-to-kick correlation is:

$$\lim_{t\to\infty} C_1 t = K^2 \cos p_0\epsilon \frac{J_0(K_\epsilon) - J_2(K_\epsilon)}{1 - J_0^2(K_\epsilon)} \tag{6.15}$$

Note that since $J_0(K_\epsilon) \to 1$ for $K_\epsilon \to 0$, the time-dependent summation saturates slowly for small K_ϵ, and the kick-to-kick correlation may persist for relatively long times in the 2δ-KR. The asymptotic diffusion rate $D = C_1 = 0$ at $t \to \infty$.

Fig.6.1 shows the behaviour of the kick-to-kick correlation (shown with stars) in time (counted in pairs of kicks). Parameters are $K = 7$ and $\epsilon = 0.05$, as in Chapter 5, leading

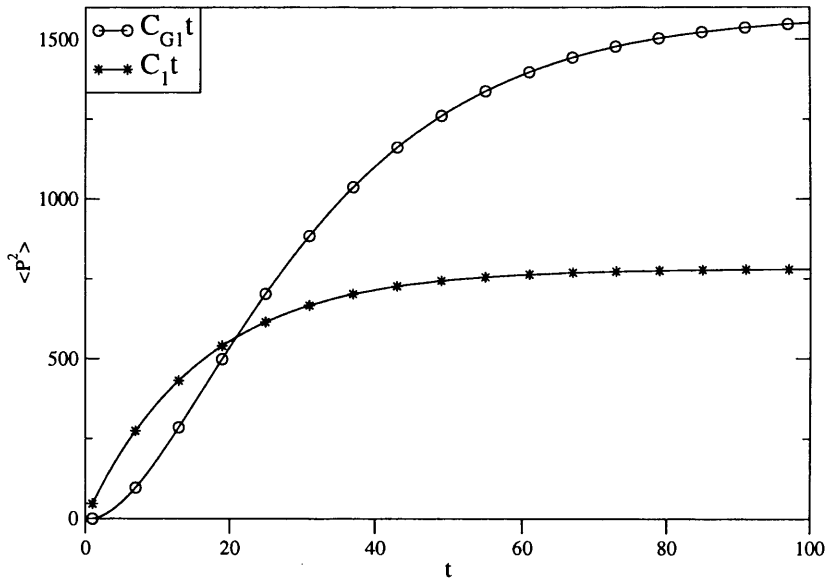

Figure 6.1: Behaviour of the kick-to-kick correlation $C_1 t$ (stars) in the double kicked rotor, in contrast with the lowest order global correlation family $C_{G1} t$ (circles) comprised of all n-kick correlations with $n \geq 2$. Parameters are $K = 7$ and $\epsilon = 0.05$, leading to $K_\epsilon = 0.35$. Absolute values $|C|t$ of maximum energy absorption ($\cos p_0\epsilon = 1$) caused by these correlations are shown. Time is counted in numbers of pairs of kicks ($t = N/2$, where N is the (even) individual number of kicks). At early times $C_1 t$ increases linearly with time, whereas $C_{G1} t$ increases quadratically with time. Thus the global correlation family eventually overtakes the kick-to-kick correlation in terms of effect on the diffusion rate and is found to saturate to a value roughly twice that of $C_1 t$.

to $K_\epsilon = 0.35$. Absolute values $|C_1|t$ of maximum energy absorption ($\cos p_0\epsilon = 1$) are shown. The non-linear time behaviour is clearly seen; in comparison the main corrections found in the δ-KR all have a linear time dependence, as for the background diffusion rate D_0. At early times it is seen that the kick-to-kick correlation also grows linearly

with time, since for small K_ϵ the Bessel function J_0 is near unity as mentioned above, and $J_0(K_\epsilon) \gg J_2(K_\epsilon)$. Hence the correlation is $\simeq K^2 t \cos p_0 \epsilon$ for small t. This can also be shown by using the approximation $J_0(K_\epsilon) \simeq 1 - K_\epsilon^2/4$ and expanding Eq.6.14:

$$\frac{1 - J_0^{2t}(K_\epsilon)}{1 - J_0^2(K_\epsilon)} \simeq \frac{1 - (1 - \frac{K_\epsilon^2}{4})^{2t}}{1 - (1 - \frac{K_\epsilon^2}{4})^2} \simeq \frac{1 - (1 - t\frac{K_\epsilon^2}{2})}{K_\epsilon^2/2} = t \tag{6.16}$$

In Fig.6.1 the linear regime of the kick-to-kick correlation extends to about $t \simeq 10$. In contrast to the linear correlations in the δ-KR, which remain the same at all times t, the correlation between kicks in a pair for the 2δ-KR becomes weaker in time, as kick pairs accumulate. Eventually at long times beyond $t \simeq 80$ the correlation saturates to the value in Eq.6.15, and hence the diffusion correction due to this correlation vanishes.

If one plots the average energy absorption for various times as a function of initial momentum p_0 of the particles, the effect of the kick-to-kick correlation on the diffusion in the system becomes evident. This is shown in the first panel of Fig.6.2 for $t = 5$ (after 5 kick pairs or alternatively 10 single kicks). Note that the quantity $\langle p^2 \rangle$ is used as before. The dashed curves in all panels are obtained from a numerical simulation of the 2δ-KR using an ensemble of 100,000 classical particles for the same parameters as in Fig.6.1. The solid curves are analytical calculations comprising the various diffusion corrections presented in this chapter.

In panel (a) the basic cosine shape of the kick-to-kick correlation is clearly visible. The solid curve is actually composed of several different kick correlations, which will be presented later, however $C_1 t$ is by far dominant, so the average energy can be approximated by $\langle p^2 \rangle \simeq K^2 t + C_1 t$. The trapping regions are located at $p_0 \simeq \pm(2n+1)\pi/\epsilon$ as expected, where the energy absorption at early times can be seen to be almost zero. Particles remain near their initial momentum. Conversely at $p_0 \simeq 2n\pi/\epsilon$, energy absorption is high. Note the flattened tops of the cosine curve however, which are due to higher order correlations presented in the next section. This shows that the absorption and hence acceleration rate through momentum space is not perfectly sinusoidal. Throughout most of the central parts of the cells in phase space, the diffusion rate is roughly the same (slightly less than twice the background rate $K^2 t \simeq 250$), but falls off rather quickly to zero when the cell boundaries are approached.

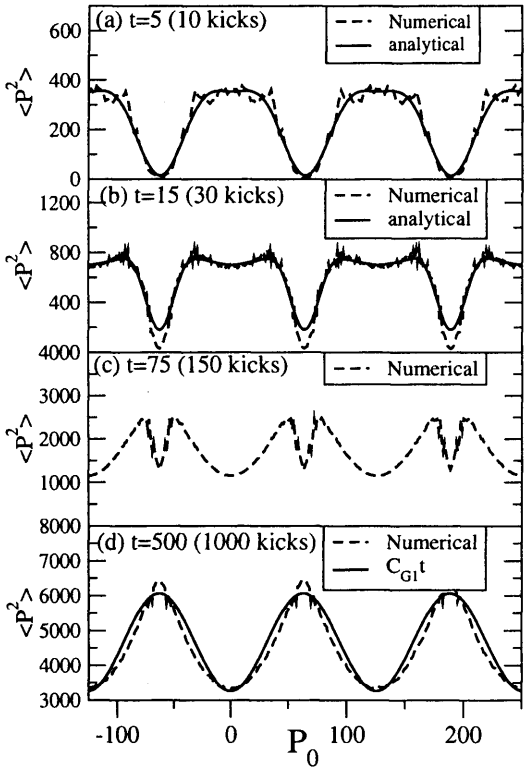

Figure 6.2: Average energy absorption in the double kicked rotor vs. initial momentum p_0 at various times $t = N/2$ counted in kick pairs, where N is the number of individual kicks. Parameters are as in Fig.6.1, with $K = 7$ and $\epsilon = 0.05$, leading to $K_\epsilon = 0.35$, and $\tau = 1.95$. Agreement between numerical simulations and analytical diffusion corrections is shown. In (a) the correlations included are $C_1 t$, $C_{G1} t$ and the lowest order $C_{\overline{G2}}$ term labelled IIa in Table 6.1. In (b) all correlations given in Table 6.1 are included. Agreement is very good at early times, but at intermediate times as in (c) many higher order correlations are needed for good agreement, hence the analytical curve has been omitted for this case. In (d) only $C_{G1} t$ has been included which dominates the diffusive behaviour almost completely. Notice the gradual change from a cosine to a sine shape in time, with dips persisting at the trapping regions for considerable times.

6.3 Global Kick Correlations

When looking at the subsequent panels in Fig.6.2 a gradual change from a cosine to a sine curve is seen, where particles initially trapped end up absorbing significantly more energy than those starting at the centres of diffusion cells. This agrees with Fig.5.5 where momentum diffusion was shown for ensembles of particles starting near the centre of a cell and at a cell boundary. Since those starting in a trapping region only need to traverse half of it on average to escape into the neighbouring cells, the long time energy absorption of initially trapped particles is in fact higher. Particles starting near the

centre of a cell will need to traverse the entire trapping region lying either side of it, before accelerating through the next cell.

The persistence of dips in the energy absorption at the trapping regions for considerable times should be noted however. Initially trapped particles end up with a higher average energy gain after $t \simeq 75$, which coincides roughly with the point at which $C_1 t$ saturates to a constant value in Fig.6.1. This shows that the kick-to-kick correlation is primarily responsible for the hindered diffusion at trapping regions.

It should be further noted that neither the higher energy gain of initially trapped particles, nor the decay of the kick-to-kick correlation, signifies an actual change in the diffusion mechanism of the 2δ-KR at long times. Regions of high and low acceleration in momentum space exist asymptotically, and individually particles will still experience trapping at every cell boundary they traverse. In Fig.6.2 however, the average energy $\langle p^2 \rangle$ of the entire ensemble of particles in the system is shown. At early times particles remain inside a cell or trapping region, so a graph of average energy gain reflects the structure of phase space accurately. At long times on the other hand, particles fill many cells, and on average roughly equal numbers will be located inside cells and trapping regions, regardless of the initial starting location. Hence the original phase space imprint on the average energy absorption is lost, however an asymptotic momentum dependence remains due to the different behaviour at earlier times. The gradual weakening of the kick-to-kick correlation in time either signifies the eventual escape of a subset of particles initially inside trapping regions, or more generally, the change from describing a localized ensemble in one area of phase space to one that extends over several cells.

The gradual change from initial to asymptotic energy absorption can be shown analytically from higher order kick correlations. The key difference to diffusion in the kicked rotor is not only a strong momentum dependence, but the fact that they exist as families of global long-range correlations, coupling all kicks in time. It will be shown later that such global correlations can be derived mathematically for the kicked rotor in the same way as shown here, however their effect is negligible in that system.

The lowest order global kick correlation family, responsible for the change in energy absorption seen in Fig.6.2, is derived from setting $m_j = \pm 1$ in Eq.6.8, as for the kick-to-kick correlation. For the case of $m_j = +1$ this results in Eq.6.9 as before. Now however, one chooses a collection of terms from the S summation of the form $\sin x_j^{(2)} \sin x_k^{(r)}$, where $r = 1, 2$ and $k < j$ but otherwise arbitrary. This represents choosing correlations between

the second kick in a given pair and kicks in all previous pairs. In other words this is the family of n-kick correlations with $n \geq 2$, derived from the case of $m_j = \pm 1$ in Eq.6.8, hence the term 'global' correlations. It should be noted that the global correlations are all with the second kick in a given pair ($\sin x_j^{(2)}$), since correlations between the first kick in a pair ($\sin x_j^{(1)}$) and other pairs, would require $m_j^{(1)} = \pm 1$ resulting in a dependence on τ; hence such terms are negligible as previously mentioned (other than the kick-to-kick correlation of course).

With the above choice from the S summation, the diffusion rate is:

$$D = \lim_{t\to\infty} \frac{1}{t} \int_0^{2\pi} \frac{dx_t^{(2)}}{2\pi} \int_0^{2\pi} \frac{dx_t^{(1)}}{2\pi} \cdots \int_0^{2\pi} \frac{dx_1^{(2)}}{2\pi} \int_0^{2\pi} \frac{dx_1^{(1)}}{2\pi} 2K^2 \sum_{j=2}^{t} \sum_{r=1}^{2} \sum_{k=1}^{j-1} \sin x_j^{(2)} \sin x_k^{(r)} \times \exp(i(x_j^{(2)} - x_j^{(1)} - p_0\epsilon - K\epsilon \sin x_j^{(1)} - \sum_{l=1}^{j-1} \sum_{r=1}^{2} K\epsilon \sin x_l^{(r)})) \tag{6.17}$$

The integral involving $x_j^{(2)}$ is again solved as in Eq.2.24 and that involving $x_j^{(1)}$ as in Eq.2.29. Integrals over variables $x_1^{(r)} \ldots x_{j-1}^{(r)}$ with $r = 1, 2$ are solved as in Eq.2.37, except for the $x_k^{(r)}$ variable for which the integration is as follows:

$$\int_0^{2\pi} \frac{dx_k^{(r)}}{2\pi} \sin x_k^{(r)} \sum_{n=-\infty}^{+\infty} J_n(K\epsilon) e^{-inx_k^{(r)}} = \frac{1}{2i}(J_1(K\epsilon) - J_{-1}(K\epsilon)) = -iJ_1(K\epsilon) \tag{6.18}$$

Since there are $2j-2$ choices of $x_k^{(r)}$, the number of J_0 factors remaining is $2j-3$ and the diffusion rate becomes:

$$D = -\lim_{t\to\infty} \frac{1}{t} K^2 \sum_{j=2}^{t} J_1^2(K\epsilon)(2j-2) J_0^{2j-3}(K\epsilon) e^{-ip_0\epsilon} \tag{6.19}$$

Adding the complex conjugate solution $m_j = -1$ and again multiplying through by t due to the transient nature of the correlations, the lowest order global correlation family is:

$$C_{G1}t = \sum_{n=2}^{2t-1} C_n t = -2K^2 \cos p_0\epsilon J_1^2(K_\epsilon) \sum_{j=2}^{t} (2j-2) J_0^{2j-3}(K_\epsilon) \tag{6.20}$$

The notation $G1$ denotes the lowest order global correlation family of cosine order 1 (later correlations will be seen to depend on $\cos np_0\epsilon$ with $n \geq 1$).

As for the kick-to-kick correlation, all the individual correlations in this family (and hence the overall summed term) are transient and eventually decay to zero. The saturation value of $C_{G1}t$ can easily be found by realising that the summation in Eq.6.20 is

the derivative of that for $C_1 t$ in Eq.6.14:

$$\sum_{j=2}^{t}(2j-2)J_0^{2j-3}(K_\epsilon) = \frac{d}{dJ_0}J_0^2\frac{1-J_0^{2(t-1)}(K_\epsilon)}{1-J_0^2(K_\epsilon)}$$
$$= 2\frac{J_0(K_\epsilon) - tJ_0^{2t-1}(K_\epsilon) + (t-1)J_0^{2t+1}(K_\epsilon)}{(1-J_0^2(K_\epsilon))^2} \tag{6.21}$$

and hence:

$$\lim_{t\to\infty} C_{G1}t = -4K^2\cos p_0\epsilon\frac{J_0(K_\epsilon)J_1^2(K_\epsilon)}{(1-J_0^2(K_\epsilon))^2} \tag{6.22}$$

In Fig.6.1 the time behaviour of this global correlation family is shown with open circles in comparison to the kick-to-kick correlation. The absolute value $|C_{G1}|t$ is shown for clarity, although the difference in sign to the 1-kick correlation is very important. Again, the behaviour is non-linear with time. It is seen that the absolute value of the global correlation family saturates to about twice that of $\lim_{t\to\infty} C_1 t$. This can also be shown by comparing Eqs.6.15 and 6.22, and using the following approximations for the Bessel functions for small arguments $x = K_\epsilon$:

$$J_0(x) \simeq 1 - \frac{x^2}{4}$$
$$J_1(x) \simeq \frac{x}{2}$$
$$J_2(x) \simeq \frac{x^2}{8} \tag{6.23}$$

to give:

$$\frac{\lim_{t\to\infty}|C_{G1}t|}{\lim_{t\to\infty}|C_1 t|} = 4\frac{J_0(K_\epsilon)J_1^2(K_\epsilon)}{(J_0(K_\epsilon)-J_2(K_\epsilon))(1-J_0^2(K_\epsilon))} \simeq 4\frac{(1-\frac{K_\epsilon^2}{4})\frac{K_\epsilon^2}{4}}{(1-\frac{3K_\epsilon^2}{8})\frac{K_\epsilon^2}{2}} \simeq 2 \tag{6.24}$$

At early times the global correlation family grows approximately quadratically with time, which can be shown both by evaluating the summation in Eq.6.20 directly, or by expanding its equivalent expression in Eq.6.21 binomially, using the approximation for J_0 in Eq.6.23:

$$2\frac{1-\frac{K_\epsilon^2}{4}-t(1-\frac{K_\epsilon^2}{4})^{2t-1}+(t-1)(1-\frac{K_\epsilon^2}{4})^{2t+1}}{(1-(1-\frac{K_\epsilon^2}{4})^2)^2} \simeq$$
$$2\frac{1-\frac{K_\epsilon^2}{4}-t(1-(2t-1)\frac{K_\epsilon^2}{4})+(2t^2-3t+1)\frac{K_\epsilon^4}{16}+(t-1)(1-(2t+1)\frac{K_\epsilon^2}{4})+(2t^2+t)\frac{K_\epsilon^4}{16}}{K_\epsilon^4/4}$$
$$= t^2 - t \tag{6.25}$$

Therefore the correlation family can be approximated to:

$$C_{G1}t \simeq -K^2\frac{K_\epsilon^2}{2}(t^2-t)\cos p_0\epsilon \tag{6.26}$$

for small t, where J_1^2 has been replaced by the expression from Eq.6.23.

Given the initial quadratic rise of $C_{G1}t$, the kick-to-kick correlation dominates the diffusion at early times as seen from Fig.6.1 and in agreement with Fig.6.2. As more kicks are added however, the combined effect of the global kick correlations, results in $C_{G1}t$ becoming much more significant. Individually each n-kick correlation in $C_{G1}t$ is of the form:

$$C_n t = -2K^2 \cos p_0 \epsilon J_1^2(K_\epsilon) \sum_{j=2}^{t} J_0^{2j-3}(K_\epsilon) \tag{6.27}$$

Such correlations are much weaker than the strong correlation between kicks in a pair, since $J_1^2(K_\epsilon) \ll (J_0(K_\epsilon) - J_2(K_\epsilon))$, however when summed over n and time, the entire family of correlations eventually dominate diffusive transport in the 2δ-KR. Since $C_{G1}t \propto -\cos p_0\epsilon$ reaches saturation at a later time and higher value than $C_1 t$, this explains the asymptotic sinusoidal imprint in momentum dependent energy absorption shown in the bottom panel of Fig.6.2, where the analytical curve is simply $\langle p^2 \rangle = K^2 t + C_{G1}t$. The crossing point between the kick-to-kick correlation and $C_{G1}t$ shows the time t_G at which the combined n-kick global correlations ($n > 1$) become more dominant than the 1-kick correlation. This occurs at $t_G \simeq 20$, so shortly after the time shown in the second panel of Fig.6.2, where the first hint of a sign reversal of the cosine envelope is seen. In the first panel $C_{G1}t$ is included in the analytical curve, but since at $t = 5$ the kick-to-kick correlation still dominates, the main effect of adding the global correlations is simply to flatten the tops of the cosine curve, as mentioned previously.

The remarkable property of the kick correlations making up the global family above is that they are all equal in size, as Eq.6.27 shows, regardless of the separation between two kicks. The only correlation which is of a different form is the kick-to-kick correlation within a pair of kicks; all other correlations are of equal strength at a given time, but transient as time passes. This is exactly the opposite behaviour to the case of the main correlations in the δ-KR, where decay with increasing separation between kicks at a given time occurs, but correlations remain constant in time. Intuitively one would expect the latter behaviour in a chaotic system, with short-range correlations dominating the dynamics. The situation in the 2δ-KR, where there is a sort of long term memory in the system, persisting for reasonable times ($t_{sat} \simeq 60 - 120$ for the correlations in Fig.6.1) and affecting the dynamics significantly, is highly unusual for a chaotic system and has not been observed before. It is this transient long term memory that causes the persistent strong dependence of energy diffusion on initial momentum in the double

kicked rotor. In the next sections it will be seen that higher order momentum dependent kick correlations follow the same pattern of decay in time but not significantly with kick separation, while correlations independent of momentum, resulting in alterations of the background diffusion rate K^2t, display the opposite behaviour, as in the δ-KR.

It should be noted once more that the eventual domination of the global kick correlations in terms of the energy diffusion does not change the trapping mechanism in momentum space. The dephasing of the approximate kick cancellations, represented by $C_{G1}t$, only applies to individual particles starting in the trapping regions, which eventually escape into the neighbouring cells. As particles move through momentum space they encounter further trapping regions, but these are no longer obvious from graphs of average energy absorption shown in Fig.6.2, since the entire ensemble of particles spreads over several cells.

6.4 Poisson Correlation Families

A multitude of higher order kick correlations, dependent on the initial momentum of particles, can be derived from Eq.6.8, for various combinations of certain m_j being non-zero. These can be seen to be responsible for the narrow dips in energy absorption persisting at the trapping regions for significant times (Fig.6.2), due to a dependence on $\cos np_0\epsilon$ for integer $n > 1$. The combined effect of these correlations yields inverted near δ-functions at the trapping momenta due to the following version of the Poisson sum formula presented in Eq.2.15:

$$\sum_n (-1)^n \cos np_0\epsilon = \sum_m \delta(p_0\epsilon - (2m+1)\pi) \tag{6.28}$$

hence these correlations have been termed 'Poisson correlations'. They represent the slow increase in energy of initially trapped particles over a considerable amount of time (dips persist well beyond $t = 75$ in Fig.6.2), until eventually the energy absorption is a maximum for such particles. All Poisson correlations exist as global correlation families consisting of various n-kick correlations; indeed $C_{G1}t$ is the lowest order Poisson correlation family.

Derivations of Poisson correlations are tedious, yet reasonably straightforward, as all follow either the pattern of the kick-to-kick correlation C_1t or the lowest order global family $C_{G1}t$. Nevertheless, full derivations of a considerable number of such correlations are beyond the scope of this thesis, hence a few example derivations will be shown here

in more detail, for the lowest order $n = 2$ terms, while exact forms of all correlations included in the analytical curves of Fig.6.2 (as well as some others) are given in the appendix. General forms of the two different types of Poisson correlations will however be given below.

The Poisson correlations arise when more than one m_j coefficient is set to ± 1 and $\sum_j m_j = n$, i.e. the algebraic sum of the coefficients defines the cosine order $n \geq 0$. Terms with $|m_j| > 1$ include Bessel functions of increasingly higher orders; since $J_n(K_\epsilon) \to 0$ more rapidly for increasing n, as $\epsilon \to 0$, such terms are less significant in the 2δ-KR. Terms resulting in negative n are simply the complex conjugate solutions of the corresponding positive n cases and combine to form one single family of order $|n|$. Terms of order $n = 1$ include the lowest order global kick correlation family $C_{G1}t$ and simply alter the overall shape of the cosine curve in Fig.6.2, but do not contribute to the dips at the trapping regions. Finally, terms of order $n = 0$ are independent of initial momentum and will be investigated in the next section; these are analogous to the background diffusion corrections found in the δ-KR.

As mentioned above, all Poisson correlations exist as global correlation families of different numbers of kick correlations, and follow the derivation pattern of C_1t or $C_{G1}t$. Different diffusive behaviour emerges depending on the form of the correlation families. In both cases the correlations are represented in general by $\sin x_j^{(2)} \sin x_k^{(r)}$ ($r = 1, 2$ and $k < j$), as for $C_{G1}t$, where $m_j = \pm 1$ necessarily. In one case $m_k = \pm 1$ and correlations include a $J_0 - J_2$ factor as for C_1t (in this case the correlation $\sin x_j^{(2)} \sin x_j^{(1)}$ is also possible, i.e. higher order kick-to-kick correlations). In the other case $m_k = 0$ and correlations include a $2J_1$ factor as for $C_{G1}t$ (cf. Eqs.6.18 and 6.20). It is found that the former result in an increase in the size of the dips in the energy absorption at trapping regions and thus favour hindered diffusion, while the latter act to decrease the size of the dips, thus favouring enhanced energy absorption for initially trapped particles at later times. The correspondence to the case of C_1t and $C_{G1}t$ should be noted. For this reason the global Poisson correlation families are termed C_{Gn}^- (hindered diffusion) and C_{Gn}^+ (enhanced diffusion) in this thesis, for some cosine order n. It should be noted that in the original publication [49] the notation was different: terms resulting in hindered diffusion were termed $C_{Gn}^{(1)}$ since they derive from correlations with kicks in a pair associated with a $m_k = \pm 1$ coefficient. Correspondingly, diffusion enhancing terms were termed $C_{Gn}^{(0)}$. This purely mathematical notation has been replaced by a slightly

more intuitive notation here.

The two lowest order C_{G2} terms shall now be derived from Eq.6.8 for illustrative purposes. Both terms are derived from setting $m_j = \pm 1$ and $m_l = \pm 1$, where $l < j$ but otherwise arbitrary, and summing over j and l. For C_{G2}^- the kick correlations are $\sin x_j^{(2)} \sin x_j^{(1)}$ and $\sin x_j^{(2)} \sin x_k^{(r)}$, where $r = 1, 2$ and $k = l$. The diffusion rate due to this family for $m_j = m_l = +1$ is:

$$D = \lim_{t\to\infty} \frac{1}{t} \int_0^{2\pi} \frac{dx_t^{(2)}}{2\pi} \int_0^{2\pi} \frac{dx_t^{(1)}}{2\pi} \cdots \int_0^{2\pi} \frac{dx_1^{(2)}}{2\pi} \int_0^{2\pi} \frac{dx_1^{(1)}}{2\pi} 2K^2 \sum_{j=2}^{t} \sum_{k=1}^{j-1} (\sin x_j^{(2)} \sin x_j^{(1)}$$
$$+ \sum_{r=1}^{2} \sin x_j^{(2)} \sin x_k^{(r)}) \exp(i(x_j^{(2)} - x_j^{(1)} - p_0\epsilon - K\epsilon \sin x_j^{(1)} - \sum_{i=1}^{j-1} \sum_{r=1}^{2} K\epsilon \sin x_i^{(r)}))$$
$$\times \exp(i(x_k^{(2)} - x_k^{(1)} - p_0\epsilon - K\epsilon \sin x_k^{(1)} - \sum_{i=1}^{k-1} \sum_{r=1}^{2} K\epsilon \sin x_i^{(r)})) \tag{6.29}$$

The integral involving $x_j^{(2)}$ is solved as in Eq.2.24, while integrals involving $x_j^{(1)}$, $x_k^{(2)}$ and $x_k^{(1)}$ are solved as in Eqs.2.29 and 2.36, depending on whether the integral involves a sine factor or not. Arguments of Bessel functions now change between $K\epsilon$ and $2K\epsilon$ depending on the number of $\exp(-iK\epsilon \sin x)$ factors present for a given term. For example, if $k = j - 2$ and one looks at the $\sin x_j^{(2)} \sin x_{j-2}^{(2)}$ term, the three integrals are respectively:

$$\int_0^{2\pi} \frac{dx_j^{(1)}}{2\pi} e^{-ix_j^{(1)}} e^{-iK\epsilon \sin x_j^{(1)}} = \int_0^{2\pi} \frac{dx_j^{(1)}}{2\pi} e^{-ix_j^{(1)}} \sum_{n=-\infty}^{+\infty} J_n(K\epsilon) e^{-inx_j^{(1)}} = -J_1(K\epsilon) \tag{6.30}$$

$$\int_0^{2\pi} \frac{dx_{j-2}^{(2)}}{2\pi} \sin x_{j-2}^{(2)} e^{ix_{j-2}^{(2)}} e^{-iK\epsilon \sin x_{j-2}^{(2)}} = \int_0^{2\pi} \frac{dx_{j-2}^{(2)}}{2\pi} \sin x_{j-2}^{(2)} e^{ix_{j-2}^{(2)}} \sum_{n=-\infty}^{+\infty} J_n(K\epsilon) e^{-inx_{j-2}^{(2)}}$$
$$= \frac{i}{2}(J_0(K\epsilon) - J_2(K\epsilon)) \tag{6.31}$$

(cf. Eq.2.36) and

$$\int_0^{2\pi} \frac{dx_{j-2}^{(1)}}{2\pi} e^{-ix_{j-2}^{(1)}} e^{-i2K\epsilon \sin x_{j-2}^{(1)}} = \int_0^{2\pi} \frac{dx_{j-2}^{(1)}}{2\pi} e^{-ix_{j-2}^{(1)}} \sum_{n=-\infty}^{+\infty} J_n(2K\epsilon) e^{-inx_{j-2}^{(1)}} = -J_1(2K\epsilon) \tag{6.32}$$

For $x_k^{(1)}$ Bessel arguments are always $2K\epsilon$. Notice also the sign changes between $x_k^{(2)}$ and the other two variables. Integrals over all other variables are solved as in Eq.2.37. Combining all the terms, adding the complex conjugate solution $m_j = m_l = -1$ and multiplying through by t gives:

$$C_{G2}^{-}t = -K^2 \cos 2p_0\epsilon J_1(2K_\epsilon)J_1^2(K_\epsilon)(2\frac{J_0(K_\epsilon) - J_2(K_\epsilon)}{J_1(K_\epsilon)} + \frac{J_0(2K_\epsilon) - J_2(2K_\epsilon)}{J_1(2K_\epsilon)}) \times \sum_{j=2}^{t}\sum_{\alpha_1=0}^{j-2} J_0^{2\alpha_1}(K_\epsilon)J_0^{2(j-2-\alpha_1)}(2K_\epsilon) \quad (6.33)$$

Note the similarity to C_1t in Eq.6.13, however there are three slightly different cases depending on which kicks are being coupled. The diffusion hindering Poisson families in general always include higher order kick-to-kick correlations $\sin x_j^{(2)} \sin x_j^{(1)}$, as well as correlations between the second kick in a given pair and kicks in other previous pairs ($m_k = \pm 1$). C_1t as the lowest order member of the C_{Gn}^{-} Poisson family includes only the basic kick-to-kick correlation and is thus a special case.

For C_{G2}^{+} the kick correlations are $\sin x_j^{(2)} \sin x_k^{(r)}$, where $r = 1, 2$ and $k < j$, with $m_k = 0$. The correlations are still derived from the case $m_j = m_l = \pm 1$ with $l < j$, however now $l \neq k$. This changes the derivation as follows for $m_j = m_l = +1$:

$$D = \lim_{t\to\infty} \frac{1}{t} \int_0^{2\pi} \frac{dx_t^{(2)}}{2\pi} \int_0^{2\pi} \frac{dx_t^{(1)}}{2\pi} \cdots \int_0^{2\pi} \frac{dx_1^{(2)}}{2\pi} \int_0^{2\pi} \frac{dx_1^{(1)}}{2\pi} 2K^2 \sum_{j=3}^{t}\sum_{l<j}\sum_{r=1}^{2}\sum_{k\neq l}^{k<j} \sin x_j^{(2)} \sin x_k^{(r)} \times \exp(i(x_j^{(2)} - x_j^{(1)} - p_0\epsilon - K\epsilon \sin x_j^{(1)} - \sum_{i=1}^{j-1}\sum_{r=1}^{2} K\epsilon \sin x_i^{(r)})) \times \exp(i(x_l^{(2)} - x_l^{(1)} - p_0\epsilon - K\epsilon \sin x_l^{(1)} - \sum_{i=1}^{l-1}\sum_{r=1}^{2} K\epsilon \sin x_i^{(r)})) \quad (6.34)$$

The integral involving $x_j^{(2)}$ is again solved as in Eq.2.24. Integrals involving $x_j^{(1)}$, $x_l^{(2)}$ and $x_l^{(1)}$ are solved as in Eqs.6.30 and 6.32 shown above, with the Bessel argument being $2K\epsilon$ in the final case. Integrals involving the $x_k^{(r)}$ variables appearing in the sine correlations are solved as in Eq.6.18. Note that due to the two summations in the exponentials of Eq.6.34, the Bessel argument is $K\epsilon$ for $l < k < j$ and $2K\epsilon$ for $k < l$. Finally, integrals over all other variables are again solved as in Eq.2.37. Upon inserting all the results from the integrations, adding the complex conjugate solution and multiplying

through by t this correlation family is:

$$C^{+}_{G2}t = 2K^2 \cos 2p_0\epsilon J_1(2K_\epsilon)J_1^2(K_\epsilon)$$
$$\times \sum_{j=2}^{t}\sum_{\alpha_1=0}^{j-2}(2\alpha_1\frac{J_1(K_\epsilon)}{J_0(K_\epsilon)} + 2(j-2-\alpha_1)\frac{J_1(2K_\epsilon)}{J_0(2K_\epsilon)})J_0^{2\alpha_1}(K_\epsilon)J_0^{2(j-2-\alpha_1)}(2K_\epsilon) \quad (6.35)$$

Note the similarity to $C_{G1}t$ in Eq.6.20, which is the lowest order member of the diffusion enhancing Poisson family C^{+}_{Gn}. It is also worth noting the opposite sign to C^{-}_{G2}, showing that these two families oppose each other in terms of the effect on the diffusion rate.

For a specific pattern of zero and unity m_j coefficients in Eq.6.8, resulting in two sets of Poisson correlations of order $n > 0$ (the special case of $n = 0$ will be discussed in the next section), the most general and exact forms of these can be written as:

$$C^{-}_{Gn}t = (-1)^{n-1}K^2 \cos np_0\epsilon J_1(nK_\epsilon)[\prod_{m=1}^{M-1}J_1^2(S_mK_\epsilon)](\frac{J_0(nK_\epsilon)-J_2(nK_\epsilon)}{J_1(nK_\epsilon)}$$
$$+\sum_{m=1}^{M-1}2\frac{J_0(S_mK_\epsilon)-J_2(S_mK_\epsilon)}{J_1(S_mK_\epsilon)})\sum_{j=M}^{t}\sum_{\alpha_1=0}^{j-M}\cdots\sum_{\alpha_m=0}^{j-M-S_\alpha}\cdots\sum_{\alpha_{M-1}=0}^{j-M-S_\alpha}(\prod_{m=1}^{M}J_0^{2\alpha_m}(S_mK_\epsilon)) \quad (6.36)$$

$$C^{+}_{Gn}t = (-1)^n 2K^2 \cos np_0\epsilon J_1(nK_\epsilon)[\prod_{m=1}^{M-1}J_1^2(S_mK_\epsilon)]$$
$$\times \sum_{j=M}^{t}\sum_{\alpha_1=0}^{j-M}\cdots\sum_{\alpha_m=0}^{j-M-S_\alpha}\cdots\sum_{\alpha_{M-1}=0}^{j-M-S_\alpha}(\sum_{m=1}^{M}2\alpha_m\frac{J_1(S_mK_\epsilon)}{J_0(S_mK_\epsilon)})(\prod_{m=1}^{M}J_0^{2\alpha_m}(S_mK_\epsilon)) \quad (6.37)$$

Here M is the number of non-zero m_j coefficients, not to be confused with n, the algebraic sum of the non-zero coefficients. For example if any three coefficients are set to $+1$, $+1$ and -1 respectively, $M = 3$ but $n = 1$ (remembering that $-1, -1, +1$ would simply give a complex conjugate solution for the same order $|n|$). Furthermore S_m is defined to be the cumulative sum $\sum_k m_k$, starting from highest k, of the first m non-zero coefficients and thus $S_M = n$. In the above example the values would be $S_1 = 1$, $S_2 = 2$, $S_3 = S_M = 1$. Note that $S_m \neq 0$ in all cases for momentum dependent correlations. Finally, $S_\alpha = \sum_{l=1}^{m-1}\alpha_l$ is the cumulative sum of the first $m-1$ α-coefficients preceding α_m, and $\alpha_M = j-M-\sum_{l=1}^{M-1}\alpha_l$ in all cases. This simply ensures that the correct number of variables are counted. Note that the equations are valid for $n > 0$ and $|m_j| = 0, 1$ only. Terms with $|m_j| > 1$ exist, in which case the formulae change slightly with Bessel functions being of different orders depending on the permutations of the coefficients. Such terms however are generally less significant than the ones presented here.

The above equations seem somewhat cumbersome, but after a few derivations done individually, they are easy to follow, and higher order terms can be written down straightforwardly. The complicated formulae of course also stem from the fact that they are simply an attempt at combining a large number of individual correlations in one term. Note again the difference in sign between the two families for all orders n and all m_j patterns.

All Poisson correlation families above, dependent on the initial momentum of the particles p_0, are transient in time and eventually decay to zero. Saturation values and times can be obtained from the formulae but this is computationally more demanding than for the lowest order global correlation family, due to the large number of summations. It should also be noted that the various n-kick correlations comprising a given Poisson family are of similar, but not necessarily equal strength at a given time t, in contrast to the correlations in the lowest order family $C_{G1}t$. This means that the long term memory for higher order correlation families is not as stable as for the lowest order one, but correlations still affect the diffusion rate for much longer than in the δ-KR, where only correlations independent of momentum are significant.

It can be shown that each additional non-zero $m_k = \pm 1$ coefficient in Eq.6.8 leads to the addition of two multiplicative J_1 Bessel factors in Eqs.6.36 and 6.37 of possibly different arguments. The $\prod_m J_1^2$ prefactor thus continuously decreases the significance of the correlations as more non-zero m_k coefficients are added, particularly given the Bessel arguments $nK\epsilon$, since $J_1(x) \to 0$ as $x \to 0$. Hence the dominant correlation families are those of lowest order in J_1 and thus with few non-zero m_k coefficients. For the second panel in Fig.6.2 at $t = 15$ all Poisson correlations up to $O(J_1) = 10$ have been included. These are listed in Table 6.1 with the corresponding m_j patterns and the values of the maximum diffusion corrections ($\cos np_0\epsilon = 1$) at $t = 15$ (for the parameters in Fig.6.2). If diffusion hindering terms C_{Gn}^- are of order J_1^β, then diffusion enhancing terms C_{Gn}^+ are of order $J_1^{\beta+2}$, as is seen from inspecting Eqs.6.36 and 6.37. Terms of $O(J_1) = 10$ are about 100 times smaller than the lowest order kick-to-kick and global correlations, hence higher order terms can safely be neglected at early times in the system evolution. The agreement between the analytical and numerical curves in Fig.6.2 can be seen to be very good for $t = 15$. At longer times however higher order terms with $O(J_1) > 10$ are needed for good agreement. Given that the evaluation of terms becomes more and more resource intensive in terms of computing power as $O(J_1)$ increases, it was not attempted

Term	m_j pattern	$O(J_1)$	Value ($t = 15$)
Ia (C_1,C_{G1})	± 1	0,2	+472,-355
Ib (C^-_{G1},C^+_{G1})	$\pm 1,\pm 1,\mp 1$	4,6	+100,-33
Ic (C^-_{G1},C^+_{G1})	$\pm 1,\pm 1,\pm 1,\mp 1,\mp 1$	8,10	+14,-4
IIa (C^-_{G2},C^+_{G2})	$\pm 1,\pm 1$	2,4	-227,+113
IIb (C^-_{G2},C^+_{G2})	$\pm 1,\pm 1,\pm 1,\mp 1$	6,8	-59,+24
IIIa (C^-_{G3},C^+_{G3})	$\pm 1,\pm 1,\pm 1$	4,6	+82,-39
IIIb (C^-_{G3},C^+_{G3})	$\pm 1,\pm 1,\pm 1,\pm 1,\mp 1$	8,10	+29,-12
IVa (C^-_{G4},C^+_{G4})	$\pm 1,\pm 1,\pm 1,\pm 1$	6,8	-29,+14

Table 6.1: Diffusion correlations shown in Fig.6.3.

to calculate an analytical curve for the third panel in Fig.6.2 at $t = 75$. Given that the basic behaviour of the 2δ-KR can easily be shown from a few lower order correlation families only, further calculations would primarily be mathematical exercises. Exact forms of all the correlations shown in Table 6.1 are found in the appendix.

Fig.6.3 shows the behaviour of all the Poisson families in Table 6.1 in terms of energy absorption in time caused by the correction to the diffusion rate. Parameters are as in Figs.6.1 and 6.2. In all cases absolute values $|C|t$ of maximum energy absorption at $\cos np_0\epsilon = 1$ are shown, but the change of sign between the two different types of Poisson families should be remembered. Panel (a) shows the kick-to-kick correlation $C_1 t$ and lowest order global correlation family $C_{G1}t$ again, as in Fig.6.1, together with two higher order $n = 1$ Poisson families of each type. The labels refer to the entries of Table 6.1. Poisson correlations of order $n = 1$ only contribute to the overall cosine envelope in Fig.6.2, not to the actual Poisson dips observed. Exact forms of these correlations are also given in the appendix. It is seen that terms decrease in importance as $O(J_1)$ increases, with saturation values decreasing continuously. The saturation times however increase with higher J_1 orders, making such terms decay slower; this results in the relatively long persistence of the dips in Fig.6.2. Most noticeably however, the behaviour in terms of correlation evolution for higher order terms is exactly as for the lowest order ones: diffusion enhancing terms are always less significant at earlier times due to a slow rise, but end up becoming dominant at longer times. The crossing point is seen to shift to later times with increasing order $O(J_1)$, again contributing to the persistence of the Poisson dips. Finally, the difference in saturation energies becomes smaller with higher

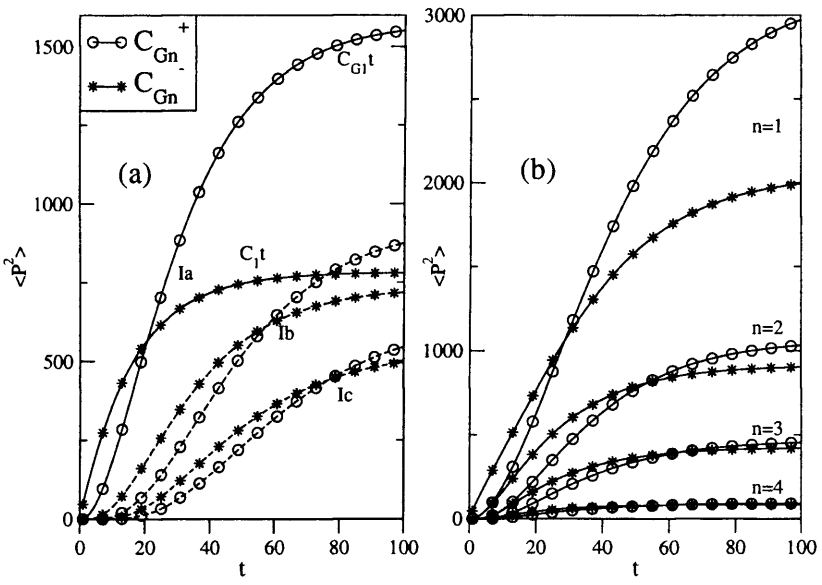

Figure 6.3: Behaviour of global Poisson correlations $C_{Gn}t$ with number of pairs of kicks ($t = N/2$, where N is the individual number of kicks). Parameters are as in Figs.6.1 and 6.2. Absolute values $|C|t$ of maximum energy absorption ($\cos np_0\epsilon = 1$) caused by these correlations are shown. Diffusion hindering terms C_{Gn}^- are shown with stars and diffusion enhancing terms C_{Gn}^+ with circles. Panel (a) shows the comparison between individual correlation families for order $n = 1$, including nearest neighbour kick-to-kick correlation C_1t and lowest-order global family $C_{G1}t$, both shown in Fig.6.1. The labels correspond directly to those in Table 6.1 showing explicit values at $t = 15$. Panel (b) shows the comparison between different cosine orders n, with curves made up of the various correlations given in Table 6.1 for each order. In all cases diffusion enhancing terms end up more dominant than diffusion hindering terms at long times, with the former increasing as $\sim t^n$ and the latter as $\sim t^{n+1}$ at early times. Crossing points are seen to shift to later times for higher order terms, and overall importance in terms of diffusion corrections decreases with higher orders.

orders, so eventually the difference in diffusion behaviour is negligible for very high order terms.

Panel (b) shows the combined effect on the diffusion rate of Poisson families for each order $1 \leq n \leq 4$. The curves are made up of the correlations shown in Table 6.1 for each, i.e. the $n = 1$ curves comprise the three correlation families shown in panel (a). The behaviour with increasing order n is analogous to that with increasing $O(J_1)$. Diffusion enhancing terms C_{Gn}^+t always end up more dominant than the corresponding diffusion hindering terms C_{Gn}^-t, but again the crossing point where the change in significance takes place shifts to later times with higher orders n. Both the actual values of

Poisson correlation families. Since these dominate the diffusive behaviour at every order n, the asymptotic imprint in the average energy absorption of the particles in the system is due entirely to such correlations.

The correlation families presented in this chapter fully explain the basic diffusive behaviour found in the double kicked rotor in terms of trapping regions and cellular phase space structure. Half of the correlations act to trap individual particles at the boundaries between different cells, while the other half act to increase energy absorption for such trapped particles. However, as mentioned earlier, the correlations only describe the initial situation for individual particles at the beginning of the system evolution; at later times they describe the diffusive behaviour of the ensemble of particles moving through phase space, and hence individual trapping mechanisms are no longer apparent. The decay of the transient momentum dependent correlations $C_{Gn}t(p_0)$ does not signify the decay of the actual trapping mechanism which persists asymptotically, but is averaged over at long times due to the large number of particles.

6.5 Self-correlations

As a final note there is one more category of momentum dependent correlation families not mentioned previously. The dominant correlations in the 2δ-KR arise only from terms in Eq.6.8 with various patterns of $m_j = \pm 1$. Setting the coefficients to higher values than unity, usually results in less significant correction terms, as verified numerically, although some cases contribute to the diffusion rate at intermediate times (e.g. $t = 75$ in Fig.6.2). Importantly, the highest coefficient with $j = j_{max}$ can only be $m_j = \pm 1, \pm 2$ to result in a non-zero correction term, since otherwise there are exponentials which cannot be paired with Bessel summations or sine factors and hence vanish when integrated over. The case of $m_j = \pm 2$ for $j = j_{max}$, with possibly further non-zero m_k coefficients where $k < j$, is an interesting one mathematically, as it describes self-correlations of a kick with itself, namely $\langle \sin^2 x_i \rangle$. It should be noted that of course in some sense the background diffusion rate D_0 trivially consists of self-correlations as well.

The basic example of a single $m_j = +2$ coefficient in Eq.6.8 results in correlations

the saturation energies and the difference between the two correlation families become smaller for higher order terms. It can be seen that the $n = 4$ correlations are far less significant than the lower order terms, which can also be confirmed from the explicit values of the diffusion corrections at $t = 15$ in Table 6.1. The eventual dominance of $C^{+}_{Gn}t$ is fairly intuitive, since these families are comprised of more individual correlations (with kicks in a pair for which $m_k = 0$) than the $C^{-}_{Gn}t$ families comprised of only correlations with kicks for which $m_k = \pm 1$. Since the most dominant terms are those with few non-zero m_k coefficients, this explains the imbalance. For the simple case of $C_{G1}t$ this is of course obvious, as it is comprised of many individual correlations in comparison to the single kick-to-kick correlation $C_1 t$.

It can be shown numerically that diffusion hindering terms $C^{-}_{Gn}t$ increase at early times as $\sim t^n$, while diffusion enhancing terms $C^{+}_{Gn}t$ increase as $\sim t^{n+1}$, thus initially rising slower but eventually overtaking the former. Remember that for the kick-to-kick correlation and $C_{G1}t$ where $n = 1$, a linear and quadratic rise respectively were found both numerically and analytically, in agreement with the formulae shown here. The time behaviour for higher order terms can be shown approximately, with some difficulty, from Eqs.6.36 and 6.37, but this is omitted in the present work, due to time and resource constraints.

The analytical curve in the first panel of Fig.6.2 is comprised of $C_1 t$, $C_{G1}t$ and the lowest order $n = 2$ diffusion hindering term C^{-}_{G2} labelled IIa in Table 6.1. The curve in the second panel includes all correlations shown in Table 6.1. The agreement between the numerical and analytical curve at $t = 15$ is very good, except that a few higher order terms are needed to accurately describe the Poisson dip. If the numerical maximum energy absorption ($\cos np_0\epsilon = 1$) is calculated for different Poisson orders n and compared to the analytical values at $t = 15$ in Table 6.1, it is found that the percentage errors are: 6% ($n = 1$), 14% ($n = 2$), 26% ($n = 3$) and 64% ($n = 4$). The large discrepancy at higher orders shows that more terms are needed to accurately model the diffusive behaviour, however the lesser importance of such terms in Fig.6.3 justifies neglecting these. In the third panel the analytical curve has been left out as mentioned previously, due to constraints in computing power, however the effect of the kick correlations on the diffusion in the double kicked rotor is evident from the study of earlier times. In the final panel only $C_{G1}t$ is included and gives reasonable agreement. The pointed tops of the sine curve are caused by the diffusion enhancing

$\sin^2 x_j^{(2)}$, i.e. self-correlations of the second kick in a given pair. The diffusion rate is:

$$D = \lim_{t\to\infty} \frac{1}{t} \int_0^{2\pi} \frac{dx_t^{(2)}}{2\pi} \int_0^{2\pi} \frac{dx_t^{(1)}}{2\pi} \cdots \int_0^{2\pi} \frac{dx_1^{(2)}}{2\pi} \int_0^{2\pi} \frac{dx_1^{(1)}}{2\pi} K^2 \sum_{j=1}^{t} \sin^2 x_j^{(2)}$$
$$\times \exp(2i(x_j^{(2)} - x_j^{(1)} - p_0\epsilon - K\epsilon \sin x_j^{(1)} - \sum_{i=1}^{j-1}\sum_{r=1}^{2} K\epsilon \sin x_i^{(r)})) \qquad (6.38)$$

The integral over $x_j^{(2)}$ is:

$$\int_0^{2\pi} \frac{dx_j^{(2)}}{2\pi} \sin^2 x_j^{(2)} e^{2ix_j^{(2)}} = -\frac{1}{4} \qquad (6.39)$$

and the integral over $x_j^{(1)}$ is solved similarly to Eq.2.29:

$$\int_0^{2\pi} \frac{dx_j^{(1)}}{2\pi} e^{-2ix_j^{(1)}} \sum_{n=-\infty}^{+\infty} J_n(2K\epsilon) e^{-inx_{j-1}} = J_2(2K\epsilon) \qquad (6.40)$$

Integrals over all other variables are solved as usual according to Eq.2.37 with Bessel arguments $2K\epsilon$. Combining all terms, adding the complex conjugate solution $m_j = -2$ and multiplying through by t as usual gives this correlation of order $n = 2$ as:

$$C_0 t = -\frac{K^2}{2} \cos 2p_0\epsilon J_2(2K_\epsilon) \sum_{j=1}^{t} J_0^{2j-2}(2K_\epsilon) \qquad (6.41)$$

This is a single transient and momentum dependent self-correlation $C_0 t$, of a similar form to the kick-to-kick correlation $C_1 t$, but of cosine order $n = 2$, thus contributing to the Poisson dips. However, given the J_2 prefactor which is much smaller than the dominant J_0 factor for $C_1 t$ in Eq.6.13, this self-correlation has a much smaller impact on the diffusive behaviour. Since the summation above is the same as for the kick-to-kick correlation, the saturation value of this self-correlation is:

$$\lim_{t\to\infty} C_0 t = -\frac{K^2}{2} \cos 2p_0\epsilon \frac{J_2(2K_\epsilon)}{1 - J_0^2(2K_\epsilon)} \qquad (6.42)$$

and at early times it grows linearly with time.

This specific self-correlation is of the same sign as the diffusion hindering terms for $n = 2$ and hence contributes to increasing the size of the Poisson dips, however at $t = 15$ the maximum diffusion correction for $\cos 2p_0\epsilon = 1$ of this self-correlation is -17, which is very small compared to the dominant correlation families in Table 6.1. Higher order self-correlations exist with additional non-zero m_j coefficients, which can be of any order n, however these are smaller still, the most significant ones being about half the size of the basic lowest order term above. Together, the self-correlations can be grouped into

families similar to the other Poisson correlations, of general forms similar to Eq.6.36 with the $J_0 - J_2$ factors replaced by J_2 of some Bessel argument, and other prefactors consisting of Bessels of various orders and arguments depending on the m_j pattern. It is interesting to note that all self-correlations (except the ones contained in D_0 of course) are diffusion hindering terms and so favour trapping of particles. However given the small size of these correlations, they do not affect the diffusive behaviour of the 2δ-KR significantly and have not been included in the analytical curves of Fig.6.2, but are mentioned here for completeness.

6.6 Asymptotic Diffusion Corrections: Momentum Independent Correlations

The final category of kick correlations affecting the diffusion rate of the double kicked rotor is the case of $n = 0$, for which there is no momentum dependence and the above Eqs.6.36 and 6.37 are not valid. Such correlations are of course analogous to the dominant ones found in the δ-KR, which simply alter the overall diffusion rate for all particles, but do not distinguish between individual particle groups. They exist in the same form in the 2δ-KR and are found to significantly alter the background diffusion rate $\langle p^2 \rangle = D_0 t = K^2 t$ (cf. Eq.6.1). This becomes particularly important in the asymptotic regime where transient momentum dependent Poisson correlations have saturated, and the diffusion rate is linear with time for all particles.

The most important asymptotic diffusion corrections in the 2δ-KR are presented below. It should be noted that since there is no momentum dependence for these, terms depending on the long timescale τ may be considered when evaluating kick correlations, similar to the Standard Map case with $\tau \simeq T$. However it is found that τ-dependent terms are still far less significant than the ones depending on ϵ only, and will thus be neglected in what follows. A further note on the τ-dependence of correlations will be given at the end of the section.

In the Standard Map or δ-KR one of the main single correlations found to affect the diffusion rate was the lowest order 3-kick correlation C_3 (Eq.2.31). This lowest order term is also found in the 2δ-KR and can be derived in the same way, starting with $m_j = \pm 1$ and $m_{j-1} = \mp 1$ in Eq.6.8. The correlation involves the $\sin x_j^{(2)} \sin x_{j-1}^{(1)}$ term

and is derived in the same way as shown for the δ-KR in Chapter 2 to obtain:

$$C_3 = -K^2 J_1^2(K_\epsilon) \tag{6.43}$$

Note that since the behaviour of all momentum independent correlation terms is linear with time, the asymptotic time limit can be taken and the actual correction to the diffusion rate calculated (as opposed to $C_{Gn}(p_0)t$ in the previous sections). In contrast to the Standard Map however the basic 2-kick correlation term (Eq.2.27) does not contribute significantly in the 2δ-KR as it depends on the long timescale τ (starting with $m_j^{(2)} = \pm 1$ and $m_j^{(1)} = \mp 1$ in Eq.6.6). It is found that the above 3-kick correlation is part of a family of n-kick correlations all derived from $m_j = \pm 1$ and $m_k = \mp 1$ with $k < j$, but which only includes odd n. The form of each lowest order odd n-kick correlation is:

$$C_n = -K^2 J_1^2(K_\epsilon) J_0^{\frac{n-3}{2}}(K_\epsilon) \tag{6.44}$$

which can easily be derived from Eq.6.8 using the integral in Eq.2.37. Obviously $n \geq 3$ since the kick-to-kick correlation C_1 is a momentum dependent term. Even n-kick correlations all depend on the long timescale τ and are hence negligible in comparison to Eq.6.44 above.

It should be noted at this point that for the δ-KR the same set of n-kick correlations can be derived, including all possible n, to give the general form of a correlation between any two kicks ($\sin x_j \sin x_{j-n}$) as:

$$C_n^{SM} = -K^2 J_1^2(K) J_0^{n-3}(K) \tag{6.45}$$

for $n \geq 3$ (the 2-kick correlation is of a different form as shown in Eq.2.27). It will be seen however that, as opposed to the double kicked rotor where families of momentum independent correlations affect the asymptotic diffusion rate significantly, in the Standard Map, correlations between kicks that lie far apart have a negligible effect on the diffusion rate, hence these terms were neglected in Chapter 2. This will be shown graphically later on.

If one includes all odd n-kick correlations in the 2δ-KR, the corrected asymptotic background diffusion rate can be written as:

$$D = K^2[1 - J_1^2(K_\epsilon) \sum_{n\geq 3}^{n\ odd} J_0^{\frac{n-3}{2}}(K_\epsilon)] = K^2[1 - \frac{J_1^2(K_\epsilon)}{1 - J_0^2(K_\epsilon)}] \tag{6.46}$$

for $\langle p^2 \rangle$ (the rate is halved for $\langle E \rangle$). Alternatively one can write the combination of all lowest order odd n-kick correlations as:

$$C_{G0}t = -K^2 J_1^2(K_\epsilon) \sum_{j=2}^{t} \sum_{\alpha=0}^{j-2} J_0^{2\alpha}(K_\epsilon) \tag{6.47}$$

Here the infinite time limit is not taken, and instead the equation is multiplied through by t, as for the Poisson correlations, to show the time behaviour of the correlations independent of initial momentum. A whole family of kick correlations is represented, which are all activated at different times, hence the overall behaviour of the entire family is non-linear at early times. However, individually all n-kick correlations show a linear time dependence, and asymptotically the time behaviour is linear for the entire family as well. The nomenclature C_{G0} shows the mathematical link with the Poisson correlations; these momentum independent terms can be considered as a global correlation family of cosine order $n = 0$.

Higher order terms can be derived for various patterns of non-zero m_j coefficients with a total sum of $\sum_j m_j = n = 0$. As for the Poisson correlations the dominant terms are those with $|m_j| = 0, 1$ only. The general form of momentum independent $n = 0$ global correlation families for a specific pattern of zero and unity m_j coefficients in Eq.6.8 is:

$$C_{G0}t = -K^2 [\prod_{m=1}^{M-1} J_1^2(S_m K_\epsilon)] \sum_{j=M}^{t} \sum_{\alpha_1=0}^{j-M} \cdots \sum_{\alpha_m=0}^{j-M-S_\alpha} \cdots \sum_{\alpha_{M-1}=0}^{j-M-S_\alpha} (\prod_{m=1}^{M-1} J_0^{2\alpha_m}(S_m K_\epsilon)) \tag{6.48}$$

with all symbols defined as for Eqs.6.36 and 6.37. Note that $S_M = 0$ in all cases but the cumulative sum $S_m \neq 0$ for $m < M$ (otherwise terms are zero-valued). The aforementioned family of odd n-kick correlations in Eq.6.47 is the lowest order term given by Eq.6.48. Again, terms with $|m_j| > 1$ exist, involving Bessel functions of different orders, but they are less significant.

It is noticeable from Eq.6.48 that all significant momentum independent correlations are of the same sign and opposite to the background random walk $+K^2$. This means that these correlations all act to lower the overall diffusion rate of particles in the system. Fig.6.4 shows the time behaviour of the two lowest order global correlation families from Eq.6.48 in terms of energy absorption (panel (a)), as well as the corrected diffusion rate (panel (b)). In panel (a) both the lowest order correlation family given in Eq.6.47 and the next highest order with a coefficient pattern of $m_j = \pm 1, \pm 1, \mp 1, \mp 1$ for some m_j are included (the exact form of this higher order family is given in the appendix, but can

easily be derived from Eqs.6.8 and 6.48). Absolute values of the correlations are shown in comparison to the random walk rate K^2t.

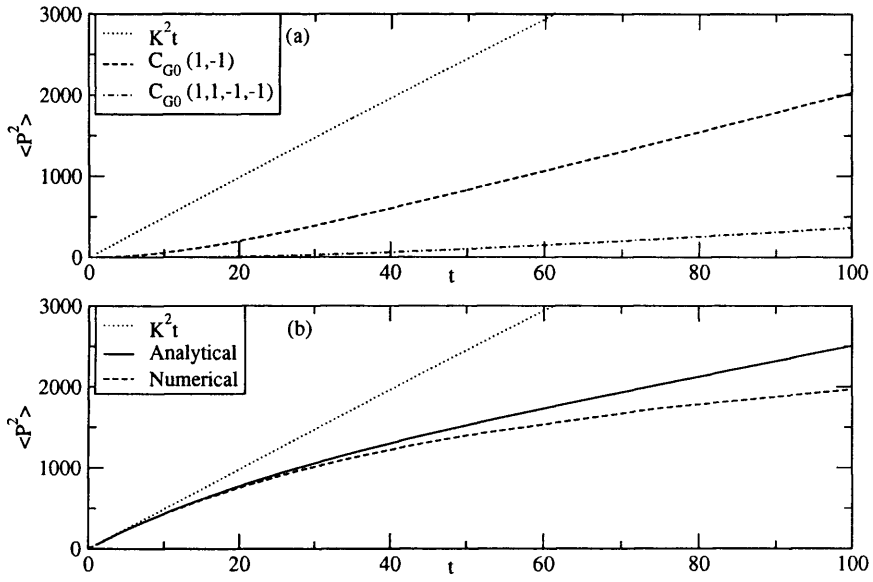

Figure 6.4: Effect of momentum independent correlations on the overall rate of energy absorption in the 2δ-KR. Parameters are $K = 7$ and $\epsilon = 0.05$, leading to $K_\epsilon = 0.35$. Panel (a) shows the two lowest order correlation families in comparison to the uncorrelated random walk. Absolute values $|C_{G0}|t$ are plotted, but all correlations oppose the random walk. Panel (b) shows the corrected diffusion rate in comparison to the random walk D_0, both numerically and analytically, with good agreement. The analytical curve is composed of the two correlation families in (a) and is hence $K^2t - C_{G0}t(\pm 1, \mp 1) - C_{G0}t(\pm 1, \pm 1, \mp 1, \mp 1)$. The correlations are seen to lower the diffusion rate significantly.

It can be seen that while the lowest order family results in a sizeable contribution to the diffusion rate, even the next highest order contributes significantly less, particularly at early times. The behaviour is non-linear with time at the beginning, however as mentioned previously, this is due to the continuous addition of correlations to the families in time, as more and more kicks occur. Individually correlations are all linear and hence asymptotic in time. However, as for the correlations in the δ-KR, and in contrast to the momentum dependent Poisson correlations presented earlier, these correlations do decay with kick separation at a given time. Hence they represent a short term memory in the system, but which persists asymptotically. At long times the behaviour in panel (a) reverts to a linear relationship.

In panel (b) the actual effect on the overall diffusion rate of the two correlation families in panel (a) is shown by the analytical curve, in comparison to both the nu-

merically calculated diffusion rate and the uncorrected random walk K^2t. Again, due to the accumulation of various correlations, the diffusion rate changes at early times, but eventually saturates to an asymptotic value at long times. Since correlations decay with kick separation, those added at longer times coupling kicks that lie temporally far apart do not contribute significantly, and hence do not alter the diffusion rate any further. It is seen that the correlations lower the rate of diffusion for the double kicked rotor significantly, and the agreement between the analytical and numerical curves is reasonable, even when including only two families, which shows the dominance of these on the diffusive behaviour.

The asymptotic limit of higher order correlations in Eq.6.48 can be found straightforwardly by taking the infinite time limit and the general form is:

$$C_{G0} = -K^2 \prod_{m=1}^{M-1} \frac{J_1^2(S_m K_\epsilon)}{1 - J_0^2(S_m K_\epsilon)} \tag{6.49}$$

where S_m is the cumulative sum of the m_j coefficients as before. For example, for the higher order term included in Fig.6.4, for which $S_1 = 1$, $S_2 = 2$ and $S_3 = 1$, the asymptotic diffusion correction is:

$$C'_{G0} = -K^2 \frac{J_1^4(K_\epsilon) J_1^2(2K_\epsilon)}{(1 - J_0^2(K_\epsilon))^2 (1 - J_0^2(2K_\epsilon))} \tag{6.50}$$

As for the Standard Map the diffusion rate changes with the control parameter K_ϵ. In Fig.2.2, taken from [15], the relationship between the diffusion rate in the SM and the control parameter for the δ-KR, K_T, was shown. This is shown once more in Fig.6.5a, this time generated directly from Eq.2.34, in comparison to the double kicked rotor case in Fig.6.5b. In both cases the ratio D/D_0 is shown, although it should be remembered that while for the Standard Map $D_0 = \langle p^2 \rangle / t = K_T^2/2$ in scaled momenta p_T, in the double kicked rotor the random walk term is $D_0 = \langle p^2 \rangle / t = K_\epsilon^2$ for scaled momenta p^ϵ, due to the redefinition of time in pairs of kicks. Both a numerically obtained curve and a series of analytical curves derived from Eq.6.49 are shown for the double kicked rotor. The analytical curves successively include higher order correlation families grouped by the maximum $O(J_1)$ of any argument $S_m K_\epsilon$, i.e. the correction in Eq.6.50 includes $O(J_1^4)$, while the basic lowest order correlation family in Eq.6.46 is $O(J_1^2)$. For the Standard Map the analytical curve includes all the corrections given in Eq.2.34, but only for $K_T \gtrsim 4$, since below this value phase space becomes mixed and the diffusion equation (Eq.2.17) is no longer valid.

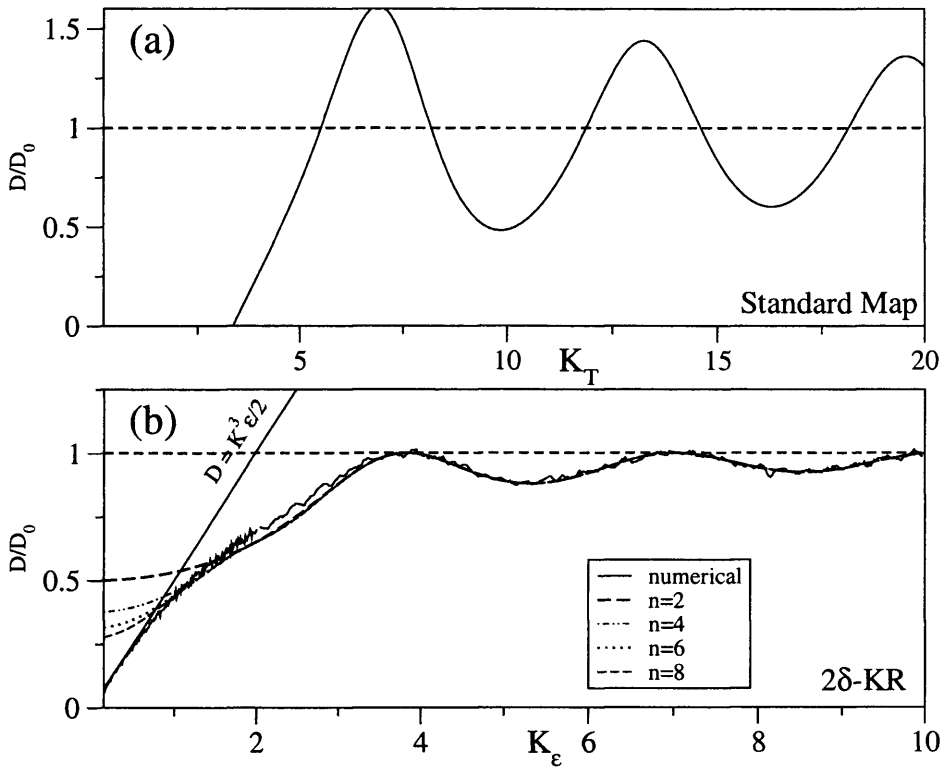

Figure 6.5: Comparison of the diffusion rates vs. control parameter in the Standard Map and the 2δ-KR. Ratios D/D_0 are shown in both cases, where the uncorrelated random walk is $D_0 = K_T^2/2$ for the Standard Map (a), where time is counted in numbers of individual kicks N, and $D_0 = K_\epsilon^2$ for the double kicked rotor (b), where time is counted in pairs of kicks $t = N/2$. Panel (a) is nearly equivalent to Fig.2.2 except for the inclusion of the 4-kick correlation term. Here the rate oscillates about the random walk value and the maxima coincide with values of K_T for which accelerator modes exist. In (b) it is seen that the diffusion rate in the double kicked rotor never exceeds the random walk but approaches it asymptotically. Analytical curves up to maximum order $O(J_1^n)$ are shown, including progressively higher order correlation terms from Eq.6.49. At large K_ϵ there is excellent agreement between the numerical and analytical curves including only $n = 2$, however for low K_ϵ many higher order terms are needed for good agreement. The regime in which clear signatures of the momentum trapping effect exist is $0.1 \lesssim K_\epsilon \lesssim 1$, where the numerical result $D = K^3\epsilon/2$ and hence $D/D_0 = K_\epsilon/2$ is obtained.

It is seen that the behaviour in the double kicked rotor is similar to that in the Standard Map. For low K_ϵ the behaviour of D/D_0 is almost linear with the control parameter, whereas for higher K_ϵ the behaviour is oscillatory due to the Bessel functions. As $K_\epsilon \to \infty$ the diffusion rate tends to the random walk $D \to D_0$, since $J_1(x) \to 0$ for large x. The Bessel functions decay as $1/\sqrt{K_\epsilon}$ for large K_ϵ, hence for most values of the control parameter the agreement between the numerical result and the analytical

curve, including only the lowest order global correlation family given in Eq.6.46, is very good. However, for low values of K_ϵ higher order terms are needed for good agreement, as shown. It is seen that for very small $K_\epsilon < 1$ the diffusion rate approaches the linear form $D \simeq K_\epsilon^3/2$ for scaled momenta (or $D \simeq K^3\epsilon/2$ for unscaled momenta) and hence $D/D_0 \simeq K_\epsilon/2$ as shown in Fig.6.5b. This is the important regime where the momentum trapping and characteristic diffusive behaviour of the double kicked rotor is strongest (cf. Chapter 5). Upon closer inspection there are in fact two linear regimes in Fig.6.5b: for $K_\epsilon \lesssim 1$ the rate is $D \simeq K_\epsilon^3/2$ as mentioned, and for $1 \lesssim K_\epsilon \lesssim 3$ the rate changes to $D \simeq K_\epsilon^3/4$, i.e. half of the previous value.

The exact origin of the gradients of the linear regimes of D/D_0 are not known, however it is interesting to note that the cubic dependence of the diffusion rate on the control parameter is similar to the scaling properties of the Standard Map near the golden ratio cantori. As mentioned in Chapter 2 the golden ratio cantori are the last invariant tori to break at the transition to unbounded diffusion in phase space at $K_{crit} \simeq 1$ and occur at momenta $p \simeq 2\pi R \pm 2\pi$ or $p \simeq 2\pi(1-R) \pm 2\pi$, where $R = (\sqrt{5}-1)/2$ is the golden mean. In [52] it was shown that in the mixed phase space regime of the kicked rotor (where the diffusion equation Eq.2.17 is not valid) for $1 \lesssim K_T \lesssim 4.5$, a numerical diffusion rate $D \simeq 0.3(K - K_{crit})^\eta$ can be obtained (here $T = 1$). From the scaling properties of the map near the golden ratio cantori the value $\eta = 3$ was obtained, resulting in a cubic dependence on the control parameter $K_T = K$. Since the fractal structures found at the centres of the momentum trapping regions in the double kicked rotor for τ not too large can be linked to the golden ratio cantori (cf. Chapter 5), it was suggested that the cubic dependence of the 2δ-KR diffusion rate for low values of K_ϵ originates from a similar scaling property derived from the trapping regions. However it must once more be remembered that trapping regions can exist independently of the cantori structures found at low values of τ/ϵ, thus there may well not be a link between the two cases.

If one compares the 2δ-KR behaviour with that of the Standard Map, the most striking difference is that in the double kicked rotor the diffusion is always bounded from above by the basic random walk term $D = K^2 t$, whereas in the Standard Map the diffusion rate can be higher or lower than D_0, depending on the value of the control parameter K_T. In both cases the diffusion rate tends to the uncorrelated random walk $D \to D_0$ for very high values of the control parameter. For low values of K_ϵ the hindered

asymptotic diffusion in the 2δ-KR could be seen to be due to the trapping regions in momentum space slowing down the average diffusion rate of particles, but for large K_ϵ the trapping effect no longer occurs. From Eq.6.49 it is clear that all momentum independent global correlation families oppose the random walk term K^2t, and thus lower the diffusion rate for a large range of values of the control parameter. In contrast, in the Standard Map, diffusion corrections can be of either sign. In particular the 2-kick correlation $C_2 = -K^2 J_2(K_T)$, which significantly affects the diffusive behaviour in the SM, is absent in the double kicked rotor, as all other even n-correlations. The 2-kick correlation is the only main diffusion correction which changes sign depending on the value of the Bessel function, since all other terms involve squares. Hence its absence further explains the hindered diffusion in the 2δ-KR, since for the SM the maxima correspond roughly to $J_2 = -1$.

In addition to the above there are no accelerator modes in the double kicked rotor, which in the δ-KR occurred at the maxima of the diffusion rate in Fig.2.2. Again, this is fairly intuitive as the temporal asymmetry in the double kicked rotor ensures that a periodic maximum momentum transfer, as in the kicked rotor for $K_T \simeq 2\pi n$ and $T = 1$, is not possible. Correspondingly, transporting islands are absent in the chaotic regime of the double kicked rotor.

It was shown in Eq.6.45 that all lowest order n-kick correlations, for any n, exist in the Standard Map, analogous to the 2δ-KR case. If one combines these to form a global correlation family as in Eq.6.46 the asymptotic correction to the diffusion rate is:

$$\sum_{n=3}^{\infty} C_n^{SM} = -K^2 J_1^2(K_T) \sum_{n=3}^{\infty} J_0^{n-3}(K_T) = -K^2 \frac{J_1^2(K_T)}{1 - J_0(K_T)} \tag{6.51}$$

where the similarity to the 2δ-KR case should be noted. However, in the Standard Map this correlation family has no significant effect on the diffusive behaviour in the chaotic regime for $n \gtrsim 4$. Higher order correlation families can be derived mathematically of similar asymptotic forms as given in Eq.6.49, but these are obviously of even lesser importance.

Fig.6.6a shows an enlargement of Fig.6.5a for low values of K_T, but this time the ratio D/D_0 is calculated for all values $K_T > 0$. The solid curve is only composed of the basic 2-kick and 3-kick correlations given in Eq.2.34, whereas subsequent curves include correlations from Eq.6.51 up to a given kick separation n. It is seen that in the fully chaotic regime $K_T \gtrsim 5$ the higher order kick correlations have almost no effect on the diffusion rate; Eq.2.34 is found to give good agreement with numerical

results, as shown in Fig.2.2, except for $K_T \simeq 2\pi n$ where accelerator modes are located (cf. Chapter 2). Even for $3 \lesssim K_T \lesssim 5$, where structures appear in the mixed phase space, higher order kick correlations still have no observable effect. For very low K_T mathematical differences appear, however the diffusion rate becomes negative and hence unphysical below $K_T \simeq 3.5$. This is because, as mentioned earlier, Eq.2.17 from which all diffusion correlations are derived, is only valid in the predominantly chaotic regime and breaks down for low values of K_T, where diffusion in phase space is affected by regular trajectories.

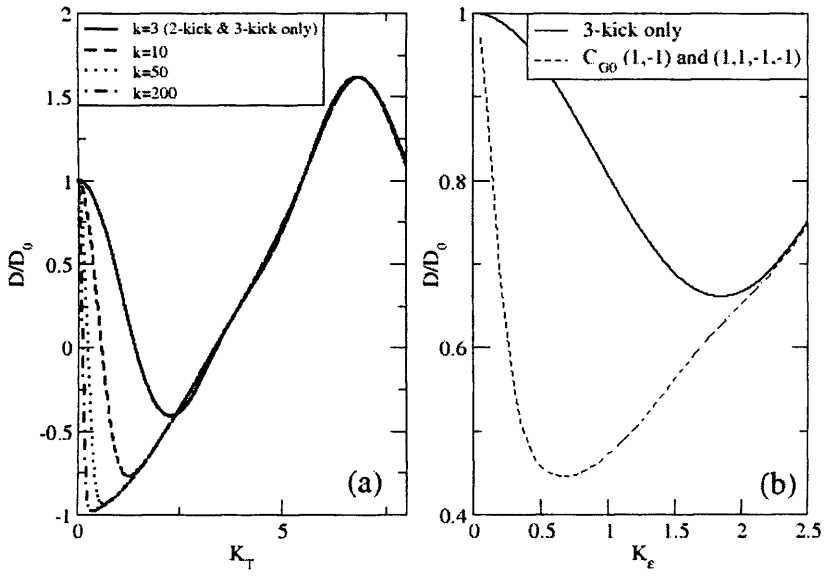

Figure 6.6: Effect of global correlations on the diffusion rate for low values of the control parameter in the Standard Map (a) and the 2δ-KR (b). For the SM inclusion of global correlations for low K_T results in unphysical negative diffusion rates; global correlations only have a mathematical effect in the SM for parameter ranges for which the diffusion equation Eq.2.17, from which the correlations are derived, is not valid. For the double kicked rotor however global correlations have a significant effect on the diffusion rate for a broad parameter range, including the regime in which momentum trapping occurs: $0.1 \lesssim K_\epsilon \lesssim 1$. The diffusion rate in this case never becomes unphysical since the chaotic regime extends down to very small $K_\epsilon \gtrsim 0.075$.

Despite its unphysical diffusion rates Fig.6.6a has been included here, as when one compares it to the case of the double kicked rotor, almost the same curves are obtained

for families of odd n-kick correlations, but given that the transition to full chaos occurs for much smaller values of the control parameter K_ϵ, these higher order terms have a significant impact on diffusion rates, well into the chaotic regime. This is essentially shown in Fig.6.5b, where higher order correlations alter the diffusion rate significantly for $K_\epsilon \lesssim 1.5$. In comparison it was shown in Chapter 5 that the momentum trapping effect found in the predominantly chaotic regime of the 2δ-KR occurs at values $0.1 \lesssim K_\epsilon \lesssim 1$, so the global correlation families are essential in explaining the diffusive behaviour of the double kicked rotor. Fig.6.6b is a somewhat simplified enlargement of the low K_ϵ section of Fig.6.5b. The solid curve is the ratio D/D_0 obtained when including only the lowest order 3-kick correlation (Eq.6.43) in the 2δ-KR, whereas the dashed curve includes both global correlation families given in Fig.6.4, hence the graph is analogous to the Standard Map case in Fig.6.6a. Indeed the behaviour is very similar to that of the unphysical low K_T regime in the Standard Map, but this time the global correlation families have a significant effect on the diffusion rate well into the chaotic regime. Since Eq.6.8 is valid for all $K_\epsilon \gtrsim 0.075$, the diffusion rate is also always positive and the mathematical behaviour never becomes unphysical.

The above shows that global correlation families are not really a new discovery, in the sense that they exist mathematically in the Standard Map but do not affect the diffusive behaviour in the chaotic regime. The double kicked rotor seems to be the first system where such higher order correlations coupling any kicks in a temporal sequence result in a long term 'memory', and affect the system evolution significantly.

A final comment should be made regarding the insensitivity of kick correlations in the double kicked rotor to the long timescale τ. As mentioned several times before, the diffusive behaviour of the double kicked rotor is almost completely independent of τ, provided $\tau \gg \epsilon$. Momentum dependent Poisson correlations that show a dependence on the long timescale τ result in small negligible oscillations with $\sim p_0$, and background correlations such as presented in this section, dependent on τ but independent of p_0, are also found to be less significant than those dependent solely on ϵ. The largest τ dependent C_{G0} correlations were found to have a smaller effect than the higher order correlation family shown in Fig.6.4. In addition these correlations can be of either sign, so their effect on the overall diffusion is further reduced. Some numerical data was gathered both for the momentum dependent and linear background diffusion, and the variation in energy absorption obtained by changing the ratio between the long and short timescales

from $\tau/\epsilon \simeq 20$ to $\simeq 200$ is no more than 10%-20%. For $\tau/\epsilon \gtrsim 200$ the diffusive behaviour remains almost unchanged, including the non-KAM random phase limit $\tau \rightarrow \infty$, and the non-periodic limit of choosing different τ for each time step. Hence introducing fixed random phases for the free evolution between kick pairs (the infinite τ limit) does not significantly affect kick correlations, and neither does a sequence of completely random τ values. The time interval between kick pairs is of almost no concern for the evaluation of kick correlations in the double kicked rotor, provided that it is always much greater than the interval between the kicks in a pair.

6.7 Summary: Energy Diffusion in the Double Kicked Rotor

To conclude the classical analysis of the double kicked rotor Fig.6.7 shows a summary of the diffusive behaviour of particles in the system in comparison to the Standard Map. Parameters are as usual $K = 7$ and $\epsilon = 0.05$, leading to $K_\epsilon = 0.35$. The energy absorption in time both for particles starting at the centre of a cell with $p_0 = 0$ and for those starting in a trapping region $p_0 = p_{trap}$ is shown, with the SM random walk diffusion shown with a dotted line. Time is counted in numbers of individual kicks N in this figure to avoid confusion, since in the double kicked rotor $t = N/2$. The inset shows the early time behaviour.

Essentially there are three diffusive regimes in the double kicked rotor at different timescales. At very early times particles that start with $p_0 = p_{trap}$ remain trapped at that momentum, while those starting near the centres of diffusion cells experience rapid intra-cellular transport towards the trapping regions at the boundaries. This is illustrated in the inset, where the diffusion rate for $p_0 = 0$ in the double kicked rotor is initially higher than that in the Standard Map. At intermediate times initially trapped particles diffuse into the neighbouring cells, due to diffusion enhancing global kick correlations, and inter-cellular transport occurs. These particles gain energy faster than those initially at the centres of diffusion cells, as the time taken for the former to initially escape from the trapping regions is less than that for the latter to traverse them after the initial fast diffusion within a cell. The non-linear regime in Fig.6.7 is derived directly from the behaviour of the Poisson correlation families in Fig.6.3. Finally, at very long times the diffusion rate becomes linear for both sets of particles, but remains significantly

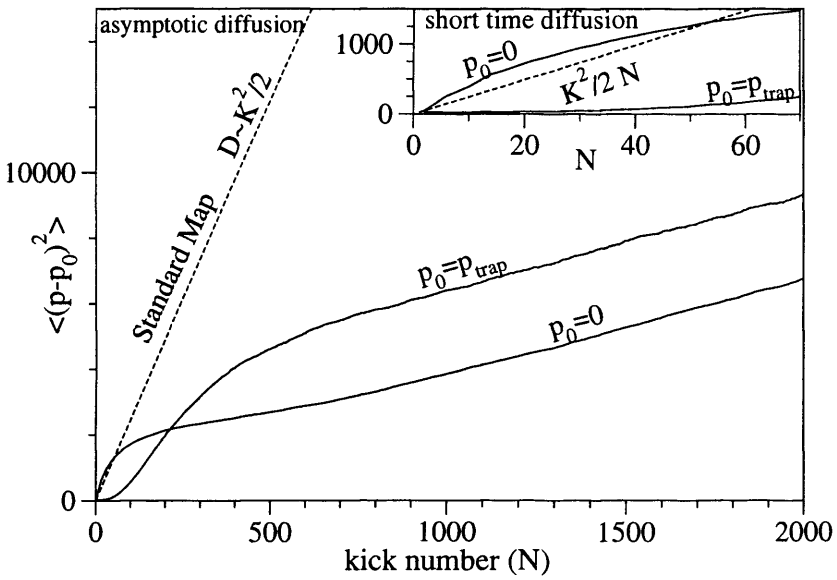

Figure 6.7: Energy diffusion in the double kicked rotor in comparison to the Standard Map or δ-KR. Parameters are $K = 7$ and $\epsilon = 0.05$. Time is counted in individual kicks N. Diffusion for particles with $p_0 = 0$ starting at the centre of a diffusion cell in the double kicked rotor and for $p_0 = p_{trap}$ starting at a trapping region is shown. The inset shows the early time behaviour. Particles starting at $p_0 = 0$ initially absorb energy very rapidly at a rate faster than that of the SM random walk. In contrast, particles starting in a trapping region absorb very little energy as expected. Due to the global kick correlations affecting the diffusion rate in the double kicked rotor, initially trapped particles however end up absorbing more energy at later times, since the diffusion rate increases at intermediate times. At long times the rate is linear for both starting conditions, despite the persistence of trapping regions in phase space, since the average energy of a large ensemble of particles is taken and the trapping effect is averaged out.

lower than that of the SM, due to the hindered diffusion through trapping regions in momentum space. The linearity arises since the average energy absorption of a large ensemble of particles is shown. At long times roughly equal numbers of particles will be located within diffusion cells as at the trapping regions, so individual local diffusion rates will be averaged over. However the average rate will still be significantly lower than in the SM due to the slow transport of those particles at cell boundaries (given appropriate parameter values).

It should also be noted that the same three diffusion regimes exist for variation with K_ϵ, as illustrated by Fig.6.5b and mentioned in Chapter 5. At very low $K_\epsilon \lesssim 0.075$, near the critical transition limit from a chaotic to a mixed phase space, there is almost no transport between diffusion cells, as seen in Fig.6.5b. For low kick strengths K, particles

are essentially trapped either within one diffusion cell or within the trapping regions. As K_ϵ increases, so does the diffusion rate, as inter-cellular transport becomes favoured. At high kick strengths, and correspondingly K_ϵ, the diffusive behaviour becomes increasingly similar to that of the Standard Map, as particles move faster through trapping regions. Eventually, at very high kick strengths, the particles diffuse through phase space almost entirely unperturbed, since trapping regions no longer exist. However, the diffusion rate is still always bounded from above by the uncorrelated random walk K^2t, due to the persistence of diffusion hindering global correlations and the absence of accelerator modes.

Chapter 7

The Quantum Double Kicked Rotor

Following on from the extensive classical analysis of the double kicked rotor in the previous two chapters, here the quantum version of the system is presented. A strong correspondence exists between the classical diffusion effects and the quantum behaviour of the double kicked rotor. First the mathematical formalism is shown with two different forms of the quantum evolution operator, which is represented by a band diagonal matrix of oscillatory bandwidth, denoting the cellular structure of phase space in the classical analysis. Experimental results are presented, obtained using a similar setup of cold atoms pulsed by standing waves of laser light, as for the QKR. Energy absorption of atoms is found to occur as predicted by the diffusion rates found in Chapter 6. The localisation properties of momentum distributions and the Floquet states of the quantum double kicked rotor are investigated. Localisation occurs mainly due to the trapping regions and gives the momentum distributions and eigenstates a characteristic cellular structure. The quantum transport of atoms through regions of fast and slow energy absorption is also investigated, in the context of localisation within single diffusion cells or across several cells. Unusual fractional scaling of localisation lengths and other quantum properties is found. Although the scaling is reminiscent of that obtained in the QKR near golden ratio cantori, it persists for the quantum version of the non-KAM random-pair-kicked rotor, in which the quantum phase of the free propagator in between pulse pairs is randomised, and for which, in the classical analogue, no regular structures remain in the trapping regions. Thus the scaling observed here is more likely to be of pure quantum origin. The chapter concludes with a brief review of the statistics for the eigenenergies of the quantum double kicked rotor.

7.1 The Quantum Evolution Operator

In analogy to the QKR it is possible to formulate the double kicked rotor quantum mechanically [53] and apply it to experimental situations. It will be seen that there is a strong correspondence between the classical and quantum cases, with the quantum double kicked rotor (2δ-QKR) featuring the momentum trapping effect as described in the previous chapters. This correspondence is of course expected from quantum chaos theory, where the quantum mechanical system must still appropriately describe a classically chaotic system such as the double kicked rotor. The trapping regions in momentum space are evident both from the experimental results and the mathematical quantum evolution operator. In this chapter the usual case of momentum trapping will be investigated in a system of cold atoms, very similar to that in Chapter 3. In the next chapter a different realisation of the double kicked rotor will also be looked at, where trapping occurs in position space along a spin chain system.

The quantum evolution operator for the double kicked rotor is a straightforward extension of that for the QKR in Eq.3.13, allowing for evolution over two time steps, consisting in each case of a kick and a free evolution following it. The Floquet operator thus defines periodicity in terms of kick pairs, as for the classical 2δ-KR:

$$\hat{U}^F = \hat{U}_{kick}\hat{U}_\epsilon\hat{U}_{kick}\hat{U}_\tau = e^{-i\frac{K}{\hbar}\cos x}e^{-\frac{i\hat{p}^2\epsilon}{2\hbar}}e^{-i\frac{K}{\hbar}\cos x}e^{-\frac{i\hat{p}^2\tau}{2\hbar}} \tag{7.1}$$

The matrix elements for this operator in a basis of plane wave momentum states can also be derived in the same way as for the QKR in Chapter 3, involving coupling between momentum states given by Bessel functions. In analogy to Eq.3.21 the matrix elements for the 2δ-QKR can be written as:

$$U_{lm} = \sum_k \langle m|\hat{U}_{kick}\hat{U}_\epsilon|k\rangle\langle k|\hat{U}_{kick}\hat{U}_\tau|l\rangle = i^{l-m}e^{-\frac{il^2\hbar\tau}{2}}\sum_k J_{l-k}(\frac{K}{\hbar})J_{k-m}(\frac{K}{\hbar})e^{-\frac{ik^2\hbar\epsilon}{2}} \tag{7.2}$$

The first kick in a pair evolves the system from a state $\Psi_l = \sum_l A_l|l\rangle$ to a state $\Psi_k = \sum_k A_k|k\rangle$. The second kick then transforms the latter into the state after a kick pair $\Psi_m = \sum_m A_m|m\rangle$, and the intermediate momentum k is summed over. As for the QKR the kick operator can also be written as $U_{kick} = \exp(-\frac{i}{\hbar}K\sin x)$, leading to the absence of the unimportant phase factor i^{l-m}.

By diagonalising U_{lm} the Floquet states and corresponding quasienergies of the double kicked system can be found; these will be investigated later in this chapter and will be seen to display clear signatures of the momentum trapping regions. It should be remembered that the Floquet states belonging to $\hat{U}^F$ are only stationary during the long

free evolution τ between kick pairs, but do vary during the short time interval ϵ between kicks in a pair.

The control parameters for the 2δ-QKR are $K_\epsilon = K\epsilon$ and $\hbar_\epsilon = \hbar\epsilon$, in analogy to K_T and $\hbar_T$ in the QKR. Eq.7.2 may be rescaled appropriately to show the emergence of these parameters. Similar to the classical case, the parameter $\hbar_\tau = \hbar\tau$ is found not to affect the quantum system significantly, provided that $l^2\hbar\tau \gg 2\pi$, in which case the free propagator $\exp(-il^2\hbar_\tau/2)$ contributes a near-random phase. An exception is in the resonant regime where $\hbar_\tau = 4\pi n$ with integer n, which sets the propagator to unity for integer l^2. In this case the effects of kick pairs accumulate over time to produce similar resonances in the energy growth as for the QKR (cf. Chapter 3). Further types of resonances are found for the more general case $n = a/b$. This chapter however will deal exclusively with the non-resonant case of phase randomisation due to the free propagator.

As for the QKR the Bessel functions in Eq.7.2 only couple momentum states that lie close together, since $J_n(K/\hbar) \to 0$ for $n \gtrsim K/\hbar$. For the QKR in Chapter 3 it was seen that this gave the evolution matrix U_{lm}^{QKR} a banded structure along the diagonal, as observed in Fig.3.1. Here however the presence of the summation over k changes the form of the matrix to a band of oscillating width along the diagonal, as shown in Fig.7.1. This effectively partitions the matrix into a number of momentum cells of

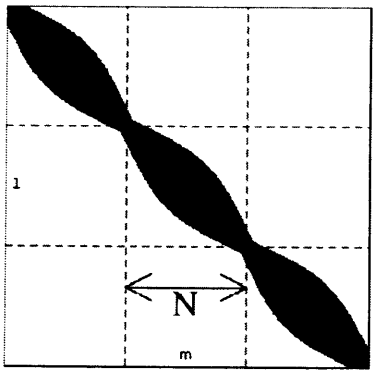

Figure 7.1: Oscillating band structure of the evolution matrix for the 2δ-QKR. The black areas represent significant non-zero entries, while the white area represents negligible entries $\simeq 0$. An analytical form of the bandwidth observed here is given by Eq.7.7. The evolution matrix is composed naturally of a number of subcells of dimension $N = 2\pi/\hbar_\epsilon$ corresponding to the diffusion cells in the classical double kicked rotor.

dimension $N = 2\pi/\hbar_\epsilon$, which is of course a signature of the cellular form of the classical phase space of the double kicked rotor. The half-bandwidth of $U_{lm}^{2\delta-QKR}$ varies from

a minimum of $b_{min} \simeq 0$ at the cell boundaries to a maximum of $b_{max} = 2K/\hbar$ in the centres of the cells, in comparison to the fixed half-bandwidth $b_{QKR} = K/\hbar$ of the quantum kicked rotor. This is in agreement with the classical analysis in Chapter 5, where particles remain near their initial momentum in the trapping regions, but near the centres of cells energy absorption is roughly twice as high as in the δ-KR.

The oscillating band structure can also be shown analytically from the evolution operator by evaluating the matrix elements differently to Eq.7.2, as shown in [53]. One can assume that the intermediate momentum k lies close to both l and m, since large momentum jumps do not occur for either kick in a pair. Hence the kick operator $\hat{U}_\epsilon$ for $\hat{p} = \hat{k}\hbar$ can be written as:

$$\hat{U}_\epsilon = e^{-\frac{i\hat{p}^2\epsilon}{2\hbar}} = e^{-\frac{i(k_0+\hat{k}_1)^2\hbar\epsilon}{2}} \simeq e^{-\frac{ik_0^2\hbar\epsilon}{2}} e^{-ik_0\hbar\epsilon\hat{k}_1} \tag{7.3}$$

where the substitution $\hat{k} = k_0 + \hat{k}_1$ has been made, and k_0 is a momentum value close to l and m. The final term in the expansion above can be neglected for small ϵ, since $\hbar\epsilon\hat{k}_1^2 \ll 1$ for a momentum change of $|k_1| = |m-k| = |k-l| \lesssim K/\hbar$ (from the Bessel function behaviour). Substituting in $\hat{k}_1 = -i\partial/\partial x$ and making use of the shift operator $\exp(a\partial/\partial x)f(x) = f(x+a)$, one can obtain matrix elements for the direct conversion from momentum state l to state m:

$$\begin{aligned} U_{lm} &\simeq e^{-\frac{i\hbar}{2}(l^2\tau+k_0^2\epsilon)}\langle m|e^{-i\frac{K}{\hbar}\cos x}e^{-k_0\hbar\epsilon\frac{\partial}{\partial x}}e^{-i\frac{K}{\hbar}\cos x}|l\rangle \\ &= e^{-\frac{i\hbar}{2}(l^2\tau+k_0^2\epsilon)}\langle m|e^{-i\frac{K}{\hbar}\cos x}e^{-i\frac{K}{\hbar}\cos(x-k_0\hbar\epsilon)}e^{-ilk_0\hbar\epsilon}|l\rangle \end{aligned} \tag{7.4}$$

for the usual basis of plane waves $|l\rangle = (1/\sqrt{2\pi})\exp(ilx)$ and similarly for m. Using the trigonometric identity for a sum of cosines Eq.7.4 can be further simplified to:

$$U_{lm} \simeq e^{-\frac{i\hbar}{2}(l^2\tau+k_0^2\epsilon+2lk_0\epsilon)}\langle m|e^{-i\frac{2K}{\hbar}\cos\frac{k_0\hbar\epsilon}{2}\cos(x-\frac{k_0\hbar\epsilon}{2})}|l\rangle \tag{7.5}$$

Finally the integration is performed with the help of the following identity:

$$\frac{1}{2\pi}\int_{-\pi}^{\pi} e^{-i\beta\cos(x-a)}e^{i(l-m)x} = e^{i(l-m)(a-\frac{\pi}{2})}J_{l-m}(\beta) \tag{7.6}$$

and one can replace k_0 by l or m to result in:

$$U_{lm} \simeq e^{-i\phi}J_{l-m}(\frac{2K}{\hbar}\cos\frac{p^\epsilon}{2}) \tag{7.7}$$

where $p^\epsilon = p\epsilon$ as previously, and $p = l\hbar$ or $p = m\hbar$ depending on the choice of k_0. The phase ϕ again depends on the choice of the latter to give:

$$\phi = \frac{\hbar}{2}(l^2\tau + 2l^2\epsilon + lm\epsilon) + (l-m)\frac{\pi}{2} \simeq \frac{\hbar}{2}(l^2\tau + 2m^2\epsilon + lm\epsilon) + (l-m)\frac{\pi}{2} \tag{7.8}$$

From Eq.7.7 a momentum dependent half-bandwidth $b(p) \simeq (2K/\hbar)\cos(p^{\epsilon}/2)$ can be inferred, as shown in Fig.7.1, resulting in $b_{min} \simeq 0$ and $b_{max} \simeq 2K/\hbar$ as earlier. For a kick pair the resultant change in momentum of particles is $|l - m| \leq 2K/\hbar$.

7.2 Experimental Results for the Quantum Double Kicked Rotor

The experimental verification of the 2δ-QKR system was carried out at University College London by Jones et al in 2004 [51]. As mentioned in the introduction to the thesis in Chapter 1, this cold atom experiment was the starting point of the present work and was performed as a natural limit to the period-perturbed kicked rotor and ratchet systems presented in Chapter 4. Instead of having a two-kick sequence with time periods slightly perturbed by a small amount ϵ from the usual kicked rotor period, i.e. $T_1 = T + \epsilon$ and $T_2 = T - \epsilon$ with $T = 1$, the limit of large deviations from unit time steps was investigated, leading to the double kick sequence $T_1 = \epsilon$ and $T_2 = \tau$ with $\tau \gg \epsilon$. This led to experimental results which showed energy absorption dependent on initial momentum as for the PPKR, however important differences were noticed, which were later explained by the mathematical analysis of the 2δ-KR given in Chapters 5 and 6.

The experimental setup used was very similar to the one described in Chapter 3 used by Raizen et al for the demonstration of the QKR. Again, a cloud of cold atoms, this time caesium, was collected in a 6-beam MOT and cooled in an optical molasses to a temperature of 6μK. The cloud was then pulsed periodically by standing waves of near-resonant laser light, but this time with altered pulse periods to the case of the QKR. The standing waves are created by two counter-propagating beams derived from a titanium sapphire laser, with an intensity of $4\times10^3 I_{sat}$ in each beam (where $I_{sat} = 1.12\text{mWcm}^{-2}$ is the saturation intensity) and detuned 2000 linewidths to the low frequency side of the D2 cooling transition in caesium, with the natural linewidth $\Gamma = 2\pi \times 5.22\text{MHz}$. With this detuning the photon scattering rate is roughly $500s^{-1}$, corresponding to about 2×10^{-4} scattering events per kick. This ensures a good signal-to-noise ratio and preservation of coherence over the timescale of the experiment (up to about 50 kick pairs or 100 individual kicks). The experimental setup, without the trapping and cooling apparatus, is shown in Fig.7.2.

The original laser beam is split by the first half-wave plate (HWP1) and polarising

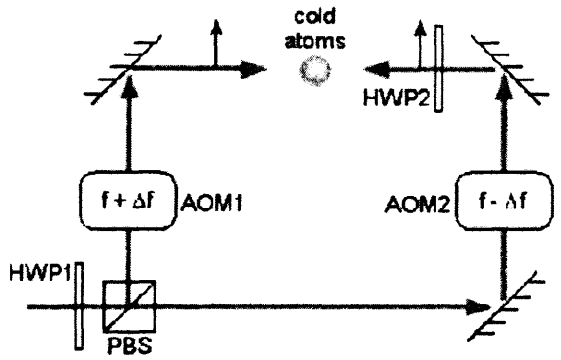

Figure 7.2: Schematic of the experimental setup used for the realisation of the quantum double kicked rotor. The half-wave plate HWP1 and polarising beam splitter PBS are used to create two equal intensity laser beams, which are shifted in frequency by the two acousto-optic modulators AOM1 and AOM2. The second half-wave plate HWP2 is used to make the polarisations of the two beams parallel, before they hit the cloud of cold atoms. The latter is collected in a magneto-optic trap and cooled in an optical molasses (both not shown). The cold atoms are then periodically hit by closely spaced pairs of laser pulses in time. Courtesy of Phil Jones.

beam splitter (PBS) to give two equal intensity beams. These are sent through two acousto-optic modulators (AOM1 and AOM2), which create pulses as short as t_p = 300ns, with frequencies $f \pm \Delta f$. The frequency difference $2\Delta f$ is imposed so that the sinusoidal potential formed by the standing wave moves with constant velocity in the laboratory frame, as already described in Chapter 4. This means that the momentum dependence of energy absorption from the lasers by the atoms can be investigated, since in the rest frame of the potential the atomic momentum distribution has a non-zero mean value. The second half-wave plate (HWP2) is used to make the polarisations of the two beams parallel. The radii of the two laser beams are then 0.95 ± 0.05mm.

The experimental Hamiltonian is essentially of the form given in Eqs.3.27-3.30, with the same scalings used, but with different kicking periods of course. The laser pulses are applied at times nT and $nT + \Delta$ for integer n, where $T = 9.47\mu$s, and values of $\Delta = 0.45\mu$s-1.5μs were used. In rescaled variables the usual time periods of the double kicked rotor emerge, namely $\epsilon = \Delta/T \simeq 0.045 - 0.16$ and $\tau = 1 - \epsilon$. Up to $N = 100$ kicks were applied (i.e. 50 kick pairs) before the atom cloud was allowed to evolve freely in the dark for 15ms. The spatial distribution was recorded on a CCD using fluorescence imaging as usual, and the momentum distribution calculated with the help of the free drift time. In the experiments an effective value of $\hbar = 1$ results from the parameters

given above, and the kick strength is $K = 3.3 \pm 10\%$ (the uncertainty is due mainly to difficulties in measuring the exact intensity of the laser beams).

The left panels (a-c) of Fig.7.3 show the experimental results (solid lines) for the quantum double kicked rotor, in terms of average energy absorption $\langle \rho^2 \rangle$ of the atom cloud vs. initial starting momentum ρ_0 in the rest frame of the standing wave. Three different values of ϵ, the temporal separation of kicks in a pair, are investigated, namely $\epsilon = 0.045, 0.094, 0.16$, resulting in values of the control parameter $K_\epsilon \approx 0.15, 0.3, 0.53$, i.e. all three cases are within the regime where the momentum trapping effects are observed clearly in the double kicked rotor. In every case the atom cloud initially starts with $\langle \rho^2(t = 0) \rangle \simeq 30$ shown by the dot-dashed line in all panels. The experimental curves are compared to numerical simulations for the same parameters. Although there are significant discrepancies in the energy absorption, the basic behaviour agrees well enough to confirm the behaviour of the double kicked rotor. It is noticeable that the numerical data agrees reasonably well at low ϵ, but at higher values of the kick separation the energy absorption in the experiment is generally lower, except in the trapping regions which are less pronounced than expected. The main reason for the discrepancies is that a broad distribution of atoms is used in the experiment with initial non-zero momentum and energy as mentioned above, while in the numerical calculations particles start with zero momentum and plane wave states are used.

The results shown in the first panel (a) are not really too different from the momentum dependent sinusoidal energy absorption curve for the rocking ratchet shown in Fig.4.4. For low values of ϵ (and hence K_ϵ) the absorption varies cosinusoidally with ρ_0, as opposed to the sinusoidal variation for the ratchet. Results for higher values of ϵ however are different to the ratchet case and were not fully understood at first. Sharp dips in the energy absorption are observed for values of $\rho_0 \simeq \pm(2n+1)\pi/\epsilon$, but which disappear at large values of ϵ. With the help of the classical analysis of the double kicked rotor in Chapters 5 and 6, these results are of course straightforward to explain. The cellular structure of momentum space is clearly visible, and trapping regions are marked by the dips in energy absorption, while absorption is much higher for values of $\rho_0 \simeq 2n\pi$ at low ϵ. At higher values of ϵ the absorption in the trapping regions increases in proportion to that near the centres of diffusion cells. One should of course remember that changing ϵ also changes the positions of the trapping regions as shown by the experimental results and in Fig.5.8.

The similarity between Figs.7.3 and 6.2 should be noted, where in the former behaviour with increasing ϵ is shown, and in the latter behaviour with increasing number of kicks or time $t = N/2$. It was seen in Chapter 6 that the kick-to-kick correlation dominates the diffusive behaviour at short evolution times with $C_1 t \simeq K^2 t \cos p_0 \epsilon$ for small t, while the lowest order global correlation family $C_{G1} t \propto -\cos p_0 \epsilon$ dominates diffusion at later times, through the accumulation of individual n-kick correlations. Poisson families of higher order kick correlations lead to the formation of the dips in energy absorption at the trapping momenta for early and intermediate times, as well as their eventual disappearance at very long times.

The reasons that the experimental results for the 2δ-QKR in Fig.7.3 for variation with ϵ are reminiscent of the diffusive behaviour of the classical double kicked rotor in time, lie in the phenomenon of dynamical localisation which is observed in the quantum double kicked rotor, as for the QKR described in Chapter 3. Energy absorption does not continue indefinitely but saturates after a short time, after which the momentum distribution of the atomic cloud remains essentially unchanged. Localisation takes place after the quantum break time which for all three panels is $t^* \sim 30$, where time is counted as usual in kick pairs ($N^* \sim 60$). Later in this chapter it will be shown that the break time is in fact momentum dependent, however for the parameters used here t^* is roughly the same for all momenta, except near trapping regions, where it is significantly lower. Remembering that $t^* \sim L/\hbar$, this is of course obvious, since there is a far greater localisation effect inside a trapping region (and hence smaller localisation length L), than in the centre of a diffusion cell.

Up to the break time the diffusive behaviour of the atomic system evolves as shown in Fig.6.2, but for $t \gtrsim 30$ the dependence of energy absorption on initial momentum remains the same in time. The evolution is halted at whichever behaviour dominates at the quantum break time. Since the kick correlations given in Chapter 6 all depend on K_ϵ, the times at which different correlations become dominant vary with this parameter.

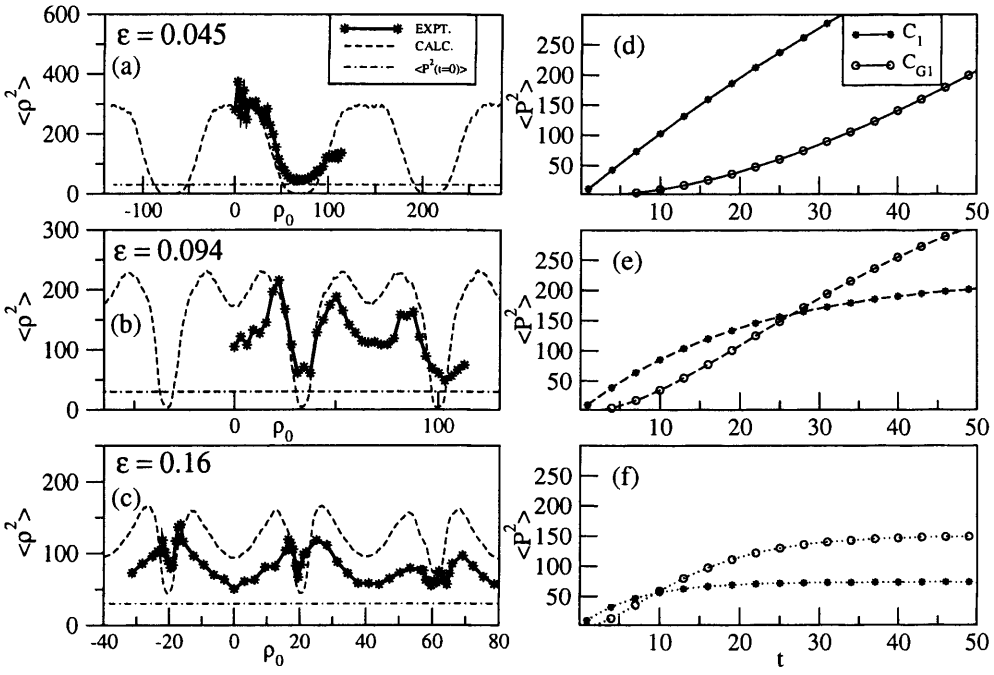

Figure 7.3: Experimental results for the 2δ-QKR (left hand panels). Graphs a-c show energy absorption of an ensemble of cold caesium atoms (solid lines) for $K_\epsilon \approx 0.15, 0.3, 0.53$ respectively and $\hbar_\epsilon = \epsilon = 0.045, 0.094, 0.16$. Measurements are taken after the quantum break time $t^* \sim 30$ when energies have saturated. Comparisons are made to numerical calculations (dashed lines), with reasonable qualitative agreement. As ϵ and thus K_ϵ increase, the energy absorption, dependent on initial momentum ρ_0, shows a similar behaviour as for variation with time for fixed K_ϵ in Fig.6.2. This is explained by the fact that a variation in K_ϵ results in a change in t_G, the time at which global diffusion corrections C_{G1} become dominant in relation to the kick-to-kick correlation C_1. Panels d-f show the time behaviour of the two correlations (C_1 (stars), C_{G1} (circles)) for the parameters in a-c. The time t_G can be taken to be near the crossing point of $C_{G1}t$ and $C_1 t$. In (a) and (d) $t^* \ll t_G$, and the quantum system is arrested in a regime where C_1 dominates (cf. Fig.6.2a). Atoms prepared in trapping regions absorb almost no energy. In (b) and (e) $t^* \simeq t_G$, so C_{G1} almost exactly cancels out C_1. Since higher order Poisson correlations vary on different timescales, diffusion hindering C_{Gn} terms with $n > 1$ are still dominant at this point, thus trapping regions remain visible in the energy absorption (cf. Fig.6.2b). In (c) and (f) $t^* > t_G$, and the system evolves long enough for global correlations to dominate the diffusion. Initially trapped atoms start to absorb energy rapidly (cf. Fig.6.2c). Experimental results courtesy of Phil Jones.

The three panels on the right (d-f) of Fig.7.3 show the behaviour of the kick-to-kick correlation $C_1 t$ and the lowest order global correlation family $C_{G1} t$ with time for the same values of K_ϵ as in the corresponding left panels (a↔d, b↔e, c↔f). It can be seen that K_ϵ controls the relative importance of the diffusion correlations at various times. As K_ϵ increases it is seen that the time taken for the global correlations to dominate the diffusive behaviour is greatly reduced. This timescale is denoted by t_G which can be taken to be near the crossing point of the kick-to-kick correlation $C_1 t$ and the $C_{G1} t$ family. Note that usual momenta p are used in the right-hand panels, compared to the scaled momenta ρ in the experiment; a comparison can however still be made as only the relative energy absorption with respect to initial momentum (scaled or unscaled) is of importance, not absolute values.

The three experimental results can now be explained individually. All measurements are made well after the quantum break time, so energy evolution has been halted in the diffusive regime given by the corresponding correlation behaviour on the panel to the right. In the top panels $t_G \simeq 100 \gg t^*$, hence the experimental behaviour corresponds to a regime where the kick-to-kick correlation is still clearly dominant ($t \simeq 30$ in (d)), and energy absorption varies cosinusoidally with p_0 as shown in (a) and predicted by the form of $C_1 t$. The experimental curve clearly follows the basic cosine shape. In the middle panels $t_G \simeq t^* \sim 30$, so here the experimental absorption is halted just near the point at which global correlations are becoming important. The near zero energy absorption at the trapping regions still persists, however absorption at the centres of diffusion cells is starting to decrease in relation to near the cell boundaries, signalling the gradual change to a sine curve, as predicted by the form of $C_{G1} t \propto -\cos p_0 \epsilon$. As the two correlations in the right-hand panel almost exactly cancel each other out at the break time (remembering that they are of opposite signs, and absolute values of maximum energy absorption, where $\cos p_0 \epsilon = 1$, are shown in d-f), the dips in absorption at the trapping regions, caused by the higher order Poisson correlations, are very distinctive for these parameters, with average energy values differing greatly over a small range of initial momenta. As shown in Fig.6.3 the crossing points between diffusion hindering and enhancing correlation families C_{Gn} vary for different terms. The time taken for diffusion enhancing terms C_{Gn}^+ to overtake their diffusion hindering partners C_{Gn}^- increases with both increasing cosine order n and $O(J_1)$. This means that in particular for variation with n, at the point where $C_1 t \simeq C_{G1} t$ the diffusion hindering Poisson terms ($n > 1$)

are still dominant in relation to the diffusion enhancing terms, hence the dips in energy absorption at the trapping regions persist.

In the bottom panels finally $t_G \simeq 10 < t^*$ and the quantum system follows classical energy predictions long enough for the global correlation family to start dominating diffusion. Poisson dips at the trapping regions still exist, due to the crossing points for higher order correlations $n > 1$ occurring at times longer than t^*, however some energy absorption now occurs at $p_0 \simeq \pm(2n+1)\pi/\epsilon$. With the exception of the trapping regions, the change to a sine curve for the average energy absorption can be seen, similar to the case of Fig.6.2c.

It should be noted that saturation values of correlations in (d-f) decrease with increasing K_ϵ, in other words the effect of kick correlations in terms of corrections to the energy diffusion rate becomes less significant at higher values of K_ϵ. This is of course expected since it was found in Chapter 5 that as the control parameter of the double kicked rotor is increased, the distinctive diffusive behaviour in terms of trapping regions in momentum space eventually disappears for $K_\epsilon \gtrsim 2$. Mathematically this can be shown to be due to the kick correlations becoming continuously weaker; that includes higher order correlation families, which are of course weaker than the main kick-to-kick correlation and $C_{G1}t$ family anyway. For all diffusion corrections due to kick correlations one obtains $\lim_{t\to\infty} Ct \to 0$ for $K_\epsilon \gtrsim 2$. This is valid for both the momentum dependent Poisson correlations, including $C_1 t$, and the asymptotic background correlations independent of initial momentum, as was shown in Fig.6.5b, where correlations only make a significant difference to the diffusion rate at low K_ϵ.

7.3 Momentum Distributions: Localisation and Quantum Transport

The trapping regions of the quantum double kicked rotor can also be observed directly from localised momentum distributions, given appropriate parameter values. Two examples of quantum numerical simulations are shown in Fig.7.4 for values of $\hbar = 1/30$ (top panel) and $\hbar = 1/8$ (bottom panel). The parameters here are $K = 20$ and $\epsilon = 0.0175$, leading to the value of the control parameter much used in Chapters 5 and 6, $K_\epsilon = 0.35$. All atoms start at $p_0 = 0$, and the momentum distributions are calculated well after the quantum break time. It can be seen that sections where the distribution is nearly

uniform alternate with sharp drops in probability. The near uniform parts of the distribution in fact signify the diffusion cells, whereas the locations of the drops in probability coincide with the trapping regions at $p \simeq \pm(2n+1)\pi/\epsilon$. This gives the distribution a characteristic staircase structure superposed onto the usual exponentially localised shape, with each step representing one diffusion cell, as verified by the $2\pi/\epsilon$ width of these steps. The quantum distributions mirror the cellular structure of classical phase space perfectly: diffusion of atoms across individual cells or steps is fast, and hence a near uniform distribution is quickly obtained, whilst diffusion across cell or step boundaries is a slow process. The distributions can be compared directly to the phase spaces in Figs.5.3 and 5.5, which are for the same value of the control parameter (although different values of ϵ mean that the trapping regions are in different locations). The quantum-classical correspondence for the double kicked rotor is striking.

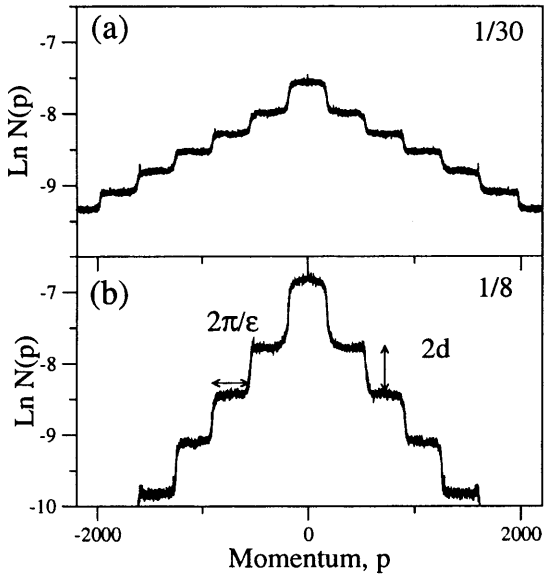

Figure 7.4: Examples of momentum distributions, obtained from numerical simulations of the quantum double kicked rotor, for $K_\epsilon = 0.35$. The values of $\hbar$ are 1/30 and 1/8 in (a) and (b) respectively, leading to $\hbar_\epsilon = 0.000583$ and 0.0021875 respectively. All atoms start at $p_0 = 0$ and the distributions are calculated well after the quantum break time. A characteristic staircase structure is superposed onto the exponentially localised distribution in both cases, clearly denoting the cellular structure of momentum space. Atoms rapidly diffuse across individual cells or steps to give a near uniform distribution, however at momenta corresponding to the trapping regions, sharp drops in probability are observed, characterised by the parameter $2d$. The width of the diffusion cells is $2\pi/\epsilon$ as expected.

The staircase structure was also observed for momentum distributions obtained from

cold atom experiments [48], however only the first few steps were seen, and the results were not as clear as the energy absorption variation shown in Fig.7.3. It is interesting to note that an earlier experiment with cold atoms using pairs of broad pulses [54], as opposed to the very short pulse durations approaching δ-functions in time in the experiments described here, also showed a steep drop in probability over narrow regions of the momentum distribution. This was attributed to the presence of cantori in those regions, which of course is similar to the case of the 2δ-QKR where small fractal structures were identified at the trapping regions for certain parameters. However, the trapping regions can of course exist independently of regular structures. Also, the broad pulse system does not have the momentum periodicity of the 2δ-QKR and is effectively integrable at large p. Nevertheless, at $p \simeq 0$ the classical dynamics of the two systems are similar; the same is true for the comparison between the usual δ-kicked QKR and a kicked rotor with much longer pulse durations.

As was shown by the experimental energy absorption in the quantum double kicked rotor in Fig.7.3, where absorption is halted at different times, exponential localisation still occurs in the 2δ-QKR. The staircase structures in Fig.7.4 follow a characteristic triangular shape on the logarithmic intensity scale, signifying dynamical localisation. The general exponential shape of the distributions follows $N(p) \sim \exp(-2|p|/L_p)$ as for the QKR in Eq.3.31, with the localisation length $L_p = (2\pi)/(d\epsilon)$, where $2d$ is the drop in probability between subsequent steps of the staircase, as shown in Fig.7.4. At each step the drop in probability is described by:

$$N^+(p') = e^{-2d} N^-(p) \tag{7.9}$$

where $N^-(p)$ is the probability of the higher step, and $N^+(p')$ is the probability of the lower step, hence $|p'| > |p|$. It should be noted that usually the probability drop between the central and neighbouring cells can be larger than the ones in subsequent trapping regions. This will be seen more clearly later in this section and is due to the localisation properties across the initial starting cell, including adjacent trapping regions, being slightly different to those across the entire distribution in momentum space. Hence the overall localisation length of the staircase is denoted as L_p to distinguish it from other quantities.

The localisation effect is very useful in the quantum double kicked rotor as it asymptotically preserves the staircase structure due to the asymmetric momentum diffusion between cells and trapping regions. In the absence of localisation the distribution would

eventually become entirely uniform over all momentum ranges. Dynamical localisation was already seen to be very useful for preserving the asymmetries in the ratchet systems investigated in Chapter 4. It should be noted that the staircase structure is of course only seen if the kick strength is large enough (in relation to $\hbar$), otherwise localisation may stop the diffusion process before atoms have traversed the first trapping regions.

The parameter d is related to the transport of atoms through the trapping regions, as it denotes the height of each step in the staircase structure. It can be seen that the location of the trapping regions and hence steps only depends on ϵ and not on the quantum parameter $\hbar$. In both panels of Fig.7.4 the drops in probability between diffusion cells occur at the same momenta. Varying $\hbar$ has two connected effects however. Firstly, the distribution is found to spread further in momentum before localisation, as $\hbar$ is lowered. This is fairly intuitive since in the classical limit $\hbar \to 0$ localisation is completely absent, and the distribution continues spreading until halted by system dimensions. Secondly, the step height, and hence drop in probability between neighbouring cells, increases for larger $\hbar$. Hence atoms pass through trapping regions more easily at lower $\hbar$, which of course also results in greater spreading of the momentum distribution. For large enough $\hbar$ (with fixed K) on the other hand, the localised distribution is restricted to only one cell, and no transport occurs at all. The same is true for low K, or more generally a low ratio $K_\epsilon/\hbar_\epsilon$.

Since the quantum control parameters are K_ϵ and $\hbar_\epsilon$, studying variation with $\hbar$ or ϵ individually is only of limited use. In the classical limit $\hbar \to 0$, the control parameter $\hbar_\epsilon \to 0$ also, resulting in a step size $d \to 0$. The dependence of d on $\hbar_\epsilon$ is found to be $d \sim \hbar_\epsilon^\sigma / f(K_\epsilon)$, where the inverse dependence on some function of the control parameter K_ϵ is due to the step size decreasing as the diffusion rate through trapping regions increases, which in Chapter 6 was found to be $D \propto K_\epsilon^3$ for $K_\epsilon \lesssim 3$. The above means that the localisation length of the staircase depends on the scaled Planck constant as:

$$L_p = \frac{2\pi}{d\epsilon} \sim \frac{2\pi}{\hbar^\sigma \epsilon^{\sigma+1}} \tag{7.10}$$

It was seen in Chapter 3 that the QKR localisation length is $L \simeq 2D/\hbar$, hence the dependence on the scaled Planck constant is $L \propto \hbar^{-1}$. For the quantum double kicked rotor however two different fractional exponents were found for the scaling with $\hbar$ [50], namely $\sigma \simeq 0.65$ for small $\hbar_\epsilon$ and $\sigma \simeq 1$ for larger $\hbar_\epsilon$ values.

The $\hbar^{0.65}$ scaling is shown in Fig.7.5. Series of momentum distributions for $K_\epsilon = 0.4$ and $\tau/\epsilon = 49$ have been rescaled by the above factor, i.e. $\ln(N(p))/\hbar^{0.65}$ is shown,

shifted by an appropriate constant. It can be seen that there is almost no difference in the scaled distributions between $\hbar_\epsilon = 1/2500$ and $\hbar_\epsilon = 1/250$, i.e. the scaling is valid across this entire parameter range. For larger values of $\hbar_\epsilon = 1/25$ however, the scaling starts to change to $\sim \hbar$ for the long range localisation of the staircase.

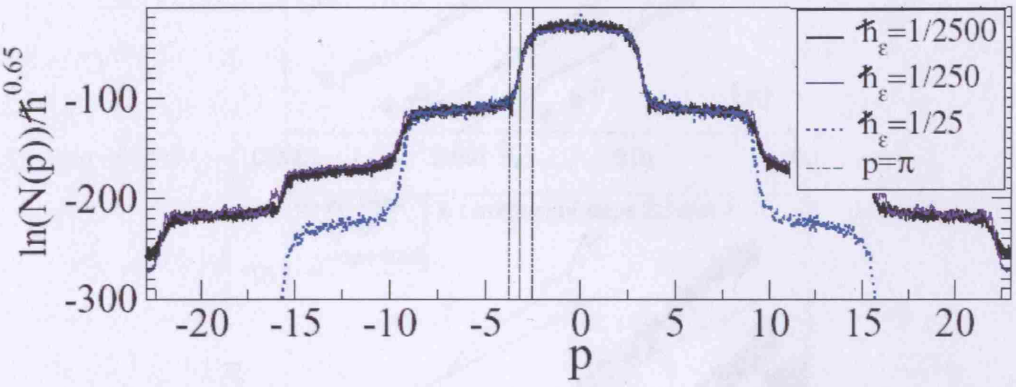

Figure 7.5: Momentum distributions for $K_\epsilon = 0.4$ and $\tau/\epsilon = 49$ rescaled by a factor $\hbar^{0.65}$, for three different values of $\hbar$ as shown. There is almost no difference between the rescaled distributions for $\hbar = 1/2500$ and $\hbar = 1/250$, however for larger values of $\hbar = 1/25$, the scaling is no longer valid for the outer steps. For the central step however the scaling holds across the entire range of $\hbar$, showing that the localisation properties of the trapping regions behave as $\sim \hbar^{0.65}$. Note that the drop in probability across the first trapping region (denoted by the vertical lines) is larger than for the other steps. Courtesy of Tania Monteiro.

These results are confirmed in the bottom panel of Fig.7.6. For several different values of K_ϵ the quantity $2d$ is plotted against $\hbar_\epsilon$. The $K_\epsilon = 0.4$ curve corresponds to the distributions in Fig.7.5. An average of the measurements of $2d$ from the second, third and fourth steps of the distributions is taken, i.e. neglecting the probability drop either side of the central cell, which is larger than the ones further out. The results shown here are in fact mainly derived from the quantum version of the random-pair-kicked rotor introduced in Chapter 5, for which the limit $\tau \to \infty$ is taken. This limit will be seen to be relevant to the origin of the fractional scaling with $\hbar$ in the 2δ-QKR, but the actual scaling is the same as for lower values of τ used here. For lower values of $\hbar_\epsilon$ the results in all cases lie on near straight lines of slope 0.65, whereas with increasing $\hbar_\epsilon$ this slope increases to nearer the aforementioned value of unity.

The top panel shows the same scaling of $2d$ with $\hbar_\epsilon$, but this time taken only from the first steps either side of the central cell in which the atoms start. This defines a local scaling specific to the trapping regions, since the subsequent steps in the distribution

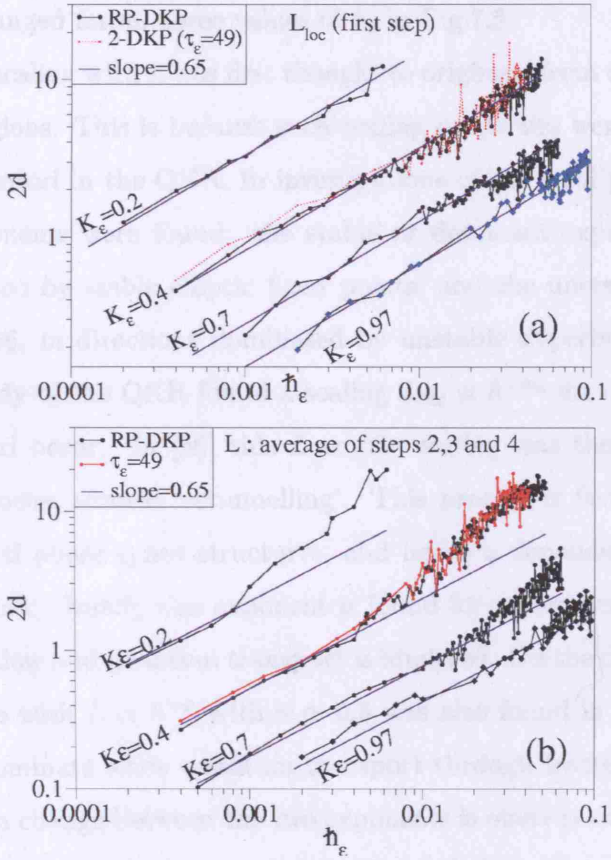

Figure 7.6: Scaling of the step height $2d$ of the double kicked momentum distributions with $\hbar_\epsilon$ for various values of K_ϵ. The results for $K_\epsilon = 0.4$ correspond to the distributions shown in Fig.7.5. The top panel (a) shows the scaling of the first step only, i.e. the step height either side of the central diffusion cell. This reveals the scaling of the localisation properties local to trapping regions, which is found to be $L_{loc} \propto \hbar^{0.65}$ for almost the entire $\hbar_\epsilon$ range and all values of K_ϵ. The bottom panel (b) shows the average scaling of the other steps in the distribution; this corresponds to the scaling of the long range localisation length of the entire staircase. This also scales as $L \propto \hbar^{0.65}$ for low $\hbar_\epsilon$, but for large values of the quantum control parameter a scaling exponent nearer unity is observed. The results are obtained both from the usual double kicked rotor with $\tau/\epsilon = 49$ and from the random-pair-kicked rotor (particle) (RP-DKP) in the limit $\tau \to \infty$, where the quantum phases in between pairs of kicks are randomised. There is good agreement between the two sets of results. Courtesy of Tania Monteiro.

represent later times in the system evolution, when atoms have spread over several cells. Hence, while the bottom panel shows the scaling properties of the entire localised distribution across many cells, the top panel shows the local scaling properties of diffusion across the trapping regions. It is seen that in the latter case the 0.65 scaling persists for nearly the entire range of $\hbar_\epsilon$ shown, which is also confirmed by the fact that the first

step remains unchanged for all three values of $\hbar_\epsilon$ in Fig.7.5.

The fractional scaling with $\hbar$ was first thought to originate from the cantori remnants in the trapping regions. This is because such scaling properties were found locally near the golden ratio cantori in the QKR. In investigations of the local phase space [52] two characteristic exponents were found: the stable or dominant exponent $\sigma_s \simeq 0.75$, in directions dominated by stable elliptic fixed points, and the unstable or subdominant exponent $\sigma_u \simeq 0.66$, in directions dominated by unstable hyperbolic fixed points. In [55] a previous study of the QKR found a scaling $L_{loc} \propto \hbar^{+\sigma_u}$ for momenta near where golden ratio cantori occur. In [56] this $L \propto \hbar^{\sigma_u}$ scaling was then associated with a tunnelling type process termed 'retunnelling'. This process is favoured near unstable points in the fractal phase space structures, and hence a dependence on the unstable exponent σ_u is found. Usually this exponent is found for parameters where momentum diffusion is rather slow and quantum transport is hindered. On the other hand an abrupt change to a regime with $L \propto \hbar^{-\sigma}$ with $\sigma \simeq 0.5$ was also found in [56], for localisation processes which dominate when quantum transport through fractal cantoral regions is increased. The sign change between the two exponents is obvious since both the amount of localisation and tunnelling increase with $\hbar$. Hence L depends inversely on the scaled Planck constant for dynamical localisation, but the opposite behaviour is seen for the quantum effect of tunnelling. Significant scaling with the dominant exponent $\sigma_s \simeq 0.75$ has on the other hand not previously been discovered in the QKR or similar systems.

It should be noted that the σ_u scaling described above applies only to local regions of the QKR, where many stable phase space structures exist and diffusion through these is slow. In the quantum double kicked rotor however the fractional scaling with $\hbar$ can apply to the global localisation length of the entire momentum distribution across phase space. This suggests that localisation is heavily influenced by the trapping regions; indeed the local momentum distribution across one diffusion cell becomes uniform once several cells are spanned (for very low diffusion exponentially localised distributions within one cell can occur). On the other hand the exponent $\simeq 1$ dominates for the long range localisation properties of the entire momentum distribution for large $\hbar_\epsilon$, where local properties of trapping regions appear to be less important.

Although the golden ratio cantori in the QKR and the cantori remnants in the trapping regions of the double kicked rotor can be considered phenomenologically similar, the fractional scaling in the 2δ-QKR is likely to have a different origin. The reason is

that in Chapter 5 it was seen that the trapping regions can exist independently of any fractal structures in the large τ and hence random phase limit. As $\tau \to \infty$ the positions of particles change randomly in between kick pairs in modulo 2π. This was found to correspond to the non-KAM limit, so any scaling properties derived from typical KAM related structures, such as the stable and unstable exponents near golden ratio cantori, are not expected to be found in this limit.

The random-pair-kicked rotor can also be implemented in the 2δ-QKR by replacing $l^2\hbar_\tau/2$ in the free propagator in Eq.7.2 by a momentum dependent random phase $\phi_\zeta(l)$:

$$\hat{U}_\tau = e^{-i\phi_\zeta(l)} \tag{7.11}$$

In other words a random phase in the interval $[0, 2\pi]$ is chosen for each momentum state l separately. It is found that this randomisation of the free evolution phase does not change the behaviour of the 2δ-QKR much, as shown in Fig.7.7. The staircase structure remains almost unchanged for variation of $\tau/\epsilon \gg 1$, and also for the implementation of a random phase in the free propagator. Hence the trapping mechanism is also not affected greatly. Thus the quantum double kicked rotor is largely insensitive to the parameter $\hbar_\tau$ as mentioned previously. This is in analogy to the insensitivity of the classical double kicked rotor to τ. The case of choosing a different random phase after each kick pair, i.e. a time-dependent phase $\phi_\zeta(l,t)$, analogous to the non-periodic classical random τ case, is more difficult to implement in the quantum random-pair-kicked rotor, since the Floquet operator $\hat{U}^F$ describes a periodically recurring system evolution. Altering the period of free evolution between kick pairs affects the Floquet states of the system, and hence localisation properties.

These results show that both the characteristic double kick trapping mechanism in momentum space, and hence the fractional scaling with $\hbar$ of the localisation length of the staircase in the momentum distribution, persist for non-KAM regimes where no stable structures remain in the trapping regions of the corresponding classical phase spaces. This was also shown by the results for the random-pair-kicked rotor in Fig.7.6, which were near equivalent to those for $\tau/\epsilon = 49$.

The persistence of the fractional scaling into the non-KAM regime, where no regular structures remain in the trapping regions, has prompted an alternative explanation for the 0.65 exponent observed in the 2δ-QKR [57], derived from the properties of the quantum evolution operator, rather than any properties of classical phase space structures. If one looks at the form of the evolution operator in Eq.7.7, $U_{lm} \simeq \exp(-i\phi)J_{l-m}(x)$,

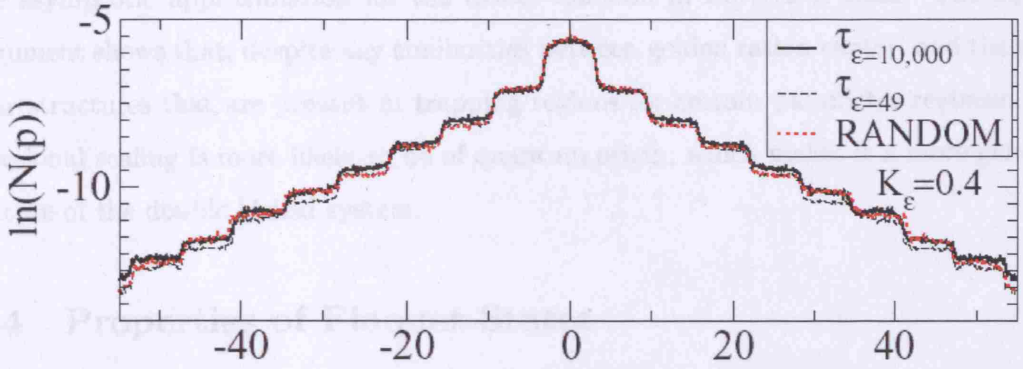

Figure 7.7: Comparison of momentum distributions for $\tau/\epsilon = 49$ and 10000, and for the case of randomised quantum phases corresponding to the random-pair-kicked rotor. The distributions are almost the same irrespective of the value of τ and hence the quantum phase in the free propagator in between kick pairs.

which describes the oscillating band matrix in Fig.7.1 with a half-bandwidth of $b = x = 2K/\hbar\cos(p\epsilon/2)$, then it was seen earlier that the matrix elements are zero for $|l-m| \gtrsim x$, since $J_{l-m} \to 0$ in this limit. For there to be a significant probability of a momentum change $\Delta p = |l-m|\hbar$ the condition $|l-m| \lesssim x$ has to be fulfilled. For sizeable K and small $\hbar$, as used for the investigations on the scaling properties, $|l-m|$ can however be fairly large. Thus, in the limit $|l-m| \gg 1$, an asymptotic approximation for the Bessel function can be used:

$$J_{l-m} \sim \frac{2^{1/3}}{|l-m|^{1/3}} Ai(-2^{1/3}z) \tag{7.12}$$

with Ai being an Airy function and $x = |l-m| + (z/|l-m|^{1/3})$. The transition probability for the momentum change Δp above is $|U|^2$, so is hence proportional to $|l-m|^{-2/3} = (\hbar/\Delta p)^{2/3}$. The local diffusion coefficient for the double kicked rotor D is also proportional to $|U|^2$ and hence to $\hbar^{2/3}$. For the QKR, where the bandwidth of the evolution matrix is constant, the localisation length was found to be $L \simeq 2D/\hbar$. This would imply a scaling $L \propto \hbar^{-1/3}$. For the double kicked rotor however the bandwidth oscillates with momentum, so this effect has to be taken into account as well. From the argument of the Airy function in Eq.7.12 it can be seen that $z = |l-m|^{1/3}(x-|l-m|)$. This shows that the half-bandwidth $b = x$ scales with $|l-m|^{1/3} = (\Delta p/\hbar)^{1/3}$, so the localisation length is multiplied by this factor to give $L \sim \hbar^{-2/3}$. This corresponds to the scaling of the localisation lengths in the double kicked rotor with the exponent 0.65 seen for small $\hbar$. The result is valid in the regime $\hbar/(2K) \ll \cos(l\hbar/2) \ll 1$, for which

the asymptotic approximation for the Bessel function in Eq.7.12 is valid. The above argument shows that, despite any similarities between golden ration cantori and the regular structures that are present in trapping regions for certain parameter regimes, the fractional scaling is more likely to be of quantum origin, which makes it a more generic feature of the double kicked system.

7.4 Properties of Floquet States

Having investigated the Floquet states of the QKR in Chapter 3, and those of the PPKR and ratchet systems in Chapter 4, which all showed signatures of the same effects found in the overall momentum distributions, it is not surprising that the Floquet states of the 2δ-QKR have the same structure as the momentum distributions in Fig.7.4. Indeed the characteristic staircase structure and localisation of the momentum distributions arise from the individual properties of the Floquet states of the system [58]. Fig.7.8 shows examples of states for different values of K and $\langle p \rangle$, calculated from the cylindrical system representation in Eq.7.2, hence momentum is unbounded. In all cases $\epsilon = 0.025$ and $\hbar = 0.5$ leading to $\hbar_\epsilon = 0.0125$. A small linear term $\pm Ax$ with $A = 0.01\pi$ was added to the kick potential for this calculation, in order to desymmetrise the eigenstates in momentum space and remove any accidental degeneracies. This additional term makes no significant difference to the results. It must also be remembered that the Floquet states are calculated for the periodic time interval $\epsilon + \tau$ in the double kicked rotor. In between two kicks of a pair the states can change dramatically, since the first kick results in a large spread in momentum. This is in contrast to the QKR case where the Floquet states vary only slightly with time within the repeating time intervals.

In panel (a) the kick strength $K = 1$ is very low resulting in $K_\epsilon = 0.025$. In Chapter 5 it was found that this corresponds to a classical regime where phase space is mixed, with some larger islands remaining, although chaotic diffusion covers large areas. For such low values of K_ϵ localisation lengths are small, and quantum wavepackets do not spread much in momentum space. Nevertheless signatures of the trapping mechanism can still be seen even in this regime. States centred on $p \simeq \pm\pi/\epsilon \simeq \pm 125$ are very sharply localised over a small momentum range, clearly defining the trapping regions (which can exist even in a mixed phase space, provided regular structures do not cover too much of it). The localisation lengths for these states are so low that they are effectively pure plane wave states, hence almost no evolution of the initial state takes place in the

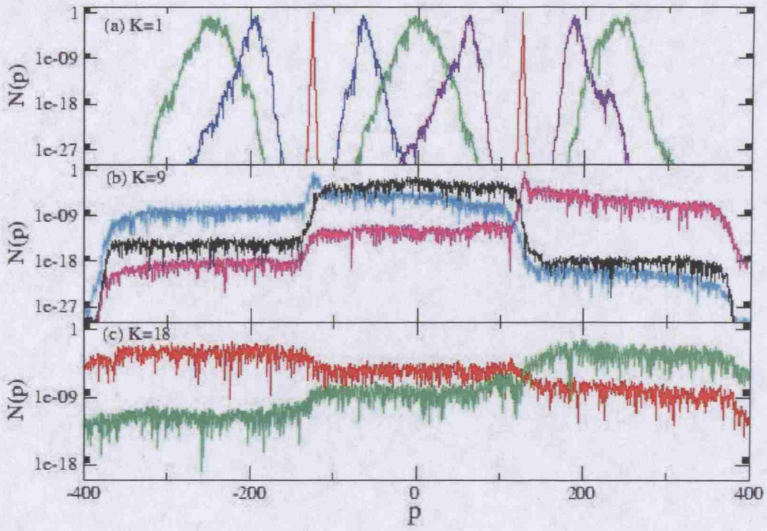

Figure 7.8: Floquet states for the quantum double kicked rotor in a basis of angular momentum states. Parameters are $\epsilon = 0.025$ and $\hbar = 0.5$. For $K = 1$ ($K_\epsilon = 0.025$) the kick strength is so low that states localise within single diffusion cells or trapping regions. The states nearest the centre of the cells are spread out much more in momentum than the highly localised trapped states. Note however the logarithmic intensity scale and hence the very low probabilities for the edges of the distributions. Localisation lengths are seen in Fig.7.9 to be very small in this case. States centred on momenta in between the centre of a cell and a trapping region are asymmetric, with extended probability towards the centre of the cell. This generates quantum currents. For $K = 9$ ($K_\epsilon = 0.225$) states are localised over the entire central cell and are starting to spread into neighbouring diffusion cells. For $K = 18$ ($K_\epsilon = 0.45$) the states are delocalised over several cells, and full staircases equivalent to the momentum distributions in Fig.7.4 are seen. Courtesy of Gwangok Hur.

trapping region. States centred on $p = 0$ or $p \simeq \pm 2\pi/\epsilon \simeq \pm 250$ on the other hand have much larger localisation lengths and cover a much broader range of momenta, in relation to trapped states. Note the overall low probabilities on the logarithmic intensity scale for the edges of distributions however. States localised in between these momentum values are extended in momentum towards the centre of each diffusion cell, but strongly localised towards the trapping regions, where there is little spreading of wavepackets. This is of course similar to the case of the Floquet states of the rocking ratchet in Fig.4.6, where states are extended either towards positive or negative momenta and localised in the other direction. In the double kicked rotor however the asymmetries are caused by the existence of the trapping regions and reverse on either side of the centre of a

diffusion cell. The asymmetry of course also means that a (small) quantum current can be generated by starting a wavepacket near a trapping region, however the effect is only observed clearly over one diffusion cell.

For the QKR it was found that $L \simeq K^2/(4\hbar) = b^2\hbar/4$,where $b = K/\hbar$ is the half-bandwidth of the band diagonal evolution matrix in Fig.3.1. This is valid for both the localisation of the overall momentum distribution and the individual Floquet states of the QKR. Correspondingly one can define a local momentum dependent localisation length for the momentum distribution and eigenstates of the 2δ-QKR [53]:

$$L(p) = \frac{b^2(p)\hbar}{4} = \frac{K^2}{\hbar}\cos^2(\frac{p^\epsilon}{2}) \tag{7.13}$$

where the result $b(p) = (2K/\hbar)\cos(p^\epsilon/2)$ was obtained earlier in Eq.7.7. This expression for the localisation length is valid in the limit $2K/\hbar \ll N$, i.e. when the maximum half-bandwidth is small compared to the cell dimension N. This corresponds to the limit of states localising within a single diffusion cell or trapping region. The oscillations of localisation lengths with the central momentum value of the corresponding Floquet states is clearly seen in Fig.7.8a.

Although the low K_ϵ regime results in all states localised within one cell or trapping region and thus prevents quantum transport, it displays perhaps the clearest signs of the underlying diffusion mechanism of the 2δ-QKR, with fast and slow diffusion areas of momentum space easily identifiable. The small localisation lengths of course mean that states near the centres of cells are localised symmetrically without any additional features, as in the QKR. As K_ϵ increases in panels (b) and (c), quantum transport is enabled, and eigenstates spread over several diffusion cells. Here the usual staircase structure is observed, with steep drops in probability amplitudes at the trapping regions (note that these are in the same location for all three panels since ϵ is unchanged). In panel (b) the control parameter is $K_\epsilon = 0.225$, and in panel (c) it is $K_\epsilon = 0.45$. Both values correspond to the regime where the trapping mechanism is clearly visible in the 2δ-QKR, but transport of atoms through the trapping regions is possible. Essentially Floquet states are now delocalised over several cells; pure exponential localisation as in panel (a) no longer occurs. This again shows the importance of localisation effects due to trapping regions for the overall localisation of the staircase in the momentum distribution. As K_ϵ and hence D, the classical diffusion rate, increase, so does the quantum transport (since d, the step size, depends inversely on K_ϵ), and eventually the trapping regions disappear, as well as the staircase structure of the Floquet states and

momentum distributions. In this limit the usual featureless exponential localisation is observed again.

The localisation lengths of the Floquet states are calculated from the variance $L_\sigma = \sqrt{\langle p^2 \rangle - \langle p \rangle^2}$ as already mentioned in Chapter 3. As expected the variance L_σ is not necessarily equal to the localisation length of the long-range staircase structure L_p in the 2δ-QKR. For the QKR with featureless exponential distributions, one finds $L_\sigma = L_p$ in all cases, i.e. the momentum variance is equal to the range of momenta over which the Floquet states are localised. Localisation lengths of Floquet states in the quantum double kicked rotor may of course also vary greatly depending on their central momentum value $\langle p \rangle$, as is seen in Fig.7.8, panel (a) in particular. Fig.7.9 shows the localisation lengths L_σ of states for the same parameters as in Fig.7.8. It is seen that L can vary by up to

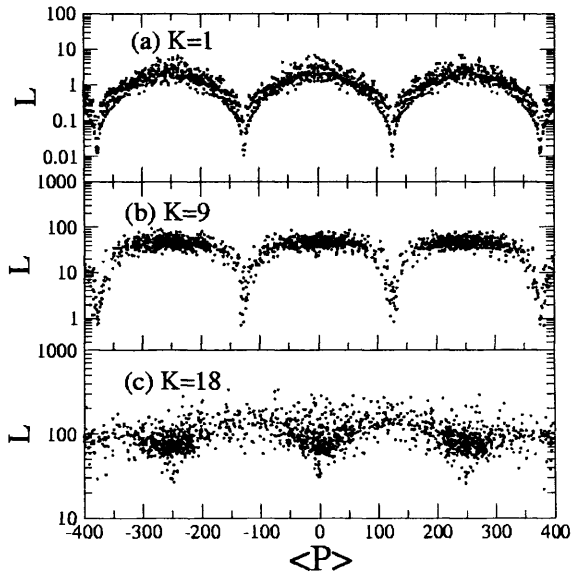

Figure 7.9: Localisation lengths L of the Floquet states of the quantum double kicked rotor for the same parameters ($\epsilon = 0.025$ and $\hbar = 0.5$) as in Fig.7.8. Each dot represents one eigenstate. In (a) the kick strength is very low and correspondingly so are the localisation lengths. States are entirely localised within one cell or trapping region. The latter are clearly denoted by extremely low L. In (b) localisation lengths increase but states centred on trapping regions still have lower L. For large kick strengths in (c) it is seen that the localisation lengths of states centred on trapping regions are in fact slightly larger than for states centred on diffusion cells. This is because states are now essentially delocalised over a few cells in momentum space, and those starting in a trapping region have spread further after the initial trapping. This behaviour corresponds to the spreading of classical particle ensembles in Fig.5.5. Courtesy of Gwangok Hur.

three orders of magnitude for low K and hence K_ϵ. In (a) the Floquet states localised in the trapping regions have extremely low L, as mentioned previously for Fig.7.8a. In comparison states centred on large stable islands in mixed phase space usually have $L \simeq 1$, whereas these trapped states have $L \simeq 0.01$. The overlaps with other states are vanishingly small, hence Floquet states in trapping regions localise essentially in the form of the initial plane wave state. States localised near the centres of diffusion cells on the other hand have $L \simeq 1$. Localisation lengths follow roughly the relationship in Eq.7.13. Note that states are entirely localised within one single diffusion cell or trapping region, as shown in Fig.7.8a. In (b) the trapping regions are still denoted clearly by much smaller localisation lengths than for states centred on momenta well away from cell boundaries. For $K = 9$ ($K_\epsilon = 0.225$) states are generally localised over an entire diffusion cell or starting to spread into neighbouring cells, hence localisation lengths are nearly the same for all states except those centred on the trapping regions. The variation in L here is still two orders of magnitude.

Finally for the last case in (c) one finds much less variation in L. Localisation lengths are roughly given by $L_p = 2\pi/(d\epsilon)$ from Eq.7.10. States centred on trapping regions actually have slightly greater localisation lengths than other states, with the lowest L now occurring for states centred in the middle of diffusion cells. For high kicking strengths and larger K_ϵ the system evolves much quicker, and hence quantum wavepackets spread over several cells before localisation occurs. This results in the same effect as in Fig.5.5, where states started in a trapping region gain more energy after a given time than those started near the centre of a diffusion cell, thus L is greater for the former. This effect is only seen if the system evolves long enough for wavepackets to fill several cells before the quantum break time. In (a) and (b) system evolution is slower, and states fill either only a single cell or in addition the neighbouring cells (as shown in Fig.7.8).

As for the ratchet systems in Chapter 4, the break time in the 2δ-QKR depends on the average momentum of quantum states, since $t^*(p) \sim L/\hbar \simeq D(p)/\hbar^2$, where $D(p)$ is the momentum dependent diffusion rate. Hence one can define a local break time for states with different $\langle p \rangle$ as for the PPKR. The break time can be calculated from the mean energy level spacing Δ of the Floquet quasienergies [59]: $t^* \simeq 2\pi\hbar/\Delta$, where $\Delta = \pi/N$ and N is the number of eigenstates which overlap with the initial coherent wavepacket with an overlap coefficient of $|C_n|^2 = |\langle \psi_n | \Phi \rangle|^2 \geq 0.05$. The quasienergies

are calculated in modulus π, hence the energy level spacing is given as above. Some further comments on energy level spacings and statistics are given at the end of this chapter.

Fig.7.10 shows the calculated momentum dependent quantum break time in comparison to $L(p)$ for $K = 3.4$, $\epsilon = 0.06$, $\hbar = 1$ and an additional small linear term $\pm Ax$ in the potential with $A = 0.01\pi$ for desymmetrisation purposes as mentioned earlier. Control parameters are $K_\epsilon = 0.204$ and $\hbar_\epsilon = 0.06$. Note that time is counted in number

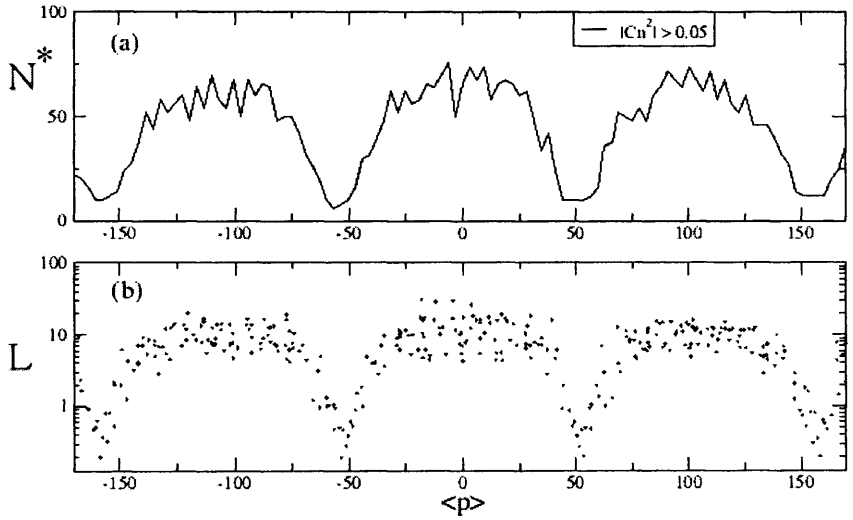

Figure 7.10: Behaviour of local break time vs. initial momentum of states, in comparison to variation of localisation lengths of Floquet states with momentum. Parameters are $K = 3.4$, $\epsilon = 0.06$ and $\hbar = 1$, leading to $K_\epsilon = 0.204$ and $\hbar_\epsilon = 0.06$. Note that time is counted in number of single kicks N here, so the break time t^* in terms of pairs of kicks is halved. As predicted by $t^* \sim L$ (for $\hbar = 1$), the break times show the same variation with $\langle p \rangle$ as the localisation lengths. States centred on trapping regions localise very rapidly ($N^* \simeq 10$) and thus have small L, while states near the centres of diffusion cells take much longer to localise ($N^* \simeq 60$) and hence spread further in momentum. Courtesy of Gwangok Hur.

of single kicks, hence $t^* = N^*/2$; the break time shown here is halved if calculated in terms of kick pairs. The break time mimics the behaviour of the localisation lengths with $\langle p \rangle$ very closely as expected. States centred on trapping regions localise after a few kick pairs and thus have a very small spread in momentum. In contrast localisation occurs much later ($N^* \simeq 60$) for states centred on momenta away from the trapping regions. The parameter values here are comparable to those in the cold atom experiment in Fig.7.3, hence it is reasonable to take $t^* = N^*/2 \simeq 30$ for most initial momenta in

the experiment, with the break time being significantly lower for atoms in the trapping regions. Note that the same correspondence between the local break time and variation of localisation lengths with momentum is also found for the PPKR and rocking ratchet as shown in [58].

From the Floquet states of the 2δ-QKR it can be seen that the process of dynamical localisation occurs somewhat differently in the double kicked rotor system than in the QKR. DL is mainly caused by the existence of trapping regions between diffusion cells, except in regimes of low K_ϵ where usual exponential localisation within one cell occurs, as in the kicked rotor. Even in the latter case however, asymmetries in the localisation profiles are observed due to nearby trapping regions. As K_ϵ is increased states become localised over several cells. For cylindrical boundary conditions (i.e. unbounded momentum space) this can be interpreted as a delocalisation of states (or the entire rotor distribution) from one cell to several, although technically DL is still present of course, albeit in an altered form with the staircase structure superposed. In the case of toroidal boundary conditions, described in the next section, with a periodic momentum space, essentially only one diffusion cell is considered, so in this case delocalisation of states beyond this cell is not directly observed.

A final interesting property of the 2δ-QKR related to its Floquet states is tunnelling between trapped momentum states of opposite sign. As for the QKR, states in the double kicked rotor exist as symmetric or antisymmetric combinations of plane waves:

$$\psi_l^{\pm} = \frac{1}{\sqrt{2}}(|l\rangle \pm |-l\rangle) \tag{7.14}$$

where $|\pm l\rangle = (1/\sqrt{2\pi})\exp(\pm ilx)$ as usual (except for $l = 0$ where $\psi_0^+ = \sqrt{2}|0\rangle$), and here again states couple only with states of the same symmetry, i.e. $\langle\psi_n^{\pm}|\hat{U}^F|\psi_l^{\mp}\rangle = 0$ (cf. Eqs.3.25 and 3.26). Oscillations of the form $\cos(E^+ - E^-)t$, where $E^{\pm}$ are the energies associated with the $|\pm l\rangle$ states, can be observed due to tunnelling effects. These oscillations are found to be greatly enhanced by the quantum chaos present for $K_\epsilon \gtrsim 0.075$.

7.5 Momentum Periodicity

It was seen that the QKR can be considered in a torus representation with periodic momentum boundary conditions $N\hbar_T = 2M\pi$, with M being an integer noncommensurate with the matrix dimension N to avoid quantum resonances. For the QKR there is no

preferred choice for M and N, however the quantum double kicked rotor can be made periodic in momentum with a natural choice of N, since momentum space is divided into cells of fast energy diffusion. One can choose $\hbar_\epsilon = 2\pi/N$, which partitions the matrix in Fig.7.1 into submatrices of dimension $N = 2\pi/\hbar_\epsilon$ as shown. Remembering that the trapping regions at the cell boundaries are $2\pi/\epsilon$ apart in momentum space, the resultant periodicity on the torus is $p + N\hbar = p + (2\pi/\epsilon) = p$. Essentially the bounded torus represents a single diffusion cell of the quantum double kicked rotor.

The toroidal representation is very useful for finding the eigenstates and eigenvalues of the Floquet operator $\hat{U}^F$, since only one submatrix needs to be diagonalised. For this purpose one can choose additionally $\hbar_\tau = M\hbar_\epsilon = 2\pi M/N$, where M is the closest integer to τ/ϵ but noncommensurate with N, again to avoid quantum resonances. This is the same condition for momentum periodicity as for the QKR above. A unitary matrix of dimension N can now be constructed, following the approach in [20],[22]. The two momentum transitions $|l\rangle \rightarrow |k\rangle$ and $|k\rangle \rightarrow |m\rangle$ can be expressed as separate matrices and combined at the end. In each case the momentum can be written as $l = n + aN$ where $1 \leq n \leq N$ and $-\infty < a < \infty$, and similarly for k and m. The momentum periodicity is $n + aN = n$, remembering that $p = l\hbar$.

The following expression from Bloch theory is used to convert the potentially infinite dimensional matrix $U_{lm} = U_{n+aN,n'+a'N}$ into a $N \times N$ matrix $U_{nn'}$:

$$U_{nn'}(T_i, \theta) = \sum_a e^{-i\theta a} U_{n,n'+aN}(T_i) \tag{7.15}$$

where $0 \leq \theta \leq 2\pi$ is the analogue of the wavevector or quasimomentum in a Bloch wave (cf. Eq.3.5). Note that since the present equation is for momentum periodicity θ is in fact a Bloch phase in the p direction, while the quasimomentum q in Eq.3.5 is a Bloch phase in the x direction. Both phases will however be used in the toroidal representation of the double kicked rotor, as will be seen below.

For the transition $n \rightarrow n' + aN$ in one of the two separate evolution matrices $\langle m|\hat{U}|k\rangle$ or $\langle k|\hat{U}|l\rangle$, and using the operators given in Eq.7.1 one obtains:

$$U_{nn'}(T_i, \theta) = \frac{1}{2\pi} e^{-\frac{in^2\hbar T_i}{2}} \int_0^{2\pi} e^{-i\frac{K}{\hbar}\cos x} e^{i(n-n')x} \sum_{a=-\infty}^{\infty} e^{-ia(\theta+Nx)} dx \tag{7.16}$$

where $T_1 = \tau$ and $T_2 = \epsilon$. It should be noted that this expression is of course also valid for $T_i = T = 1$ which leads to the toroidal representation of the QKR. Using the

following identity:

$$\sum_{a=-\infty}^{\infty} e^{i2\pi a\beta} = \sum_{j=-\infty}^{\infty} \delta(\beta - j) \tag{7.17}$$

with $\beta = -(\theta + Nx)/(2\pi)$ and substituting $x = -(2\pi j + \theta)/N$ into Eq.7.16, the matrix can be written as:

$$U_{nn'}(T_i, \theta) = e^{-\frac{in^2\hbar T_i}{2}} e^{-i\frac{(n-n')\theta}{N}} \frac{1}{N} \sum_{j=1}^{N} e^{-i\frac{K}{\hbar}\cos(\frac{2\pi j+\theta}{N})} e^{-i\frac{2\pi j(n-n')}{N}} \tag{7.18}$$

where the 2π-periodic integral has been replaced by a finite sum over N equally spaced points on a circle on a Bloch sphere, with a $2\pi/N$ spacing. Additionally to the Bloch phase θ in Eq.7.18, a quasimomentum can be introduced to result in two Bloch phases, one in the p direction, $\theta \rightarrow \theta_p$, and one in the x direction, $q \rightarrow \theta_x$. This leads to:

$$U_{nn'}(T_i, \theta_x, \theta_p) = e^{-\frac{i(n+\theta_x)^2\hbar T_i}{2}} \frac{1}{N} \sum_{j=-N_1}^{N_1} e^{-i\frac{K}{\hbar}\cos(\frac{2\pi j+\theta_p}{N})} e^{-i\frac{(n-n')(2\pi j+\theta_p)}{N}} \tag{7.19}$$

where $N_1 = (N-1)/2$ to give a symmetric distribution of N points. Eq.7.19 with $T_i = T = 1$ is the toroidal representation of the QKR, while for the quantum double kicked rotor the full matrix for a pair of kicks is simply:

$$U^{2\delta}_{nn'} = U_{nn'}(\epsilon) U_{nn'}(\tau) \tag{7.20}$$

The matrix in Eq.7.20 can be diagonalised to obtain N eigenvalues and eigenstates (as for the finite sized QKR matrix). To remove parity conservation effects one can choose $\theta_p \neq 0, \pi$ and $\theta_x \neq 0, 0.5$, in which case parity is not a good quantum number. This means all eigenvalues can be used in the statistics of $U^{2\delta}$ regardless of parity. One may also average over several values of θ_p and θ_x when calculating spectral statistics of the system. A brief summary of novel statistics in the double kicked system will be given in the next section.

For both cases of boundary conditions on momentum a 'filling factor' R can be introduced [53] to characterise the spread of momentum distributions or eigenstates in relation to the dimensions of a diffusion cell. The filling factor essentially represents the ratio of the localisation length to the cell dimension N. The same factor also exists for the QKR for the case of a finite N-dimensional evolution matrix, where $R \simeq L/(N\hbar)$ for a momentum periodicity of $\Delta p = N\hbar$. For the double kicked rotor one can define the filling factor as:

$$R = \frac{K^2}{N\hbar^2} = \frac{K_\epsilon^2}{2\pi\hbar_\epsilon} \tag{7.21}$$

where $L_{max} = K^2/\hbar$ from Eq.7.13 (as opposed to the long range localisation length of the staircase over several cells in Eq.7.10) and $N = 2\pi/\hbar_\epsilon$. An important property of the double kicked rotor is that the degree of filling of one cell characterised by R can be varied independently from the quantum transport between cells characterised by d. The latter depends on the permeability of the trapping regions at the cell boundaries. The form of the map in Eq.5.8 dominates for transport through the barriers, and depending on the values of the control parameters K_ϵ and $\hbar_\epsilon$ both R and d can be varied independently. For $R < 1$ states are localised within one cell as shown in Fig.7.8a. Using the toroidal momentum-periodic boundary conditions the degree of filling of the one-cell $N \times N$ matrix can be investigated. It should be noted however that in the toroidal case, or if there is no transport between diffusion cells, the localisation lengths remains as $L \simeq N\hbar = 2\pi/\epsilon$ even if $R > 1$. Thus a filling factor greater than unity does not necessarily represent a spreading of states across several cells, unless an unbounded momentum space is used and there is significant coupling between cells ($d < 2$), i.e. the quantum control parameters are such that transport through trapping regions is possible.

7.6 Energy Levels and Spectral Statistics

To end this chapter some brief remarks on the energy level spacings and statistics of the 2δ-QKR will be given. Full details of these investigations can be found in [53]. Here only a summary of the most important results is presented.

In Chapter 1 the energy level behaviour for quantum chaotic systems was introduced. Quantum systems that correspond to classically integrable motion show uncorrelated level behaviour with Poisson statistics and level crossings. The spacing of nearest neighbour levels is typically exponential, i.e. $P(s) = \exp(-s)$. Chaotic systems on the other hand show level repulsion of linear, quadratic or quartic degrees, i.e. $P(s) \propto s^\beta$ for $s \to 0$ and $\beta = 1, 2, 4$. These three classes correspond to the Gaussian orthogonal, unitary and symplectic ensembles respectively (GOE, GUE, GSE). The Brody and Berry-Robnik distributions for mixed classical phase spaces were also introduced, which reduce to the Poisson and Wigner (GOE) distributions in the limiting cases.

In the case of the QKR, statistics correspond to Band Random Matrix Theory as mentioned in Chapter 3, and dynamical localisation results in the limit $b \ll N$ being Poissonian, where b is the half-bandwidth of the evolution matrix and N its dimensionality. This also corresponds to the $R \ll 1$ limit in terms of the filling factor. Eigenstates

centred on momenta further apart than the localisation length are uncorrelated, and hence level repulsion does not occur. In the limit $b \to N$ or $R \to 1$ however, a transition to GOE behaviour is observed.

Investigations of the spectral statistics for the 2δ-QKR found that both the one-cell localisation limit ($d > 2$ and $R < 1$), where states are strongly localised within part of one diffusion cell as in Fig.7.8a, and the delocalisation limit ($d < 2$ and $R \gg 1$), where states spread over many diffusion cells, show Poissonian statistics with uncorrelated eigenvalues. In the case of toroidal boundary conditions however, delocalisation does not occur since only one cell is being investigated, so for $R \gg 1$ and $d < 2$ the statistics instead tend towards the GOE form with level repulsion. For $d > 2$ on the other hand boundary conditions do not have a significant impact on the statistical behaviour. Nearest neighbour level spacing distributions can be found in [53] and show the Poissonian and GOE limits. It should be noted that the same transition from Poisson to GOE statistics for periodic boundary conditions on the momentum variable occurs in the QKR, however while the transition in this case is a fairly rapid one, in the 2δ-QKR the transition is much slower with increasing R.

The regime $R \simeq 1$, where states fill approximately one diffusion cell, is found to display intermediate statistical behaviour for both types of boundary conditions. Near linear variances are found of the form:

$$\Sigma_2(l) = \langle (n - \langle n \rangle)^2 \rangle \simeq \chi l \tag{7.22}$$

where, as mentioned in Chapter 1, n is the number of levels contained in an energy interval of length l, and the above result is valid for large l. The slope was found to be $\chi \simeq 0.125$. A connection was suggested to the near linear variances observed for critical statistics, found for example in relation to the Metal Insulator Transition (MIT) in disordered metals, as well as other systems. In that case the slope $\chi \simeq (1 - D_2/d_s)/2$ is related to the fractal dimension D_2 obtained from the second moment of the wavefunction and to the spatial dimension of the system d_s. The parameter D_2 thus describes a relation between the multifractality of the wavefunction and the spectral fluctuations of the eigenvalue statistics of the system. Considering however that the near linear scaling persists for parameter ranges where fractal structures are absent from the trapping regions in the double kicked rotor, it does not seem probable that there is a connection to the specific fractal scaling derived from critical statistics. The intermediate statistical regime arises more likely from the quantum localisation properties of the 2δ-QKR system.

The level spacing distributions for the intermediate regime can be found in [53],[58], where comparisons with other distributions, such as GOE, Brody or Berry-Robnik are also shown. A further comparison is made to the semi-Poissonian distribution found in some previous cases of intermediate statistics, including the MIT [60]:

$$P(s) = 4s\exp(-2s) \tag{7.23}$$

This distribution displays a long-range Poisson tail at large s, but Wigner (GOE) behaviour as associated with random matrix theory for small s. The intermediate 2δ-QKR distribution shows some, but not perfect agreement with the semi-Poisson form for certain values of K_ϵ.

A best fit to the Berry-Robnik distribution was also investigated, and a parameter value of $\rho = 0.66$ was found. In Chapter 1 it was mentioned that in mixed phase space systems ρ indicates the fraction of phase space which is chaotic, with the integrable Poisson limit corresponding to $\rho = 0$ and the GOE limit to $\rho = 1$. Since the phase space of the double kicked rotor is almost entirely chaotic for $K_\epsilon \gtrsim 0.075$, the narrow trapping regions at the cell boundaries therefore mimic the effects of regular structures covering about one third of phase space.

As a summary to the entire chapter, it has been seen that the quantum double kicked rotor shows clear signatures of the corresponding classical double kicked system investigated in Chapters 5 and 6. The specific transport mechanism of particles through momentum space, with alternating regions of fast and slow acceleration, is observed for cold atoms pulsed by standing waves of laser light. Dynamical localisation acts to preserve asymmetries in the system, and novel scaling properties in connection with localisation, quantum evolution and spectral fluctuations are observed, including a new form of intermediate statistics. Although the scaling seems to originate from pure quantum effects, the existence of trapping regions in momentum space is linked to all observed effects in the double kicked rotor. From the experimental results it is clear that the trapping regions may be used to filter atoms according to their velocities; this may have applications in atom optics or atom chips for example. In the next chapter a different realisation of the double kicked rotor is presented, where trapping occurs in position space along spin chains pulsed by magnetic fields. This demonstrates the generic nature of the double kicked system and its trapping mechanism.

Chapter 8

Kicked and Double Kicked Rotor Phenomena in Spin Chain Systems

Having analysed the theoretical models of the kicked and double kicked rotors extensively throughout the previous chapters and shown experimental realisations with cold atoms, this chapter presents another system which both models can be applied to, namely a Heisenberg spin chain pulsed periodically by magnetic fields. The usual spin chain with an applied static external field corresponds to the resonant QKR case and can permit perfect state transmission of a spin excitation along the chain. The general non-resonant QKR can be modelled by additionally applying a pulsed parabolic field, which results in dynamical localisation of excitations, and accelerator modes of rapidly propagating coherent spin states. The analogy with the double kicked rotor is completed by varying the strength of the parabolic field in alternate time steps, which produces the usual trapping effect, but this time in position space along the spin chain.

8.1 Excitations in the Heisenberg Spin Chain

In the previous chapter the quantum double kicked rotor was extensively investigated both theoretically and in relation to an experimental realisation using cold atoms pulsed by laser light. This particular system was of course a natural choice since the first experiment to demonstrate the QKR had already been carried out using cold atoms and standing waves of laser light. However, given that both the QKR and the 2δ-QKR are essentially theoretical constructs, it is to be expected that these models may be applied to other systems as well. This is indeed the case, since it has been recently discovered that spin chains pulsed periodically by magnetic fields can exhibit analogous behaviour to the energy evolution in the cold atom experiments [61],[62]. In the case of spin chains however diffusion occurs in position space, hence spin excitations are localised along sections of the entire chain. It should be noted here that there is no experimental study of the spin chain analogies to the QKR and 2δ-QKR yet; the results presented here are based on numerical and analytical calculations.

For the analogies presented in this chapter the well studied case of a Heisenberg spin chain with nearest neighbour coupling between spins is used:

$$\hat{H}_{HC} = -J\sum_n \hat{S}_n \cdot \hat{S}_{n+1} - \sum_n B\hat{S}_n^z \tag{8.1}$$

The first term represents the coupling between spins, with total spin operator $\hat{S}$ and the second term an external, static magnetic field in the z direction. The chain has a ferromagnetic ground state in the case of $J > 0$, where all spins point in the same direction (e.g. up: $|\uparrow,\uparrow,\ldots,\uparrow,\uparrow\rangle$). The case $J < 0$ leads to an antiferromagnetic state, which will not be considered here.

In [63] the quantum state transmission of a single spin flip along the ferromagnetic Heisenberg chain was investigated. A single spin at a given position n along the chain is changed to point in the opposite direction to all others ($|\uparrow,\uparrow,\ldots,\downarrow,\ldots,\uparrow,\uparrow\rangle$), thus causing an excitation which affects the nearest neighbour spins due to the coupling between them. After a given amount of time the spin at site n can revert back to pointing in the ground state direction, but instead one of the neighbouring spins $n \pm 1$ flips to point in the opposite direction. In this way the spin excitation caused by the single flip can travel along the chain as a spin wave. Since this is a quantum effect, the excitation may in fact propagate in both directions simultaneously, with certain probability amplitudes of finding the spin flip at a given position. In [64] it was further

shown that perfect transmission along the chain of a coherent spin state of appropriate width can be achieved in the presence of an external static parabolic magnetic field. Such a quantum state transfer is of considerable interest for potential uses in quantum information applications. However, the preparation of a coherent spin state of specified width presents a significant technical challenge.

For the kicked rotor analogies it is sufficient to use states of the Heisenberg chain with single spin flips at some point along the chain [63], provided the static magnetic field is far stronger than the random fluctuations: $\hbar B \gg kT$. In contrast, Gaussian spin excitation packets can be used in other studies of quantum chaos in spin chain systems, particularly when the underlying classical phase space is mixed and stable islands remain. The studies here will however be restricted to the fully chaotic regimes of both the QKR and 2δ-QKR, where no large stable structures exist in the corresponding phase spaces.

If one considers the basis of states $|n\rangle$ which are composed of a single spin at site n pointing in the opposite direction to all the other spins (e.g. down at site n, up elsewhere, as before: $|\uparrow,\uparrow,\ldots,\downarrow,\ldots,\uparrow,\uparrow\rangle$) along the $\hat{z}$ axis, then the eigenstates and eigenenergies of $\hat{H}_{HC}$ in this basis can be found using the Bethe Ansatz [65]. The spin coupling in the Hamiltonian in Eq.8.1 can be expanded as follows:

$$\hat{S}_n \cdot \hat{S}_{n+1} = \frac{1}{2}(\hat{S}_n^+ \hat{S}_{n+1}^- + \hat{S}_n^- \hat{S}_{n+1}^+) + \hat{S}_n^z \hat{S}_{n+1}^z \tag{8.2}$$

where $\hat{S}_n^{\pm} = \hat{S}_n^x \pm i\hat{S}_n^y$ are spin flip operators changing the direction of a given spin. Taking $\hbar = 1$, the action of the spin operators in the $\hat{z}$ direction in which the spins lie, is of course $\hat{S}_n^z|\uparrow\rangle = 1/2|\uparrow\rangle$ and $\hat{S}_n^z|\downarrow\rangle = -1/2|\downarrow\rangle$. Rotational symmetry about the $\hat{z}$ axis means that the total spin component in this direction is conserved, hence $[\hat{H}, S_z] = 0$. If one considers a certain number of up and down spins along the chain, the basis vectors of the system can be sorted according to $S_z = N/2 - r$, where N is the total number of spins and r the number of spins pointing in the opposite direction to all others. For a specific value of r with an initial state ψ_0 comprised of r spins pointing e.g. down, the state at a later time ψ_t can then be obtained in the basis of states $|r\rangle$ which all have r spins pointing down and the others up.

The Hamiltonian $\hat{H}$ can be block diagonalised for each value of r giving the eigenstates and eigenenergies for a certain number of excitations or magnons along the spin chain. For simplicity periodic boundary conditions can be imposed on the chain such that $n+N = n$, in other words one considers a spin ring. This will be seen to correspond to periodic momentum boundary conditions for the atomic 2δ-QKR, since there is an in-

verse mapping between the position and momentum variables between the double kicked rotor and the spin chain system. For large N there are no significant differences between using a spin ring or a long open spin chain when calculating the system evolution for the QKR and 2δ-QKR analogies, although the case of the open chain can result in additional corrections for states at the edges of the chain. Hence for most of what follows spin rings will be used unless otherwise stated. The mathematical forms of evolution operators and eigenstates change slightly between the two cases of an open spin chain and the spin ring, but this does not have a significant impact on the dynamics of the system, other than the absence of edge corrections for the spin ring.

The trivial case of $r = 0$ gives the ferromagnetic ground state $|F\rangle = |\uparrow,\uparrow,\ldots,\uparrow,\uparrow\rangle$ for which the ground state energy E_0 can easily be calculated from the action of the Hamiltonian $\hat{H}_{HC}$ with the spin coupling expanded as in Eq.8.2:

$$\hat{H}_{HC}|F\rangle = -J\sum_{n=1}^{N}[\frac{1}{2}(\hat{S}_n^+\hat{S}_{n+1}^-|F\rangle + \hat{S}_n^-\hat{S}_{n+1}^+|F\rangle) + \hat{S}_n^z\hat{S}_{n+1}^z|F\rangle] - \sum_{n=1}^{N}B\hat{S}_n^z|F\rangle$$
$$= \sum_{n=1}^{N}(-\frac{J}{4}|F\rangle - \frac{B}{2}|F\rangle) = E_0|F\rangle \quad (8.3)$$

Hence the ground state energy is:

$$E_0 = -\frac{N}{2}(\frac{J}{2} + B) \quad (8.4)$$

The $r = 1$ case with a single spin flip excitation gives the one-magnon solution for which the calculation of eigenstates and eigenenergies is particularly simple. A basis of states consisting of a single spin flip at site n is used: $|n\rangle = \hat{S}_n^-|F\rangle$. The total spin state of the chain can then be written as $|\psi\rangle = \sum_n a(n)|n\rangle$. Formally the solution for the coefficients $a(n)$ can be found from the action of the Hamiltonian on $|\psi\rangle$, or for simplicity simply on the individual states $a(n)|n\rangle$:

$$\hat{H}_{HC}a(n)|n\rangle = -J\sum_{\tilde{n}=1}^{N}[\frac{1}{2}(\hat{S}_{\tilde{n}}^+\hat{S}_{\tilde{n}+1}^-a(n)|n\rangle + \hat{S}_{\tilde{n}}^-\hat{S}_{\tilde{n}+1}^+a(n)|n\rangle) + \hat{S}_{\tilde{n}}^z\hat{S}_{\tilde{n}+1}^z a(n)|n\rangle]$$
$$-\sum_{\tilde{n}=1}^{N}B\hat{S}_{\tilde{n}}^z a(n)|n\rangle = -J[\frac{1}{2}(a(n)|n+1\rangle + a(n)|n-1\rangle) + (\frac{N-2}{4} - \frac{1}{2})a(n)|n\rangle]$$
$$-B(\frac{N-1}{2} - \frac{1}{2})a(n)|n\rangle = Ea(n)|n\rangle \quad (8.5)$$

Here, dummy indices n and $\tilde{n}$ are used to avoid confusion between the summations over operators in the Hamiltonian and the individual state $|n\rangle$, although both of course denote the same basis states. Relabelling the coefficients in the first two terms gives the

following relation:

$$-J[\frac{1}{2}(a(n-1)+a(n+1))+(\frac{N}{4}-1)a(n)]-B(\frac{N}{2}-1)a(n)=Ea(n) \tag{8.6}$$

and after rearranging:

$$J(2a(n)-a(n-1)-a(n+1))=(2E+J\frac{N}{2}+BN-2B)a(n)=2(E-E_0-B)a(n) \tag{8.7}$$

where the ground state energy E_0 is given by Eq.8.4, and due to the periodic boundary conditions $a(n+N)=a(n)$. The general N linearly independent solutions for the coefficients are $a(n)=\exp(ik_m n)$, with $k_m=2\pi m/N$ and $m=0,1,\ldots,N-1$ in integer steps.

The above result for $a(n)$ can, in the $r=1$ case, also be obtained simplistically by considering the translational symmetry in the spin chain. The Hamiltonian $\hat{H}$ must be invariant to discrete translations by any number of lattice spacings along the spin ring. Thus the action of the translation operator T, shifting the spin excitation by one site, is to add a phase ϕ:

$$T|\psi\rangle=e^{i\phi}|\psi\rangle=e^{i\frac{2\pi m}{N}}|\psi\rangle \tag{8.8}$$

where $m=0,1,\ldots,N-1$. If one chooses the action of T on the basis states $|n\rangle$ to be $T|n\rangle=|n-1\rangle$, then:

$$\sum_n a(n)T|n\rangle=\sum_n a(n)|n-1\rangle=\sum_n e^{i\phi}a(n)|n\rangle \tag{8.9}$$

and thus $a(n+1)=\exp(i\phi)a(n)$. For $n=0$ and choosing $a(0)=1$ one thus finds $a(1)=\exp(i\phi)$, and by extension $a(n)=\exp(i\phi n)$. From this argument and the previous solution found for $a(n)$ one can write the eigenstates of the $r=1$ solution as:

$$|\psi\rangle=\frac{1}{\sqrt{N}}\sum_{n=1}^{N}e^{ik_m n}|n\rangle \tag{8.10}$$

where the phase ϕ has been written as the wavevector $k_m=2\pi m/N$, and the prefactor $1/\sqrt{N}$ is due to normalisation. These states represent one-magnon excitations in which the ferromagnetic ground state $|F\rangle$ is periodically disturbed by a spin wave with $\lambda=2\pi/k_m$. The single spin flip travels along the spin ring and thus periodically returns to its original position. One can also define the individual components of $|\psi\rangle$ as $\psi_n=(1/\sqrt{N})\exp(ik_m n)|n\rangle$, where $|n\rangle$ simply denotes the spin orientations along the chain,

with a single spin flip at site n. The dispersion relation for the one-magnon case can be obtained by inserting $a(n) = \exp(ik_m n)$ into Eq.8.7. The energies are found to be:

$$E_m = E_0 + J(1 - \cos k_m) + B \tag{8.11}$$

For the periodic case of the spin ring it is convenient to have integer $-N/2+1 \leq m \leq N/2$ in order to achieve 2π periodicity of the wavevector, with range $-\pi+(2\pi/N) \rightarrow +\pi$. In this case, for a constant total number of spins N, the labelling of site positions is equivalently $-N/2 \rightarrow N/2$ with the end points denoting the same site of course.

As it turns out the $r = 1$ case is simple enough that the complete formalism of the Bethe Ansatz is in fact not needed. The eigenstates and dispersion relation can be obtained straightforwardly as above. For $r > 1$ however the situation would be more complicated, e.g. for $r = 2$, the two-magnon solution with two single spin excitations in the chain, one may write $|\psi\rangle = \sum_{1 \leq n_1 < n_2 \leq N} a(n_1, n_2)|n_1 n_2\rangle$ and use the ansatz $a(n_1, n_2) = A\exp(i(k_1 n_1 + k_2 n_2)) + A'\exp(i(k_1 n_2 + k_2 n_1))$ to solve for the eigenstates and eigenvalues of the system.

8.2 Kicked Rotor Phenomena: Dynamical Localisation and Accelerator Modes

The time evolution operator for the one-magnon spin wave in the Heisenberg chain can as usual be written $\hat{U}_{HC} = \exp(-i\hat{H}_{HC}t/\hbar)$ for the time independent Hamiltonian $\hat{H}_{HC}$ given in Eq.8.1. This evolves the initial state $|\psi_0\rangle$ into the state at a later time $|\psi_t\rangle$. Again taking $\hbar = 1$ and using the previous results for the eigenstates (Eq.8.10) and eigenenergies (Eq.8.11) of the Hamiltonian, the evolution operator in the single excitation basis of states $\psi_n = (1/\sqrt{N})\exp(ik_m n)|n\rangle$ is:

$$U_{nn'} = \langle\psi_{n'}|\hat{U}_{HC}|\psi_n\rangle = \frac{1}{N}\sum_{m=-N/2+1}^{N/2} e^{i(n-n')k_m} e^{-i(E_0+J(1-\cos k_m)+B)t} \tag{8.12}$$

which evolves the state $|n\rangle$ into $|n'\rangle$. If this expression is compared to the Floquet operator of the QKR in terms of angular momentum basis states in Eq.3.19, a correspondence can be seen provided that the free evolution propagator $\exp(-il^2\hbar T/2)$ is set to unity. This is the case of the resonant QKR where $\hbar T/2 = 2\pi n$ with integer n, which was investigated in Chapter 3. The time evolution of the single excitation spin wave in the Heisenberg spin chain is thus seen to be analogous to the regime of quantum resonance

in the kicked rotor. The state transmission due to the spin wave occurs since there are usually no localisation effects associated with the resonant QKR regime. Ballistic energy growth is observed for plane wave momentum basis states in the kicked rotor, and correspondingly rapid state transmission is observed for single spin flips in the Heisenberg chain.

To obtain a full analogy with the QKR however, the more generic case of the non-resonant regime featuring dynamical localisation must exist in the Heisenberg spin chain. For this, the system must be made periodic in time with external perturbations corresponding to the δ-kicks in the QKR. This can be achieved by adding a periodic sequence of short magnetic pulses from an additional external parabolic magnetic field B_Q. These magnetic pulses have the same effect on the spin chain system as the pulsed standing waves of laser light on the cold atom distributions. The full Hamiltonian of the pulsed Heisenberg spin chain can then be written as:

$$\hat{H}_Q = \hat{H}_{HC} + \sum_{n=-N/2+1}^{N/2} \frac{B_Q}{2}(n-n_0)^2 \hat{S}_n^z \sum_j \delta(t - jT_0) \tag{8.13}$$

where T_0 is the period of the pulse sequence and $\hat{H}_{HC}$ the Hamiltonian of the freely evolving spin chain from Eq.8.1. The action of the full Hamiltonian $\hat{H}_Q$ on $a(n)|n\rangle$ is then:

$$\begin{aligned}\hat{H}_Q a(n)|n\rangle &= \hat{H}_{HC} a(n)|n\rangle + \sum_{\tilde{n}} \frac{B_Q}{2}(\tilde{n}-n_0)^2 \sum_j \delta(t-jT_0)\hat{S}_{\tilde{n}}^z a(n)|n\rangle \\ &= \hat{H}_{HC} a(n)|n\rangle + \frac{B_Q}{4}\sum_j \delta(t-jT_0)\Big(\sum_{\tilde{n}\neq n}(\tilde{n}-n_0)^2 - (n-n_0)^2\Big)a(n)|n\rangle \end{aligned} \tag{8.14}$$

with $\hat{H}_{HC} a(n)|n\rangle$ given by Eq.8.5. By substituting in $a(n) = \exp(ik_m n)$ and finding the dispersion relation as in Eq.8.11, the energies of the system can thus be found to change correspondingly to:

$$E_m = E_0 + J(1-\cos k_m) + B + \frac{B_Q}{2}\sum_j \delta(t-jT_0)\Big(\sum_{\tilde{n}\neq n}(\tilde{n}-n_0)^2 - (n-n_0)^2\Big) \tag{8.15}$$

Finally, the evolution operator for the pulsed spin chain in the ψ_n basis can now be written:

$$\begin{aligned}U_{nn'}(T_0) = \langle\psi_{n'}|\hat{U}_Q|\psi_n\rangle &= e^{-i\frac{B_Q}{2}(\sum_{\tilde{n}\neq n}(\tilde{n}-n_0)^2-(n-n_0)^2)} \\ &\times \frac{1}{N}\sum_{m=-N/2+1}^{N/2} e^{i(n-n')k_m} e^{-i(E_0+J(1-\cos k_m)+B)T_0}\end{aligned} \tag{8.16}$$

noting that for the newly added term the magnetic pulse acts over a time interval δt which, as in Eqs.2.5 and 3.11, can be set to unity. Also note that this is now a time-periodic Floquet operator evolving the system in time steps of T_0.

Several of the terms in Eq.8.16 can however be neglected when studying the dynamics of the spin chain in the kicked rotor analogy, as they merely contribute an overall phase factor. This is the case for no less than four individual terms, namely the ground state energy term $\exp(-iE_0T_0)$, the phase factor $\exp(-iJT_0)$, the static field term $\exp(-iBT_0)$ and the pulsed field terms for all $\tilde{n} \neq n$, i.e. $\exp(-iB_Q/2\sum_{\tilde{n}}(\tilde{n}-n_0)^2)$. All of these terms merely add the same overall phase to any state transformation $|n\rangle \rightarrow |n'\rangle$. It should be noted however that in an experimental realisation the external static field B would be significant since it introduces an energy gap with the ferromagnetic ground state $|F\rangle$. For the dynamics of interest here this effect can be neglected, and formally one can set $BT_0 = 2\pi$.

After removing all the above mentioned terms (or setting the phase factors to unity) the evolution operator for the pulsed chain is simply:

$$U_{nn'}(T_0) = e^{i\frac{B_Q}{2}(n-n_0)^2}\frac{1}{N}\sum_{m=-N/2+1}^{N/2} e^{i(n-n')k_m}e^{iJT_0\cos k_m} \tag{8.17}$$

where in most cases the applied parabolic field B_Q is such that $n_0 = 0$, i.e. the lowest intensity is at the centre of the chain. This expression can be compared directly to the matrix elements of the QKR evolution operator in Eq.3.19:

$$U_{lm} = e^{-\frac{il^2\hbar T}{2}}\frac{1}{2\pi}\int_{-\pi}^{\pi} e^{i(l-m)x}e^{-\frac{i}{\hbar}K\cos x}dx \tag{8.18}$$

A direct mathematical correspondence between the two systems is observed but with an inverse mapping between position and momentum, as well as between the kicking and free evolution terms. The part of the spin chain operator describing the free evolution appears as a discretised version of the kick term in the QKR, while the pulsed field term in the spin chain maps on to the free propagator in the QKR. Thus it is also seen that the spin sites n map onto the angular momentum states l, and conversely the magnon wavenumber k_m, which denotes the energy levels of the spin chain, maps onto the position x in the kicked rotor. In the spin system it is the wavevectors that are summed over, and evolution of spin excitations takes place in the position space of the chain.

Taking $T = 1$ in the QKR as usual, the analogy is completed if the pulsed magnetic field strength acts as an effective scaled Planck constant $-B_Q \rightarrow \hbar$, and the stochasticity

parameter is thus $JT_0B_Q \rightarrow K$, with T_0 being the period of the magnetic pulses and J the spin coupling between nearest neighbour sites. Note that if the relative signs of the external impulse terms in the Hamiltonians of the QKR (Eq.3.1) and the pulsed Heisenberg spin chain (Eq.8.13) are changed, the mapping becomes $B_Q \rightarrow \hbar$; the sign does not make any differences to the dynamics however. Note also that $\hbar$ was earlier set to unity in the spin operators and when calculating the matrix elements of the spin chain evolution operator. The additional $\hbar$ factors could be included, but do not change the analogy between the QKR and the pulsed spin chain; for simplicity they have been omitted here. For general $T \neq 1$ the full analogy to the quantum parameters of the QKR is $\hbar_T \rightarrow B_Q$ and $K_T = JT_0B_Q$.

From the straightforward mapping between the quantum kicked rotor and the pulsed spin chain, one expects the latter system to display the usual characteristics of the QKR found in Chapter 3, however this time with respect to the diffusion of spin excitations in position space. The rate of diffusion of energy in the classical kicked rotor due to the external kicking was found to be $\langle p^2 \rangle = \langle l^2\hbar^2 \rangle = D(K)t$, with the corrected diffusion rate D given by Eq.2.34. The corrections were obtained from the various correlations between kicks a few time steps apart. It is found that such correlations between the magnetic impulses in the spin chain system exist equivalently and lead to the same type of corrected random walk behaviour for the diffusion of the spin flip excitation along the chain at the start of the system evolution. Starting from a spin flip on any site $n = n_0$, one finds that for early times the excitation diffuses along the chain according to:

$$\langle (n - n_0)^2 B_Q^2 \rangle = D(JT_0B_Q)t \tag{8.19}$$

which, given the earlier parameter analogies, is exactly the diffusion mechanism expected of the QKR.

The diffusion does not continue indefinitely but is arrested after the quantum break time, which for the spin chain parameters is $t^* \sim (JT_0)^2$. For $t > t^*$ the usual process of dynamical localisation is observed, in this case in relation to spin excitations. The distributions of the excitations along the chain take on the characteristic exponential form:

$$P(n) \sim \frac{2}{L} e^{-\frac{2|n-n_0|}{L}} \tag{8.20}$$

with a localisation length of $L \simeq J^2T_0^2B_Q/4$. Examples of distributions for two values of B_Q are shown in Fig.8.1b, taken from [61]. The typical triangular shape on a logarithmic

probability scale is clearly seen in both cases, showing dynamical localisation. Note that these results were obtained using a long open spin chain, but given the localisation there are of course no edge effects. The top panel (a) shows the diffusion rate of the spin

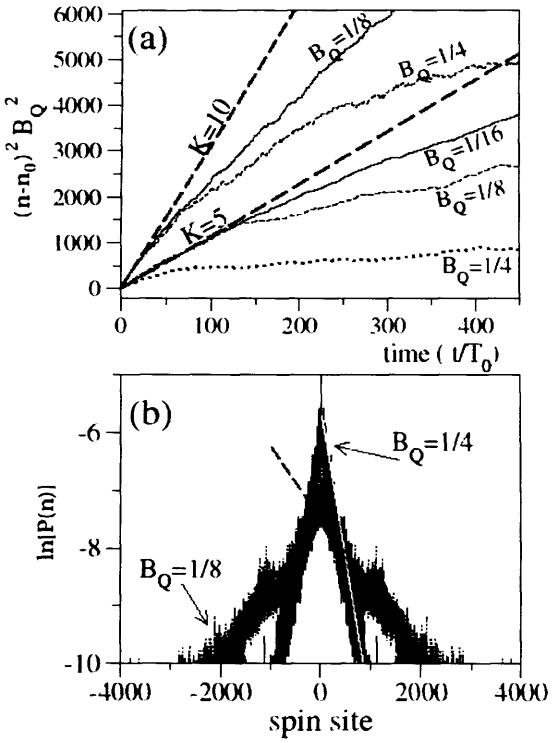

Figure 8.1: Dynamical localisation of spin excitations along an open chain. Spin sites are denoted by $n - n_0$, where n_0 is the site at which the excitation, in the form of a single spin flip, starts. In the top panel (a) the rate of spreading of the spin excitation is shown. Time is counted in pulse numbers t/T_0. The heavy dashed lines show the classical linear diffusion rates corresponding to Eq.8.19, for two values of $K_T = JT_0B_Q$. Diffusion of excitations in the quantum system is seen to follow the classical predictions for short times up to the quantum break time, after which the spreading of excitations eventually stops. As the effective Planck constant B_Q is decreased, the system follows the classical predictions for longer. In the bottom panel (b) two distributions of spin excitations along the chain are shown for differing values of B_Q. Localisation is clearly observed, with the distribution spreading further for lower B_Q, as expected. The analogy to the QKR behaviour is evident. Courtesy of Tom Boness.

excitations. The stochasticity parameter is $K = JT_0B_Q$, and the quantum evolution of the spin chain follows the classical diffusion predictions in Eq.8.19 for short times, but at longer times excitations localise. The smaller B_Q, the longer the system follows the usual linear diffusion rate. The localisation process in the pulsed Heisenberg chain is of course

in contrast to the delocalised excitations in the freely evolving chain, corresponding to the resonant QKR regime, where the diffusion rate is quadratic in time.

A final, perhaps most useful analogy between the QKR and the spin chain system is the existence of accelerator modes for the transport of spin excitations. These were found in Chapters 2 and 3 to be essentially of classical origin, due to small transporting stable islands reappearing in phase space for resonant values of $K \simeq 2\pi n$, which cause ballistic transport of particles rather than the usual linear diffusion rate. Quantum accelerator modes were also observed, underlining the quantum-classical correspondence. Unsurprisingly these exist in the spin chain system as well for $JT_0B_Q \simeq 2\pi n$ [61]. Note that the accelerator modes are quite stable for a fairly broad range near $2\pi n$, so no particular fine tuning of the parameter JT_0B_Q is necessary. Fig.8.2 shows accelerator modes in the Heisenberg spin chain. Parameters used are $B_Q = 1/15$ and $JT_0 = 100$. Time is counted in pulse numbers $j = t/T_0$ similar to the case of the QKR. The top panel shows the excitation distribution after three pulses. A chaotic central part is observed with two large peaks either side of it, denoting the accelerator modes. Up to 30% of the total probability of finding the spin excitation is represented by these peaks. In the bottom panel one can see that the probability peaks rapidly move along the chain, advancing about $2\pi/B_Q \simeq 94$ spin sites each period, while excitations in the central chaotic part move along the chain much slower.

It should be noted that in the cold atom experiments where quantum accelerator modes have been observed [36], the effective Planck constant $\hbar \gtrsim 1$ is usually fairly large. Since the condition for quantum states to fit inside transporting islands is $\hbar \lesssim A$, where $A \sim 10\%$ is the typical phase space area covered by the accelerator mode islands, the large $\hbar$ values lead to diluted accelerator effects with states overlapping into the chaotic phase space areas nearby. In the spin chain system the signatures of accelerator modes can be seen more clearly since the low $\hbar$ regime simply requires a weak magnetic field B_Q. Nevertheless for finite $\hbar \to B_Q$ there is an eventual decay of the accelerator modes and the ballistic transport, as the amplitude of the peaks is gradually reduced by tunnelling out of the stable islands. However, estimates show that in the spin chain for $B_Q = 1/10$ there remains a substantial amplitude in the accelerator modes at least up to about 30 pulses. For the value of $B_Q = 1/15$ used in Fig.8.2 the islands can in fact support more than one eigenstate, leading to the observed slight oscillations in amplitude of the peaks.

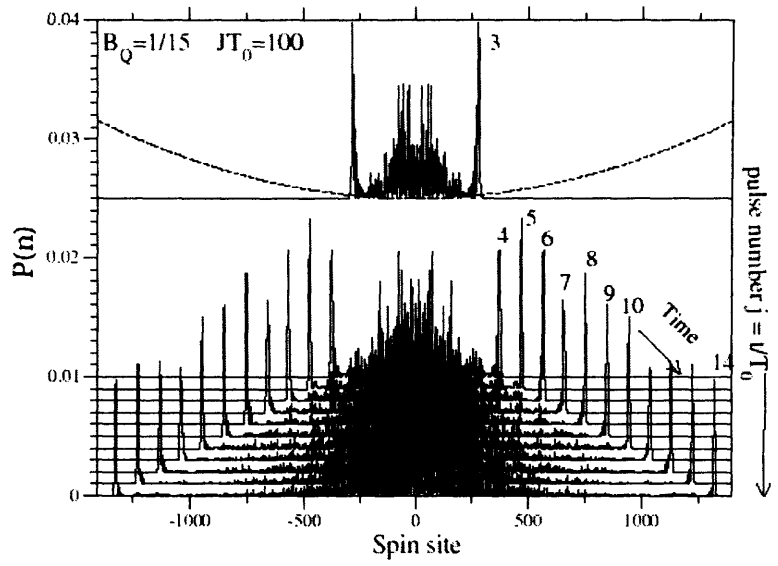

Figure 8.2: Accelerator modes in the pulsed Heisenberg spin chain. An open chain is used as in Fig.8.1, and time is counted in pulse numbers $j = t/T_0$. Distributions of spin excitations evolving in time are shown, with pulse number increasing downwards and labelled for the individual distributions. Parameters are $B_Q = 1/15$ and $JT_0 = 100$ as shown. The system is started with a single spin flip at the centre of the chain, and excitations propagate outwards to the edges. While the central part of the distribution spreads slowly, two distinct peaks are seen to propagate rapidly along the chain, representing the accelerator modes, which contribute up to 30% of the total probability. The dotted line in the top panel shows the form of the applied pulsed parabolic magnetic field, with lowest intensity at the centre of the chain. Courtesy of Tania Monteiro.

The potential usefulness of these spin accelerator modes lies in the fact that they represent coherent states ejected from the chaotic excitation remnant in the centre. In the usual non-resonant pulsed chain, transport of excitations is slow, and the spreading of the distributions stops completely after the break time, thus state transfer is not easily achievable. In the general resonant freely evolving Heisenberg chain, states can be transmitted with perfect or near-perfect fidelity, given appropriate conditions, however there the problem is to construct a well defined coherent state of specific width. The coherent accelerator states could be used for this purpose since their widths are simply determined by the effective $\hbar = B_Q$. The system could be evolved for some time, allowing the accelerator modes to separate from the states in the chaotic remnant, upon which these accelerator states could then be allowed to propagate into static field regions and be transmitted onwards.

The most useful application of accelerator mode states would be in the context of

quantum information. It has been noted [64],[66] that information could be transmitted along a Heisenberg spin chain by encoding it in Gaussian wavepackets of spin excitations. The presence and absence of such wavepackets represent the logical $|1\rangle$ and $|0\rangle$ states of a qubit respectively. The difficulty with this scenario is again the preparation of such superposition states of present and absent Gaussian wavepackets. From the results of the pulsed spin chain evolution with accelerator modes, it can be seen that, starting with a single spin flip excitation at the centre of the chain, after a few pulses a superposition of two Gaussian wavepackets travelling rapidly in opposite directions and an exponentially localised state near the centre is created. If one denotes the left and right propagating wavepackets as $|G_L\rangle$ and $|G_R\rangle$ (each denoting a Gaussian distribution of spin down flips), and the absence of these as $|0_L\rangle$ and $|0_R\rangle$ (each denoting spin up states at all sites where the wavepackets would otherwise be), the maximally entangled state $|G_L\rangle|0_R\rangle + |0_L\rangle|G_R\rangle$ is created. This state has been shown above to survive for several pulses. After creation, the state could then be transmitted through a region with a static parabolic field, in which the Gaussian wavepackets can travel significant distances without distortion [64].

8.3 Double Kicked Rotor Phenomena: Spin Excitation Trapping

Since the magnetically pulsed Heisenberg spin chain is fully analogous to the quantum kicked rotor and displays the same effects in terms of diffusion of spin excitations along the chain, it is reasonable to expect that the double kicked rotor may also be implemented in the spin system. Usually the modification made to the kicked rotor to achieve the double kicked system is to change the timing of the external kicks, such that a sequence of pairs of impulses is created. Thus the fixed period T is replaced by two alternating periods ϵ and τ of short and long duration, which creates the asymmetry needed for the double kicked rotor.

In the spin chain system a similar asymmetry is required to create an analogy to the 2δ-QKR, however it is not the timing of the magnetic pulses that is changed. For the usual momentum diffusion of double kicked particles, the free propagator in Eq.8.18 is replaced by the two propagators $\exp(-il^2\hbar\epsilon/2)$ for the short time interval ϵ between kicks in a pair, and $\exp(-il^2\hbar\tau/2)$ for the long time interval τ between kick pairs. From the mathematical analogy between the pulsed spin chain in Eq.8.17 and the QKR form

in Eq.8.18, it was seen that the free propagator actually corresponds to the pulse term in the spin chain, with $B_Q \to \hbar$. More precisely of course one may write $B_Q \to \hbar T$, since the period T of the QKR was set to unity earlier. Thus it can be seen that to achieve an analogy with the quantum parameters $\hbar_\epsilon$ and $\hbar_\tau$, the strength of the applied pulsed field B_Q is alternated [62], rather than its period T_0, which only appears in the discrete summation of Eq.8.17.

The evolution operator for the spin chain analogy to the double kicked rotor can thus be written simply as:

$$U_{nn'} = U_\tau U_\epsilon = \frac{1}{N^2} e^{i\frac{B_\tau}{2}(n-n_0)^2} \Big(\sum_{m=-N/2+1}^{N/2} e^{i(n-n')k_m} e^{iJT_0 \cos k_m} \Big) \times e^{i\frac{B_\epsilon}{2}(n-n_0)^2} \Big(\sum_{m=-N/2+1}^{N/2} e^{i(n-n')k_m} e^{iJT_0 \cos k_m} \Big) \qquad (8.21)$$

where $B_\tau \gg B_\epsilon$, i.e. the former is a strong magnetic field, the latter a weak field. The labels τ and ϵ have been used here in analogy to the double kicked rotor, although they do not represent time intervals in this case. A sequence of pairs of magnetic pulses of different field strengths occurs, but with the time interval T_0 between individual pulses remaining the same. The parameters of the doubly pulsed spin chain are $B_\epsilon \to \hbar_\epsilon$, $B_\tau \to \hbar_\tau$ and $JT_0 B_\epsilon \to K_\epsilon$, although, as for the long time interval τ in the 2δ-QKR, it will be seen that the strong magnetic field B_τ does not play a significant role. Hence the spin chain analogy has two natural quantum parameters as usual.

Given the above mapping, the pulsed spin chain with alternating field strengths behaves in a completely analogous way to the double kicked rotor. Here however, trapping of course now occurs in position space; spin excitations can be trapped within short segments of the chain. Fig.8.3 shows distributions of spin excitations for the doubly pulsed chain obtained after the quantum break time, this time for a spin ring. The characteristic staircase structure observed in the double kicked rotor is seen. Parameters here are $B_\epsilon = 0.05$ and $JT_0 = 7$, which corresponds to the values of $K_\epsilon = 0.35$ and $\hbar = 1$. The value of B_τ will be seen to be largely irrelevant.

The initial single spin flip at first spreads out into a roughly uniform distribution over a segment of the ring of approximate width $2\pi/B_\epsilon$, which corresponds exactly to one diffusion cell in Fig.5.3 (where the same value of $K_\epsilon = 0.35$ is used), except that diffusion is in position rather than momentum space. Near spin sites $n = \pm(2m+1)\pi/B_\epsilon$ the propagation of excitations is greatly slowed down. If a single spin flip or a Gaussian

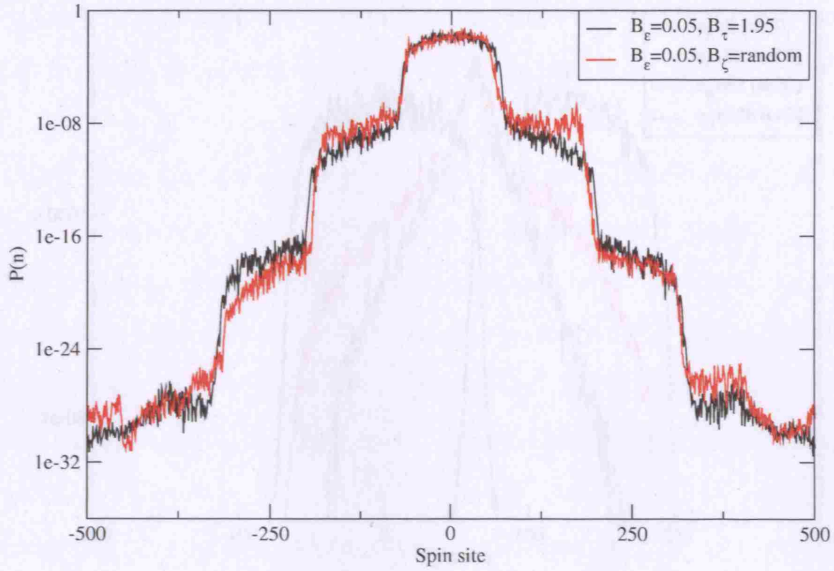

Figure 8.3: Distributions of spin excitations along a doubly pulsed spin ring with alternating magnetic field strengths. Parameters are $B_\epsilon = 0.05$ and $JT_0 = 7$, corresponding to $K_\epsilon = 0.35$ and $\hbar = 1$, and distributions are calculated well after the quantum break time. The characteristic staircase structure of the double kicked rotor is observed, with excitations spreading rapidly along segments of the ring of width $2\pi/B_\epsilon$, corresponding to diffusion cells, but diffusing very slowly across segment boundaries, corresponding to trapping regions in position space at sites $n = \pm(2m+1)\pi/B_\epsilon$. Replacing the strong magnetic field by one of randomly varying magnitude along the ring, which is analogous to the random-pair-kicked rotor, does not change the distribution significantly. This reveals the insensitivity of the doubly pulsed spin system to B_τ.

wavepacket of excitations is placed in these areas of the ring, it can remain trapped within only a few spin sites for a significant duration, before rapidly spreading over the neighbouring segments. Fig.8.4 shows early time evolution for spin excitations starting at different points along the ring, with the same parameters as in Fig.8.3. While excitations started in the centre of a diffusion segment spread rapidly across it, those started in a trapping region extend over a smaller number of spin sites. For low coupling J between spin sites, and hence low $JT_0B_\epsilon \rightarrow K_\epsilon$, excitation states can be localised within one segment or trapping region beyond the quantum break time, whereas for larger coupling states eventually distribute themselves over several segments of the ring as in Fig.8.3.

In both the classical and quantum double kicked rotors it has been shown that the long time interval τ between kick pairs does not affect the system dynamics significantly provided that $\tau \gg \epsilon$. In the random-pair-kicked rotor the free evolution phase $l^2\hbar\tau/2$ in the 2δ-QKR can be replaced by a momentum dependent random phase in the interval

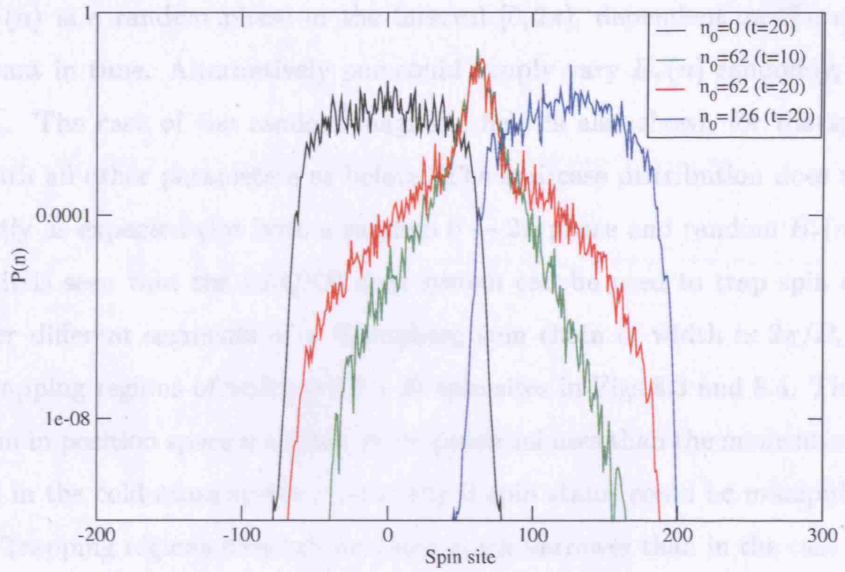

Figure 8.4: Early time evolution in the doubly pulsed spin ring. Parameters are as in Fig.8.3. Spin excitations are started at different initial sites as shown. The black and blue distributions denote excitations that have started at the centres of two neighbouring diffusion cells, roughly $2\pi/B_\epsilon$ apart (with $B_\epsilon = 0.05$). For these starting conditions the excitations rapidly fill the entire cell. The green and red distributions denote excitations starting in the trapping region ($\simeq \pi/B_\epsilon$) between the two cells, for two different times (counted in numbers of double pulses). For this case the distributions spread over a much smaller number of spin sites ($\simeq 30-40$) for early times, but at $t = 20$ (40 single pulses) excitations start to escape into the neigbouring cells. These results are asymptotically valid in the strong localisation regime, in which case excitations remain trapped within one cell or trapping region. Otherwise the distributions eventually spread over the entire ring, as in Fig.8.3.

$0 \to 2\pi$, and the diffusion mechanism is largely unchanged. The implementation of the random-pair-kicked rotor in the Heisenberg spin chain system is particularly significant, as it means that the strong magnetic field B_τ can be replaced by a field B_ζ of randomly varying magnitude along the chain [62]. This corresponds to the non-KAM $\tau \to \infty$ limit in the double kicked rotor. Although sufficiently strong magnetic fields can be created in laboratories, a weaker random magnetic field would be much easier to achieve experimentally, particularly in a delicate setup. Hence the random-pair-kicked rotor analogy could be very useful in the spin chain system. The form of the strong pulse term in the evolution operator changes in the following way:

$$e^{i\frac{B_\tau}{2}(n-n_0)^2} \to e^{iB_\zeta(n)} \tag{8.22}$$

where $B_\zeta(n)$ is a random phase in the interval $[0, 2\pi]$, dependent on the spin site n, but constant in time. Alternatively one could simply vary $B_\tau(n)$ randomly, as long as $B_\tau \gg B_\epsilon$. The case of the random magnetic field is also shown for the spin ring in Fig.8.3 with all other parameters as before. The staircase distribution does not change significantly as expected (for both a random $0 \rightarrow 2\pi$ phase and random $B_\tau(n)$).

Thus it is seen that the 2δ-QKR spin system can be used to trap spin excitations either over different segments of a Heisenberg spin chain of width $\simeq 2\pi/B_\epsilon$, or inside narrow trapping regions of width $\simeq 20 - 30$ spin sites in Figs.8.3 and 8.4. The trapping mechanism in position space may have more potential uses than the momentum trapping presented in the cold atom system, especially if spin states could be manipulated while trapped. Trapping regions here can be made much narrower than in the case of barriers to excitation propagation due to mixed phase spaces with large regular structures in the classical analogues. The segmentation of the spin chain could also be used to control interactions between spin states in different locations. Further thoughts on the possible uses of the double kicked rotor system in general are presented in the conclusions to this thesis in Chapter 9.

To conclude this chapter it should be mentioned that of course all other properties of the double kicked rotor are expected to be relevant to the spin chain system as well. The division of the chain into areas of fast and slow diffusion of spin excitations is essentially due to the same type of global correlations as found in Chapter 6, although the analogy of the closely spaced kick pairs and the correlations between them obviously breaks down here. As mathematical constructs however, the equations given in Chapter 6 remain valid for a classical analysis of the underlying diffusion mechanism. Other results found for the quantum double kicked rotor in Chapter 7 are also expected to be valid for the spin chain system, including properties of the eigenstates and quantum transport phenomena, although again care may need to be taken with the specific mapping and analogies. Of primary importance are of course simply the observable diffusion effects in the numerical (and perhaps later experimental) realisations of both the QKR and 2δ-QKR spin chain systems; the mathematical analysis can be carried out for the generic double kicked rotor case.

Chapter 9

Conclusions

The first section in what follows provides an overview of the completed work, in particular the peculiarities of the novel double kicked rotor. The system is contrasted with the standard kicked rotor case and earlier asymmetric systems, and the new results are put into perspective in relation to other research. Some suggestions for further theoretical work are given. The second section then discusses a few potential applications of the double kicked rotor model in terms of experimental realisations, as well as ideas for future investigations. Exploitations of the trapping effect in particular are mentioned. Finally some comments on the addition of entanglement to kicked systems are made, in relation to quantum information.

9.1 The Double Kicked Rotor as a Generic Theoretical System

The double kicked rotor has turned out to display a wealth of new and interesting features, perhaps somewhat surprisingly, since it is essentially a fairly simple extension of the well-studied kicked rotor and related perturbed period ratchet systems. Adding temporal asymmetries to the perfectly periodic kicked rotor seemed a natural line of investigation, and sure enough kicking periods which were slightly altered led to interesting new effects, namely the ratchet effects presented in Chapter 4, with momentum dependent diffusion of particles and hence quantum currents. It was at first however not necessarily expected that increasing the asymmetry would result in a rather different system with novel diffusion properties.

It has been shown in Chapters 5 and 6 that the classical double kicked rotor is a generic theoretical model, applicable to probably several different experimental situations, two of which were presented in Chapters 7 and 8. The necessary system feature is a large asymmetry in one of the parameters related to the periodic external impulses. In the usual case implemented in cold atom experiments, the asymmetry is in the timing of the impulses, with periodic sequences of short and long time intervals, whereas in the spin chain system the asymmetry arises due to alternating the strength of the external magnetic impulses. The double kicked rotor model may well be applied to other systems with similar asymmetries.

The asymmetrical timescales in the double kicked rotor lead to a very particular diffusion mechanism for particles in relation to one of the phase space variables, momentum in the standard case, position for the pulsed spin chains. Classical phase space has a cellular structure and is divided into areas of fast and slow diffusion, the latter termed trapping regions (in momentum or position). Varying diffusive behaviour depending on phase space location can also be found in the kicked rotor and similar systems for mixed phase spaces containing regular structures. The double kicked diffusion mechanism however persists for a broad parameter range in the fully chaotic regime, where no significant regular structures remain. Usually the diffusive behaviour associated with chaos is locally a random walk for individual particles, and globally for the entire ensemble a steady linear increase of the second moment of the relevant variable in time. Such behaviour only occurs inside the individual cells in the double kicked rotor, but overall the new mechanism adds important features to the chaotic diffusion and transport. Any

system such as the double kicked rotor that displays distinguishing behaviour between different groups of constituent particles in a simple way can be very useful. Although the trapping of particles in phase space is not permanent, it has potential applications in quantum (and perhaps classical) systems as discussed in the next section.

Mathematically the diffusion behaviour is of considerable interest, since it is seen to arise from correlations between impulses which have both a long spatial and temporal range. This is highly unusual for a chaotic system. One of the key characteristics of chaos are short-lived correlations, but in the case of the double kicked rotor a type of long term memory is present, responsible for the existence of trapping regions in phase space. Although one cannot in general predict the trajectory of any individual particle, the trapping regions result in an additional confinement of particles, absent in the fully chaotic kicked rotor.

The correlations are all derived using the same approach as for the Standard Map or ratchet systems, for which higher order terms were (justifiably) neglected. The existence of the short time interval ϵ between impulses (or the weak magnetic field in the spin chains) results in these higher order terms becoming important in the double kicked rotor. Although somewhat cumbersome, the derivations are straightforward, and correlations can be grouped according to mathematical form and resulting diffusive behaviour.

Beyond the Poisson correlations responsible for the trapping mechanism, there are also higher order correlation terms independent of phase space variables, which contribute to the overall asymptotic diffusion rate. Again, the behaviour is different from the Standard Map, since the diffusion rate is always bounded from above by the uncorrelated rate D_0. Impulse correlations never enhance the overall diffusion beyond the standard random walk rate. Accelerator modes as found in the kicked rotor are also absent. In the regime where diffusion cells and trapping regions exist, the diffusion rate is found to vary as $D \propto K_\epsilon^3$. The origin of this scaling is not yet entirely clear but may be related to some particular mathematical behaviour of the long range correlations.

Quantum versions of the classical double kicked rotor are easily implemented as shown in Chapters 7 and 8, and show striking correspondences to the classical case. The characteristic diffusion mechanism is observed with atoms or spin excitations, in momentum or position space respectively. Quantum particles can be stuck in trapping regions for significant times during the early system evolution, and upon release they experience the same alternating fast and slow diffusion as in the classical case. Both the

numerical simulations and the experimental results, energy variation and momentum distributions alike, clearly show signatures of the characteristic diffusion mechanism in the double kicked rotor. This is also the case for the underlying Floquet states of the systems, as well as for the form of the matrix representation of the evolution operator. Dynamical localisation of eigenstates and state distributions helps to preserve the characteristics of the diffusive behaviour for certain parameter ranges. The amount of quantum transport through trapping regions can be varied not only directly from the impulse strength and value of the effective Planck constant, but also indirectly from the quantum break time. States can either be localised entirely within trapping regions or cells if the break time is short, or evolve to extend over several cells, resulting in the characteristic staircase structure of probability distributions.

The specific diffusion mechanism encountered in the quantum double kicked rotor also affects scaling behaviour and energy level statistics. Fractional scaling of localisation lengths (and other properties) with $\hbar$ are observed, in contrast to the $L \propto 1/\hbar$ result in the QKR. A form of intermediate level statistics is found for the regime in which states start to extend beyond one diffusion cell, which is neither of the random matrix form derived from the Wigner-Dyson law, nor semi-Poissonian as observed for critical statistics in e.g. the Metal-Insulator transition. Both phenomena arise directly from the existence of the trapping regions which heavily influence localisation properties in the double kicked rotor.

Many of the novel properties of the double kicked rotor, both classical and quantum mechanical, were at first attributed to classical fractal structures, namely cantori, found in the trapping regions for certain parameters. From a purely phenomenological point of view these are very similar to the golden ratio cantori in the kicked rotor, which are the final barriers to diffusion before phase space becomes fully chaotic. The locations of the two sets of cantori in their respective phase spaces are found to be analogous. Furthermore most of the properties of the double kicked rotor exist in some form or other in relation to the golden ratio cantori. This includes the fractional scaling of localisation lengths as $\hbar^{2/3}$, the existence of intermediate spectral statistics with near linear variances and the cubic dependence of the diffusion rate on the classical control parameter. The previous study of a double pulsed system with temporally broad pulses [54], mentioned in Chapter 7, also showed behaviour connected to the presence of cantori. Since it is intuitive to associate the slow diffusion of particles across cell boundaries with

the cantori present in these, it is tempting to ascribe all the novel properties to these regular structures as well. This would complete a nice analogy between the kicked and double kicked rotors.

The one observation which puts the link between the above phenomena and the fractal structures within the trapping regions in serious doubt however, is that all properties of the double kicked rotor persist in the non-KAM limit of randomised phases every second time step. It was found both for the classical case in Chapter 5 and the quantum cases in Chapters 7 and 8, that the random-pair-kicked rotor, in which the long time interval τ or strong magnetic field were replaced by random classical or quantum phases, still displayed all the features of the double kicked rotor, in particular the characteristic diffusive behaviour including trapping regions. This is formally the limit in which the ratio between the asymmetric parameter values becomes infinite, i.e. $\tau/\epsilon \rightarrow \infty$, which corresponds to completely randomising the relevant phase space variable. Classically the ratio may even vary between different time steps of the system evolution, thereby creating a non-periodic double kicked system; yet the diffusive behaviour persists. The only change observed in the non-KAM limit is the absence of cantori in the trapping regions for large ratios τ/ϵ. Thus the diffusion mechanism, and all other observable classical and quantum effects associated with the double kicked rotor, are largely insensitive to τ, but the fractal structures in phase space are not.

The fact that trapping regions and hence all associated scaling properties and statistical quantities can exist independently of cantori, has prompted alternative explanations for the origin of these properties. It seems more likely that they arise purely through the quantum evolution of the system and localisation effects, as shown for the $\hbar$ scaling in Chapter 7. This could be a highly significant discovery, since, as mentioned above, most of the scaling properties found in the double kicked rotor, exist in other systems and are generally associated with cantori, KAM tori or other regular structures in phase space, e.g. the 2/3 exponent for the scaling of the localisation lengths with $\hbar$, which has also been found for the penetration depths of KAM tori in the kicked rotor [55]. The double kicked rotor displays a different form of generic behaviour to that of the usual kicked rotor system, insofar as a novel diffusion mechanism, and associated localisation properties in the quantum case, can exist in a completely chaotic regime with no regular structures whatsoever. Thus, the double kicked rotor is a significant addition to both classical and quantum chaos theories.

Further investigations into both the classical scaling of the asymptotic diffusion rate with K_ϵ, and the quantum scaling of localisation lengths and variances in the double kicked rotor would be useful. More extensive studies of the interactions between kick correlations leading to diffusion corrections may reveal further links to the asymptotic scaling or diffusive behaviour. Of particular interest is the relationship between fractal structures and the trapping mechanism, and hence associated scaling, or indeed the absence thereof. Provided the fractional scaling of localisation lengths in the quantum double kicked rotor is of pure quantum origin, this raises further questions as to the role of cantori remnants in the double kicked rotor, or perhaps other systems as well.

9.2 Potential Experimental Applications and Further Investigations

The quantum double kicked rotor has been shown to be more than simply a theoretical model, through its experimental realisation in pulsed cold atoms. Momentum dependent energy variations, and probability distributions of both the rotor state and underlying Floquet states, clearly showed the existence of alternate regions of fast and slow momentum diffusion, corresponding to the classical cellular phase space. More recently an experimental investigation of the 2δ-QKR in magnetically pulsed Heisenberg spin chains has been suggested, as described in Chapter 8. Indeed one could also devise a classical experimental situation to test and perhaps exploit the particular diffusive behaviour of the double kicked rotor.

In the usual realisation including momentum trapping, be it classically or quantum mechanically, it is obvious that the system could be used as a velocity selector. Particles, or more specifically atoms, could be filtered according to their momenta, given the different diffusive behaviour between trapping regions and within the individual cells in phase space. Since particles in a trapping region absorb virtually no energy from the external impulses for a given amount of time, they remain at their starting momenta, while other particles accelerate away rapidly. A useful investigation here would be to see how narrow a trapping region can be made. As was seen in Chapter 5 the width of the cell boundaries is not affected greatly by the system parameters, although the presence or absence of cantori has a slight effect. However, the comparatively small width observed in the cold atom experiment (Fig.7.3), particularly in the regime where

Poisson correlations cause a sharp dip in the energy absorption (panel (b)), could be sufficient for application as a filter. The trapping regions are found to cover at most roughly a sixth of the momentum range that a diffusion cell covers. In a classical experiment or a quantum experiment with a long break time, the trapping effect is of course only transient for a given group of particles. By either decreasing the break time or the amount of quantum transport through trapping regions, states can however be trapped asymptotically with the help of dynamical localisation. Some states will be narrowly localised within a trapping region, while others will spread over an entire diffusion cell.

A velocity filter could possibly be used in atomic manipulation devices such as atom chips [67], where a flow of ultracold atoms, usually interacting with light, could be used to create quantum logic gates and optical networks. Atoms may be trapped in a one-dimensional line on the surface of a magnetic atom mirror using electric gradients. The mirror is used to reflect atoms with almost perfect specular reflection. Tiny interferometers, waveguides and other control devices could be created on these surfaces.

A further investigation for the double kicked rotor would be to see precisely how stable or unstable the diffusion mechanism and dynamical localisation are to random quantum phases in time, which corresponds to the non-periodic classical case of varying long time intervals between kick pairs. This relates to studies of decoherence in kicked systems, as mentioned at the end of Chapter 3, where localisation was shown to be very sensitive to spontaneous emission events [30]. On the other hand the large temporal asymmetry in the double kicked rotor, as well as time independent random phases in the free propagator, merely result in changes to localisation phenomena, but not in the absence of the latter. While in the spin chain systems the non-KAM limit can be implemented by using a magnetic field of randomly varying magnitude along the chain, adding random quantum phases to the cold atom system is more difficult. Investigating the random-pair-kicked rotor by increasing the time interval between pairs of impulses is possible, but depending on the sensitivity of the trapping mechanism and localisation to non-periodicity, a series of random shorter intervals may be easier to implement.

A very recent study [68] has shown a nonlinear analogue of the QKR in Bose-Einstein condensates (BECs) subject to short pulses from standing waves of light, where instabilities of the condensate are investigated in relation to the kicking period and nonlinearity. An extension to this using temporally closely spaced pairs of opposing kicks is very

similar to the double kicked rotor, and introduces new features into the system. These findings once again show that the kicked and double kicked rotors are generic theoretical systems applicable to a variety of experimental situations.

The trapping of spin excitations along Heisenberg chains in the other realisation of the double kicked rotor described in this thesis also has potential applications. Again the ability to distinguish between different propagation behaviour of excitations, depending on location along the chain, can be useful for selecting certain states. This is particularly the case if a further manipulation of trapped states is possible. In Chapter 8 the idea of using accelerator modes in the spin chain as coherent states for the transmission of quantum information had already been looked at. Highly localised states in trapping regions may serve a similar purpose.

The spin chain system also highlights a further possibility in the kicked systems, namely interactions between constituent particles. In the standard visualisation of the kicked and double kicked rotor particle interactions are largely neglected, however in an experimental situation these are of course possible. In a cold atom cloud the interactions are generally weaker than for the spin chain coupling in a Heisenberg chain, although dipole-dipole interactions may occur. An interesting study would be to investigate the effect of non-nearest-neighbour interactions in the spin chain on the accelerator modes of the kicked rotor and the excitation trapping of the double kicked rotor.

Another interesting type of interaction is of course quantum entanglement, achievable in both systems, either between spins or cold atoms. Indeed entire rotor states may become entangled with each other as well. Entanglement in quantum chaotic systems has been studied previously. Of key interest is the relationship between the chaoticity of a system and the amount of entanglement present. There is so far no clear agreement yet whether quantum chaos enhances or suppresses entanglement in general, however some results have been obtained in relation to specific entanglement measures. In a study of two coupled kicked rotors [69] a clear enhancement of entropy was found for parameter ranges corresponding to classical chaotic motion, leading to entanglement between the rotor states. An upper bound on entanglement production was however observed [70]. The drawback with this study was that only two systems were considered. In a further study [71], using a multiqubit system described by the quantum kicked top (a different type of kicked spin system), it was then observed that while the bipartite entanglement between a pair of qubits and the rest of the system is enhanced for chaotic conditions, the

pairwise entanglement between the two qubits in the pair was strongly suppressed. Other investigations of entanglement production in quantum chaotic systems were also carried out, often studying bipartite entanglement [72], but also for the pairwise entanglement or concurrence [73].

One of the reasons of the large interest in entanglement studies, other than the intrinsic quantum mechanical behaviour, is of course the resource it provides for quantum information and quantum computation. Thus there is also much current interest in the interface between quantum chaos and quantum information [74]. The spin chain system may be the more obvious candidate here, since much work has already been carried out on the entanglement of discrete spin states and transmission of states along spin chains. The discreteness of position space in the pulsed spin chains in Chapter 8 is in contrast to the usual kicked and double kicked rotor including momentum trapping, which may describe a continuous variable (CV) system. Although the mathematical formalism in this thesis was carried out for integer momentum states, and the angular momentum states of individual atoms of course lie on a discrete spectrum, the positions and momenta of particles represent continuous variables. Discrete spin sites in Heisenberg chains offer certain advantages for quantum information, particularly for the construction of quantum logic gates, since constituent parts of the system can be addressed more easily. Continuous variable systems, such as atomic kicked rotors for example, are less likely candidates for actual quantum computation. Using neutral atoms in an atom trap instead of spins for quantum computation is possible [75], but the atoms in the double kicked rotor experiments are only 'trapped' in momentum space, otherwise they are free to move about. Instead however CV systems could be useful for bulk transport of coherent quantum states. This is also similar to the case of transmission of Gaussian wavepackets along the spin chains. It is interesting to note that while information protocols in discrete systems are often probabilistic, their CV counterparts are usually deterministic.

A final investigation worth mentioning here, is the effect of entanglement on the double kicked rotor specifically. The coupled rotors in [69] are of course QKR systems, so it would be interesting to see if the characteristic diffusion mechanism is affected by entanglement of two or more double kicked rotors, or vice versa. In particular one may investigate whether coupling between rotors, collisional interactions between atoms, or other types of interactions leading to entanglement, could lead to unwanted disturbances

in the periodic pulse sequence and thus a dephasing of the trapping effect, depending on the type and timing of interactions. Provided that the trapping is robust enough, it would furthermore be of interest whether entangled trapped states could be used either in experimental applications or for further studies of into the nature of quantum chaos and entanglement.

Appendix

A.1 Kick Correlation Terms

This appendix gives the exact forms of all the kick correlation terms used for calculations in the analysis of the double kicked rotor in Chapter 6. Eqs.A.1-A.16 are the terms listed in Table 6.1, denoted by type of correlation family and pattern of non-zero m_j coefficients in Eq.6.8. These are the Poisson correlations leading to momentum dependent diffusion corrections and responsible for the trapping mechanism. Eqs.A.1 and A.2 are simply the kick-to-kick correlation and lowest order global correlation family $C_{G1}t$ respectively, corresponding to Eqs.6.13 and 6.20. Eqs.A.7 and A.8 are the two Poisson terms derived in detail in Chapter 6 (Eqs.6.33 and 6.35).

Eqs.A.17 and A.18 are the two lowest order correlation families independent of momentum shown in Fig.6.4, which act to lower the overall asymptotic diffusion rate in the double kicked rotor in comparison to the Standard Map rate. Eq.A.17 corresponds to Eq.6.47.

All the terms can either be derived from Eq.6.8, for a given choice of m_j, or written down straightforwardly from Eqs.6.36, 6.37 and 6.48. Note the similar algebraic patterns in the terms below. Also note the key feature of diffusion hindering terms C^{-}_{Gn} being of opposite sign to diffusion enhancing terms C^{+}_{Gn} at every Poisson order n.

Early time behaviour and asymptotic values can be obtained for each term, by evaluating the time dependent summations explicitly, similar to the cases shown in Chapter 6. Note that for momentum dependent terms the asymptotic limit denotes saturation values, the actual correction to the diffusion rate for $t \to \infty$ vanishes ($C \to 0$ but $Ct \to C_{sat}$, where C_{sat} is the saturation value).

A.1 Kick Correlation Terms

Labels below refer to Table 6.1.

Momentum Dependent Poisson Correlations

Ia (C_1,C_{G1}), $m_j = \pm 1$

$$C_1 t = K^2 \cos p_0 \epsilon (J_0(K_\epsilon) - J_2(K_\epsilon)) \sum_{j=1}^{t} J_0^{2j-2}(K_\epsilon) \tag{A.1}$$

$$C_{G1} t = -2K^2 \cos p_0 \epsilon J_1^2(K_\epsilon) \sum_{j=2}^{t} (2j-2) J_0^{2j-3}(K_\epsilon) \tag{A.2}$$

Ib (C_{G1}^-,C_{G1}^+), $m_j = \pm 1, \pm 1, \mp 1$

$$C_{G1}^- t = K^2 \cos p_0 \epsilon J_1^3(K_\epsilon) J_1^2(2K_\epsilon) (3\frac{J_0(K_\epsilon) - J_2(K_\epsilon)}{J_1(K_\epsilon)} + 2\frac{J_0(2K_\epsilon) - J_2(2K_\epsilon)}{J_1(2K_\epsilon)}) \times \sum_{j=3}^{t} \sum_{\alpha_1=0}^{j-3} \sum_{\alpha_2=0}^{j-3-\alpha_1} J_0^{2(j-3-\alpha_2)}(K_\epsilon) J_0^{2\alpha_2}(2K_\epsilon) \tag{A.3}$$

$$C_{G1}^+ t = -2K^2 \cos p_0 \epsilon J_1^3(K_\epsilon) J_1^2(2K_\epsilon) \sum_{j=3}^{t} \sum_{\alpha_1=0}^{j-3} \sum_{\alpha_2=0}^{j-3-\alpha_1} (2(j-3-\alpha_2)\frac{J_1(K_\epsilon)}{J_0(K_\epsilon)} + 2\alpha_2 \frac{J_1(2K_\epsilon)}{J_0(2K_\epsilon)}) \times J_0^{2(j-3-\alpha_2)}(K_\epsilon) J_0^{2\alpha_2}(2K_\epsilon) \tag{A.4}$$

Ic (C_{G1}^-,C_{G1}^+), $m_j = \pm 1, \pm 1, \pm 1, \mp 1, \mp 1$

$$C_{G1}^- t = K^2 \cos p_0 \epsilon J_1^3(K_\epsilon) J_1^4(2K_\epsilon) J_1^2(3K_\epsilon) (3\frac{J_0(K_\epsilon) - J_2(K_\epsilon)}{J_1(K_\epsilon)} + 4\frac{J_0(2K_\epsilon) - J_2(2K_\epsilon)}{J_1(2K_\epsilon)} + 2\frac{J_0(3K_\epsilon) - J_2(3K_\epsilon)}{J_1(3K_\epsilon)}) \sum_{j=5}^{t} \sum_{\alpha_1=0}^{j-5} \sum_{\alpha_2=0}^{j-5-\alpha_1} \sum_{\alpha_3=0}^{j-5-(\alpha_1+\alpha_2)} \sum_{\alpha_4=0}^{j-5-(\alpha_1+\alpha_2+\alpha_3)} J_0^{2(j-5-(\alpha_2+\alpha_3+\alpha_4))}(K_\epsilon) \times J_0^{2(\alpha_2+\alpha_4)}(2K_\epsilon) J_0^{2\alpha_3}(3K_\epsilon) \tag{A.5}$$

$$C_{G1}^+ t = -2K^2 \cos p_0 \epsilon J_1^3(K_\epsilon) J_1^4(2K_\epsilon) J_1^2(3K_\epsilon) \sum_{j=5}^{t} \sum_{\alpha_1=0}^{j-5} \sum_{\alpha_2=0}^{j-5-\alpha_1} \sum_{\alpha_3=0}^{j-5-(\alpha_1+\alpha_2)} \sum_{\alpha_4=0}^{j-5-(\alpha_1+\alpha_2+\alpha_3)} (2(j-5-(\alpha_2+\alpha_3+\alpha_4))\frac{J_1(K_\epsilon)}{J_0(K_\epsilon)} + 2(\alpha_2+\alpha_4)\frac{J_1(2K_\epsilon)}{J_0(2K_\epsilon)} + 2\alpha_3 \frac{J_1(3K_\epsilon)}{J_0(3K_\epsilon)}) \times J_0^{2(j-5-(\alpha_2+\alpha_3+\alpha_4))}(K_\epsilon) J_0^{2(\alpha_2+\alpha_4)}(2K_\epsilon) J_0^{2\alpha_3}(3K_\epsilon) \tag{A.6}$$

IIa (C_{G2}^{-},C_{G2}^{+}), $m_j = \pm 1,\pm 1$

$$C_{G2}^{-}t = -K^2 \cos 2p_0\epsilon J_1^2(K_\epsilon)J_1(2K_\epsilon)(2\frac{J_0(K_\epsilon) - J_2(K_\epsilon)}{J_1(K_\epsilon)} + \frac{J_0(2K_\epsilon) - J_2(2K_\epsilon)}{J_1(2K_\epsilon)}) \times \sum_{j=2}^{t}\sum_{\alpha_1=0}^{j-2} J_0^{2\alpha_1}(K_\epsilon)J_0^{2(j-2-\alpha_1)}(2K_\epsilon) \quad \text{(A.7)}$$

$$C_{G2}^{+}t = 2K^2 \cos 2p_0\epsilon J_1^2(K_\epsilon)J_1(2K_\epsilon)\sum_{j=2}^{t}\sum_{\alpha_1=0}^{j-2}(2\alpha_1\frac{J_1(K_\epsilon)}{J_0(K_\epsilon)} + 2(j-2-\alpha_1)\frac{J_1(2K_\epsilon)}{J_0(2K_\epsilon)}) \times J_0^{2\alpha_1}(K_\epsilon)J_0^{2(j-2-\alpha_1)}(2K_\epsilon) \quad \text{(A.8)}$$

IIb (C_{G2}^{-},C_{G2}^{+}), $m_j = \pm 1,\pm 1,\pm 1,\mp 1$

$$C_{G2}^{-}t = -K^2 \cos 2p_0\epsilon J_1^2(K_\epsilon)J_1^3(2K_\epsilon)J_1^2(3K_\epsilon)(2\frac{J_0(K_\epsilon) - J_2(K_\epsilon)}{J_1(K_\epsilon)} + 3\frac{J_0(2K_\epsilon) - J_2(2K_\epsilon)}{J_1(2K_\epsilon)} + 2\frac{J_0(3K_\epsilon) - J_2(3K_\epsilon)}{J_1(3K_\epsilon)})\sum_{j=4}^{t}\sum_{\alpha_1=0}^{j-4}\sum_{\alpha_2=0}^{j-4-\alpha_1}\sum_{\alpha_3=0}^{j-4-(\alpha_1+\alpha_2)} J_0^{2\alpha_1}(K_\epsilon)J_0^{2(j-4-(\alpha_1+\alpha_3))}(2K_\epsilon)J_0^{2\alpha_3}(3K_\epsilon) \quad \text{(A.9)}$$

$$C_{G2}^{+}t = 2K^2 \cos 2p_0\epsilon J_1^2(K_\epsilon)J_1^3(2K_\epsilon)J_1^2(3K_\epsilon)\sum_{j=4}^{t}\sum_{\alpha_1=0}^{j-4}\sum_{\alpha_2=0}^{j-4-\alpha_1}\sum_{\alpha_3=0}^{j-4-(\alpha_1+\alpha_2)}(2\alpha_1\frac{J_1(K_\epsilon)}{J_0(K_\epsilon)} + 2(j-4-(\alpha_1+\alpha_3))\frac{J_1(2K_\epsilon)}{J_0(2K_\epsilon)} + 2\alpha_3\frac{J_1(3K_\epsilon)}{J_0(3K_\epsilon)})J_0^{2\alpha_1}(K_\epsilon)J_0^{2(j-4-(\alpha_1+\alpha_3))}(2K_\epsilon)J_0^{2\alpha_3}(3K_\epsilon) \quad \text{(A.10)}$$

IIIa (C_{G3}^{-},C_{G3}^{+}), $m_j = \pm1,\pm1,\pm1$

$$C_{G3}^{-}t = K^2\cos 3p_0\epsilon J_1^2(K_\epsilon)J_1^2(2K_\epsilon)J_1(3K_\epsilon)(2\frac{J_0(K_\epsilon)-J_2(K_\epsilon)}{J_1(K_\epsilon)}+2\frac{J_0(2K_\epsilon)-J_2(2K_\epsilon)}{J_1(2K_\epsilon)}$$
$$+\frac{J_0(3K_\epsilon)-J_2(3K_\epsilon)}{J_1(3K_\epsilon)})\sum_{j=3}^{t}\sum_{\alpha_1=0}^{j-3}\sum_{\alpha_2=0}^{j-3-\alpha_1}J_0^{2\alpha_1}(K_\epsilon)J_0^{2\alpha_2}(2K_\epsilon)J_0^{2(j-3-(\alpha_1+\alpha_2))}(3K_\epsilon) \tag{A.11}$$

$$C_{G3}^{+}t = -2K^2\cos 3p_0\epsilon J_1^2(K_\epsilon)J_1^2(2K_\epsilon)J_1(3K_\epsilon)\sum_{j=3}^{t}\sum_{\alpha_1=0}^{j-3}\sum_{\alpha_2=0}^{j-3-\alpha_1}(2\alpha_1\frac{J_1(K_\epsilon)}{J_0(K_\epsilon)}+2\alpha_2\frac{J_1(2K_\epsilon)}{J_0(2K_\epsilon)}$$
$$+2(j-3-(\alpha_1+\alpha_2))\frac{J_1(3K_\epsilon)}{J_0(3K_\epsilon)})J_0^{2\alpha_1}(K_\epsilon)J_0^{2\alpha_2}(2K_\epsilon)J_0^{2(j-3-(\alpha_1+\alpha_2))}(3K_\epsilon) \tag{A.12}$$

IIIb (C_{G3}^{-},C_{G3}^{+}), $m_j = \pm1,\pm1,\pm1,\pm1,\mp1$

$$C_{G3}^{-}t = K^2\cos 3p_0\epsilon J_1^2(K_\epsilon)J_1^2(2K_\epsilon)J_1^3(3K_\epsilon)J_1^2(4K_\epsilon)(2\frac{J_0(K_\epsilon)-J_2(K_\epsilon)}{J_1(K_\epsilon)}+2\frac{J_0(2K_\epsilon)-J_2(2K_\epsilon)}{J_1(2K_\epsilon)}$$
$$+3\frac{J_0(3K_\epsilon)-J_2(3K_\epsilon)}{J_1(3K_\epsilon)}+2\frac{J_0(4K_\epsilon)-J_2(4K_\epsilon)}{J_1(4K_\epsilon)})\sum_{j=5}^{t}\sum_{\alpha_1=0}^{j-5}\sum_{\alpha_2=0}^{j-5-\alpha_1}\sum_{\alpha_3=0}^{j-5-(\alpha_1+\alpha_2)}\sum_{\alpha_4=0}^{j-5-(\alpha_1+\alpha_2+\alpha_3)}$$
$$J_0^{2\alpha_1}(K_\epsilon)J_0^{2\alpha_2}(2K_\epsilon)J_0^{2(j-5-(\alpha_1+\alpha_2+\alpha_4))}(3K_\epsilon)J_0^{2\alpha_4}(4K_\epsilon) \tag{A.13}$$

$$C_{G3}^{+}t = -2K^2\cos 3p_0\epsilon J_1^2(K_\epsilon)J_1^2(2K_\epsilon)J_1^3(3K_\epsilon)J_1^2(4K_\epsilon)\sum_{j=5}^{t}\sum_{\alpha_1=0}^{j-5}\sum_{\alpha_2=0}^{j-5-\alpha_1}\sum_{\alpha_3=0}^{j-5-(\alpha_1+\alpha_2)}\sum_{\alpha_4=0}^{j-5-(\alpha_1+\alpha_2+\alpha_3}$$
$$(2\alpha_1\frac{J_1(K_\epsilon)}{J_0(K_\epsilon)}+2\alpha_2\frac{J_1(2K_\epsilon)}{J_0(2K_\epsilon)}+2(j-5-(\alpha_1+\alpha_2+\alpha_4))\frac{J_1(3K_\epsilon)}{J_0(3K_\epsilon)}+2\alpha_4\frac{J_1(4K_\epsilon)}{J_0(4K_\epsilon)}$$
$$\times J_0^{2\alpha_1}(K_\epsilon)J_0^{2\alpha_2}(2K_\epsilon)J_0^{2(j-5-(\alpha_1+\alpha_2+\alpha_4))}(3K_\epsilon)J_0^{2\alpha_4}(4K_\epsilon \tag{A.14}$$

IVa (C^{-}_{G4},C^{+}_{G4}), $m_j = \pm1,\pm1,\pm1,\pm1$

$$C^{-}_{G4}t = -K^2\cos 4p_0\epsilon J_1^2(K_\epsilon)J_1^2(2K_\epsilon)J_1^2(3K_\epsilon)J_1(4K_\epsilon)(2\frac{J_0(K_\epsilon)-J_2(K_\epsilon)}{J_1(K_\epsilon)}+2\frac{J_0(2K_\epsilon)-J_2(2K_\epsilon)}{J_1(2K_\epsilon)}$$
$$+2\frac{J_0(3K_\epsilon)-J_2(3K_\epsilon)}{J_1(3K_\epsilon)}+\frac{J_0(4K_\epsilon)-J_2(4K_\epsilon)}{J_1(4K_\epsilon)})\sum_{j=4}^{t}\sum_{\alpha_1=0}^{j-4}\sum_{\alpha_2=0}^{j-4-\alpha_1}\sum_{\alpha_3=0}^{j-4-(\alpha_1+\alpha_2)} J_0^{2\alpha_1}(K_\epsilon)J_0^{2\alpha_2}(2K_\epsilon)$$
$$\times J_0^{2\alpha_3}(3K_\epsilon)J_0^{2(j-4-(\alpha_1+\alpha_2+\alpha_3))}(4K_\epsilon) \tag{A.15}$$

$$C^{+}_{G4}t = 2K^2\cos 4p_0\epsilon J_1^2(K_\epsilon)J_1^2(2K_\epsilon)J_1^2(3K_\epsilon)J_1(4K_\epsilon)\sum_{j=4}^{t}\sum_{\alpha_1=0}^{j-4}\sum_{\alpha_2=0}^{j-4-\alpha_1}\sum_{\alpha_3=0}^{j-4-(\alpha_1+\alpha_2)}(2\alpha_1\frac{J_1(K_\epsilon)}{J_0(K_\epsilon)}$$
$$+2\alpha_2\frac{J_1(2K_\epsilon)}{J_0(2K_\epsilon)}+2\alpha_3\frac{J_1(3K_\epsilon)}{J_0(3K_\epsilon)}+2(j-4-(\alpha_1+\alpha_2+\alpha_3))\frac{J_1(4K_\epsilon)}{J_0(4K_\epsilon)})$$
$$\times J_0^{2\alpha_1}(K_\epsilon)J_0^{2\alpha_2}(2K_\epsilon)J_0^{2\alpha_3}(3K_\epsilon)J_0^{2(j-4-(\alpha_1+\alpha_2+\alpha_3))}(4K_\epsilon) \tag{A.16}$$

Momentum Independent Correlations

C_{G0}, $m_j = \pm1,\mp1$

$$C_{G0}t = -K^2J_1^2(K_\epsilon)\sum_{j=2}^{t}\sum_{\alpha_1=0}^{j-2}J_0^{2\alpha_1}(K_\epsilon) \tag{A.17}$$

C_{G0}, $m_j = \pm1,\pm1,\mp1,\mp1$

$$C_{G0}t = -K^2J_1^4(K_\epsilon)J_1^2(2K_\epsilon)\sum_{j=4}^{t}\sum_{\alpha_1=0}^{j-4}\sum_{\alpha_2=0}^{j-4-\alpha_1}\sum_{\alpha_3=0}^{j-4-(\alpha_1+\alpha_2)}J_0^{2(\alpha_1+\alpha_3)}(K_\epsilon)J_0^{2\alpha_2}(2K_\epsilon) \tag{A.18}$$

Bibliography

[1] see e.g.:

K.T. Alligood, *Chaos: an introduction to dynamical systems*, Springer Verlag New York, LLC (1997)

G. Casati and B.V. Chirikov, *The legacy of chaos in quantum mechanics* in *Quantum Chaos: Between order and disorder*, Cambridge University Press (1995)

R.L. Devaney, *An Introduction to Chaotic Dynamical Systems, 2nd ed*, Westview Press (2003)

J.P. Gollub and G.L. Baker, *Chaotic dynamics*, Cambridge University Press (1996)

M. Gutzwiller, *Chaos in Classical and Quantum Mechanics*, Springer Verlag New York, LLC (1990)

F. Haake, *Quantum Signatures of Chaos*, Springer Verlag (1992)

A.J. Lichtenberg and M.A. Lieberman, *Regular and Chaotic Dynamics*, Springer Verlag New York (1992)

F. Moon, *Chaotic and Fractal Dynamics*, Springer Verlag New York, LLC (1990)

E. Ott, *Chaos in Dynamical Systems*, Cambridge University Press New York (2002)

S. Strogatz, *Nonlinear Dynamics and Chaos*, Perseus Publishing (2000)

[2] V.M. Alekseev and M.V. Yakobson, Phys. Reports **75**, 287 (1981)

[3] M. Born, Z. Phys. **153**, 372 (1958)

G. Casati, B.V. Chirikov and J. Ford, Phys. Lett. A **77**, 91 (1980)

[4] F. Haake, *Quantum Signatures of Chaos*, pg.2, Springer Verlag (1992)

[5] G. Casati and B.V. Chirikov, *The legacy of chaos in quantum mechanics* in *Quantum Chaos: Between order and disorder*, Cambridge University Press (1995)

[6] *Quantum Measurement and Chaos*, Eds. E. Pike and S. Sarkar, Plenum, New York (1987)

Quantum Chaos - Quantum Measurement, Eds. P. Cvitanovic, I. Percival, A. Wirzba, Kluwer (1992)

[7] M.V. Berry and M. Tabor, Proc. R. Soc. London **A356**, 375 (1976)

[8] G.M. Zaslavskii and N.N. Filonenko, Sov. Phys. JETP **38**, 317 (1974)

M.V. Berry and M. Tabor, Proc. R. Soc. London **A349**, 101 (1976)

M.V. Berry, *Chaotic Behavior of Deterministic Systems* in Les Houches Session XXXVI 1981, Eds. G. Iooss, R.H. Helleman, R. Stora, North-Holland, Amsterdam (1983)

G. Bohigas and M.-J. Giannoni, in *Mathematical and Computational Methods in Nuclear Physics* in Lecture Notes in Physics **209**, Springer, Berlin, Heidelberg (1984)

[9] see e.g.:

M.L. Mehta, *Random Matrices and the Statistical Theory of Energy Levels*, Academic, New York (1965)

Statistical Theories of Spectra, Ed. C.E. Porter, Academic, New York (1965)

[10] T.A. Brody, T. Flores, J.B. French, P.A. Mello, A. Pandy and S.S.M. Wong, Rev. Mod. Phys. **53**, 385 (1981)

[11] M.V. Berry and M. Robnik, J. Phys. A **17**, 2413 (1984)

[12] G. Casati, F.M. Izrailev and L. Molinari, J. Phys. A: Math. Gen. **24**, 4755 (1991)

[13] see e.g.:

H.-J. Stöckmann, *Quantum Chaos: an Introduction*, Cambridge University Press (1999)

[14] G. Casati, B.V. Chirikov, J. Ford and F.M. Izrailev, Lecture Notes in Physics **93**, 334, Springer, Berlin (1979)

B.V. Chirikov, Phys. Rep. **52**, 263 (1979)

[15] A.B. Rechester and R.B. White, Phys. Rev. Lett. **44**, 1586 (1980)

[16] A.J. Lichtenberg and M.A. Lieberman, *Regular and Chaotic Dynamics*, Springer Verlag New York (1992)

[17] see e.g.:
D.L. Shepelyansky, Phys. Rev. Lett. **56**, 677 (1986)
G. Casati, B.V. Chirikov, J. Ford and F.M. Izrailev, Lecture Notes in Physics **93**, 334, Springer, Berlin (1979)
S. Fishman, D.R. Grempel and R.E. Prange, Phys. Rev. Lett. **49**, 509 (1982)

[18] K. Husimi, Proc. Phys. Math. Soc. Jpn. **22**, 264 (1940)
E. Prugovecki, Ann. Phys. (New York) **110**, 102 (1978)

[19] S.B. Lee and M.D. Feit, Phys. Rev. E **47**, 4552 (1993)

[20] M. Feingold, S. Fishman, D.R. Grempel and R.E. Prange, Phys. Rev. B **31**, R6852 (1985)
F.M. Izrailev, Phys. Rep. **196**, 299 (1990)

[21] F.M. Izrailev, Phys. Rev. Lett. **134A**, 13 (1988); Phys. Rep. **196**, 299 (1990); Phys. Rev. Lett. **56**, 541 (1986)

[22] M. Feingold and S. Fishman, Physica D **25**, 181 (1987)
M. Feingold, S. Fishman, D.R. Grempel and R.E. Prange, Phys. Rev. Lett. **61**, 377 (1988)
S.-J. Chang and K.-J. Shi, Phys. Rev. A **34**, 7 (1986)

[23] F.L. Moore, J.C. Robinson, C.F. Bharucha, B. Sundaram and M.G. Raizen, Phys. Rev. Lett. **75**, 4598 (1995)

[24] D.R. Graham, M. Schlautmann and P. Zoller, Phys. Rev. A **45**, R19 (1992)

[25] S. Fishman, D.R. Grempel and R.E. Prange, Phys. Rev. A **29**, 1639 (1984)
G. Casati, J. Ford, I. Guarneri and F. Vivaldi, Phys. Rev. A **34**, 1413 (1986)

[26] D.L. Shepelyansky, Phys. Rev. Lett. **56**, 677 (1986)

[27] G. Hur, C.E. Creffield, P.H. Jones and T.S. Monteiro, Phys. Rev. A **72**, 013403 (2005)

[28] F. Haake, *Quantum Signatures of Chaos*, pg.5, Springer Verlag (1992)

[29] T. Dittrich and R. Graham, Ann. of Phys. **200**, 363 (1990)

[30] H. Ammann, R. Gray, I. Shvarchuck and N. Christensen, Phys. Rev. Lett. **80**, 4111 (1998)

[31] S. Fishman, D.R. Grempel and R.E. Prange, Phys. Rev. Lett. **49**, 509 (1982)

[32] P.W. Anderson, Phys. Rev. **109**, 1492 (1958); Rev. Mod. Phys. **50**, 191 (1978)

[33] F. Haake, *Quantum Signatures of Chaos*, pg.162, Springer Verlag (1992)

[34] F.M. Izrailev and D.L. Shepelyansky, Sov. Phys. Dokl. **24**, 996 (1979); Theor. Math. Phys. **43**, 553 (1980)

[35] S. Wimberger, I. Guarneri and S. Fishman, *nlin*/0212033 (2002); Phys. Rev. Lett. **92**, 084102 (2004)

[36] B.G. Klappauf, W.H. Oskay, D.A. Steck and M.G. Raizen, Phys. Rev. Lett. **81**, 4044 (1998)
M.K. Oberthaler, R.M. Godun, M.B. d'Arcy, G.S. Summy and K. Burnett, Phys. Rev. Lett. **83**, 4447 (1999)
M.B. d'Arcy, R.M. Godun, M.K. Oberthaler, D. Cassettari and G.S. Summy, Phys. Rev. Lett. **87**, 74102 (2001)

[37] D.A. Steck, W.H. Oskay and M.G. Raizen, Phys. Rev. Lett. **88**, 120406 (2002); Science **293**, 274 (2001)
W.K. Hensinger, H. Hffner, A. Browaeys, N.R. Heckenberg, K. Helmerson, C. McKenzie, G.J. Milburn, W.D. Phillips, S.L. Rolston, H. Rubinsztein-Dunlop and B. Upcroft, Nature **412**, 52 (2001)

[38] E.J. Heller, Phys. Rev. Lett. **53**, 1515 (1984)
D. Delande and J.C. Gay, Phys. Rev. Lett. **59**, 1809 (1987)
R.L. Waterland, J.-M. Yuan, C.C. Martens, R.E. Gillilan and W.P. Reinhardt, Phys. Rev. Lett. **61**, 2733 (1988)
B. Eckhardt, G. Hose and E. Pollak, Phys. Rev. A **39**, 3776 (1989)
R.V. Jensen, M.M. Sanders, M. Saraceno and B. Sundaram, Phys. Rev. Lett. **63**, 2771 (1989)

[39] Z.-Y. Ma, M.B. d'Arcy and S.A. Gardiner, Phys. Rev. Lett. **93**, 164101 (2004)

[40] P. Szriftgiser, J. Ringot, D. Delande and J.-C. Garreau, Phys. Rev. Lett. **89**, 224101 (2002)

[41] T.S. Monteiro, P.A. Dando, N.A.C. Hutchings and M.R. Isherwood, Phys. Rev. Lett. **89**, 194102 (2002)

T. Jonckheere, M.R. Isherwood and T.S. Monteiro, Phys. Rev. Lett. **91**, 253003 (2003)

[42] P.H. Jones, M. Goonasekera, H.E. Saunders-Singer, T.S. Monteiro and D.R. Meacher, *physics*/0504096 (2005)
P.H. Jones, M. Goonasekera, D.R. Meacher, T. Jonckheere and T.S. Monteiro, Phys. Rev. Lett. **98**, 073002 (2007)

[43] R.P. Feynman, R.B. Leighton and M. Sands, *The Feynman Lectures on Physics*, Addison-Wesley, Reading (1963)

[44] P. Reimann, Phys. Rep. **361**, 57 (2002)

[45] T. Cheon, P. Exner and P. Seba, Journal of the Physical Society of Japan, **72**, 1087 (2003)

[46] M.R. Isherwood, Ph.D. thesis (2004)

[47] T.S. Monteiro, P.A. Dando, N.A.C. Hutchings and M.R. Isherwood, Phys. Rev. Lett. **89**, 194102 (2002)
N.A.C. Hutchings, M.R. Isherwood, T. Jonckheere and T.S. Monteiro, Phys. Rev. E **70**, 036205 (2004)

[48] M. Goonasekera, Ph.D. thesis (2004)

[49] M.M.A. Stocklin and T.S. Monteiro, Phys. Rev. E **74**, 026210 (2006)

[50] J. Wang and T.S. Monteiro, *cond-mat*/0702670 (2007)

[51] P.H. Jones, M.M.A. Stocklin, G. Hur and T.S. Monteiro, Phys. Rev. Lett. **93**, 223002 (2004)

[52] S. Fishman, D.R. Grempel and R.E. Prange, Phys. Rev. A **36**, 289 (1987)

[53] C.E. Creffield, G. Hur and T.S. Monteiro, Phys. Rev. Lett. **96**, 024103 (2006)
C.E. Creffield, S. Fishman and T.S. Monteiro, Phys. Rev. E **73**, 066202 (2006)

[54] K. Vant, G. Ball, H. Ammann and N. Christensen, Phys. Rev. E **59**, 2846 (1999)

[55] T. Geisel, G. Radons and J. Rubner, Phys. Rev. Lett. **57**, 2883 (1986)

[56] N.T. Maitra and E.J. Heller, Phys. Rev. E **61**, 3620 (2000)

[57] J. Wang, T.S. Monteiro, S. Fishman, J.P. Keating and R. Schubert, *to be published* (2007)

[58] G. Hur, Ph.D. thesis (2005)

[59] D. Delande, *Quantum Chaos in Atomic Physics* in Les Houches Session LXXII 1999, (2001)

[60] B.I. Shklovskii, B. Shapiro, B.R. Sears, P. Lambrianides and H.B. Shore, Phys. Rev. B **47**, 11487 (1993)

[61] T. Boness, S. Bose and T.S. Monteiro, Phys. Rev. Lett. **96**, 187201 (2006)

[62] T. Boness, M.M.A. Stocklin and T.S. Monteiro, Progress of Theoretical Physics Supplement **166**, 85 (2007)

[63] S. Bose, Phys. Rev. Lett. **91**, 207901 (2003)

[64] T. Shi, Y. Li, Z. Song and C.P. Sun, Phys. Rev. A **71**, 032309 (2005)

[65] M. Karbach and G. Müller, Computers in Physics **11**, 36 (1997)

[66] T.J. Osborne and N. Linden, Phys. Rev. A **69**, 052315 (2004)

[67] see e.g.:
E. Hinds and I.G. Hughes, J. Phys. D **32**, 119 (1999)

[68] J. Reslen, C.E. Creffield and T.S. Monteiro, *quant-ph*/07071653 (2007)

[69] A. Lakshminarayan, Phys. Rev. E **64**, 036207 (2001)

[70] J.N. Bandyopadhyay and A. Lakshminarayan, Phys. Rev. Lett. **89**, 060402 (2002)

[71] X. Wang, S. Ghose, B.C. Sanders and B. Hu, Phys. Rev. E **70**, 016217 (2004)

[72] see e.g.:
K. Furuya, M.C. Nemes and G.Q. Pellegrino, Phys. Rev. Lett. **80**, 5524 (1998)
P.A. Miller and S. Sarkar, Phys. Rev. E **60**, 1542 (1999)
H. Fujisaki, T. Miyadera and A. Tanaka, Phys. Rev. E **67**, 066201 (2003)

[73] S. Bettelli and D.L. Shepelyansky, Phys. Rev. A **67**, 054303 (2003)

[74] see e.g.:
B. Georgeot and D.L. Shepelyansky, Phys. Rev. E **62**, 3504 (2000); Phys. Rev. Lett. **86**, 2890 (2001)

[75] D. Schrader, I. Dotsenko, M. Khudaverdyan, Y. Miroshnychenko, A. Rauschenbeutel and D. Meschede, Phys. Rev. Lett. **93**, 150501 (2004)